

# **Automated Analysis of Ground Penetrating Radar Outputs for Bridge Condition Assessment**

Mohammed Abdul Rahman

A Thesis  
In the Department  
of  
Building, Civil, and Environmental Engineering

Presented in Partial Fulfillment of the  
Requirements For the Degree of  
Doctor of Philosophy (Building Engineering)  
at Concordia University  
Montreal, Quebec, Canada

September 2023

© Mohammed Abdul Rahman, 2023

**CONCORDIA UNIVERSITY**

**SCHOOL OF GRADUATE STUDIES**

This is to certify that the thesis

prepared By: **Mohammed Abdul Rahman**

Entitled: **Automated Analysis of Ground Penetrating Radar Outputs for Bridge Condition Assessment**

and submitted in partial fulfillment of the requirements for the degree of

**Doctor of Philosophy (Building Engineering)**

complies with the regulations of the University and meets the accepted standards with respect to originality and quality.

Signed by the Final Examining Committee:

_____	Chair
Dr. René Witte	
_____	External Examiner
Dr. Imad L Al-Qadi	
_____	Examiner
Dr. Arash Mohammadi	
_____	Examiner
Dr. Fuzhan Nasiri	
_____	Examiner
Dr. Po-Han Chen	
_____	Co-Supervisor
Dr. Ashutosh Bagchi	
_____	Co-Supervisor
Dr. Tarek Zayed	

Approved by

\_\_\_\_\_  
Dr. Chunjiang An, Graduate Program Director

September 29, 2023

\_\_\_\_\_  
Dr. Mourad Debbabi, Dean of Faculty

## ABSTRACT

Automated Analysis of Ground Penetrating Radar Outputs for Bridge Condition Assessment

Mohammed Abdul Rahman, Ph.D.

Concordia University, 2023

Bridge infrastructure requires periodical inspection, repair-maintenance, or complete replacement of bridges for long-term safety and sustainability. The *visual inspection method* has been predominantly used by transportation agencies for bridge condition assessment whereby qualified bridge inspectors visually observe the surface defects and based on their knowledge, scale the bridge components according to their condition. However, this method does not provide accurate information about the bridge condition due to its inability to detect internal defects. While various non-destructive techniques are being increasingly adopted for wholesome condition assessment, Ground Penetrating Radar (GPR) is recommended for bridge evaluation due to its distinct advantages of identifying major subsurface defects rapidly. The interpretation of data obtained from GPR profiles is a major issue for bridge inspectors due to inconsistent correlation with the actual bridge condition. Federal agencies commonly employ an amplitude-based approach that involves picking amplitude values at specific locations in a GPR profile which are indicative of concrete corrosion levels. However, this approach may not always yield reliable results as it disregards the majority of the information present within a GPR profile. A novel approach based on image-based analysis involves an experienced analyst reviewing the GPR profiles and marking attenuated areas across them while considering structural and surface anomalies, and other several parameters,

which are typically ignored in amplitude-based analysis. Thus, this holistic method generates less noisy condition maps and has demonstrated good correspondence with the actual ground condition. However, this approach is highly subjective, dependent on the level of knowledge of the analyst, and time-consuming. To overcome these shortcomings, the image-based approach of analyzing GPR data has been automated based on scientific analysis and image processing tools by evaluating the GPR profiles as images since most of the information contained in these profiles can be better analyzed visually. Two successful models have been developed which generate *reliable condition maps*. The first comprehensive model is based on *Viola-Jones Algorithm*, and it identifies hyperbolic regions automatically with a trained classifier to develop condition maps using *entropy* values of detected regions and K-means clustering. The second model is relatively a more *robust* and wholesome approach for analyzing GPR data as it considers user-assisted information, identifies complex hyperbolic signatures based on downward openings and local maximums of the distance transform image, detects anomalies, and assigns an optimal cluster value to generate condition maps. As part of the validation, both these methods were implemented on real case studies that have shown good resemblance with the existing amplitude-based approach, image-based analysis, and more importantly, *correlated* with the destructive coring samples. Finally, lab tests were conducted in a controlled environment to evaluate the measured factor, entropy, used for detected regions and compare it with the amplitude values for subsurface objects and the results indicated that entropy yielded comparatively *better results* for all cases (rebars, air gaps, and water gaps). Consequently, condition maps generated based on developed models can be efficiently used by bridge inspectors in making informed decisions regarding the repair and rehabilitation of reinforced concrete bridges



## ACKNOWLEDGEMENTS

First and foremost, all praises belong to the Almighty Allah, the most merciful and most compassionate, for bestowing me with health, knowledge, and patience to carry out this research work with utmost sincerity. I wish to acknowledge Concordia University for providing me with financial support, an excellent academic environment, and research facilities during my doctoral studies.

My deepest gratitude and appreciation go to my thesis supervisor, Prof. Ashutosh Bagchi, for his constant help, guidance, and motivation during my research. He has been the strongest pillar of my support system by showing the utmost faith and confidence in me even during the toughest of times. I would like to express my sincere appreciation to Dr. Tarek Zayed for initiating my research work and shaping its development. I wish to convey my warmest gratitude to Mr. Alex Tarussov, President of Radex Detection Inc., for his relentless support, for providing relevant material, and for imparting his supreme wisdom concerning the practical application of Ground Penetrating Radar.

I wish to express my heartfelt gratitude to all the wonderful colleagues I have had the pleasure to work with, especially Dr. Fawzi Latosh and Dipesh Donda. I would like to thank the closest of my friends: Azhars', Abdul-Lateef, Abubaker, Arshad, Faizan, and Nadeem, among others who have always believed in my abilities and have given me constant encouragement. Lastly, I wish to thank and dedicate this thesis to my wonderful parents and my sweetest sister for their incessant prayers, unwavering support, and encouragement throughout my life.

# **TABLE OF CONTENTS**

<b>LIST OF TABLES .....</b>	<b>x</b>
<b>LIST OF FIGURES .....</b>	<b>xi</b>
<b>LIST OF ABBREVIATIONS .....</b>	<b>xvi</b>
<b>1 INTRODUCTION .....</b>	<b>1</b>
1.1 Problem Statement and Research Motivation .....	1
1.2 Objectives of Research.....	3
1.3 Summary of Research Methodology.....	4
1.4 Structure of the Thesis.....	5
<b>2 LITERATURE REVIEW .....</b>	<b>7</b>
2.1 Background of Bridge inspection.....	7
2.2 Bridge Management .....	8
2.3 Bridge Management System (BMS) .....	8
2.4 Bridge Inspection Overview.....	13
2.5 Types of Bridge Deck defects .....	14
2.5.1 Rebar Corrosion .....	16
2.5.2 Deck delamination .....	19
2.5.3 Vertical Cracking.....	19
2.5.4 Concrete Deterioration.....	21
2.6 Type of Bridge Inspections .....	23
2.6.1 Impact Echo .....	26
2.6.2 Ultrasonic Pulse Echo (UPE).....	27
2.6.3 Impulse Response .....	29
2.6.4 Ground-Penetrating Radar .....	30
2.6.5 Half-Cell Potential .....	33
2.6.6 Galvanostatic pulse measurement (GPM) .....	34
2.6.7 Electrical Resistivity (ER) .....	35
2.6.8 Infrared (IR) Thermography .....	36
2.6.9 Chain Dragging and Hammer Sounding.....	38
2.6.10 Visual Inspection .....	39

2.7	Selection of recommended NDT Technique – GPR .....	39
2.8	GPR inspection and data analysis .....	41
2.8.1	GPR Survey Strategies.....	41
2.8.2	GPR principles and existing approaches.....	46
2.8.3	Numerical Amplitude-Based Analysis (ABA) .....	52
2.8.4	Limitations of Numerical-ABA .....	54
2.9	GPR Image-Based Analysis (IBA) .....	55
2.9.1	Methodology .....	55
2.9.2	Significance and Limitations .....	59
2.10	Previous Efforts of Image Processing .....	61
2.11	Key Findings and Research Gap .....	65
2.12	Preliminary Investigations.....	66
2.13	Image Processing Overview.....	67
2.14	Digital Image Processing using MATLAB .....	73
2.15	Computer Vision .....	75
2.16	Methods Explored on GPR Data.....	81
2.16.1	Colormap.....	81
2.16.2	Thresholding .....	85
2.16.3	Edge Detection.....	92
2.16.4	Segmentation.....	99
2.16.5	Region Properties and Clustering .....	102
2.16.6	Texture Filters.....	104
2.16.7	Object Detection and Feature Extraction:.....	108
<b>3</b>	<b>RESEARCH METHODOLOGY.....</b>	<b>112</b>
3.1	X- Sim Method.....	113
3.1.1	Image Conversion and Preprocessing.....	113
3.1.2	Evaluate standard filter and summation.....	115
3.1.3	K-means clustering and condition mapping .....	117
3.2	Viola-Jones Algorithm-based Model (V-JAM) .....	122
3.2.1	Pre-process GPR profiles.....	123
3.2.2	Trained Classifier and Hyperbola Detections .....	127

3.2.3	Regional comparison and Statistical analysis .....	132
3.2.4	Condition Mapping .....	141
3.3	Robust User-Interactive Model (RUIM) .....	144
3.3.1	Obtain GPR scans, pre-processing, and User-Assisted input .....	145
3.3.2	Robust Open-Scan Clustering Algorithm (OSCA) (Zhou et al., 2018).....	149
3.3.3	Robust Hyperbolic Detections .....	153
3.3.4	Regional comparison, statistical analysis, and user-labeled anomalies module.....	182
3.3.5	Condition mapping.....	188
<b>4</b>	<b>CASE STUDIES FOR THE DEVELOPED MODELS .....</b>	<b>190</b>
4.1	Case Study A – Condition mapping based on the X-Sim Method.....	190
4.1.1	Data Collection of GPR data.....	191
4.1.2	Maps generated with ABA and analysis by other NDTs.....	192
4.1.3	Maps Generated based on GPR-IBA and developed X-Sim Method.....	193
4.1.4	Limitations .....	198
4.2	Case Study B – Condition Mapping based on V-JAM .....	199
4.2.1	Data Collection .....	199
4.2.2	Data Processing.....	201
4.2.3	Results and their discussion .....	202
4.2.4	Limitations .....	205
4.3	Case Study C – Condition Mapping based on RUIM .....	208
4.3.1	Data Collection .....	208
4.3.2	Results and discussion .....	208
4.4	GPR-CAT (GPR-based Condition Assessment Tool) .....	213
<b>5</b>	<b>LAB TESTS AND FURTHER CASE STUDIES .....</b>	<b>224</b>
5.1	Laboratory Testing – Entropy evaluation of subsurface objects in Concrete Slabs.....	224
5.1.1	Experimental Setup.....	224
5.1.2	Comparative analysis for rebars.....	228
5.1.3	Comparative analysis for air gaps.....	230
5.1.4	Comparative analysis for water gaps .....	231
5.1.5	Comparative analysis for different materials.....	232
5.2	Case Study D – Viaduct Elm P-13486-02.....	234

5.2.1	Data Collection .....	234
5.2.2	Condition mapping.....	236
5.3	Case Study E – Viaduct Beaurepaire P-13486-03 .....	238
5.3.1	Data Collection .....	238
5.3.2	Condition mapping.....	238
<b>6</b>	<b>CONCLUSIONS AND LIMITATIONS.....</b>	<b>240</b>
6.1	Research Summary and Conclusions .....	240
6.2	Limitations and Future recommendations.....	244
<b>7</b>	<b>REFERENCES .....</b>	<b>246</b>
<b>8</b>	<b>APPENDIX.....</b>	<b>262</b>

## LIST OF TABLES

<b>Table 2.1</b> Consequences of Deterioration in RC Structures (Bien et al., 2007).....	14
<b>Table 2.2</b> Summary of Common Problems in Concrete Bridge Decks (Yehia et al., 2007) .....	15
<b>Table 2.3</b> List of various NDTs for reinforced concrete bridge deck inspection (Gucunski & National Research Council, 2013) .....	23
<b>Table 2.4</b> Summary of NDT Techniques for Bridge Deck (Yehia et al., 2007) .....	24
<b>Table 2.5</b> Overall Value of NDT Technology in Bridge Deck Deterioration Detection (Gucunski & National Research Council, 2013) .....	40
<b>Table 2.6</b> GPR Data Analysis Improvement over the Years.....	50
<b>Table 2.7</b> Image Processing efforts of hyperbolic signatures detection in GPR Profiles .....	62
<b>Table 2.8</b> Built-in Colormaps in MATLAB (Marques, 2011) .....	84
<b>Table 2.9</b> MATLAB functions - Texture filters (The MathWorks, 2014).....	105
<b>Table 2.10</b> Local Feature Detectors - MATLAB functions (The MathWorks, 2014) .....	109
<b>Table 3.1</b> Condition and Considerations for the training set (MathWorks, 2016).....	130
<b>Table 3.2</b> Equations for measuring distance metrics (The MathWorks, 2014).....	171
<b>Table 3.3</b> Anomalies Detections based on the characteristic features in GPR Profiles .....	184
<b>Table 4.1</b> Quantitative Comparison of deteriorated areas (M Abdul Rahman & Zayed, 2016)	198
<b>Table 4.2</b> Range of entropy values in generated deterioration maps (Mohammed Abdul Rahman, Zayed, et al., 2022) .....	203
<b>Table 4.3</b> Quantitative comparison of maps based on the color distribution (concrete condition) (Mohammed Abdul Rahman, Zayed, et al., 2022) .....	204
<b>Table 4.4</b> Quantitative comparison of deteriorated areas.....	211
<b>Table 4.5</b> Validation of ground truth with GPR-IBA and RUIM condition maps.....	212
<b>Table 5.1</b> Comparison of Amplitudes for different materials (Donda et al., 2021) .....	233
<b>Table 5.2</b> Comparison of Entropies for different materials (Mohammed Abdul Rahman, Donda, et al., 2022) .....	233

## LIST OF FIGURES

<b>Figure 2.1</b> A basic BMS (Ryall, 2009) .....	12
<b>Figure 2.2</b> Components of a BMS System (Elbehairy et al., 2006).....	13
<b>Figure 2.3</b> Deck deterioration (Gucunski & National Research Council, 2013) .....	15
<b>Figure 2.4</b> Carbonation process and its effect on concrete building façade (PCA, 2016).....	18
<b>Figure 2.5</b> Corrosion due to chlorination because of penetration of deicing salts (Gucunski & National Research Council, 2013) .....	18
<b>Figure 2.6</b> Electrolytic reaction in rebars (PCA, 2016) .....	19
<b>Figure 2.7</b> Delamination observed in cores (Gucunski & National Research Council, 2013) ...	20
<b>Figure 2.8</b> Underside of Route 123 Bridge Deck Showing Cracking (Sharp & Moruza, 2009) .	21
<b>Figure 2.9</b> a) ASR and b) DEF cracking in bridge deck (Gucunski & National Research Council, 2013) .....	22
<b>Figure 2.10</b> Selection of NDT techniques based on different defects and damages (Kashif Ur Rehman et al., 2016) .....	25
<b>Figure 2.11</b> Stepper (left) and bridge deck scanner (right) (Gucunski & National Research Council, 2013).....	27
<b>Figure 2.12</b> (a) Shear-wave probe array A1220 (a), and (b) automated A1220 measurements using stepper (Gucunski & National Research Council, 2013) .....	28
<b>Figure 2.13</b> USW testing using a portable seismic property analyzer (Gucunski & National Research Council, 2013).....	29
<b>Figure 2.14</b> (a) Impulse sound testing and (b) Principles of impulse response testing (Gucunski & National Research Council, 2013) .....	30
<b>Figure 2.15</b> GPR scanning a bridge deck in Laval using wheel-mounted equipment .....	32
<b>Figure 2.16</b> GPR principle (Gucunski & National Research Council, 2013) .....	33
<b>Figure 2.17</b> HCP testing (Gucunski & National Research Council, 2013).....	34
<b>Figure 2.18</b> (a) GPM Testing and (b) GPM Principle (Gucunski & National Research Council, 2013) .....	35
<b>Figure 2.19</b> Electrical Resistivity testing using a Wenner probe (Gucunski & National Research Council, 2013).....	36
<b>Figure 2.20</b> Infrared thermography testing using IR cameras (Gucunski & National Research Council, 2013).....	37
<b>Figure 2.21</b> Principle of passive infrared thermography (Gucunski & National Research Council, 2013) .....	37
<b>Figure 2.22</b> Chain Dragging (left) and Hammer Sounding (right) (Gucunski & National Research Council, 2013).....	38
<b>Figure 2.23</b> GPR Equipment (GSSI, 2022).....	46
<b>Figure 2.24</b> A- Scan (Abdel-Qader et al., 2014).....	49
<b>Figure 2.25</b> B-Scan (marked vertical white-line represents extracted trace in Fig 2.23) (Abdel-Qader et al., 2014).....	49
<b>Figure 2.26</b> Picking of points in a GPR profile for amplitude analysis (Tarussov et al., 2013)..	53
<b>Figure 2.27</b> Marking attenuated areas using Image-based Analysis (Tarussov et al., 2013).....	57

<b>Figure 2.28</b> Zone of corrosion & anomaly distinguished by GPR-IBA (Tarussov et al., 2013) .	57
<b>Figure 2.29</b> Framework of GPR-IBA analysis (Abouhamad et al., 2017).....	58
<b>Figure 2.30</b> Image sharpening: (a) original image; (b) after sharpening (Marques, 2011).....	69
<b>Figure 2.31</b> Noise removal: (a) original (noisy) image; (b) after removing noise (Marques, 2011) .....	70
<b>Figure 2.32</b> Deblurring: (a) original blurry image (b) after removing motion (blur) (Marques, 2011) .....	70
<b>Figure 2.33</b> Edge extraction: (a) original image; (b) after extracting its most relevant edges (Marques, 2011).....	71
<b>Figure 2.34</b> Binarization (a) original grayscale image (b) conversion to a black and white binary image (Marques, 2011) .....	71
<b>Figure 2.35</b> Blurring (a) original image (b) blurred image after removing unnecessary details (Marques, 2011).....	72
<b>Figure 2.36</b> Contrast enhancement (a) original image (b) contrast enhancement after histogram equalization (Marques, 2011) .....	72
<b>Figure 2.37</b> Object segmentation and labeling (a) original image (b) image with individual objects labeled and segmented (Marques, 2011) .....	73
<b>Figure 2.38</b> Petals of a flower are easily distinguished by human vision from the background (Szeliski, 2010) .....	75
<b>Figure 2.39</b> Some examples of computer vision algorithms and applications (Szeliski, 2010) ..	77
<b>Figure 2.40</b> Some industrial applications of computer vision (Szeliski, 2010) .....	78
<b>Figure 2.41</b> Components of a computer vision system (Marques, 2011) .....	80
<b>Figure 2.42</b> Methods investigated in this study with GPR profiles .....	82
<b>Figure 2.43</b> Sample GPR Profile - Yellow zones potentially indicate areas of moderate corrosion (Mohammed Abdul Rahman et al., 2016) .....	84
<b>Figure 2.44</b> Colormap ( <i>hsv</i> ) applied over the profile.....	85
<b>Figure 2.45</b> Otsu's Threshold on GPR Profile Sample.....	89
<b>Figure 2.46</b> Basic Global Thresholding of Image.....	91
<b>Figure 2.47</b> Adaptive Thresholding of the sample GPR Profile .....	91
<b>Figure 2.48</b> Multi-thresholding of the sample GPR Profile.....	92
<b>Figure 2.49</b> Neighborhood of a pixel (a) and masks for Roberts (b), Prewitt (c) and Sobel, and (d) Edge Operators (top to bottom) (Gonzalez et al., 2010) .....	95
<b>Figure 2.50</b> Laplacian of Gaussian (a) 3D Plot; (b) 2D intensity plot; (c) cross-section of (a); and (d) a 5x5 mask approximation to the shape in (a) from (Marques, 2011) .....	96
<b>Figure 2.51</b> Application of edge detectors on sample GPR profile (a) Roberts; (b) Prewitt; (c) Sobel; (d) LoG; (e) Zerocross and (f) Canny.....	98
<b>Figure 2.52</b> (a) Grey-scale image (left); and (b) Image viewed as a topological surface with ridge lines and catchment basins (Gonzalez et al., 2010) .....	100
<b>Figure 2.53</b> Watershed Segmentation of the Sample GPR Profile .....	101
<b>Figure 2.54</b> Identifying region properties and K-means clustering of a GPR profile.....	104
<b>Figure 2.55</b> Determining Pixel Values in Range Filtered Output Image (The MathWorks, 2014) .....	106



<b>Figure 2.56</b> Texture Filters (a) entropy filter; (b) standard filter and (c) range filter .....	107
<b>Figure 2.57</b> Detections of points and regions (local features) using multiple algorithms .....	110
<b>Figure 3.1</b> Flowchart for the X-Sim method.....	114
<b>Figure 3.2</b> Image Preprocessing - Applying a contrast filter. ....	115
<b>Figure 3.3</b> (a) Sample GPR Profile; and (b) Output image with deterioration scale (Mohammed Abdul Rahman et al., 2016) .....	121
<b>Figure 3.4</b> Methodology of V-JAM to generate condition maps.....	122
<b>Figure 3.5</b> A GPR profile section of a large bridge deck (Rahman & Zayed, 2018).....	126
<b>Figure 3.6</b> A sub-section of the GPR profile after applying pre-processing steps including horizontal stretching, range gain, and background removal (Rahman & Zayed, 2018).....	126
<b>Figure 3.7</b> Framework of Cascade Object Detector (MathWorks, 2016).....	128
<b>Figure 3.8</b> A sample GPR profile showing true positives and false detections (Mohammed Abdul Rahman, Zayed, et al., 2022) .....	129
<b>Figure 3.9</b> Regional Comparison – Identifying horizontal layers and eliminating false positives .....	133
<b>Figure 3.10</b> A sample cut-out of a GPR profile after applying a custom classifier (Mohammed Abdul Rahman, Zayed, et al., 2022).....	135
<b>Figure 3.11</b> A sample cut-out of a GPR profile after complete detections (Mohammed Abdul Rahman, Zayed, et al., 2022) .....	135
<b>Figure 3.12</b> The sample GPR profile is shown with missing detections. ....	139
<b>Figure 3.13</b> Missing gaps in a GPR profile filled for varying cases.....	140
<b>Figure 3.14</b> A sample GPR profile with detections in red boxes, entropy values enclosed, and deterioration scale in color on top (Mohammed Abdul Rahman, Zayed, et al., 2022).....	142
<b>Figure 3.15</b> Flowchart of the RUIM .....	147
<b>Figure 3.16</b> (a) Three-point segments with a downward opening; (b) Three-point segments with an upward opening; and (c) Two examples that can't be defined as openings (Zhou et al., 2018) .....	150
<b>Figure 3.17</b> (a) A hyperbolic feature in binary form; (b) pixels of the hyperbola with a downward opening; (c) the main top point-segment of the opening $X_l$ to $X_r$ and (d) the obtained <i>top</i> in green along with <i>tails</i> in red (Zhou et al., 2018) .....	151
<b>Figure 3.18</b> (a) $H$ - GPR profile sample imported into MATLAB with its histogram (Mohammed Abdul Rahman et al., 2016); (b) Profile after brightening of lighter pixels with its histogram; (c) Profile showing noise of image (a) with its histogram .....	157
<b>Figure 3.19</b> (a) Profile after removing noise with histogram; (b) Profile image binarized after Otsu's multi-threshold; and (c) $BW_p$ - Final preprocessed image after morphological operations .....	158
<b>Figure 3.20</b> (a) GPR Image (Zhou et al., 2018); (b) Image preprocessed after noise removal; (c) Preprocessed binarized image.....	161
<b>Figure 3.21</b> (a) GPR Image (Zhou et al., 2018), (b) Image thresholded based on gradient information (Zhou et al., 2018), (c) Image thresholded based on (Otsu, 1979), (d) Image thresholded based on maximum entropy (Kapur et al., 1985); (e) Unimodal thresholding (Rosin, 2001) .....	161

<b>Figure 3.22</b> (a) Image preprocessed after noise removal; (b) Final preprocessed image .....	162
<b>Figure 3.23</b> (a) GPR image (Zhou et al., 2018); (b) Image thresholded based on gradient information (Zhou et al., 2018), (c) Image preprocessed (noise removal) based on the proposed model.....	162
<b>Figure 3.24</b> (a) pixel p with its 4 adjacent neighbors, p & pixel q are 4- <i>adjacent</i> ; (b) pixel p with its 4 diagonal neighbors including q ; (c) Grey-shaded foreground pixels are 4-connected (Gonzalez et al., 2010).....	164
<b>Figure 3.25</b> $BW_b$ -Boundary pixels of a binarized GPR sample .....	165
<b>Figure 3.26</b> A valid point segment in the $i^{\text{th}}$ row. ....	166
<b>Figure 3.27</b> $BW_{ps}$ - Image overlaid with valid point segments in red.....	166
<b>Figure 3.28</b> $BW_i$ - boundary pixel image with inner boundaries overlaid.....	168
<b>Figure 3.29</b> $BW_{ir}$ - boundary pixel image with filtered inner boundaries overlaid. ....	169
<b>Figure 3.30</b> A hyperbolic detection with its preprocessed image and 4 distance transformations .....	170
<b>Figure 3.31</b> Distance transform of the preprocessed image.....	172
<b>Figure 3.32</b> (a) A hyperbolic arc section of the distance transform with index values; (b) Local maximums overlaid in red color on the original image .....	173
<b>Figure 3.33</b> $BW_c$ - Possible hyperbolic clusters overlaid on the original image, $H$ .....	173
<b>Figure 3.34</b> (a) Inner boundary of the hyperbola; (b) local maximums overlaid on the hyperbola; (c) hyperbolic cluster with inner boundary overlaid. ....	177
<b>Figure 3.35</b> $BW_{pc}$ - Hyperbolic point clusters with inner boundaries overlaid on the GPR profile, $H$ .....	178
<b>Figure 3.36</b> Hyperbolic curve plotted with vertex and center.....	181
<b>Figure 3.37</b> $BW_{hc}$ – Hyperbolic curves with vertex and center overlaid on the profile, $H$ .....	182
<b>Figure 3.38</b> $BW_{tl}$ -Top layer identified based on regional comparison .....	183
<b>Figure 3.39</b> $BW_f$ – Final processed image after automated detections.....	188
<b>Figure 3.40</b> Flowchart to determine the number of optimal clusters ( $k$ ) based on user-information .....	189
<b>Figure 4.1</b> Deck O2 cross-section with 60 ft clear span (Gucunski et al., 2011).....	190
<b>Figure 4.2</b> Deck O2 Data Collection with multiple NDTs – Grid pattern at 2 ft apart (Gucunski et al., 2011) .....	191
<b>Figure 4.3</b> Map Generated based on HC Potential and GPR along with Cores 1-4 marked with repairs overlaid (Gucunski et al., 2011).....	195
<b>Figure 4.4</b> IE & Electrical Resistivity maps with repairs overlaid (Gucunski et al., 2011).....	196
<b>Figure 4.5</b> Condition maps based on GPR-IBA (M Abdul Rahman & Zayed, 2016).....	197
<b>Figure 4.6</b> Condition map based on X-Sim Method (M Abdul Rahman & Zayed, 2016) .....	197
<b>Figure 4.7</b> Parking lot scanned using GPR across both directions of the slab surface (Mohammed Abdul Rahman, Zayed, et al., 2022) .....	201
<b>Figure 4.8</b> Condition maps comparison along X-direction (Mohammed Abdul Rahman, Zayed, et al., 2022) .....	206
<b>Figure 4.9</b> Condition maps comparison along the Y-direction (Mohammed Abdul Rahman, Zayed, et al., 2022) .....	207

<b>Figure 4.10</b>	A GPR profile of Bridge deck, O2, with automated detections enclosed .....	209
<b>Figure 4.11</b>	(a) Condition map based on GPR-IBA with core locations (1-4); (b) Condition map based on developed RUIIM with core locations (1-4) .....	210
<b>Figure 4.12</b>	User-Interface of the designed app termed as GPR_CAT .....	213
<b>Figure 4.13</b>	User-Prompted to select a folder containing GPR image files. ....	214
<b>Figure 4.14</b>	Folder ‘Iowa’ containing all its 24 profiles. ....	215
<b>Figure 4.15</b>	User-assisted Input for the GPR scanned deck. ....	216
<b>Figure 4.16</b>	User is prompted to confirm if the specified layer is identified correctly. ....	217
<b>Figure 4.17</b>	User is prompted to enclose a hyperbolic region at the required layer of analysis. ....	218
<b>Figure 4.18</b>	The tool automatically splits into possible hyperbolic regions along the top layer with reasonable accuracy. ....	218
<b>Figure 4.19</b>	GPR profile with an expansion joint .....	219
<b>Figure 4.20</b>	Colormap of the profile with a user-input dialog box to assign anomalies. ....	220
<b>Figure 4.21</b>	Normalized EUC similarity matrix map of HOG features for all regions. ....	221
<b>Figure 4.22</b>	Colormap of a GPR profile with a user-input dialog box to assign anomalies. ....	222
<b>Figure 4.23</b>	Normalized EUC similarity matrix map of HOG features for all boxes. ....	223
<b>Figure 5.1</b>	GPR antenna mounted on a Model 615 handcart (Donda et al., 2021) .....	224
<b>Figure 5.2</b>	(a) Three slabs were cast in the laboratory with dimensions shown; (b) Various sizes of rebars used for testing Used (Left to Right; 6 mm, 10 mm, 18 mm, 20 mm, & FRP 21.8 mm) (Donda et al., 2021) .....	226
<b>Figure 5.3</b>	(a) Various sizes of metal strips used (Left to Right; 1 mm, 3 mm, & 4.8 mm thickness); (b) Schematic diagram to simulate water gap at 15 cm depth (Donda et al., 2021). ....	227
<b>Figure 5.4</b>	(a) Measuring amplitude at peak (red dot); and (b) Measuring Entropy for the bounded region (red box) (Mohammed Abdul Rahman, Donda, et al., 2022) .....	228
<b>Figure 5.5</b>	(a) Amplitudes for rebars of varying sizes (Donda et al., 2021); (b) Entropies for rebars of varying sizes (Mohammed Abdul Rahman, Donda, et al., 2022) .....	229
<b>Figure 5.6</b>	(a) Amplitudes for varying thicknesses of air (Donda et al., 2021); (b) Entropies for varying thicknesses of air gaps (Mohammed Abdul Rahman, Donda, et al., 2022) .....	230
<b>Figure 5.7</b>	(a) Amplitudes for varying thicknesses of water gaps (Donda et al., 2021); (b) Entropies for varying thicknesses of water gaps (Mohammed Abdul Rahman, Donda, et al., 2022) .....	231
<b>Figure 5.8</b>	Location of Elm and Beaurepaire overpass in Beaconsfield, QC .....	234
<b>Figure 5.9</b>	Viaduct Elm Plan .....	235
<b>Figure 5.10</b>	Viaduct Elm maps with the location of Cores marked as C1-C3 including (a) GPR-IBA in Surfer®; (b) GPR-IBA in Radex and (c) RUIIM-based map .....	237
<b>Figure 5.11</b>	Viaduct Beaurepaire Plan .....	239
<b>Figure 5.12</b>	Viaduct Beaurepaire maps with the location of Cores marked as C1-C3 including (a) GPR-IBA map in Surfer®; (b) GPR-IBA map in Radex and (c) RUIIM-based map .....	239

## LIST OF ABBREVIATIONS

<b>AASHTO:</b>	American Association of State Highway and Transportation Officials
<b>ABA:</b>	Amplitude Based Analysis
<b>ACI:</b>	American Concrete Institute
<b>ASR:</b>	Alkali-silica reaction
<b>ASTM:</b>	American Society for Testing and Materials
<b>BI:</b>	Binary Image
<b>BMS:</b>	Bridge Management System
<b>BRISK:</b>	Binary Robust Invariant Scalable Keypoints
<b>C3:</b>	Column-Connection Clustering algorithm
<b>CGI:</b>	Computer-Generated Imagery
<b>CIRC:</b>	Canadian Infrastructure Report Card
<b>CNN:</b>	Convolutional Neural Network
<b>CSVM:</b>	Convolutional Support Vector Machine
<b>DCSE:</b>	Double Cluster Seeking Estimate algorithm
<b>DEF:</b>	Delayed Ettringite Formation
<b>DenseNet:</b>	Densely connected convolution Networks
<b>DL:</b>	Deep Learning
<b>DO:</b>	Downward Openings
<b>EM:</b>	Electromagnetic
<b>ER:</b>	Electrical Resistivity
<b>EUC:</b>	Euclidean distance

<b>FHWA:</b>	Federal Highway Administration
<b>GA:</b>	Genetic Algorithm
<b>GANs:</b>	Generative Adversarial Nets
<b>GPM:</b>	Galvanostatic Pulse Measurement
<b>GPR:</b>	Ground Penetrating Radar
<b>GPR-CAT:</b>	GPR-based Condition Assessment Tool
<b>GSSI:</b>	Geophysical Survey Systems, Inc.
<b>GUI:</b>	Graphical User Interface
<b>HCP:</b>	Half-Cell Potential
<b>HMM:</b>	Hidden Markov Model
<b>HOG</b>	Histogram of Oriented Gradients
<b>IBA:</b>	Image-Based Analysis
<b>IDS:</b>	Ingegneria Dei Sistemi
<b>IE:</b>	Impact Echo
<b>IR:</b>	Infrared Thermography
<b>KL:</b>	Kullback-Leibler divergence
<b>LBP</b>	Local Binary Pattern
<b>LoG:</b>	Laplacian of Gaussian
<b>LSTM:</b>	Long Short-Term Memory
<b>ML:</b>	Machine Learning
<b>MLP:</b>	Multi-Layer Perceptron classifier
<b>MMSA:</b>	Multiresolution Monogenic Signal Analysis

<b>NBI:</b>	National Bridge Inventory
<b>NCHRP:</b>	National Cooperative Highway Research Program
<b>NDE:</b>	Non-Destructive Evaluation
<b>NDT:</b>	Non-Destructive Technique
<b>OCR:</b>	Optical Character Recognition
<b>OECD:</b>	Organization for Economic Co-operation and Development
<b>OSCA:</b>	Open-Scan Clustering Algorithm
<b>PCA:</b>	Portland Cement Association
<b>PCC:</b>	Portland Cement Concrete
<b>PFJ:</b>	Parabolic Fitting-based Judgment
<b>RADF:</b>	Restricted algebraic-Distance-Based fitting
<b>RANSAC:</b>	Random Sample Consensus algorithm
<b>RC:</b>	Reinforced Concrete
<b>R-CNN:</b>	Regions with CNN features
<b>ResNet:</b>	Residual neural Networks
<b>RHD:</b>	Robust Hyperbolic Detection
<b>RUIM:</b>	Robust User-Interactive Model
<b>SAFT:</b>	Synthetic Aperture Focusing Technique
<b>SGS:</b>	Système de Gestion des Structures
<b>SHM:</b>	Structural Health Monitoring
<b>SIFT:</b>	Scale-Invariant Feature Transform
<b>SSD:</b>	Single-Shot multibox Detector framework
<b>SURF:</b>	Speeded-Up Robust Features

<b>SVM:</b>	Support Vector Machines
<b>ULAM:</b>	User-Labeled Anomalies Module
<b>UPE:</b>	Ultrasonic Pulse Echo
<b>USW:</b>	Ultrasonic Surface Waves
<b>VI:</b>	Visual Inspection
<b>V-JAM:</b>	Viola-Jones Algorithm-based Model
<b>X-Sim:</b>	X-Ray Simulated method
<b>YOLO:</b>	You Only Look Once

# 1 INTRODUCTION

## 1.1 Problem Statement and Research Motivation

Bridge infrastructure requires periodical inspection, repair-maintenance, or complete replacement of bridges for long-term safety and sustainability (Mohammed Abdul Rahman et al., 2016). An efficient bridge management system (BMS) assists transportation authorities to review the state of existing bridges through regular inspections and maintenance records and take appropriate actions by allocating its budget concerning future repair or replacement of bridges. All bridges undergo deterioration due to various factors like structural aging, increased traffic volume, and vehicular overloads (Shan & Li, 2009). To assess the condition of these bridges, transportation authorities have traditionally been utilizing the *visual inspection method* whereby qualified bridge inspectors visually observe the surface defects and based on their knowledge scale the bridge components according to its condition (Heymsfield & Kuss, 2015). Even though this method is simple and effective, it has major disadvantages; two of which include a) subjective nature and b) inability to determine internal defects like corrosion, delamination, internal cracks, and others. Due to such limitations, various destructive and non-destructive techniques have been adopted which can assist in determining the wholesome health of a bridge deck. Non-destructive evaluation (NDE) techniques are preferred due to the clear advantage of avoiding damage to bridge decks (Oh et al., 2013). Some examples of NDE techniques include half-cell potential, infrared thermography, impact echo, and ground-penetrating radar (GPR). These methods enable the assessment of structural integrity without the need for destructive testing, providing valuable insights into the condition of bridge decks.



Based on a comprehensive report on non-destructive testing (NDT) to identify bridge deck deterioration (Gucunski & National Research Council, 2013), GPR is the recommended technique for overall condition assessment at the network level due to its ability to identify major subsurface defects such as corrosion, voids, and delamination within a short period. The method involves scanning a structural element such as a bridge deck using GPR equipment which consists of an electromagnetic signal emitting antenna. The reflected signals are recorded, and this obtained GPR data is analyzed through various methods found in the literature to generate deterioration maps for condition assessment. The commonly utilized method for analysis adopted by federal agencies involves picking amplitude values either at the concrete-rebar level or the relative difference of amplitude from top to bottom of a deck, and these values are indicative of concrete deterioration or corrosion levels. However, utilizing such an amplitude-based approach has various limitations which include the following: a) it majorly neglects information contained within GPR data; and b) the condition maps obtained have shown to vary from the actual ground condition when compared with results using destructive measures (Tarussov et al., 2013). Therefore, amplitude-based approaches are not completely reliable and there is a need to improve GPR data analysis.

(Tarussov et al., 2013) introduced an alternate approach for analyzing profiles obtained from GPR scans based on visual interpretation and proposed that it overcomes the major limitations of amplitude-based analysis. It involves a (typically well-versed) analyst to visually scan through each GPR profile and mark attenuated areas in them while considering several factors such as surface anomalies, reflected amplitudes at the top and bottom slab, presence of water puddle on the surface, structural anomalies like the presence of beam or column, tightly spaced reinforcing bars, variation in slab thickness among others. The resulting condition maps obtained from this approach

are less noisy and chaotic as it does not consider GPR as a mere (amplitude) measuring device, but rather an imaging device as *most of the information contained in profiles is visual in nature*. However, since this approach requires a (human) analyst for interpretation, it is highly subjective, dependent on the level of knowledge of the analyst, and time-consuming. Thus, there is a *need* to automate the image-based approach of analyzing GPR data based on scientific analysis. The present research aims to fulfill the aforesaid need by utilizing digital image processing and computer vision techniques and has developed robust model(s) for assessing GPR data. The condition maps generated based on the developed model(s) would correspond closer to the actual bridge element condition and thus, make it highly reliable for bridge inspectors to use such maps with enhanced confidence for repair and rehabilitation purposes.

## **1.2 Objectives of Research**

The primary objective, as stated earlier, is to automate the image interpretation of GPR profiles and develop a robust model(s) for GPR data analysis with an overall goal of reliable condition assessment of bridges. The following list includes the sub-objectives identified to achieve the required purpose:

- a) Review of bridge management practices, types of bridge defects, various NDTs including GPR, and its data acquisition & analysis techniques found in the literature.
- b) Review image processing techniques that have been previously employed for GPR data interpretation.
- c) Identify, investigate, and apply various approaches for image analysis of GPR data based on image processing and computer vision tools.

- d) Develop robust model(s) for automated and scientific analysis of GPR data which generate reliable condition maps.
- e) Compare & validate the results of the developed model(s) with case studies and lab tests.

### 1.3 Summary of Research Methodology

The detailed research methodology for the developed models is presented in Chapter 3. However, it can be summarized in the following steps:

**Step 1:** A compendious literature review has been done as a premier step that provides an overview of bridge management systems, types of bridge defects, and a concise explanation of various NDTs for reinforced concrete bridge evaluation including the reasons for adopting the chosen technology - GPR. Then, numerous methods of analyzing GPR data have been listed along with a brief explanation of the commonly adopted amplitude-based method with its limitations. Later, the image-based analysis methodology adopted by a GPR analyst is explained along with previous efforts of image processing algorithms employed in literature for GPR data analysis. Finally, key findings and research gaps are identified as a source of fuel for the current research.

**Step 2:** A brief review of common processing and computer vision operations is presented. Subsequently, a few methods are categorized and examined on GPR radar data to investigate the effects of applying various image processing techniques. A *three-step philosophy* was identified which includes identifying hyperbolic regions, measuring meaningful properties of detected regions, and clustering those regions to generate condition maps.

**Step 3:** The methodologies of the *three* developed models are discussed stepwise in detail. The first model, termed as the '*X-Sim*' *method*, is an initial exploratory approach and has not been recommended for condition assessment. The second model is based on *Viola-Jones Algorithm*, and it identifies hyperbolic regions automatically to develop condition maps using *entropy* values of detected regions and K-means clustering. The final model is a comprehensive robust approach for analyzing GPR data as it considers user-assisted information, identifies complex hyperbolic signatures based on downward openings, provides optimal clusters, detects anomalies, and generates reliable condition maps.

**Step 4:** Each of the developed models has been applied with real-case studies of reinforced concrete structural elements (typically bridge decks) to compare with existing approaches and validate the results with destructive coring samples.

**Step 5:** Lab tests have been performed at Concordia University, Montreal to evaluate the entropy factor on GPR scans of concrete slabs with varying materials at differing depths in a controlled environment and its comparison has been done with respective amplitude values to further validate the developed models.

## **1.4 Structure of the Thesis**

This thesis has been organized into six chapters. The following description highlights the contents presented in the chapters.

**Chapter 1** illustrates the need for this research by stating the problem statement and the motivation of this research with a brief introduction. It later enlists the objectives of the research along with a brief overview of the proposed research methodology.

**Chapter 2** provides a comprehensive literature review and background to the development of this research. It proceeds by discussing bridge management practices, and various NDE techniques and in particular focuses on GPR and its data interpretation methods. It concludes by highlighting the research gaps identified along with the limitation of existing approaches to GPR data interpretation. It also encompasses research methods investigated in detail. An overview of the various image processing and computer vision techniques are discussed briefly in this chapter along with the categorized methods explored on GPR data during the process of developing a final research methodology.

**Chapter 3** explains the complete methodology of three models which have been developed in this research in a progressive approach such that the later model is better than the former. Although the first model is not recommended for condition assessment, the advantages of the latter two models are discussed to generate reliable condition maps.

**Chapter 4** has real-case applications of developed models. Its purpose is to compare the results of these models with existing approaches and validate with coring samples, if applicable.

**Chapter 5** describes the lab tests conducted along with the results achieved and contains two additional case studies of the last and final method.

**Chapter 6** finally concludes by listing the research contributions along with limitations and suggested future works.

## 2 LITERATURE REVIEW

### 2.1 Background of Bridge inspection

Bridge inspection and maintenance have become increasingly important to bridge authorities over the years to ensure public safety. The aging infrastructure of bridges across North America is a major concern and it highlights the importance of regular inspection, repair, and rehabilitation of a vast network of bridges. The need for bridge maintenance evolved from a public safety perspective rather than the need of managing infrastructure itself. A major catastrophe on 15th December 1967, the collapse of Silver Bridge in Point Pleasant, West Virginia which caused the death of 46 people, is the single most incident responsible for creating public awareness about maintaining infrastructure in the US and elsewhere (Silano & Parsons Brinckerhoff., 1993). Bridge inspection programs were consequently established at the national and provincial level and the assessment of existing bridges revealed that the need for maintaining a database is imperative for efficient bridge inspection, repair, and rehabilitation. According to statistics published by FHWA in the USA, 341,494 (55.11%) out of a total of 629,622 bridges are rated from poor to fair among which 43,586 bridges (7.03%) are in extremely poor condition (FHWA, 2021). The statistics in Canada also paint a similar picture: according to the Canadian Infrastructure report card, 26.3% of total bridges and tunnels are rated in fair condition while 12.3% of them are rated from very poor to poor (CIRC, 2019). A previous report also estimated a \$13 billion investment needed to fully replace the bridges in fair to poor condition out of which \$2 billion was at least needed to replace poor-rated bridges with an anticipated decline in future from existing conditions (CIRC, 2016). To properly assess and maintain the huge amount of bridge infrastructure, the bridge management practice has evolved over the years and has been discussed in the next section.

## **2.2 Bridge Management**

Bridge management refers to the management or care of a collection of bridges within a region, country, or zone right from its inception until the end of its useful life (Ryall, 2009). A detailed definition of bridge management has been attempted by (OECD, 1992) as follows:

*“The term bridge management encompasses a broad range of activities aimed at ensuring the safety and functionality of bridges. An efficient bridge management scheme is necessary to support the highway and bridge agencies’ organizational set-up and their administrative and technical functions. . . . Above all, adequate qualified and well-trained manpower with clear responsibilities and duties must be ensured. The personnel must be aware of its role in the different management process.”*

The *scheme* in the preceding definition refers to a bridge management system (BMS) adopted by agencies and transportation authorities to maintain bridges at the network level. This mechanism through which the database of bridges at the network level is maintained by coordination and implementation of repair and rehabilitation strategies, the Bridge Management System (BMS) is the topic of subsequent discussion in brief.

## **2.3 Bridge Management System (BMS)**

The term bridge management has been defined in the previous section. (Mitra, 1988), in his book, defines *“A system is a group of elements, either physical or non-physical in nature, that exhibit a set of interrelations among themselves and interact towards one or more goals, objectives, or ends. The elements that comprise a system maybe of several different types... The nesting of smaller subsystems within larger ones forms a hierarchy that is characteristic of any system. A system and all its subsystems accept input and produce output.”*

The term bridge management system (BMS) came into existence as a terminology with the advent of powerful personal computers in the late 1980s, as a need for transition from managing a limited number of bridges as usual to network-level management of a database of bridges at network level built up through regular inspection and maintenance (Ryall, 2009). The definition of bridge management in (NCHRP Report 300, 1987) encapsulates this transition from bridge management to BMS as follows:

*“The objective . . . is to develop a form of effective bridge management at the network level (that is, dealing with a group of bridges rather than with a single bridge) that will ensure the effective use of available funds and identify the effects of various funding levels. Bridge management . . . requires a practical, objective, and systematic consideration of the problem with a set of economic and technical tools not previously combined to solve the problem. Specifically, a bridge management system (BMS) is a rational and systematic approach to organizing and carrying out the activities related to planning, designing, constructing, maintaining rehabilitating, and replacing bridges vital to the transportation infrastructure”*; and the discussion of BMS continues beyond this point in the report (OECD, 1992) which similarly relates the need of development of BMS through defining bridge management:

*“Bridge management addresses all bridge-related activities from the moment of construction to the replacement of a particular structure. Bridge managers require an instrument that enables them to carry out their tasks efficiently which guarantees the functionality and safety of bridges in the most economical way. In order to improve the ways and means of managing bridges which so far have been founded on an individual project-by-project approach, the sheer size of the existing bridge stock and capital invested has recently led member countries to search for a coherent and*

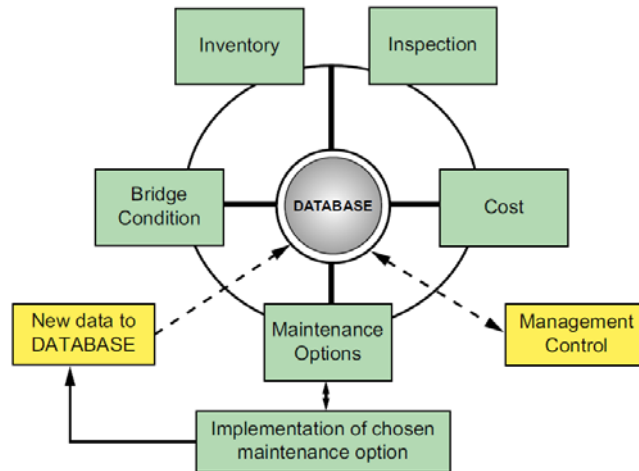


*cost-effective network approach to bridge management. Bridge Management Systems are therefore being developed to provide guidelines for managers, which identify and clarify the implications and requirements of the system as to the technical and organizational structures.*” Over the years, BMS developed as a more complex system for bridge authorities as a tool striving to optimize decision-making for the allocation of funds and resources for bridge repairs and maintenance while fully utilizing the available database of knowledge of bridges (Yanev, 2007). (FHWA, 2005) the report defines the BMS as *“a system designed to optimize the use of available resources for the inspection, maintenance, rehabilitation, and replacement of bridges.”* It is a system whereby the bridge managers are fully aware of the “health” of bridges through which they would be able to allocate the funds depending upon the condition ratings of individual bridges in the network (Ryall, 2009). A BMS typically consists of several modules depending on the size and complexity of the system, but it always has modules on *inventory, inspection, maintenance, cost, and bridge condition*. The information, stored in a database, is analyzed, and processed through *management control*. Figure 2.1 illustrates the basic structure of a BMS with all the essential modules. The inventory component contains the database of bridges and stores information pertaining to name, location, construction, drawings, and other basic components to provide an overview of the bridges along with their generic information. The inspection component contains information about its inspection reports, general condition, treatment specified, previous remedial works, and inspection drawings, if available. The maintenance component contains the bridge condition, maintenance records, and details of work performed, if available. The financial (cost) component contains the cost information about projects, financial reports, and budget allocated. The bridge condition component contains the priority rating and importance assigned at the network and/or project level based on historical data and the latest inspection reports. Finally, the management components

refer to the management of these five aforementioned components through the brains of the organization in prioritizing planned and future bridge repair and rehabilitation. (Ryall, 2009).

The selection of bridges based on their priority is a network-level decision while the selection of type of repair for a particular bridge is a project-level decision. Most of the current BMS is developed to address either network - level or project - level decisions. However, advances have been made that address both these decisions simultaneously in the literature leading to better optimal solutions (Elbehairy et al., 2006). The generic components of such a BMS model include the following as illustrated in Figure 2.2:

- a) *“Detailed BMS models (time-dependent deterioration, repair cost, and repair-dependent improvement)*
- b) *BMS constraints (industry, governmental, political, user-defined constraints, project, network, and execution constraints such as deadline, resources, etc.)*
- c) *BMS decision support module (user interface, condition assessment, and Life-cycle cost optimization)”*



**Figure 2.1** A basic BMS (Ryall, 2009)

The type of BMS adopted by countries, agencies, or provinces typically differ but the objectives and basic modules remain relatively similar as discussed earlier. In North America, each state of the US has its own BMSs; however, there are two widely utilized BMSs: PONTIS and BRIDGIT. The PONTIS was developed by Federal Highway Administration (FHWA) and is a network-level, top-down approach while the American Association of State Highway and Transportation Officials (AASHTO)'s BMS developed the BRIDGIT as a project-level approach which works from the bottom to up. In Canada, each major province has developed and implemented its own BMS system and in the province of Quebec, Canada, the Ministry of Transportation Quebec (MTQ) has adopted one of its kind, BMS in French called Système de Gestion des Structures (SGS). SGS has an advanced Strategic Planning Module (MPS) which includes a set of three analysis levels i.e., network level, project level, and element level. The system is designed consistently such that if a change is made at any of the levels, the other levels are adjusted appropriately. (Ellis et al., 2008)

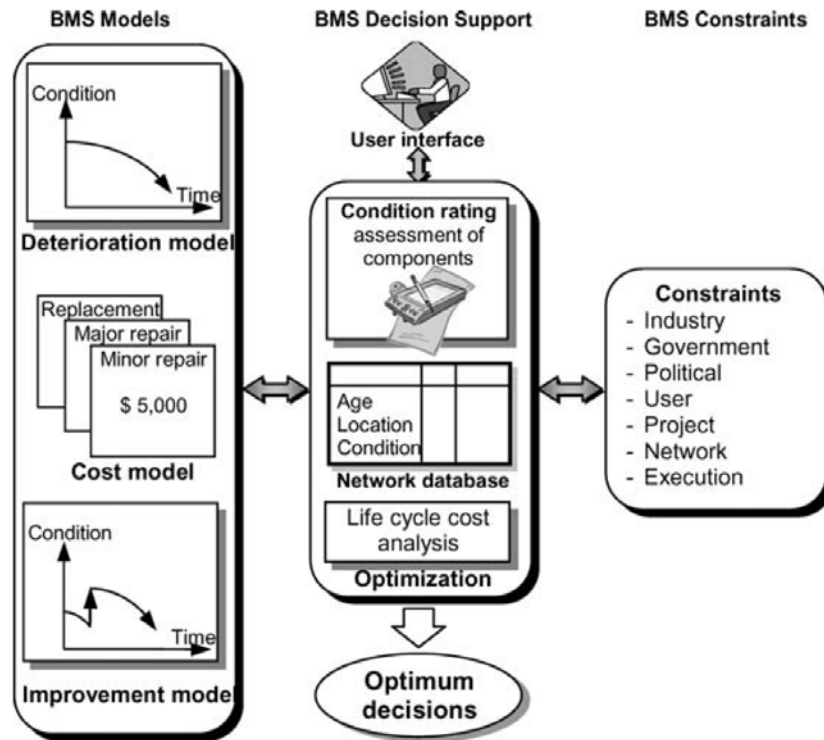


Figure 2.2 Components of a BMS System (Elbehairy et al., 2006)

## 2.4 Bridge Inspection Overview

One of the key elements in the operation of a sound bridge management system is the periodic inspection of the bridges and their elements in the network. Regular bridge inspection seeks to provide the following as described comprehensively by (Ryall, 2009):

- a) *“a consistent record of the state of the structure, which allows the significance of any changes (accidents, overloading, or environmental deterioration) to be analyzed and acted upon.*
- b) *the data upon which the safety and serviceability of the bridge can be assessed.*
- c) *information on any potential trouble spots.*
- d) *information upon which a consistent maintenance strategy can be established.*
- e) *data for monitoring the effect of any changes in traffic loads and the use of new structural forms and materials.*

- f) data for monitoring the behavior of new strengthening techniques; and
- g) data for research purposes.”

One of the primary objectives of performing a bridge inspection is to identify defects. The defects are identified using various techniques found in the literature. The next two sections enlist and describe the types of defects and inspection techniques adopted for bridge deck inspections.

## 2.5 Types of Bridge Deck defects

**Table 2.1** Consequences of Deterioration in RC Structures (Bien et al., 2007)

Sl.	Deterioration Consequences	Sl.	Deterioration Consequences
1	Corrosion	8	Creep
2	Carbonation	9	Fatigue
3	Alkali-silica reaction	10	Influence of high temperature
4	Crystallization	11	Modification of founding conditions
5	Leaching	12	Overloading
6	Oil and fat influence	13	Shrinkage
7	Salt and acid actions	14	Water penetration

Condition assessment and defect detection is very important for concrete bridge decks as they are prone to cracking, spalling and corrosion in rebars that could reduce their capacity significantly (Adhikari et al., 2012), (Adhikari et al., 2016). There are a variety of detrimental causes of deterioration of reinforced concrete structures like bridge elements which reduce its life span such as poor initial quality of concrete, damage due to deicing salts, overloading, freeze-thaw cycle induced stresses, fatigue, and, majorly, corrosion of rebars (Figure 2.3) (Gucunski & National Research Council, 2013). Table 2.1 shows the deterioration consequences identified by (Bien et al., 2007) in reinforced concrete (RC) structures. The deterioration of reinforced bridge elements

is the focus of this research. However, since the bridge deck is the most important element in a bridge, the discussion is limited to reinforced bridge decks, and it can be extended to assessing other reinforced bridge elements. Some of the common bridge deck defects have been tabulated by (Yehia et al., 2007) along with the definition and causes as shown in Table 2.2.



**Figure 2.3** Deck deterioration (Gucunski & National Research Council, 2013)

**Table 2.2** Summary of Common Problems in Concrete Bridge Decks (Yehia et al., 2007)

Defect	Definition	Cause
Spalling	Concrete falls away leaving a little hole that defines the fracture surface	Internal pressure due to freezing and thawing, insufficient consolidation during construction, and the formation of inner cracks which are later transformed into spalls
Corrosion of reinforcement	Weakening of some metals such as steel due to exposure to a corrosive environment where it becomes brittle and goes back to its ore state	Presence of a conductive solution, corrosion agent, and a corrosion cell
Leaching	Drainage or removal of soluble or constitutes in porous materials by water seeping action	Occurs due to dissolving water constituted like calcium hydroxide at crack locations
Scaling	Deterioration of concrete into smaller parts and individual aggregates	Scaling may be a result of freezing and thawing, and chemical attacks
Cracking	Breakage in the concrete causes a discontinuity without causing a complete separation of the structure	Cracks form due to tensile forces caused by shrinkage, temperature changes, bending, loading, corrosion of reinforcement, sulfates, and chemical attacks
Honeycombing	The presence of exposed coarse aggregate without enough concrete paste covering the aggregates causes the presence of small holes	Poorly graded concrete mix, the use of large coarse aggregates, and insufficient vibration at the time of placement

Delaminations	Cracks or fracture planes at or just above the level of reinforcement that grows big and can affect the integrity of the structure	Corrosion of steel reinforcement, high amount of moisture and chloride content, and the presence of cracks in the concrete surface
---------------	--	--

Among the various defects listed in Table 2.2, those which are of highest concern to bridge engineers during inspection of bridge deck inspection are listed below and discussed briefly based on the detailed report by (Gucunski & National Research Council, 2013):

- a) *Rebar corrosion*
- b) *Deck delamination*
- c) *Vertical cracking*
- d) *Concrete degradation.*

### **2.5.1 Rebar Corrosion**

The corrosion of reinforcement is a major defect in concrete bridge decks. The steel is obtained from smelting and refining iron ore and hence, it is thermodynamically unstable and undergoes decomposition because it is not in a natural state (PCA, 2016). In reinforced concrete, corrosion is protected initially due to the alkaline condition of the concrete, which forms a thin oxide layer on the steel and prevents metal ions in it from dissipating. Without this layer called a passive film, steel would corrode at a much higher rate, at least 1000 times faster, thereby reducing the lifecycle of the structure significantly (ACI 222R-01, 2001). Therefore, corrosion in concrete occurs after this passive layer is destroyed either due to a reduction in alkalinity or contamination of chloride above a certain level. The process which reduces alkalinity is called carbonation and while the process of chloride diffusion is called chlorination.

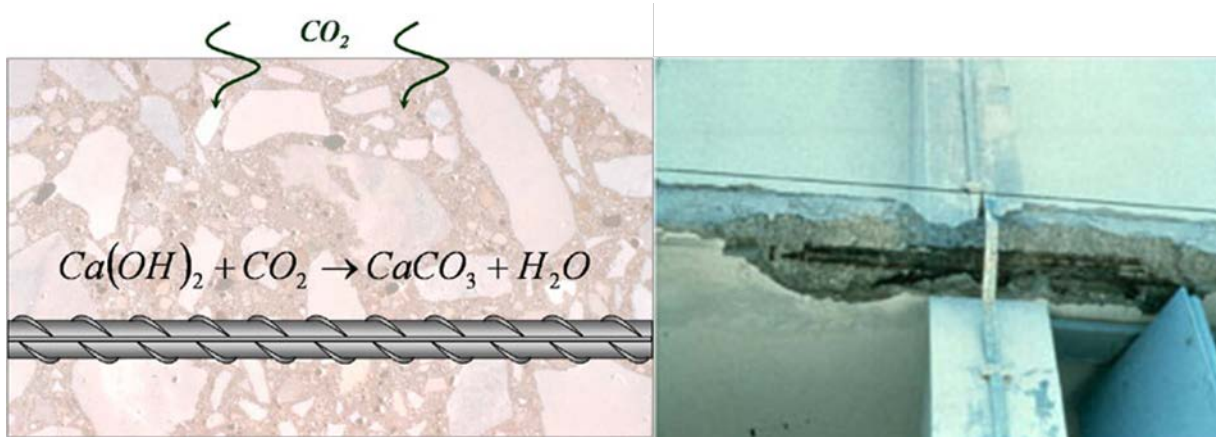
*Carbonation* occurs when the carbon dioxide present in the air penetrates and reacts with hydroxides such as calcium hydroxide or sodium hydroxide to produce carbonates. For example, the reaction with calcium hydroxide is shown in Equation 2.1.



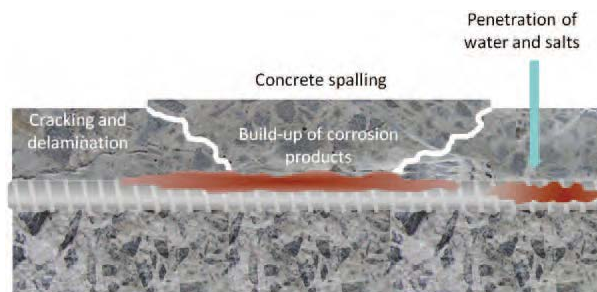
The results of such reactions in concrete reduce the pH of the porous solution to as low as 8.5 which breaks the passive film and makes it susceptible to corrosion. Carbonation is a slow process, and it is estimated to proceed at a rate of up to 0.04 inches per year in high-quality concrete. The rate of carbonation is increased due to the following factors: high water-cement ratio, low cement content, short curing period, low strength, and highly permeable or porous state. Humidity level also affects carbonation. Carbonation is highest between 50 to 75 percent of humidity level while it is insignificant below 25% and above 75%; the high level of moisture prevents carbon dioxide to penetrate (PCA, 2016). Figure 2.4 shows the effect of carbonation on a reinforced concrete façade of a building.

*Chlorination* occurs due to the intrusion of chloride ions in chlorides dissolved in water present primarily in deicing salts and seawater in North America and is the major initiator for corrosion. When the chloride contents exceed a certain threshold level, the chlorination process breaks the passive layer and causes internal stresses, cracking, and delamination which may eventually lead to spalling of concrete (Figure 2.5). Corrosion due to chlorination yields blackish rust marks while corrosion due to carbonation yields red or brownish rust stains. (Gucunski & National Research Council, 2013).





**Figure 2.4** Carbonation process and its effect on concrete building façade (PCA, 2016)



**Figure 2.5** Corrosion due to chlorination because of penetration of deicing salts (Gucunski & National Research Council, 2013)

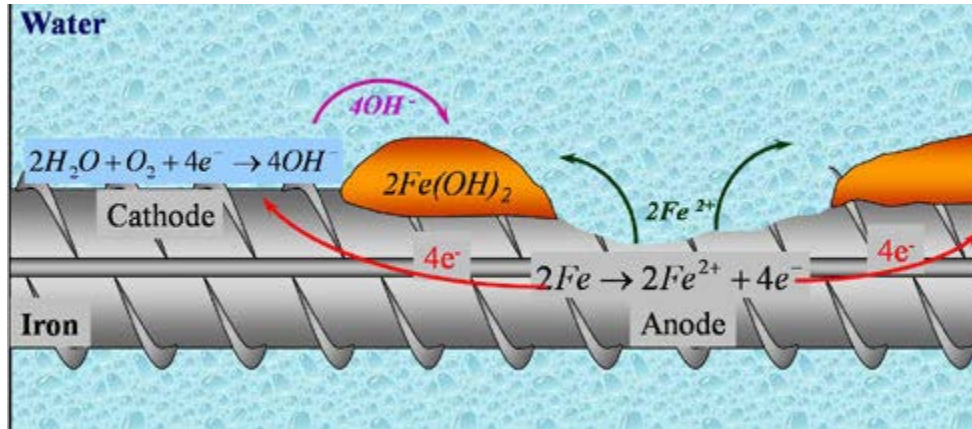
After the passive layer is broken, tiny electrolyte cells are formed at active sites of the bar, called anodes due to the loss of electrons of ferrous ions (half-cell oxidation reaction) and is represented as shown in Equation 2.2.



The water and oxygen combine with electrons released by ferrous ions to form hydroxide at the cathode, which is represented as shown in Equation 2.3.



The ferrous ions react with these hydroxides to form iron hydroxides, and these react further with dissolved oxygen to cause internal stresses leading to cracking and spalling of concrete. (Figure 2.6) (PCA, 2016)



**Figure 2.6** Electrolytic reaction in rebars (PCA, 2016)

### 2.5.2 Deck delamination

Deck delamination or horizontal cracking occurs due to corrosion of concrete which causes the reinforcing steel to expand leading to cracks or subsurface fracture planes. Such cracks can be localized to a small area or may extend over larger areas to cause delamination. Delamination could occur over different planes in concrete which might eventually affect the structural integrity of a bridge deck. Delamination is a subsurface defect i.e., it is not visible from the surface and hence, the defect is very critical. Delamination samples are shown in Figure 2.7 when cores are extracted from a bridge deck (Gucunski & National Research Council, 2013).

### 2.5.3 Vertical Cracking

Besides cracking, other factors can cause cracking in a bridge deck. Factors such as plastic shrinkage, hydration heat, ambient temperatures, geometric constraints as the deck concrete cures, traffic load, and freeze-thaw cycles induce vertical cracking in concrete. An increase in rebar corrosion

can further exaggerate vertical cracking (Gucunski & National Research Council, 2013). Figure 2.8 shows shrinkage-induced vertical cracking documented by (Sharp & Moruza, 2009) in the underside of the Route 123 bridge deck in the US.



**Figure 2.7** Delamination observed in cores (Gucunski & National Research Council, 2013)



**Figure 2.8** Underside of Route 123 Bridge Deck Showing Cracking (Sharp & Moruza, 2009)

#### **2.5.4** *Concrete Deterioration*

Concrete degradation refers to the reduction in concrete strength or its modulus and it could be a consequence of micro-cracking and macrocracking due to phenomena such as alkali-silica reaction (ASR), delayed ettringite formation (DEF), plastic shrinkage, and freeze-thaw cycles. ASR refers to the reaction between reactive silica phases in aggregates and alkali hydroxides in the concrete pore solution and it can cause two problems: a) the deformation of the structure, thereby impairing the serviceability, and b) the development of a crack network through the structure. DEF is a type of internal sulfate attack and is a consequence of improper heat curing of the concrete. The hydrous calcium aluminum sulfate mineral, ettringite, is formed due to the chemical reaction of calcium and aluminum compounds of concrete with concentrated sulfate in porous concrete. The ettringite formed causes concrete to expand, and empty cracks (gaps) form in aggregates. Figure 2.9 shows cracks formed due to ASR and DEF. Freeze-thaw cycles cause increased hydraulic pressure in

concrete causing tensile strength in concrete leading to extensive deterioration of concrete in the form of cracking, scaling, and crumbling (Gucunski & National Research Council, 2013). To identify the various type of defects in bridge decks, there are multiple approaches adopted by transportation authorities which will be discussed in the next section.



(a)



(b)

Source: ASR photograph courtesy of Dr. Moon Won, Texas Tech University. DEF damage photograph courtesy of Texas Department of Transportation Bridge Division.

**Figure 2.9** a) ASR and b) DEF cracking in bridge deck (Gucunski & National Research Council, 2013)



## 2.6 Type of Bridge Inspections

Visual Inspection (VI) is a common method for bridge inspection and evaluation. However, VI-based bridge deck condition assessment could produce incorrect and subjective results. However, appropriate Non-Destructive Testing (NDT) methods can be used to complement the information produced from visual inspection. A comprehensive list of NDT methods used to detect and characterize the defects enlisted in Section 2.5 for reinforced concrete bridge decks include the following 14 methods as shown in Table 2.3 (Gucunski & National Research Council, 2013). Structural Health Monitoring (SHM) techniques and vibration testing are also increasingly being used to gather more detailed information on the structural behaviour of bridges to aid in a more accurate assessment of their conditions (Noman Ahmed et al., 2013), (Sabamehr et al., 2018).

**Table 2.3** List of various NDTs for reinforced concrete bridge deck inspection (Gucunski & National Research Council, 2013)

Sl.	Inspection Method	Sl.	Inspection Method
1	Impact Echo	8	Half-cell potential
2	Ultrasonic pulse echo	9	Galvanostatic pulse measurement
3	Ultrasonic surface waves	10	Electrical resistivity
4	Impulse response	11	Infrared thermography
5	Ground-penetrating radar	12	Visual inspection
6	Microwave moisture technique	13	Chain-dragging and hammer sounding
7	Eddy current	14	Chloride concentration measurement

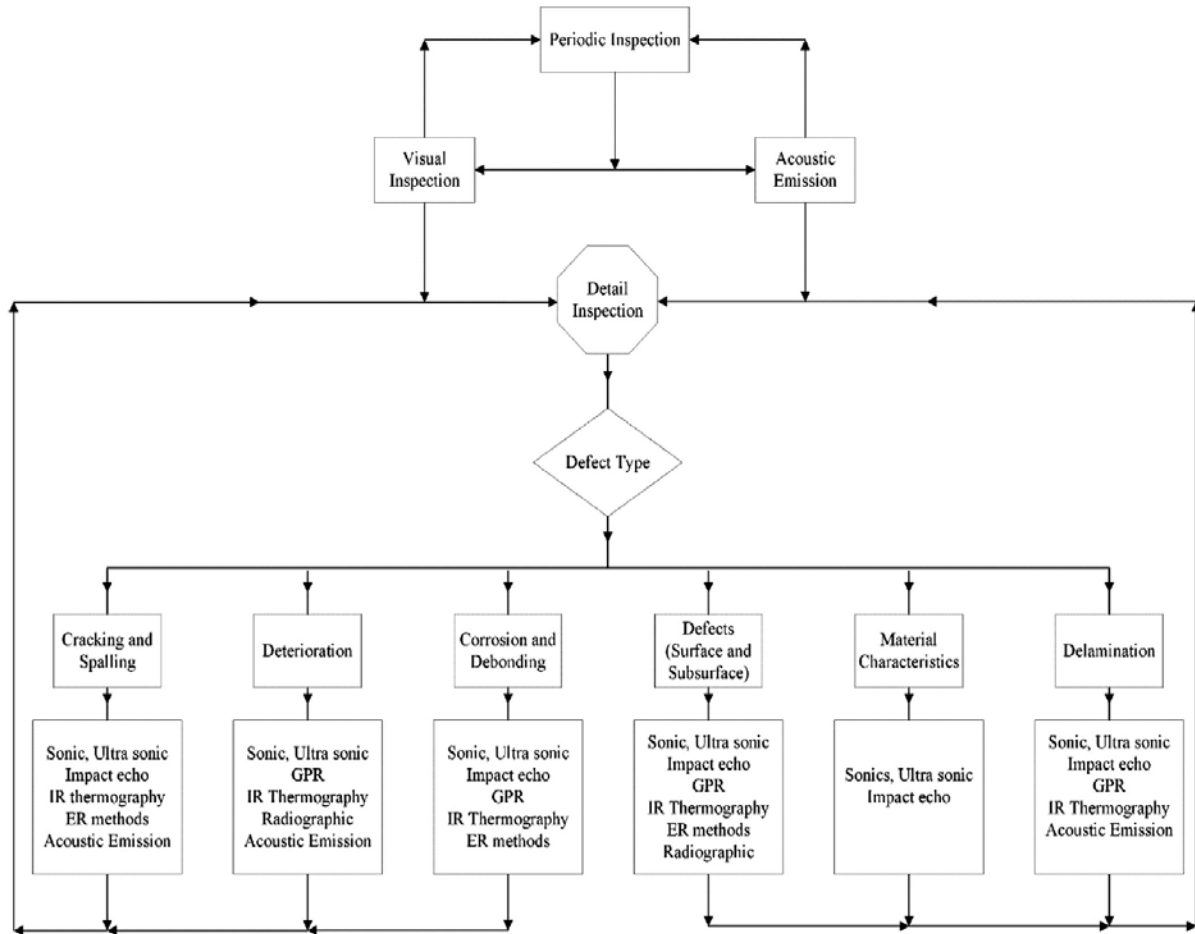
(Yehia et al., 2007) classified 9 of these NDT techniques utilized for bridge deck evaluation based on their uses (type of defects), advantages, and limitations as shown in Table 2.4. (Kashif Ur Rehman et al., 2016) also presented the selection of suitable NDT techniques based on different

defects and damages for concrete bridges in a flowchart format as shown in Figure 2.10. It classified inspection procedures into two types: a) periodic inspections, which refer to inspections done at higher frequency by simpler methods like visual inspection and/ or Acoustic Emission; and b) detailed inspection which is required based on the type of defects identified from periodic inspections.

**Table 2.4** Summary of NDT Techniques for Bridge Deck (Yehia et al., 2007)

Method	Uses	Advantages	Limitations
<b>Visual inspection</b>	<ul style="list-style-type: none"> <li>• Cracks</li> <li>• Geometry</li> <li>• Surface roughness</li> </ul>	<ul style="list-style-type: none"> <li>• Accessibility</li> <li>• Oldest known technique</li> <li>• Well established</li> </ul>	<ul style="list-style-type: none"> <li>• Subjective</li> <li>• Time-consuming</li> <li>• Qualitative results</li> </ul>
<b>Liquid penetrant dye</b>	<ul style="list-style-type: none"> <li>• Surface flaws</li> <li>• Detection of irregularities</li> </ul>	<ul style="list-style-type: none"> <li>• Portable</li> <li>• Easy interpretation</li> </ul>	<ul style="list-style-type: none"> <li>• Surface preparation</li> <li>• Exhausting for an inspector</li> <li>• Time-consuming</li> </ul>
<b>Chain drag</b>	<ul style="list-style-type: none"> <li>• Flaw detection inside decks</li> <li>• Delaminations</li> </ul>	<ul style="list-style-type: none"> <li>• Simple</li> <li>• Portable</li> <li>• Good for delaminations</li> </ul>	<ul style="list-style-type: none"> <li>• Time-consuming</li> <li>• Tedious</li> <li>• Subjective</li> <li>• Not good with overlays</li> </ul>
<b>Half-cell potential</b>	<ul style="list-style-type: none"> <li>• Detect corrosion state in concrete reinforcement</li> <li>• Corrosion rate</li> </ul>	<ul style="list-style-type: none"> <li>• Simple</li> <li>• Portable</li> <li>• Good for corrosion</li> </ul>	<ul style="list-style-type: none"> <li>• Deck needs preparation</li> <li>• Time-consuming</li> <li>• Not good for delaminations</li> <li>• Lane closure</li> <li>• Not very accurate</li> </ul>
<b>Acoustic emission</b>	<ul style="list-style-type: none"> <li>• Cracks</li> <li>• Delaminations</li> <li>• Corrosion</li> </ul>	<ul style="list-style-type: none"> <li>• Real-time response</li> <li>• No lane closures</li> </ul>	<ul style="list-style-type: none"> <li>• Qualitative results only</li> <li>• Not good with overlays</li> <li>• Interpretation</li> <li>• Costly</li> <li>• Not Reliable</li> </ul>
<b>Ultrasonic pulse velocity</b>	<ul style="list-style-type: none"> <li>• Homogeneity of concrete cracks, voids</li> <li>• Strength determination</li> </ul>	<ul style="list-style-type: none"> <li>• Portable</li> <li>• Easy test procedure at a relatively low cost</li> <li>• Relatively easy to interpret</li> </ul>	<ul style="list-style-type: none"> <li>• Not very reliable for concrete</li> <li>• Attenuation negatively affects results</li> <li>• Does not give information about the shape of the defect</li> </ul>
<b>Ground penetrating radar</b>	<ul style="list-style-type: none"> <li>• Concrete mapping, mining, geotechnical, road, and bridge</li> <li>• Forensics</li> <li>• Detection of voids, honey-combing</li> <li>• Delaminations</li> <li>• Moisture</li> </ul>	<ul style="list-style-type: none"> <li>• Versatility</li> <li>• Portability</li> <li>• Effectiveness</li> <li>• Low cost</li> <li>• Good with overlays</li> <li>• Minimum traffic control</li> <li>• Prediction of repair quantities in road</li> </ul>	<ul style="list-style-type: none"> <li>• Interpretation</li> <li>• Complexity of results</li> <li>• Interpretation of results sometimes requires destructive testing</li> </ul>
<b>Impact echo</b>	<ul style="list-style-type: none"> <li>• Detection of voids, cracks, Delaminations, unconsolidated concrete, and debonding</li> <li>• Determining thickness</li> </ul>	<ul style="list-style-type: none"> <li>• Requires one surface of the tested material to be exposed, independent of the geometry of the structure</li> <li>• Less susceptible to steel reinforcement</li> <li>• High accuracy</li> </ul>	<ul style="list-style-type: none"> <li>• Size of detected flaws is highly dependent on the impact duration</li> <li>• Less reliable in the presence of asphalt overlays</li> <li>• Interpretation of the results is difficult</li> </ul>

<b>Thermography</b>	<ul style="list-style-type: none"> <li>• Detection of thermal differences, Delaminations, cracks, voids</li> </ul>	<ul style="list-style-type: none"> <li>• Portable</li> <li>• Simple, easy interpretation</li> <li>• Minimum traffic interference</li> </ul>	<ul style="list-style-type: none"> <li>• No information about the depth of defects</li> <li>• Dependent on environmental conditions</li> </ul>
---------------------	--	---	--



**Figure 2.10** Selection of NDT techniques based on different defects and damages (Kashif Ur Rehman et al., 2016)

A brief description along with the advantages and limitations of some of the common NDT techniques as discussed by (Gucunski & National Research Council, 2013) will be summarized in this section to provide an overview of the methods for appropriate selection of NDT techniques based on various types of defects.



### **2.6.1 Impact Echo**

This method involves striking the surface of the bridge deck to be tested by inducing seismic or stress waves and measuring the response at a nearby location using simple or automated devices as shown in Figure 2.11. The deck is struck by various means, such as wire-mounted steel balls, automated projectile sources, or solenoid-type impactors, and the return frequency of the impacted signal is recorded to identify delamination. The characteristic of the recorded frequency can be interpreted to measure the presence and amount of delamination. The sound deck has a single peak in recorded frequency from the bottom of the deck while initial delamination has reflections recorded from both deck and delamination areas. However, delamination progressed to an advanced stage and will have reflections only from the delaminated area. The delaminated areas have typically shallow reflections. Thus, by studying the impact through recorded reflections, impact echo identifies delamination and does not detect corrosion. Other applications include the detection of surface-opening cracks, characterization of grouting in tendon ducts, and overlay debonding. However, the use of this method for other such applications is limited due to insufficient reliable results. The major disadvantage of this method is that it can be used suitably only with Portland Cement Concrete (PCC) overlays as with the presence of asphalt overlay on bridge decks, detection is possible only when the asphalt concrete is sufficiently low and hence, its use on asphalt overlay bridges is restricted because of unreliable results.



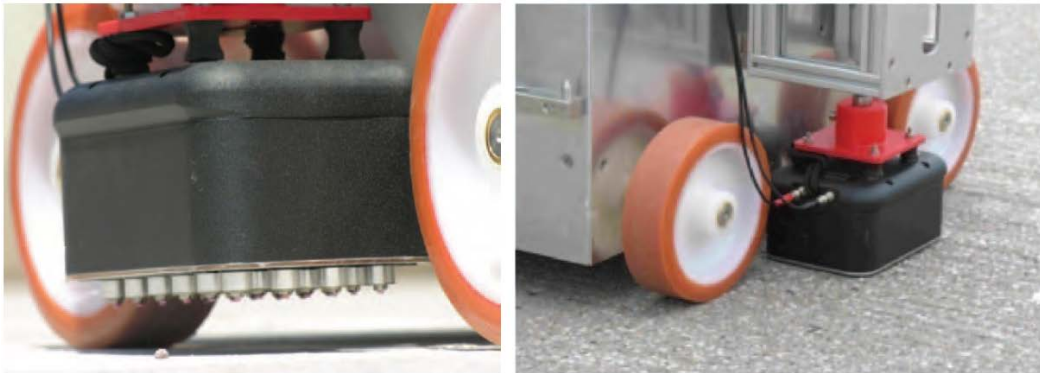
**Figure 2.11** Stepper (left) and bridge deck scanner (right) (Gucunski & National Research Council, 2013)

### **2.6.2 Ultrasonic Pulse Echo (UPE)**

UPE method uses ultrasonic (acoustic) stress waves generated by exciting a piezoelectric material to detect anomalies (cracks, voids, delamination, or horizontal cracking) in bridge decks. A dry-point contact, ultrasonic transduces unit consisting of 24 probes, 12 of which act as pulses while the remaining 12 as receivers as shown in Figure 2.12(a). Figure 2.12 (b) shows a UPE mounted on an automated device. The transit time of ultrasonic waves traveling through the medium along with the time taken for the reflected wave to come back to the surface is used for identifying defects. When the wave interfaces with a defect, a part of the energy is emitted back and hence, areas with deterioration or microcracking will have lower velocity compared to sound deck concrete. UPE is advantageous for measuring defects in concrete elements, debonding of reinforcement bars, shallow cracking, and delamination. However, it has various limitations such as the process being time-consuming due to the UPE deck survey requiring very close test points, the inability to generate sound results on rough surfaces, and some of the defects may remain undetected as UPE works only at low frequencies.

### *Ultrasonic Surface Waves (USW)*

USW method involves recording the reflected surface waves, which are elastic waves that travel along the free surface of the deck and penetrate until the concrete depth. Figure 2.13 shows the numerous devices used for generating elastic waves by impacts (steel balls, automated projectile sources, solenoid-type impactors). The surface waves propagate radially from the impact source forming a cylindrical front with a velocity dependent on the elastic properties of the medium. The USW velocity is evaluated based on the spectral analysis of the recorded signal. In the case of a sound deck, the velocity of the surface will have little variation while significant variation is indicative of the presence of anomalies. The USW method is used for detecting various defects such as ASR, DEF, freeze-thaw, vertical cracks, and other deterioration processes. However, this method is not suitable for detecting delamination in concrete decks, especially with asphalt concrete overlaid decks due to unreliable results.



(a)

(b)

**Figure 2.12** (a) Shear-wave probe array A1220 (a), and (b) automated A1220 measurements using stepper (Gucunski & National Research Council, 2013)

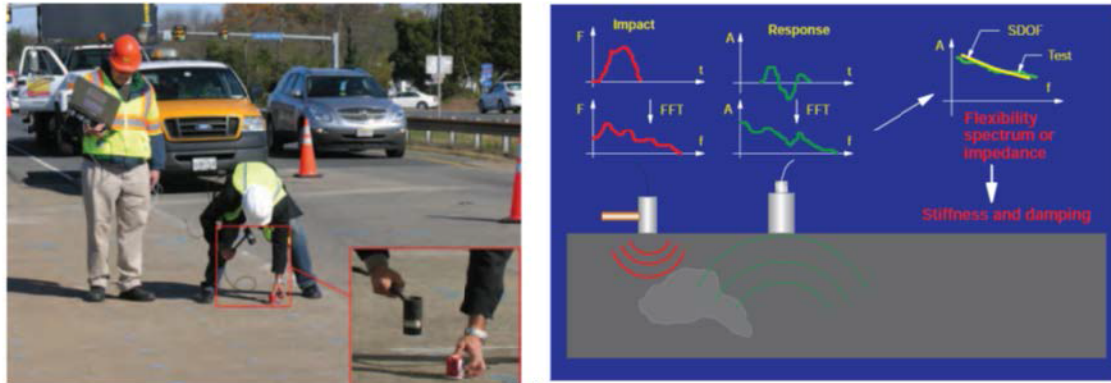


**Figure 2.13** USW testing using a portable seismic property analyzer (Gucunski & National Research Council, 2013)

### 2.6.3 *Impulse Response*

The impulse response method measures the dynamic response of the element tested, often tested in terms of mobility or flexibility spectrum to differentiate sound areas from defective areas based on the shape and amplitude of the response spectrum. The typical frequency range of impulse testing is 0 to 1 kHz and Figure 2.14 (a) shows the field-testing operation. It involves applying an impact with an instrumented hammer on a part of the bridge deck and measuring its response at a close-by location using a geophone or accelerometer. The principle behind this method is illustrated in Figure 2.14 (b) wherein the signal from the impact hammer sensor is recorded by a nearby displacement transducer, geophone (velocity transducer), or accelerometer, and the recorded signal is transferred into the frequency domain to obtain the corresponding spectra. The ratio of the displacement and impact spectra represents a flexibility spectrum, and this measured response is used to evaluate the detection of defects. The impulse response method can detect honeycombing, voids, concrete delamination, and debonding in bridge decks. The major disadvantage of this

method is it can only detect gross defects, leaving smaller defects undetected and the data obtained is highly sensitive to selected test points on the bridge deck.



**Figure 2.14** (a) Impulse sound testing and (b) Principles of impulse response testing (Gucunski & National Research Council, 2013)

#### 2.6.4 Ground-Penetrating Radar

GPR is a condition assessment tool that works by emitting electromagnetic (radio) waves into a reinforced concrete bridge element and recording the reflected signals for analysis. (Hugenschmidt & Mastrangelo, 2006). Despite being used to evaluate the condition of reinforced concrete structures for more than 30 years, GPR technology has gradually improved (Ulriksen, 1982). The premier step of GPR assessment is to utilize a mobile or manually operated antenna that emits electromagnetic (EM) waves to scan a structure, such as a bridge element, pavement, or a reinforced concrete element (Mohammed Abdul Rahman, Zayed, et al., 2022). For detailed inspections, a hand-pushed cart is typically utilized with ground-coupled GPR systems, and it is often necessary to close the entire bridge for the survey. In contrast, for mobile or aerial surveys used for reconnaissance, air coupled GPR systems are employed, typically attached to vehicles, and lane closure

is typically not necessary. Contemporary GPR systems are designed to mitigate electromagnetic disturbances and vibrations through radar design and manufacturer-recommended survey protocols. "However, regulatory guidelines must be adhered, and special care must be taken to prevent interferences at sensitive sites like airfields, prisons, defense establishments, and similar locations (Utsi, 2017). Usually, the scanning is carried out either along an element's longitudinal section or in a grid pattern with *uniform traverse spacing* to cover the entire element. Depending on the goal of a GPR survey, such as the level of detail required, the traverse spacing between scans is assigned. The selection of antenna frequency (typically ranges from 1 to 5 GHz) is a trade-off between a GPR survey's required resolution and penetration depth. In general, higher antenna frequencies offer higher resolution power but less depth of penetration, and vice versa (Gehrig et al., 2004). Accordingly, several additional GPR survey parameters are preset such as the number of samples per scan, transmit rate, number of scans per unit of distance, and dielectric constant (Varnavina et al., 2015). The energy signal reflects at various media interfaces (such as concrete air, and concrete rebar), where it is periodically recorded and known as a GPR profile (K Dinh et al., 2014). Indicators of the condition of a bridge element include the *delay time* and *amplitude* of the reflected signal at any location, which is influenced by the presence of various subsurface materials (Yehia et al., 2007). Moreover, the GPR profiles of a bridge deck can be utilized to



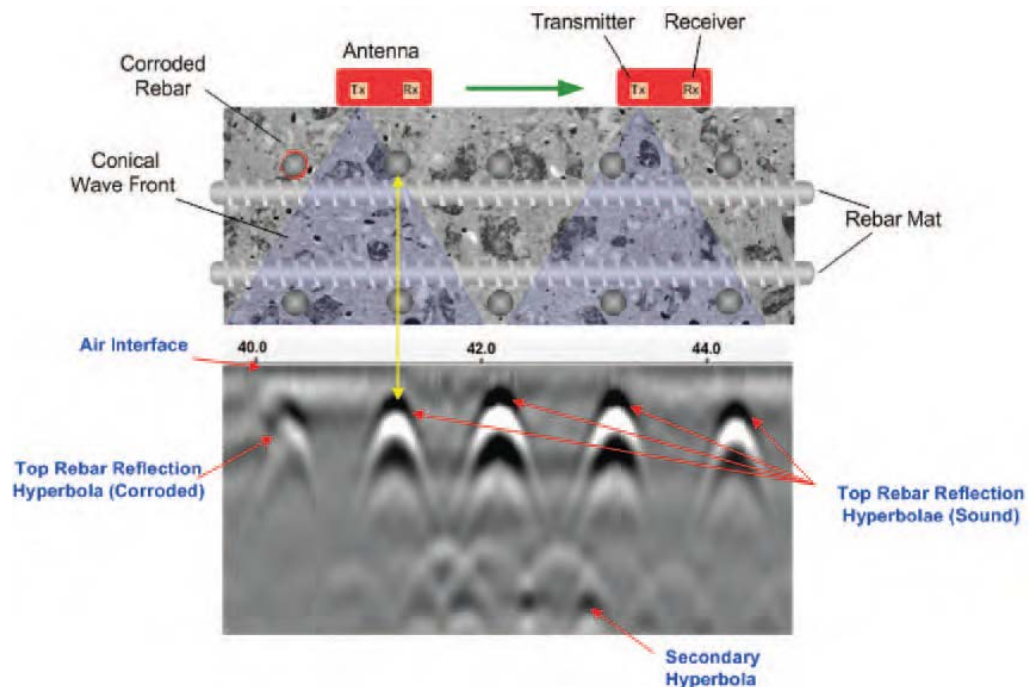
estimate the corrosiveness status because the signal attenuation is predominantly caused by an increase in conductivity at the level of the corroding rebar (Tarussov et al., 2013).



**Figure 2.15** GPR scanning a bridge deck in Laval using wheel-mounted equipment

Figure 2.15 shows an image of GPR testing of a concrete deck using the equipment in Laval, Quebec while Figure 2.16 shows a GPR scan of a sample reinforced bridge deck wherein the hyperbolae represent reflections at top rebar layer. The hyperbolae on the left section of the GPR profile is somewhat fuzzy indicating corrosion because of increased loss of signal at corroded rebar level. GPR applications include evaluation of deck thickness, measurement of concrete and rebar configuration, deterioration maps of bridge decks, characterization of delamination potential and concrete deterioration, and estimation of concrete properties. GPR limitations include its inability to detect delamination unless they are epoxy-impregnated or filled with water, negative influence

in results due to presence of moisture, extremely cold weather and one of its major limitations is *interpretation* of results (GPR profiles) obtained for corrosion detection.



**Figure 2.16** GPR principle (Gucunski & National Research Council, 2013)

### 2.6.5 Half-Cell Potential

Half-cell potential (HCP) method is an electrochemical technique to evaluate active corrosion in reinforced steel bridge deck by finding the potential difference between the reinforcement and a standard portable half-cell, typically a Cu/CuSO<sub>4</sub> standard reference electrode. Figure 2.17 shows the equipment used for Half-cell potential measurement. HCP measurements should be taken on the free concrete surface because the presence of isolating layers (asphalt, coating, and paint) make measurements erroneous. Also, since electrical connectivity is essential between the rebars, this method is not applicable for epoxy-coated reinforcements. The HCP test accurately assesses the corrosion of steel reinforcement; higher negative potential values indicate severe corrosion in



concrete, while less negative or positive potential values suggest otherwise. This method can be typically utilized to validate corrosion results from other NDTs.



**Figure 2.17** HCP testing (Gucunski & National Research Council, 2013)

### **2.6.6 Galvanostatic pulse measurement (GPM)**

The concrete corrosion rate measurement using HCP is often unreliable when concrete is wet, dense, or polymer modified. The GPM is a rapid assessment method of rebar corrosion by immersing an electrolytically conducting liquid of adequate oxidizing power. The corrosion current is indirectly measured by galvanostatically (with constant current) imposing a short-time anodic current pulse between a counter electrode at the concrete surface and the steel reinforcement. Figure 2.18 (a) shows GPM testing while Figure 2.18 (b) shows the GPM principle wherein the applied current polarizes the reinforcement anodically resulting in a measurable potential drop. Corroded areas in concrete possess an active current between the anode and cathodic sites and have lower

resistance to current flow compared to sound concrete areas. GPM like half-cell potential is a semi-destructive technique and pre-wetting of the concrete layer is essential in concrete deck covers with high resistivity.



**Figure 2.18** (a) GPM Testing and (b) GPM Principle (Gucunski & National Research Council, 2013)

### 2.6.7 Electrical Resistivity (ER)

The electrical resistivity method is used for detecting moisture which could indicate the presence of cracks. The amount of water and chlorides in concrete bridge decks are important parameters for determining the corrosion state. ER is measured using the Wenner's probe as shown in Figure 2.19 and the principle behind this method is that the presence of cracks leads to increased porosity and thus, defected areas will possess low ER values while sound concrete deck areas have higher ER values. The primary application of ER method is to characterize the concrete deck's susceptibility to corrosion. Since the ER depends on many material properties (moisture, salt content, porosity), interpreting the results of this method is a major limitation.



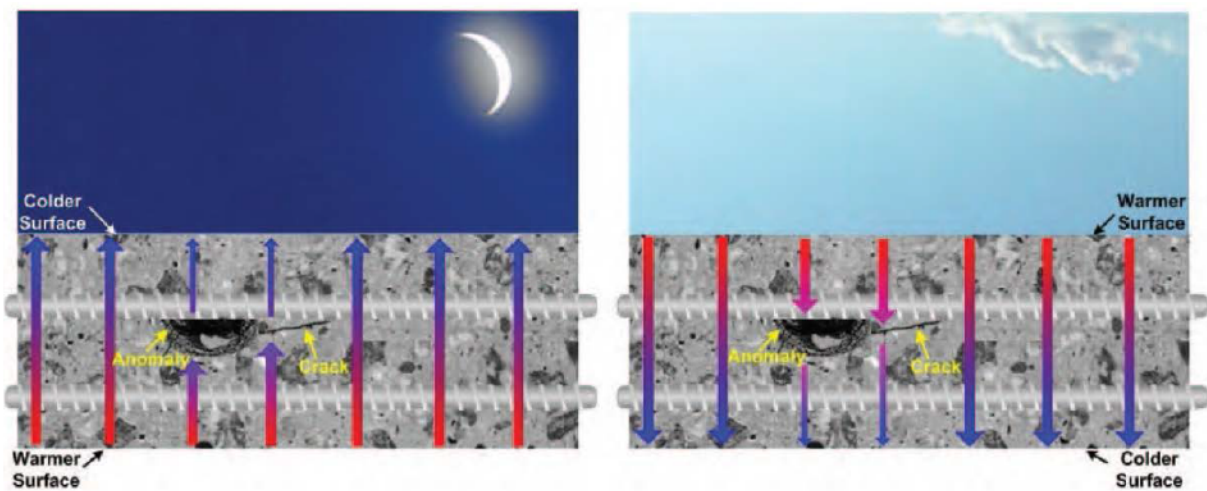
**Figure 2.19** Electrical Resistivity testing using a Wenner probe (Gucunski & National Research Council, 2013)

### **2.6.8 Infrared (IR) Thermography**

Infrared Thermography is used to measure voids and delamination in concrete decks. IR thermography method measures the thermal radiation emitted by the deck, and based on the thermal properties of various materials, the region is captured with temperature differences. IR maps of surface temperature are generated and the principle behind detecting anomalies (voids or delamination) is that areas with defects will have different thermal conductivity compared to sound concrete due to the presence of water or air. For example, delaminated areas due to the presence of air or water heat up and cool down quicker than sound concrete and thus, exhibit higher temperatures in the range of 1°C to 3°C than surrounding concrete. Figure 2.20 shows the process of testing IR thermography using infrared cameras. Figure 2.21 shows a deck under solar radiation which emits heat from all objects and the temperature variations are recorded using this method. Some limitations of this method include that it does not provide adequate information about the depth of flaws, cannot detect defects at higher depths, and is very sensitive to surface anomalies and boundary conditions.



**Figure 2.20** Infrared thermography testing using IR cameras (Gucunski & National Research Council, 2013)



**Figure 2.21** Principle of passive infrared thermography (Gucunski & National Research Council, 2013)



### **2.6.9 Chain Dragging and Hammer Sounding**

Chain Dragging and Hammer Sounding are popular techniques used by transportation authorities and it involves dragging a chain along the deck or hitting it with a hammer and listening to the sound produced to detect regions with delamination. Figure 2.22 shows the process of testing the bridge deck using the two methods. A clear ringing sound indicates a sound deck while a hollow sound indicates a delaminated area. The hollow sound is a consequence of flexural oscillations in the delaminated area of the deck. These oscillations are in the range of 1 to 3 kHz and hence, audible to the human ear. The sound generated is listened to by the bridge inspector while performing these tests for inspection. Chain drag is a relatively faster method and is used to determine the approximate location of delamination while hammer sounding is used to accurately determine the boundary of defect. The test needs to be performed without asphalt overlay which is a major limitation. Additionally, the method is very subjective as it is dependent on the operator's skill and hearing.



**Figure 2.22** Chain Dragging (left) and Hammer Sounding (right) (Gucunski & National Research Council, 2013)

### **2.6.10 Visual Inspection**

Transportation authorities have primarily been using the *visual inspection method* to evaluate the condition of the bridges, in which qualified bridge inspectors observe the defects and rate the bridge's components on a scale of 0 to 9 according to their expertise (Heymsfield & Kuss, 2015). Despite being straightforward and effective, this method has several drawbacks, two of which are its subjectivity and its inability to identify internal defects like corrosion, delamination, internal cracks, and others (M Abdul Rahman & Zayed, 2016). Therefore, it doesn't give accurate information on bridge decks, which could result in making bad decisions. (Moore et al., 2001) examined the reliability of visual inspection results of highway bridges and key findings of their report indicate that the visual inspection results are very subjective, as stated earlier, due to variable condition ratings by different agencies and that at least 48 percent of individual condition ratings for the primary elements were incorrectly assigned. Hence, transportation authorities over time have shifted their focus on *adopting NDT techniques over the years along with visual inspection* to determine the wholesome health of bridge decks or elements for better safety and management practices. Image-based assessment of the bridge deck condition has also gained some interest as a supplement to visual inspection (Adhikari et al., 2013a), (Adhikari et al., 2013b), (Adhikari et al., 2014). Some of the common NDT techniques used for bridge deck inspections have been briefly described in this section. The next step is the selection of appropriate NDT technique based on several factors and is a precursor to the motivation of choosing a suitable interpretation method of a specific NDT technique for this research.

## **2.7 Selection of recommended NDT Technique – GPR**

Various NDTs that could be used for bridge deck inspections were discussed in the previous section, each with its own benefits and drawbacks (Yehia et al., 2007). For instance, IE is highly

sensitive to the surface disposition and surrounding environment, even though it may identify delamination, cracks, and voids in the early stages of bridge elements (Oh et al., 2013). The selection of appropriate technology for a bridge deck is a challenge in itself. (Gucunski & National Research Council, 2013) performed a comprehensive study to determine the overall ranking of NDT technologies using weighted factors based on their ability to detect critical defects in bridge decks (delamination, corrosion, vertical, concrete degradation) and ranked GPR as the most recommended technique based on its ability to detect major subsurface defects within a short span of time (Table 2.5). Such studies aid in assessing the structural capacity and reliability of a structure to determine the safety issues and remaining service life (Ghodoosi et al., 2015), (Ghodoosi et al., 2018). Several other studies also indicate that GPR is the most appropriate and preferred technique among other NDTs for bridge elements inspection such as (D.J. Daniels, 2004), (Benedetto et al., 2012), and, (Alsharqawi et al., 2017). Therefore, the present research adopts GPR for inspecting bridge decks and developing condition maps. However, the interpretation of results from GPR inspection outputs based on widely applied amplitude-based analysis and its variants are not completely reliable or erroneous (Tarussov et al., 2013), due to which the transportation agencies are reluctant to depend entirely on GPR. A review of GPR data analysis is discussed in the next section along with the motivation for using a specific interpretation method adopted in this research.

**Table 2.5** Overall Value of NDT Technology in Bridge Deck Deterioration Detection (Gucunski & National Research Council, 2013)

Deterioration Type	Delamination	Corrosion	Vertical Cracks	Concrete Degradation	Overall Value	Ranking
	WF = 0.42	WF = 0.35	WF = 0.10	WF = 0.13		
Impact echo	3.0	0.0	1.0	1.0	1.5	2
Ultrasonic surface waves	2.7	0.0	2.4	3.3	1.8	2
Ground-penetrating radar	3.1	3.1	0.0	1.0	2.5	1
Half-cell potential	0.0	3.3	0.0	0.0	1.2	3

Galvanostatic pulse measurement	0.0	2.8	0.0	0.0	1.0	3
Electrical resistivity	0.0	3.6	0.0	0.0	1.3	3
Infrared thermography	2.9	0.0	0.0	0.0	1.2	3
Chain-dragging/hammer sounding	2.9	0.0	0.0	0.0	1.2	3

Note: WF - Weight Factor

## 2.8 GPR inspection and data analysis

### 2.8.1 GPR Survey Strategies

Using a "radio detection and ranging" (radar) technique for identifying hidden objects, GPR equipment uses an antenna to transmit electromagnetic (EM) waves into a bridge element to record subsurface reflections. The premier step requires the GPR operator to assess the feasibility of utilizing GPR to inspect the bridge component, considering both environmental conditions and the characteristics of the bridge deck. GPR may not function effectively in environments with high levels of free ions, such as presence of excess moisture or saltwater during winters. In such conditions, the transmitted signal dissipates into the ground as a weak electrical current, resulting in minimal to no signal return to the GPR receiver antenna, leading to data loss and limited subsurface information for analysis (Utsi, 2017). It is also important to complete a GPR survey for a bridge deck within a single day without major weather fluctuations (Varnavina et al., 2015). Additionally, if it is known a priori that certain sections of the bridge deck are exposed to moisture differently, such variations must be accounted for as areas with relatively higher moisture content will exhibit greater signal attenuation (Coleman & Schindler, 2022). GPR is not recommended on bridges with localized delamination over the reinforcements that are equipped with cathodic protection systems, or bridges containing conductive aggregate in their asphalt (ASTM D6087, 2015). Subsequently, the bridge deck to be inspected can be physically scanned using any GPR equipment produced by commercial companies such as Geophysical Survey Systems, Inc. (GSSI) or Ingegneria Dei Sistemi (IDS). Prior to scanning, it is essential to ensure that the bridge deck is in a clean, surface-dry



condition, free from soil, aggregate, or other particulate debris (ASTM D6087, 2015). The scanning procedure was briefly outlined in Section 2.6.4, which entails the selection of various survey parameters, some of which include:

- 1) Antenna frequency: When assessing a concrete bridge deck using ground-coupled GPR, it is common to employ one or more high-frequency antennas (exceeding 900MHz) to achieve the best trade-off between image depth and resolution (Gehrig et al., 2004). Typically, frequencies in the range of 1 to 2 GHz are used, but higher frequencies (such as 4 GHz) can be employed depending on the need such as when a greater level of detail is required closer to surface or in the presence of high moisture.
- 2) Number of scans per unit of distance: The number of scans per unit of distance refers to the density of individual scans and determines how closely spaced the data points are along the scanning path. It depends on both the repetition rate of EM pulses and the speed of acquisition and impacts both the lateral resolution and acquisition speed. In most cases, 24 scans per foot are adequate for imaging rebars in bridge decks, however, care must be taken if smaller anomalies need to be detected (Varnavina et al., 2015).
- 3) Transmission velocity ( $v$ ): Radar measurements are highly accurate, but any potential inaccuracies arise from the conversion of time measurements in nanoseconds into standard depth measurements. This conversion relies on knowing the transmission velocity, which is influenced by the electromagnetic properties of the materials the radar waves pass through. The relative permittivity, also known as the dielectric constant ( $\epsilon_r$ ), quantifies the electromagnetic behavior of different materials, and it can vary significantly between materials like asphalt, concrete, soil, stone, brick, air, water, or any substance where radar targets are located. The transmission velocity is determined by this relative permittivity of

the material under investigation ( $v = c/\sqrt{\epsilon_r}$ ; wherein  $c$  is the speed of light). The velocity passing through concrete ( $\sim 0.1$  m/s) varies considerably from that through air ( $\sim 0.3$  m/s) and water ( $\sim 0.01$  m/s). While it's common to assume a velocity of 0.1 m/s for concrete in bridge decks, care must be taken when calibrating and converting this velocity, especially when large voids (containing air, water and/or impurities) are present (Utsi, 2017).

- 4) Number of samples per scan: It refers to the number of discrete data points or samples taken within each individual GPR scan and should be approximately the size of or slightly smaller than the target to be detected. Using an excessively small sampling interval can slow down radar performance, even when data isn't lost, as it takes a longer time to acquire the complete data set (Utsi, 2017). Therefore, selecting an optimal value involves balancing radar speed with the required level of detail. The minimum requirement for concrete assessments within a 15 ns range is to use 256 samples per scan (Varnavina et al., 2015).
- 5) Wavelength ( $\lambda$ ): The wavelength of a radar signal depends on both the frequency and the material through which it propagates, especially the transmission velocity ( $\lambda = v/f$ ). It affects various aspects, including the depth of penetration, the smallest detectable object size, and the spacing at which adjacent objects can be distinguished. In practical terms, assessing this wavelength helps ensure that the correct antenna frequency has been chosen to detect and differentiate targets at the desired depth, such as identifying rebars in bridge decks. For example, the wavelengths must be either the same length as or shorter than the distance between the rebars (Utsi, 2017).
- 6) Penetration depth: In ideal circumstances, the maximum depth radar waves can penetrate before losing their energy is typically less than 20 wavelengths ( $\lambda$ ) (D.J. Daniels, 2004). However, real-world conditions rarely allow for such minimal signal loss, making it

essential to consider two practical implications. Firstly, when choosing an antenna for a bridge deck survey, one must account for a significantly shallower depth range than the theoretical 20 wavelengths. Secondly, the presence or absence of moisture or humidity during the survey can significantly impact the depth (Utsi, 2017).

- 7) Smallest target and its spacing: To be detectable by radar, an object (rebar for bridge decks) must be at least around 10% of the wavelength or larger. Short wavelengths are effective for finding small targets, but they limit depth penetration, creating a trade-off. High-frequency GPR is suitable for shallow small targets, while deep targets require lower frequencies, but the target size must be larger than 10% of the wavelength for detection. The choice depends on the target's depth and size. Additionally, it's essential to maintain a minimum spacing between each rebar of at least one wavelength (Utsi, 2017).
- 8) Traverse spacing: The choice of traverse spacing in a GPR survey depends on the investigation's objectives. For bridge decks, spacing of 1 to 2 feet is used to map detailed features of a bridge deck, whereas 3 to 6 feet is typically employed for a reconnaissance or quality-assurance survey (Varnavina et al., 2015).
- 9) Bandpass filters: These filters in data processing allow the selection of a specific frequency range while filtering out frequencies outside that range. In practice, GPR emits a spectrum of frequencies, with the antenna's frequency marked by a manufacturer represents its peak energy. In modern GPR systems, it is common to utilize the recommended low-pass and high-pass filters to eliminate spurious noise. For instance, when scanning a bridge deck with a 1.5 GHz antenna, one might apply a 3000 MHz low-pass filter and a 250 MHz high-pass filter to ensure the acquisition of high-quality data (Varnavina et al., 2015). Nevertheless, there may be situations, especially in complex environments, where applying these

filters to restrict frequencies to a narrow range could lead to data loss, making it challenging to analyze or interpret the results effectively. For bridge deck inspections, the application of such filters might inadvertently remove reflections from anomalies beyond rebar. A more effective approach could involve refraining from using these filters and instead conducting frequency-based anomaly separation during the subsequent data analysis phase.

Figure 2.23 shows GPR equipment installed on a wheeled cart produced by GSSI® and driven on the bridge deck manually for scanning. It has three main components: a) Antenna: which transmits and received the electromagnetic pulse; b) Control Unit: which triggers the signal, records the reflected signal, and shows it as a B-Scan on its display unit contained within; and c) Power supply: different sources ranging from small rechargeable batteries to vehicle batteries and normal 110/200-volt. The GPR antenna is dragged from one side to another to take one swab, and multiple swabs are taken at a certain distance from each other to completely scan a given bridge deck (or element) either along the longitudinal direction only or in a grid pattern. Once the scan is complete, the GPR profile data are transferred from the control unit as files onto a desktop computer/ laptop for further processing. Alternatively, GPR data can be directly obtained from an already scanned bridge deck database, if available.



**Figure 2.23** GPR Equipment (GSSI, 2022)

### ***2.8.2 GPR principles and existing approaches***

The radar reacts to variations in EM properties between any materials, making it capable of detecting any material, whether metallic or not, without relying on specific material presence. Nonetheless, it's important to understand that GPR doesn't directly provide information about the nature, type, color, or density of the target material. Such characteristics can be inferred using ancillary means such as the specific type of GPR investigation or externally provided information (Utsi, 2017). The rate of attenuation of the EM signals are dependent on the frequency of the transmitted wave, which is typically constant for a GPR survey, and the properties of the subsurface materials (Dojack, 2012). Thus, the recorded reflections of the EM waves are apparent at varying material interfaces of the element being inspected such as air/asphalt, asphalt/concrete, and concrete/rebar for reinforced structures (M Abdul Rahman & Zayed, 2016). The signal primarily responds to the electrical properties of subsurface materials, particularly their electrical conductivity and dielectric constant. The dielectric constant affects the speed of the signal as it is exclusively based on the moisture content of the medium. However, the signal loss in deteriorated concrete is predominantly

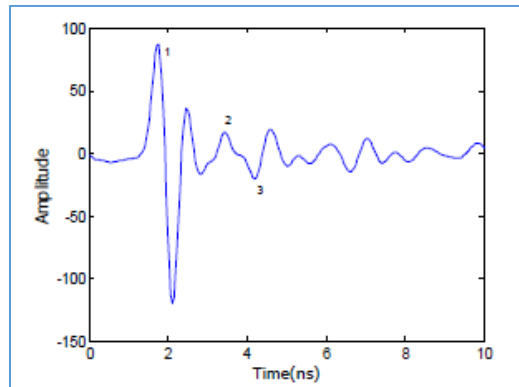
caused by the conductive loss of the material surrounding the concrete. Therefore, radar signals can *reasonably estimate* the level of corrosivity (such as severe, moderate or no corrosion) in reinforced concrete elements as it is highly sensitive to conductivity (Tarussov et al., 2013). Nevertheless, it's crucial to emphasize that GPR signals do not provide a direct measurement of corrosion or detect corrosion-induced volume changes at the millimeter level.

The radar signal emitted at a specific point or location can be shown as an amplitude vs. time graph called as an A-scan (Figure 2.24). When such A-scans recorded at regular intervals are merged across the complete section of a scanned element, it is represented as a *B-scan* as shown in Figure 2.25, where the X-axis denotes the distance along the direction of the scan and the Y-axis denotes the time or the converted depth after applying appropriate transmission velocity. A radar beam, which emits in a cone-shape widens with depth, begins detecting buried objects (typically rebars in bridge decks) before it aligns directly above them. As it approaches, the beam's edge detects the target, and this distance is recorded as its "apparent depth." However, it's longer than the true vertical depth. The apparent depth shortens as the radar approaches the target and reaches its minimum above the target's position, then increases again as the radar moves past. This relationship between depth and distance creates a hyperbolic shape when plotted (Utsi, 2017). In Figure 2.25, the B-scan displays hyperbolic patterns that correspond to radar reflections from the upper layer, with each hyperbola's peak indicating the location of rebar. The shape of each hyperbola is not determined by the contours of the target, except when the target's size significantly exceeds the radar's wavelength. The hyperbola's shape primarily results from two key factors: the radar's design, which includes the beam's shape and angle, and the electromagnetic properties of the subsurface (concrete in bridge decks), particularly the speed at which electromagnetic pulses travel

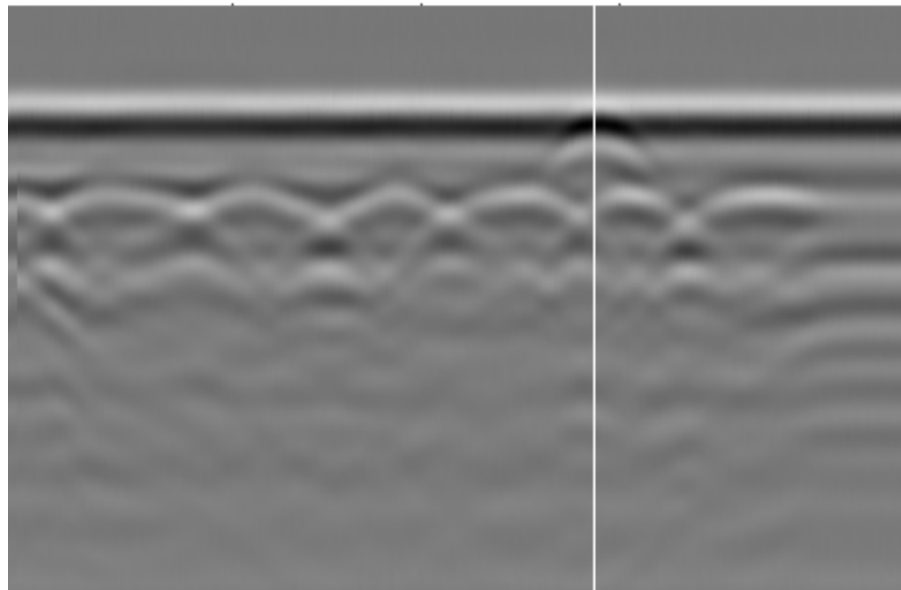
through the ground. While most aspects of the radar design are consistent, the hyperbola's appearance may vary with depth due to the widening of the beam. Consequently, each hyperbola's shape is influenced by depth and transmission velocity ( $v$ ). Specifically, if the radar waves encounter a material with a higher propagation speed, the hyperbolas may appear narrower and more elongated, while in materials with lower propagation speeds at similar depth, the hyperbolas may appear wider and more rounded. Although the standard practice is to conduct scans at a right angle to rebars, deviating from this orthogonal angle could potentially alter the hyperbolic shape, potentially introducing variations in signal strength and unwanted noise (Utsi, 2017).

When radar waves hit the rebar (steel reinforcement), they undergo a sudden change in the dielectric constant and this abrupt transition causes a portion of the radar energy to bounce back towards the surface, creating echoes. Occasionally, reflections from such highly reflective objects like rebars may manifest as 'multiples' or 'ring-down' in radar data. These occurrences are confined to the vicinity of the rebar and do not span the entire vertical section. The background echo effects, or 'ringing' occurs as recurring, regular horizontal bands in radar profiles, typically in their upper sections, and originates due to antenna system noise (Conyers, 2013). All radar systems have these faint echo effects, typically hidden by stronger reflected signals from subsurface targets. However, they become visible when no such strong signals are present (Utsi, 2017). Reverberation, akin to ring-down, generates multiples in reflection profiles. However, it arises from system noise caused by closely spaced "ringing antennae" that create such reverberations (Conyers, 2013). Finally, ringing caused by air or water gaps may manifest as repetitive hyperbolic patterns in radar profiles, resulting from abrupt changes in dielectric properties and significant variations in travel time (D. J. Daniels, 2005). GPR data analysis involves the interpretation of such radar signals, whether in

the form of A-scans or typically B-scans. While corrosion is a major defect identified, GPR can be used to identify other defects in bridge decks such as voids, honeycombing, delamination, and the presence of moisture content (Yehia et al., 2007).



**Figure 2.24** A- Scan (Abdel-Qader et al., 2014)



**Figure 2.25** B-Scan (marked vertical white-line represents extracted trace in Fig 2.23) (Abdel-Qader et al., 2014)



Several methods have been proposed in the literature to interpret data obtained from GPR scans and Table 2.6 enumerates this gradual development over the years by various researchers with a brief description. The initial methods focused on interpreting data based on individual waveforms or signatures in GPR profiles as proposed by (Clemena, 1983) and (Carter et al., 1986). A significant approach (Maser KR, 1990) involved analyzing GPR data based on normalized amplitudes while (Parrillo et al., 2006) developed deterioration maps by measuring such amplitudes at the concrete-rebar level. Subsequently, (Barnes et al., 2008) improved amplitude-based analysis by considering signal depth effects. An image-based analysis of GPR data by a human analyst was proposed by (Tarussov et al., 2010). As stated earlier, (Gucunski & National Research Council, 2013) conducted a comprehensive investigation on nine bridge decks using multiple NDEs. A time-series analysis of GPR data was proposed by (K Dinh et al., 2014) while another study suggested correlating original waveforms of GPR signals with semi-simulated waveforms at deteriorated state (Kien Dinh et al., 2017). Detection of delamination is a major issue of GPR data analysis and two recent studies investigated its reliability and the factors affecting it (Ali A. & Glenn A., 2018), (Kien Dinh & Gucunski, 2021). Additionally, a couple of studies proposed enhanced methods of signal depth correction (Kien Dinh et al., 2016), (Pashoutani & Zhu, 2023). Several holistic methods of deterioration mapping have been lately proposed which included automated detections of hyperbolic regions and considering other parameters besides amplitudes such as (Asadi et al., 2020), (Sepehr & Jinying, 2020), and (Kien Dinh et al., 2021).

**Table 2.6** GPR Data Analysis Improvement over the Years

<b>Sl.</b>	<b>Researcher &amp; Year</b>	<b>Brief description</b>
1	(Clemena, 1983)	Identified that deterioration signatures in a GPR profile are usually in a depressed shape with occasional ascending and blurred reflections.
2	(Carter et al., 1986)	Analyzed individual waveforms in GPR profiles and identified scaling and surface delamination by measuring variances in these waveforms.

3	(Chung et al., 1993)	A rating system was proposed to classify the condition of a bridge deck based on waveforms at the asphalt/concrete level in several bridge decks
4	(Maser KR, 1990)	A deck assessment technique by evaluating normalized amplitude values at the concrete surface.
5	(Maser & Bernhardt, 2000) (Romero et al., 2000)	Signal attenuation and concrete dielectric constant value were measured to assess the condition of bridge decks.
6	(Barnes & Trottier, 2004)	Evaluated GPR effectiveness by comparing with ground-truth results of numerous bridge decks and proposed that combining visual inspection data with GPR-predicted deteriorations can lead to better results.
7	(Parrillo et al., 2006)	Generated a deterioration map of a bridge deck based on amplitude values at the concrete-rebar level
8	(Barnes et al., 2008)	Proposed a linear regression model to improve GPR results by considering the signal <i>depth</i> -amplitude effects
9	(Tarussov et al., 2010) (Tarussov et al., 2013)	Condition mapping wherein an experienced analyst marks attenuated areas through GPR image analysis while considering several parameters such as surface anomalies, reflection amplitudes, rebar spacing variations, etc.
10	(Gucunski & National Research Council, 2013)	Multiple NDE techniques were applied to nine concrete bridge decks, and GPR was top-rated for identifying major subsurface defects when compared to other techniques.
11	(K Dinh et al., 2014)	Provided an alternative analysis based on evaluating the change of amplitude values over <i>time</i> to assess the condition of bridge decks.
12	(Kien Dinh et al., 2016)	Depth correction of amplitude values by accounting for geometric & dielectric loss in signals and conductive loss due to free ions individually.
13	(Kien Dinh et al., 2017)	Analyzed GPR data by correlating original waveforms with semi-simulated waveforms developed for completely deteriorated concrete.
14	(Ghodoosi et al., 2018)	Update the deterioration prediction model based on the GPR defect map to reliably estimate the remaining life of a bridge deck.
15	(Ali A. & Glenn A., 2018)	A reliability study to assess GPR's ability in detecting delamination in bridge decks.
16	(Kien Dinh et al., 2019)	Condition mapping of bridge decks by utilizing entire amplitude data of B-scans with synthetic aperture focusing technique (SAFT).
17	(Asadi et al., 2020)	Automated rebar detection in GPR images of bridge decks using a machine learning approach and condition assessment based on intensity values at identified peaks instead of amplitudes.
18	(Goulias et al., 2020)	Examined & compared A-scans at different locations in GPR profiles of a prestressed bridge deck to quantify potential concrete deterioration.
19	(Jiao et al., 2020)	Automated detections of three major defects (delamination, air-voids, and moisture) in GPR images including bridge decks through characterizing reflection signal's polarity and image shape patterns.
20	(Nicolas et al., 2020)	A new method to assess complete bridge deck condition (concrete surface condition, concrete cover, deck thickness, top rebar condition, and surface elevation) using step-frequency GPR antenna arrays.
21	(Rhee et al., 2020)	Developed a practical GPR signal interpretation method for condition assessment through statistical analysis of concrete relative permittivity for asphalt-covered bridge decks in Korean expressways.
22	(Sepehr & Jinying, 2020)	Deterioration mapping through combined analysis of three parameters at different depths instead of solely measuring signal attenuation which include: a) direct coupling amplitude map measured at the concrete surface, b) wave velocity map at cover concrete depth, and c) depth-corrected signal attenuation map from the rebar reflections.
23	(Kien Dinh et al., 2021)	Collected GPR data using the dual-polarization antenna and developed two algorithms based on the SAFT technique for 3D imaging of concrete

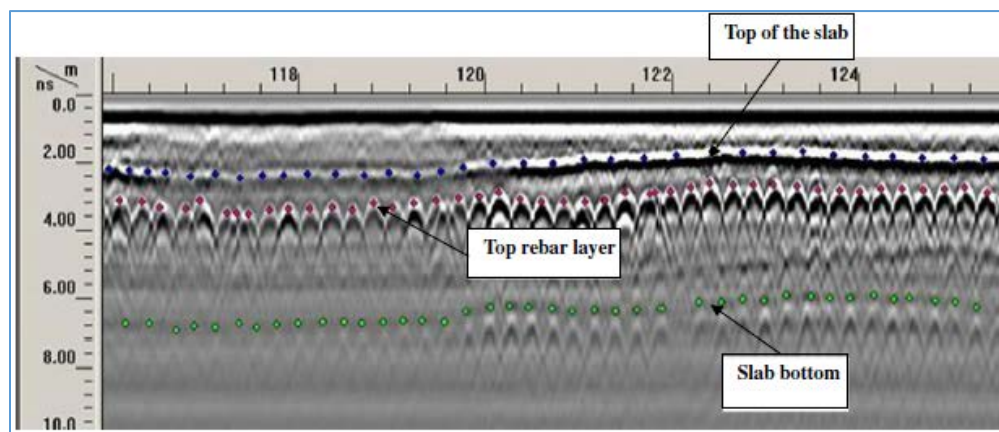
		structures to identify objects/ defects in both directions, steel bar debonding, and concrete delamination.
24	(Mohamed et al., 2021)	Proposed a formula to relate the area of corroded rebars with amplitude values based on finite-element analysis and corrosion mapping.
25	(Kien Dinh & Gucunski, 2021)	An investigative study to determine factors that affect the detectability of concrete delamination.
26	(Pashoutani & Zhu, 2023)	2 methods for depth correction using real rebar depth were proposed with a) migrated amplitude values and b) migrated and normalized amplitudes.

GPR data analysis is an active field of investigation, and the majority of proposed approaches (Table 2.6) are aimed at improving reliability through enhancing amplitude-based analysis (ABA). However, this approach of processing GPR data solely based on amplitude values suffers from an intrinsic limitation of ignoring 90% of data contained within radar profiles among others (Tarussov et al., 2013). The commonly adopted amplitude-based approach (basis of all ABAs) by transportation authorities is to analyze GPR data utilizing (ASTM D6087, 2015). This approach is explained briefly along with its drawbacks, and an alternative better approach to process GPR data utilized in this study is subsequently discussed.

**2.8.3 Numerical Amplitude-Based Analysis (ABA)**

The rebar locations in a bridge element correspond to the peak of the hyperbolas formed by the reflections at the concrete-rebar interfaces (Krause et al., 2007). The standardized procedure in (ASTM D6087, 2015) generates condition maps based on amplitude values of GPR profiles (B-Scans) obtained from scanning a bridge deck. It entails picking reflection amplitude values across B-scans at either of the two locations at regular intervals: (a) concrete-rebar interface, i.e., the peak of hyperbolas, or (b) relative amplitudes between the surface and bottom of the bridge deck. Figure 2.26 shows a sample GPR profile of a bridge deck with amplitude values taken at either of these points: a) red dots indicate amplitude values taken at the peak of hyperbolas which is rebar level,

and b) blue and green dots indicate amplitude values picked at top and bottom of slab respectively. Modern GPR data collection and processing software typically consists of a module that allows automatic rebar picking. Due to the presence of corrosion at rebar levels or any void(s), the signal attenuation, which is conversely related to amplitude, is higher compared to sound concrete. Therefore, the basic principle is that *higher values of amplitudes indicate areas of good concrete condition while lower values indicate areas of moderate-to-bad concrete condition* (Mohammed Abdul Rahman, Zayed, et al., 2022). Subsequently, a condition map is generated for the complete bridge deck by stacking amplitude values of all profiles relative to its location which shows areas of concrete with varying conditions such as good, moderately corroded, and severely corroded concrete. Such maps can be used by bridge inspectors to locate deteriorated regions that require further inspection and repairs. Modern GPR equipment manufacturers often provide their proprietary modules for automated rebar detection and deterioration mapping based on amplitude analysis, such as the ‘BridgeScan Handbook’ designed for use with the GSSI® SIR 4000 system (GSSI, 2017). Although numerical ABA is a commonly adopted approach for GPR profile analysis (K Dinh et al., 2014), it has various limitations as discussed in the next section.



**Figure 2.26** Picking of points in a GPR profile for amplitude analysis (Tarussov et al., 2013)

#### **2.8.4 Limitations of Numerical-ABA**

Firstly, it is presumed that employing numerical ABA speeds up data processing, yet this ignores the *majority of the information in a GPR profile which is visual in nature* (Tarussov et al., 2013). Secondly, the method is assumed to be objective and could produce precise results because it employs numerical values. Even so, it is untrue since several amplitude-affecting factors are disregarded such as depth, surface anomalies, reinforcing bar spacing, reinforcing bar configuration, polarization effects, apparent change in slab thickness, and others. Corollary, condition maps based on numerical-ABA analysis *can be ambiguous, noisy, and not always reliable*. (Parrillo et al., 2006) investigated an amplitude-based corrosion map of a bridge deck and proved that the color-coded results do not indicate the actual amount of deterioration. Additionally, structural or surface anomalies are not evaluated during this analysis (Tarussov et al., 2013). (Giachetti, 2000) also stated that for a bridge with no or near deterioration, rebar depth variation correction is required. The number of deterioration zones corresponding to the condition of concrete (typically three: good, moderate, and bad) and its threshold calculations are prone to interpolation and criticism as the results are not consistent and do not correlate with the actual ground conditions (Kien Dinh et al., 2015). Although the ABA analysis has been considerably improved such as accounting for variations due to depth (Barnes et al., 2008), it suffers from a major limitation of considering only a *single parameter* for GPR data analysis (amplitude). Therefore, a different approach that also considers the visual nature of GPR data and accounts for several parameters rather than just amplitude has been proposed by (Tarussov et al., 2013). This approach is known as GPR image-based analysis, and it has been discussed briefly in the next section.

## 2.9 GPR Image-Based Analysis (IBA)

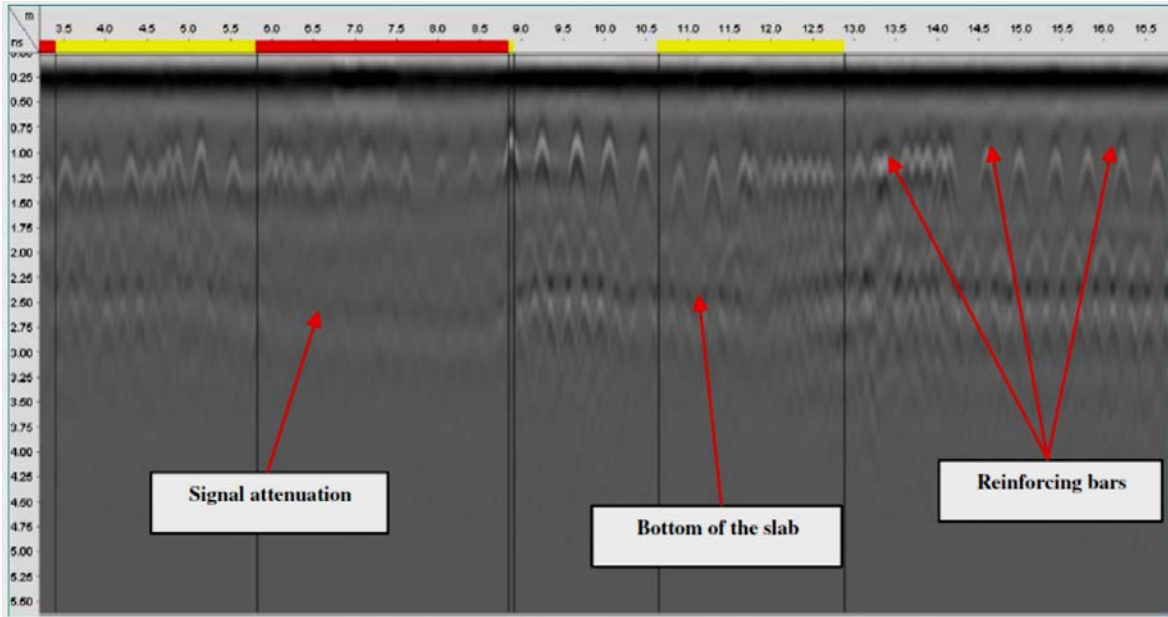
A better approach based on visually analyzing GPR profiles potentially addresses significant issues with the numerical-ABA method. The IBA method views GPR as an imaging tool as opposed to an (amplitude) measuring tool. With the help of real case examples, (Tarussov et al., 2013) validated this method by demonstrating that the condition maps generated based on his method corresponded closely with the actual condition of bridge decks.

### 2.9.1 Methodology

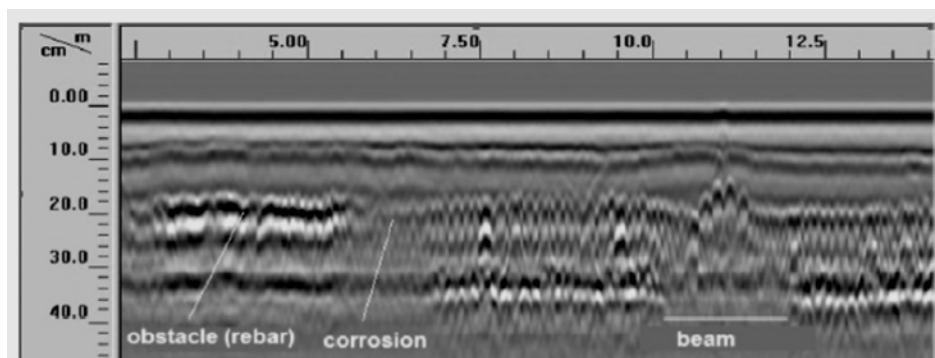
Using the proprietary software 'RADxpert' developed by Radex Detection Inc., each profile is visualized as an *image* of a GPR dataset obtained for a reinforced structural element and individually scanned by an experienced analyst based on the procedure described extensively in (Tarussov et al., 2013). The areas or *zones* are marked as *yellow or red* depending on the estimated severity of the condition (moderate or bad correspondingly) and graphically displayed overall identified zones in each GPR profile (B-scan). A zone is left alone if it is in good shape, that is, if it contains no attenuated sections, and it is automatically marked as *green*. When labeling these GPR profiles, the analyst takes into account several parameters which include surface anomalies, reflected amplitudes at the top and bottom slab, presence of water puddles on the surface, structural anomalies like the presence of beam or column, variation in rebar spacing or slab thickness, staggered rebars, pavement debonding, expansion joints, air or water voids, and previous repairs. GPR data reflects variations in the dielectric constant, and it's essential to emphasize that a hyperbola or any distinctive feature represents this change compared to its surroundings. Therefore, any hyperbola can be described as an 'anomaly,' but whether it signifies the presence of a rebar, or any other anomaly depends on the type of inspection, location, and several other factors. Moreover, corrosion, excessive moisture, and fracturing do not create distinct boundaries but rather impact radar signals

through *subtle changes* in attenuation or velocity (Tarussov et al., 2013). Therefore, in this approach, an analyst is considered best suited to distinguish rebar regions from other anomalies and identify their corrosion levels based on analyzing such nuances in GPR profiles. The resultant condition map derived using this approach is less noisy and significantly better than numerical-ABA since each profile is carefully examined for even minor variations.

A sample GPR profile demonstrates how to identify and mark red & yellow zones using the GPR-IBA method in a simple case with no anomalies present as shown in Figure 2.27. Zones with the *highest attenuation* are marked as red on top in RADxpert®, corresponding to bad condition of concrete while zones with *lower attenuation* are marked in yellow color, corresponding to moderate condition of concrete. The zones unmarked represent the good condition of concrete and would be labeled as green in the condition map developed based on this analysis. To briefly illustrate with an example how GPR-IBA is better than numerical-ABA, consider the profile shown in Figure 2.28. It contains a structural anomaly (beam) present in the right section of the B-scan which looks similar to a corrosion zone (middle-left). The ABA method would not identify such an anomaly due to amplitude values being closer to the corroded zone. However, an analyst performing the GPR-IBA approach can easily identify the absence of corrosion in the structural anomaly zone based on the visual appearance and/or location of structural members based on structural drawings, if available, and thus, such regions would be marked appropriately yielding a precise and noise-free condition map. Corollary, the GPR-IBA method considers all such anomalies and other parameters while marking attenuated areas.



**Figure 2.27** Marking attenuated areas using Image-based Analysis (Tarussov et al., 2013)

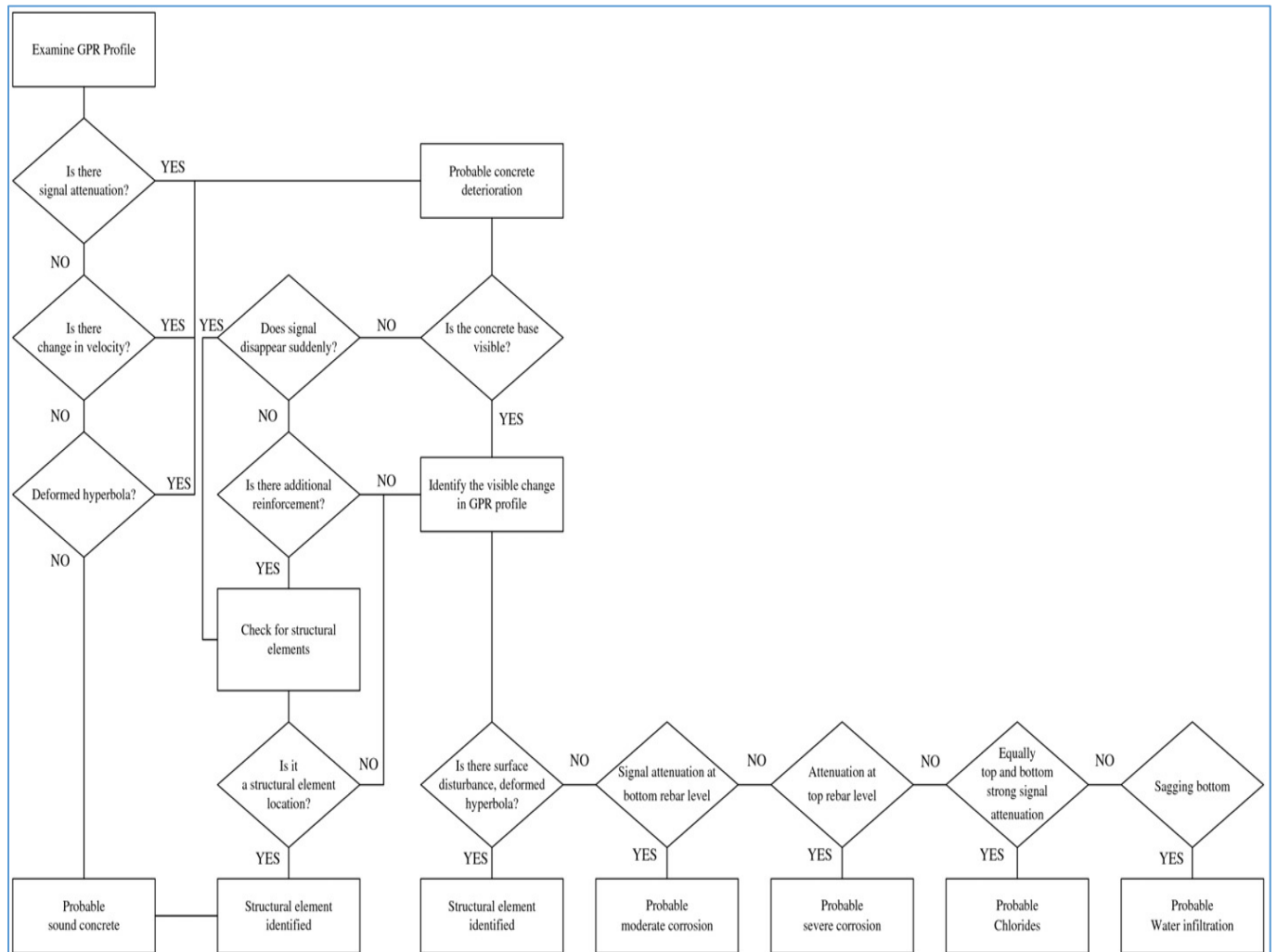


**Figure 2.28** Zone of corrosion & anomaly distinguished by GPR-IBA (Tarussov et al., 2013)

A systematic framework for the GPR-IBA method was developed with the help of experts by (Abouhamad et al., 2017) and consists of mainly two interrelated tasks: a) remove anomalies that aren't caused by rebar corrosion, and b) identify defects that are induced due to corrosion. Figure 2.29 shows the flowchart of this framework containing steps of if-then rules based on an extensive learning process while considering parameters mostly indicative of a structure corrosiveness condition. The parameters to identify deterioration include understanding the structure being



inspected, considering top and bottom rebar amplitudes, slab bottom amplitudes, deformed hyperbolas, radar velocity changes, and visible cracks/delamination. The factors relating to identifying anomalies include supporting structures such as main girders, beams, or columns, variation of rebar spacing, alignment and depth, previous repairs, and surface anomalies such as cracks.



**Figure 2.29** Framework of GPR-IBA analysis (Abouhamad et al., 2017)

On sets of concrete bridge decks scanned using GPR along a segment of the I-290 and I-294 Tollways in Chicago (IL), USA, the GPR-IBA approach was compared with extracted cores

(destructive technique), chain-drag technique, and chloride profiles. The corrosion maps based on the IBA method had better correspondence with the ground truth concrete condition when compared with amplitude-based analysis (Tarussov et al., 2013). Similarly, two bridge decks were scanned in Quebec and the resulting maps based on GPR-IBA were comparable with amplitude-based maps, visual inspection, and Half-Cell Potential results, and validated with ground-truth cores (Abouhamad et al., 2017). Based on the GPR-IBA framework, (Dawood et al., 2020) developed an integrated approach to generate condition maps that identify air/water voids in subway tunnels. A portion of a subway tunnel in Montreal, Quebec, was examined, and the map developed by the proposed model (Dawood et al., 2020) demonstrated a high degree of correlation when compared with the laser-based thermal map, visual inspection results (camera images), and extracted cores. Thus, the condition maps generated by GPR-IBA analysis have been validated to show *better correspondence with the actual in situ concrete condition*.

### **2.9.2 Significance and Limitations**

The GPR-IBA analysis of GPR profiles has the following major advantages: a) all structural and surface anomalies and several other parameters can be identified by an analyst and accounted for, instead of mistakenly identifying them as corroded zones, b) depth variations are also accounted for by the analyst, c) reduced noise due to visual filtering, and d) reasonably correct limits of corroded zones resulting in fairly accurate *in situ* condition of reinforced concrete structural elements. However, this analysis does have some shortcomings of its own (Mohammed Abdul Rahman, Zayed, et al., 2022). Firstly, it is *prone to human errors* because an analyst manually marks the attenuated areas. For instance, based on optical judgment, an analyst might categorize a certain area in a B-scan in a different way each time as either moderate or severe. Likewise, the

accuracy of a GPR survey, conducted by an operator, and the selected parameters significantly impact the resulting profiles (B-scans). Consequently, it is sensitive to both factors: the operator's scanning technique and the subsequent interpretation. Secondly, it is *subjective* because various analysts may have different visual perceptions of what constitutes areas in GPR profiles as good, moderate, or severe. Thirdly, the level of accuracy is dependent on the *expertise of the analyst*. Fourthly, the analysis could be *laborious and time-consuming*, particularly when dealing with bridge decks having large spans. Finally, GPR-based delamination detection has several limitations, primarily because the fractures or cracks in concrete are often too thin compared to the wavelength to generate a noticeable reflection (Tarussov et al., 2013). Based on findings from an experimental study, it was determined that delamination with a thickness of up to 2.4mm at the level of the top or bottom reinforcement mat in bridge decks without overlays cannot be identified when scanned with a 2.6 GHz frequency antenna (Coleman & Schindler, 2022). Another study indicates that the detectability of delamination depends on factors like its thickness, its content (air or water), signal frequency, concrete's dielectric constant, and delamination width. The detectability of delamination is also influenced by their proximity to steel reinforcement bars, as these bars are excellent reflectors of radar energy. Delamination located above or away from the bars can be readily detected, but those situated at the same level or directly beneath the bars are challenging to identify, as these may be obscured by the reflections from the rebar. In some cases, scanning along the transverse direction may improve the chances of uncovering these concealed delamination, but they still remain difficult to detect (Kien Dinh & Gucunski, 2021). While this is not a limitation inherent to the method, but rather a characteristic of GPR technology, an analyst should be mindful of it and adjust when feasible. Despite these constraints, when an analyst meticulously analyzes

GPR profiles employing GPR-IBA, it has been validated to provide corrosion maps that closely align with the actual ground truth, as previously discussed.

By using automated hyperbola detections and classification based on mathematical modeling, this research seeks to resolve the shortcomings of the GPR-IBA approach. For a given set of GPR data, a condition map generated utilizing developed model(s) would produce a *consistent (same) output devoid of any human errors*. A thorough analysis of various image processing and computer vision tools has been performed and applied to GPR data sets to develop a reliable approach based on image-based analysis. Although several researchers have proposed various approaches to identify hyperbolic signatures in GPR profiles along with noise removal, there have been no efforts in the literature to develop a comprehensive robust approach for condition mapping based on automated image analysis of GPR data. Hence, this research has identified this *need* and has developed models to analyze GPR profiles based on GPR-IBA.

## **2.10 Previous Efforts of Image Processing**

A major objective of analyzing GPR data is detecting hyperbolic signatures automatically in its profiles. Such signatures can represent varying objects depending on the type of GPR survey. They often indicate embedded rebars when assessing structures for condition evaluation, such as bridge decks, pavements, or slabs. On the other hand, if the inspection is done to map underground utilities or find buried objects, they typically indicate hidden pipelines, cables, landmines, tree roots, or even archaeological artifacts. While several methods of image processing efforts are found in the literature, Table 2.7 delineates an extensive list of identifying hyperbolic signatures in GPR profiles along with the primary algorithm employed in each approach.

**Table 2.7** Image Processing efforts of hyperbolic signatures detection in GPR Profiles

Sl.	Researcher & Year	The primary type of detection algorithm
<i>Curve-fitting based</i>		
1	(Yilmaz, 1987); (Dell'Acqua et al., 2004)	Radon transform or its variants
2	(Mallat, 1989); (Carevic, 1999); (Hui-lin et al., 2005); (Ni et al., 2010)	Wavelet transform or its variants
3	(Kaneko, 1991); (Kleinmann et al., 1993); (Capineri et al., 1998); (Simi et al., 2008); (J. Wang & Su, 2013); (Windsor et al., 2014); (Li et al., 2016)	Hough transform or its variants
4	(Shihab, 2005)	Curve fitting with the least-square method
5	(Krause et al., 2007)	Arc detection based on hyperbolic equation and other GPR data properties
6	(Yayu Liu et al., 2010)	Curve fitting based on hyperbolic echo characteristics
7	(Z. W. Wang et al., 2011)	Signature discrimination based on partial differential equations
8	(Qiao et al., 2015)	Multiresolution Monogenic Signal Analysis (MMSA) with Hough transform to locate hyperbolic targets
<i>Machine Learning based</i>		
9	(Fritzsche, 1998); (Gader et al., 2001)	Hidden Markov Model (HMM)
10	(Zhang et al., 2014); (Manandhar et al., 2015);	HMM with ML framework
11	(Delbo et al., 2000)	A fuzzy quadratic shell clustering algorithm
12	(Al-Nuaimy et al., 2000); (Gamba & Lossani, 2000); (Shaw et al., 2005); (Birkenfeld, 2010); (Singh & Nene, 2013)	(Deep) Neural networks trained on GPR datasets to classify hyperbolic regions.
13	(Besaw & Stimac, 2015); (Sakaguchi et al., 2015); (Lameri et al., 2017); (Reichman et al., 2017); (Kien Dinh et al., 2018); (Ishitsuka et al., 2018); (N Kim et al., 2019); (Namgyu Kim et al., 2020)	CNN trained on real and simulated data
14	(Lei et al., 2020)	CNN-Long Short-Term Memory (LSTM) Framework
15	(F Hou et al., 2021); (Feifei Hou et al., 2021)	Enhanced mask R-CNN
16	(Pham & Lefèvre, 2018); (Feng et al., 2020); (Jaufer et al., 2021); (Kumlu, 2022)	Faster R-CNN framework
17	(Pasolli et al., 2009); (Harkat et al., 2018); (Yanhui Wang et al., 2020)	Multi-objective Genetic Algorithms (GAs)
18	(El-Mahallawy & Hashim, 2013); (Qin & Huang, 2016)	Discrete cosines transform with SVM classifier
19	(Harkat et al., 2016)	Scale-Invariant Feature Transform (SIFT)
20	(Sagnard & Tarel, 2016); (Terrasse et al., 2016)	Template matching with a dictionary of defined objects
21	(Maas & Schmalzl, 2013)	Viola-Jones (V-J) Algorithm with Haar-like features
22	(Lee & Mokji, 2014); (Torrione et al., 2014)	HOG feature descriptor
23	(Kaur et al., 2015)	HOG with SVM classifier and curve fitting using Random Sample Consensus (RANSAC)
24	(Gibb & La, 2016)	HOG with Naïve Bayes classifier
25	(Malof et al., 2018)	HOG with improved CNN classifier
26	(Noreen & Khan, 2017)	HOG descriptor with V-J Algorithm & SVM classifier
27	(Asadi et al., 2020)	HOG with Multi-Layer Perceptron (MLP) classifier
28	(Zong et al., 2019)	YOLO (You Only Look Once) v3

29	(Ahmed et al., 2020)	Different architectures of Residual neural Networks (ResNet), and densely connected convolution Networks (DenseNet) utilized and compared
30	(Ozkaya et al., 2020)	Convolutional Support Vector Machine (CSVM)
31	(H. Liu et al., 2020); (Yu-Chen et al., 2022)	Single-Shot Multibox Detector (SSD) framework
32	(Zhang et al., 2021)	Generative Adversarial Nets (GANs) framework
33	(Wunderlich et al., 2022)	RetinaNet deep learning framework
34	(Ahmed et al., 2023)	Novel multi-stage Deep Encoder-Decoder framework
<i>Pixel-based</i>		
35	(Mertens et al., 2016)	An algorithm that detects ill-shaped hyperbolas by allocating a buzzer zone with hyperbolic fitting.
36	(Dou et al., 2017)	Novel column-connection clustering (C3) algorithm
37	(Chenxi et al., 2018)	A new drop-flow algorithm that mimics the movement of a raindrop
38	(Zhou et al., 2018)	Novel Open-Scan Clustering Algorithm (OSCA) which identifies downward-opening signatures
39	(Lei et al., 2019)	Double cluster seeking estimate (DCSE) algorithm which improved the OSCA along with faster R-CNN

The earlier methods of detecting signatures involve direct curve-fitting algorithms, such as Radon, Hough, and wavelet transform, including their variants, employed to fit the hyperbolic equation. Such approaches suffer from overfitting, leading to several false positives, excessive noise, and manual selection of parameters. The detection rate is typically low, especially in cases of complex signatures present in GPR profiles. Although neural networks (NNs) have been utilized for identifying objects in GPR data since the early 2000s such as (Al-Nuaimy et al., 2000) and (Gamba & Lossani, 2000), there has been an increasing trend in recent years to apply machine learning (ML) and deep learning (DL) approaches due to the availability of high computing power and the significant evolution of computer vision algorithms (Martoni et al., 2022). CNNs have been used extensively by several researchers as it offers the advantage of incorporating learned parameters as extracted features from the data (Travassos et al., 2020). Similarly, HOG is a common feature descriptor utilized with different classifiers (SVMs, Naïve Bayes, MLP) as it has been tested to have the best accuracy, precision, and sensitivity rate to train and categorize rebar reflections (Kaur et al., 2015). Recently, researchers have been exploring the detection of signatures in GPR datasets

through the application of diverse DL frameworks, including ResNet, DenseNet (Ahmed et al., 2020), GANs (Zhang et al., 2021), SSD (Yu-Chen et al., 2022), and RetinaNet (Wunderlich et al., 2022). ML-based methods demonstrate relatively higher accuracy in detections compared to curve-fitting methods. For instance, studies such as (Zong et al., 2019) reported accuracies up to 85%, (Kaur et al., 2015) achieved 96% accuracy, and (Namgyu Kim et al., 2020) achieved an impressive 98% accuracy. However, these methods do have limitations, and one such limitation is the availability of large, open-source GPR databases that accurately represent varied real environments. Such databases are crucial for effectively training the models and improving their performance (Martoni et al., 2022). Several methods typically have a manual threshold leading to false and missing detections. Although certain proposed approaches make use of transfer learning from extensive datasets like AlexNet (Namgyu Kim et al., 2020) or simulated data generated by tools such as GPRmax (Pasolli et al., 2009), the accuracy of detection can vary significantly across different conditions and is primarily influenced by the quality and diversity of the training data. Despite these drawbacks, ML methods are highly desirable due to their ability to significantly reduce human effort and achieve a high degree of accuracy (Martoni et al., 2022). Some recently proposed methods focus on detecting patterns in GPR profiles by analyzing hyperbolic characteristics and features within a preprocessed binary image at the pixel level. Such *pixel-based* methods enable exhaustive searches with decreased computational requirements, as they don't rely on training data and exhibit high efficiency. As an illustration, the C3 algorithm introduced in a study by (Dou et al., 2017) focuses on locating clusters of pixels that are connected vertically, while the OSCA algorithm described in a paper by (Zhou et al., 2018) specifically targets the identification of downward openings. Moreover, these techniques can be integrated with ML algorithms to enhance the detection rate. For instance, in the same study by (Dou et al., 2017), a three-layer

feedforward NN was employed after applying the C3 algorithm to further improve the results. Similarly, in the research conducted by (Lei et al., 2019), Faster-CNN was utilized as a precursor to identifying downward openings. Although these approaches can outperform ML-based methods, particularly when dealing with diverse data, it is important to note that these methods still rely on an optimal noise removal threshold to achieve an improved detection rate. Lastly, none of the existing methods have specifically aimed at developing a comprehensive approach based on image-based analysis. Consequently, there is a need for enhanced automated detection techniques in GPR profiles to generate reliable condition maps using GPR-IBA.

## **2.11 Key Findings and Research Gap**

The following lists key findings along with identified research gaps in the literature that motivated this research has been summarized as follows:

1. A novel method proposed by (Tarussov et al., 2013) utilized the GPR-IBA approach to analyze GPR profiles, and this method will be adopted in our research as it has shown better ground truth correspondence when compared with traditional numerical-ABA approaches.
2. The GPR-IBA considers various anomalies and corrosion-affecting factors during analysis and considers a GPR profile as an imaging tool instead of a measuring tool. Hence, the resulting condition map is more accurate with less noise.
3. The current GPR-IBA has the major limitation of using an expert analyst for analyzing each GPR profile and is prone to human errors. To reduce subjectivity and produce consistent results, there is a need to automate this approach using image processing tools of MATLAB® with a user-interactive approach.



4. Numerous efforts found in the literature indicate that image processing techniques have been primarily employed to pick rebar locations in GPR profiles but subsequently, these methods have applied ABA or its variations to develop condition maps. *There is a need to employ image processing techniques to locate hyperbolic regions and utilize GPR-IBA for developing condition maps instead of numerical ABA methods.*
5. Previous image processing techniques as mentioned by (Kaur et al., 2015) have various limitations. Curve fitting & thresholding techniques suffer from overfitting problems, noise, and manual selection of thresholds while machine learning techniques cause missing or false detections and typically require a large database to incorporate the diversity of shape of hyperbolas. Novel methods are needed for automated detections of regions in GPR profiles which overcome such limitations.

## **2.12 Preliminary Investigations**

After identifying research gaps through a literature review, an extensive exploration of image processing and computer vision tools was conducted. These tools were applied to sample GPR profile(s) to identify potential model(s) for efficient processing of GPR data using IBA. *The following sections does not delve into the methodology of the developed models.* Instead, it provides a brief background on typical image processing and computer vision techniques, followed by an exploration of various image-processing operations using sample GPR profiles. After the GPR bridge deck data is obtained, the radar profiles are generally pre-processed in the proprietary software of the respective GPR equipment manufacturer and these operations typically include applying display gain and background removal. After applying pre-processing steps, if needed, the profiles are converted into image files. All GPR radar profiles utilized in this research were scanned using

GSSI® equipment. The software used for pre-processing and converting the radar files was 'RADAN 7', specifically version 7.6.19.11260. The radar files have a '.dzt' extension and were converted to image files in '.bmp' format. Thus, the GPR data profiles obtained in image format become an input for performing image processing operations required for developing the models. The image processing tool utilized in this research is MATLAB (abbreviation of "MATrix LABORatory") developed by MathWorks®. The specific version used in this research was R2019b (9.7.0.1190202).

### 2.13 Image Processing Overview

This section gives a brief introduction and background of common image processing operations. A visual two-dimensional representation of an object, a person, or a scene produced by an optical device such as a mirror a lens, or a camera is called an *image*. The representation of such a two-dimensional image utilizing a finite number of points, usually referred to as *picture elements*, or *pixels*, is called a *digital image*. Each pixel can be represented by one or more numerical values: for monochrome (grayscale) images, one value representing the intensity of each pixel (usually in a [0, 255] range; or for color images, three values (e.g., representing the amount of Red (R), green (G), and blue (B)) are usually required. The term *digital image processing* refers to the science of modifying digital images using a digital computer. (Marques, 2011)

Three levels of image processing have been categorized by (Gonzalez et al., 2010):

- a) *Low-Level* processing which includes primitive operations of image preprocessing such as noise reduction, contrast enhancement, and sharpening. At this level, the input and output of the process are both images.

- b) *Mid-Level* processing involves a process in which inputs are images while outputs are extractions or attributes of the input image such as edges contours, etc.
- c) *High-Level* processing involves “making sense” of an ensemble of recognized objects and it can be extended from image analysis to performing cognitive functions normally associated with computer vision.

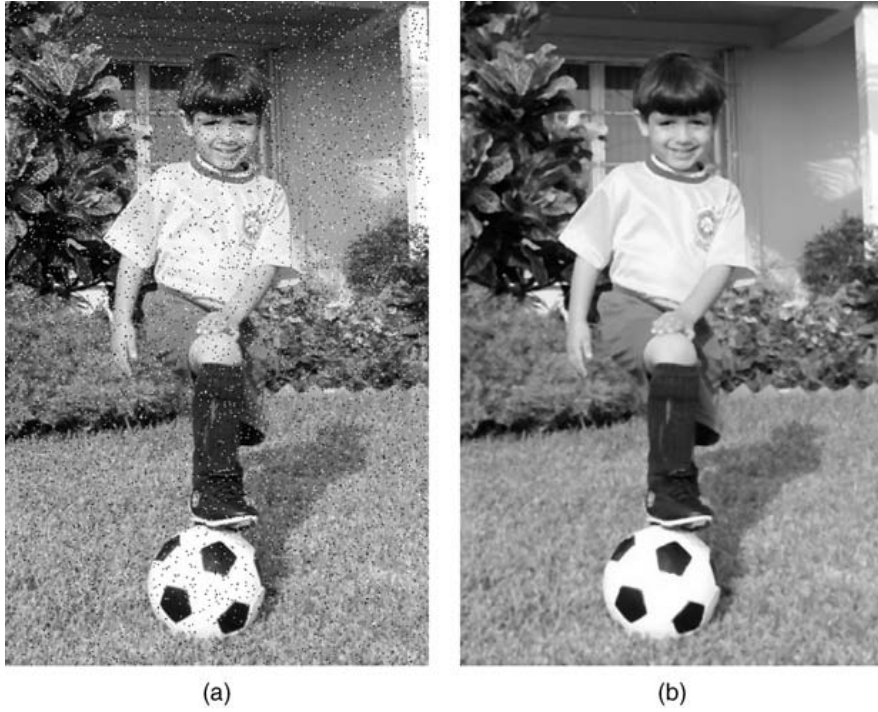
Although image processing operations cover various concepts and techniques including image analysis and extending up to computer vision, an overview of the most representative image processing operations is described below (Marques, 2011). The figures associated with each operation are a sample example of the process described.

- 1) Sharpening (Figure 2.30): Image sharpening refers to an implementation of a technique through which the edges and fine details of an image are enhanced for human viewing.
- 2) Noise Removal (Figure 2.31): It is generally a pre-processing step that involves applying filters to reduce the amount of noise in an image through the application of various techniques.
- 3) Deblurring (Figure 2.32): It refers to techniques of image processing that focus on deblurring an image for a better representation of the image.
- 4) Edge Extraction (Figure 2.33): It refers to techniques or algorithms used to extract edges from an image. Extracting edges could be a pre-processing step for separating objects of interest from one another before identification of their contents.
- 5) Binarization (Figure 2.34): It refers to reducing the number of grey levels in a monochrome image to only two levels of grey (black and white).

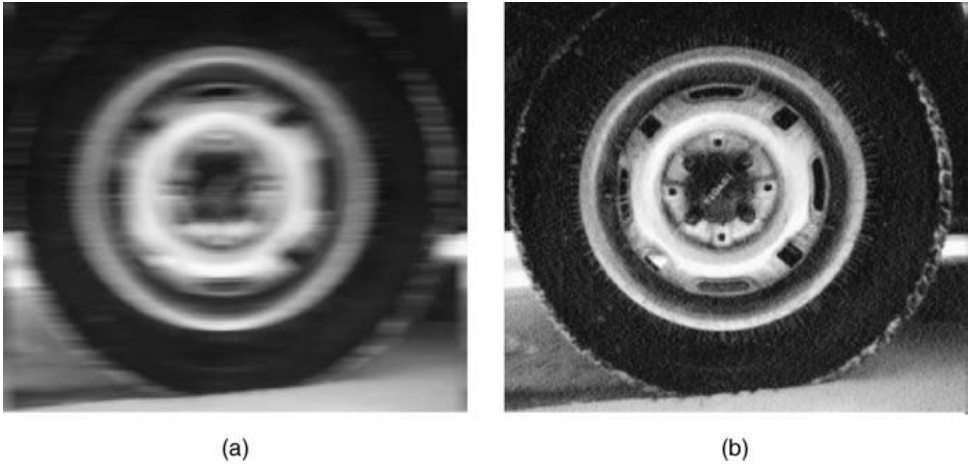
- 6) Blurring (Figure 2.35): It refers to applying techniques on an image where it is necessary to blur it to minimize the importance of texture and fine details to better recognize objects contained within the image by their shape.
- 7) Contrast Enhancement (Figure 2.36): It refers to applying techniques such as histogram processing or utilizing transformation functions to enhance the contrast of an image for better human viewing or other image processing tasks (such as edge extraction)
- 8) Object Segmentation and Labelling (Figure 2.37): It refers to segmenting objects of interest from an image and labeling which can be used to classify, compare, cluster, or recognize the detected objects. It is part of feature extraction and pattern recognition in an image.



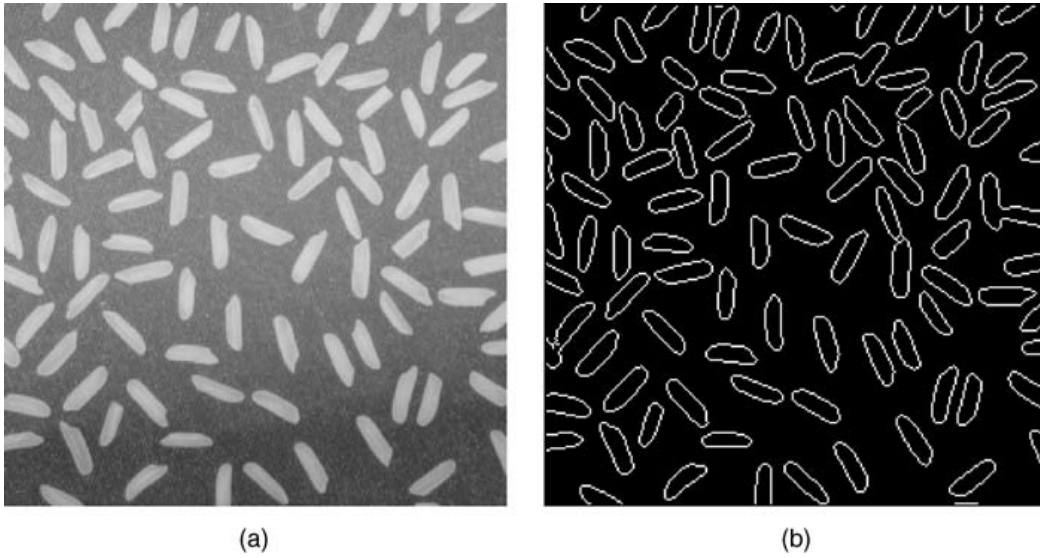
**Figure 2.30** Image sharpening: (a) original image; (b) after sharpening (Marques, 2011)



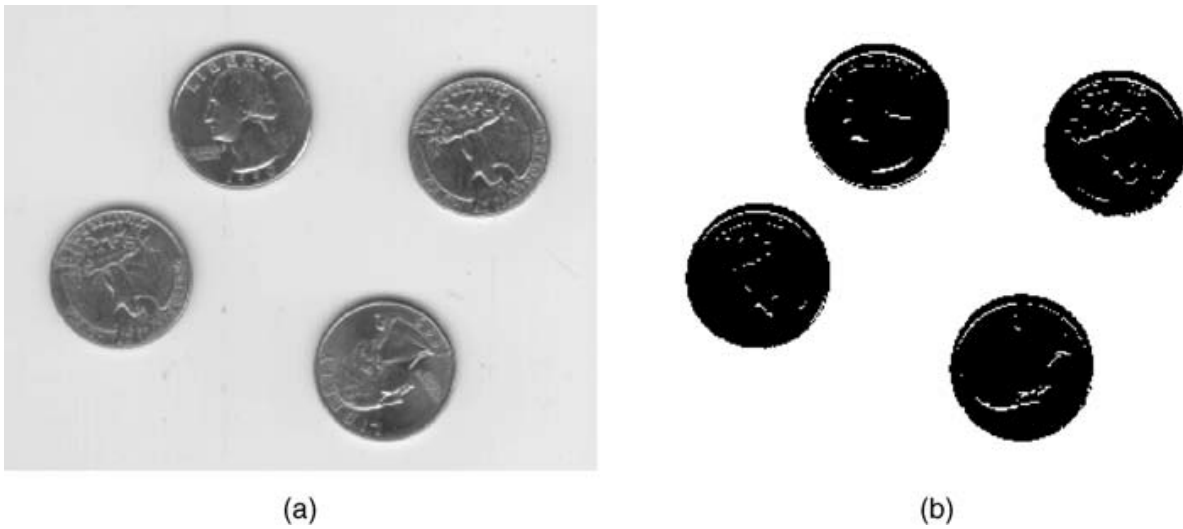
**Figure 2.31** Noise removal: (a) original (noisy) image; (b) after removing noise (Marques, 2011)



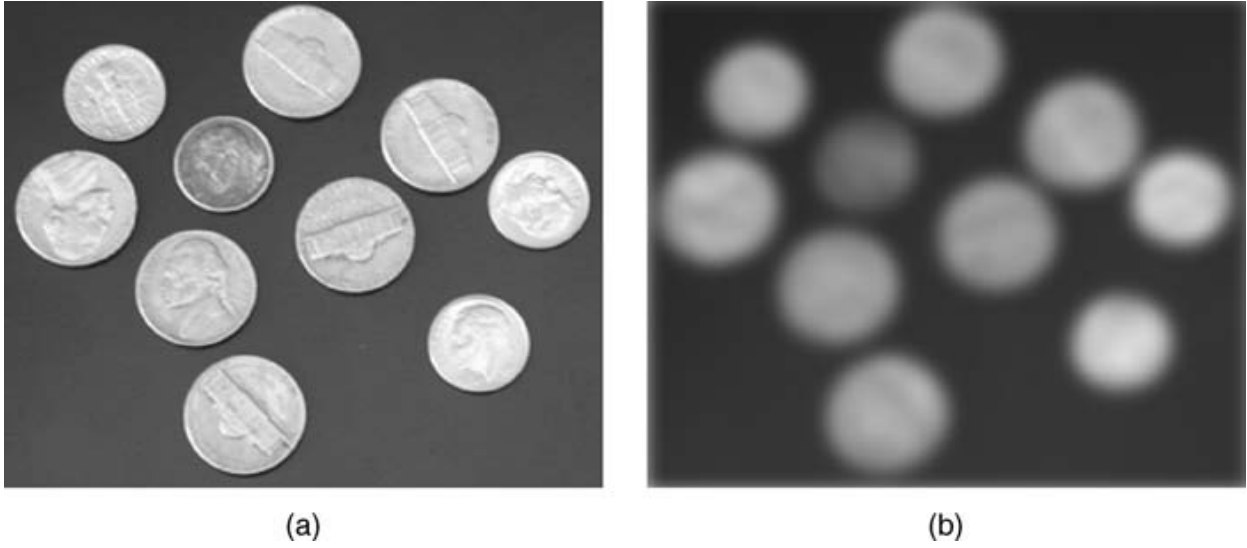
**Figure 2.32** Deblurring: (a) original blurry image (b) after removing motion (blur) (Marques, 2011)



**Figure 2.33** Edge extraction: (a) original image; (b) after extracting its most relevant edges (Marques, 2011)



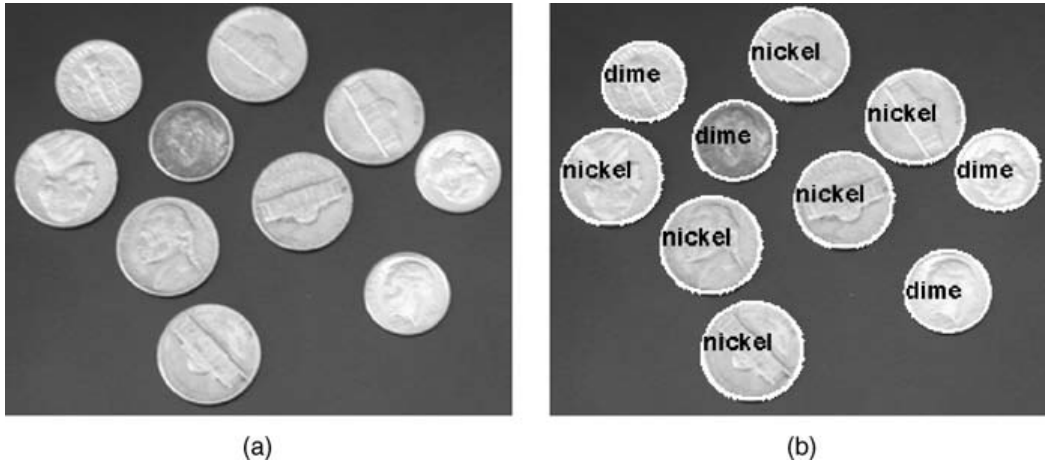
**Figure 2.34** Binarization (a) original grayscale image (b) conversion to a black and white binary image (Marques, 2011)



**Figure 2.35** Blurring (a) original image (b) blurred image after removing unnecessary details (Marques, 2011)



**Figure 2.36** Contrast enhancement (a) original image (b) contrast enhancement after histogram equalization (Marques, 2011)



**Figure 2.37** Object segmentation and labeling (a) original image (b) image with individual objects labeled and segmented (Marques, 2011)

#### **2.14 Digital Image Processing using MATLAB**

For digital image processing, commercial software is commonly used which typically consists of modules that perform specialized tasks. The process of development of image processing solutions is iterative in nature (Marques, 2011). There are many commercial tools available for image processing operations such as *MATLAB*, *OpenCV*, *Octave*, and *Halcon*. While each tool is powerful enough for performing basic to advanced image processing operations, MATLAB has been used in this research because of its a) ease of use and b) popularity of its use with scientists, engineers, and especially researchers both in industry and academia.

MATLAB is a high-performance multi-platform, data analysis, prototyping, and visualization tool with built-in support for matrices and matrix operations, rich graphics capabilities, and a friendly programming language, and development environment. It is easy to use when it comes to editing and interacting with the main functions and their parameters, which leads to valuable time savings in the software development cycle (Marques, 2011). A digital image in MATLAB is represented



as a two-dimensional matrix of real numbers as a function  $f(x,y)$ , where  $x$  and  $y$  are spatial (plane) coordinates, and the function  $f$  at any pair of coordinates  $(x, y)$  represents the *intensity or gray level* of the image at that point. If the size of a matrix is  $M \times N$ ; where  $x$  denotes the row number (from 0 to  $M - 1$ ) and  $y$  represents the column number ( from 0 to  $N - 1$ );  $f(x,y)$  is represented as shown in Equation 2.4 (Marques, 2011):

$$f(x, y) = \begin{bmatrix} f(0,0) & f(0,1) & \dots & f(0, N - 1) \\ f(1,0) & f(1,1) & \dots & f(1, N - 1) \\ \cdot & \cdot & \ddots & \cdot \\ \cdot & \cdot & \cdot & \cdot \\ f(M - 1, 0) & f(M - 1, 1) & \dots & f(M - 1, N - 1) \end{bmatrix} \quad (2.4)$$

MATLAB provides an *Image Processing Toolbox* that consists of a collection of functions that extends the basic capability of the MATLAB environment. The toolbox provides a comprehensive set of reference-standard algorithms, functions, and apps for image processing, visualization, and algorithm development. It can perform image analysis, image segmentation, image enhancement, noise reduction, geometric transformations, and image registration and support multicore processors, GPUs, and C-Code generation. Some of the key features of this toolbox are as given in (The MathWorks, 2014):

- *“Image analysis, including segmentation, morphology, statistics, and measurement*
- *Image enhancement, filtering, and deburring*
- *Geometric transformations and intensity-based image registration methods*
- *Image transforms, including FFT, DCT, Radon, and fan-beam projection*
- *Large image workflows, including block processing, tiling, and multiresolution display*
- *Visualization apps, including Image Viewer and Video Viewer*
- *Multicore- and GPU-enabled functions, and C-code generation support”*

The MATLAB functions in the toolbox are written as M-files, whose source can be inspected and edited using the MATLAB editor. These predefined functions can be powerfully used for image processing GPR profiles and extended to identify corrosion zones in concrete which will be explained in the next sections.

### 2.15 Computer Vision

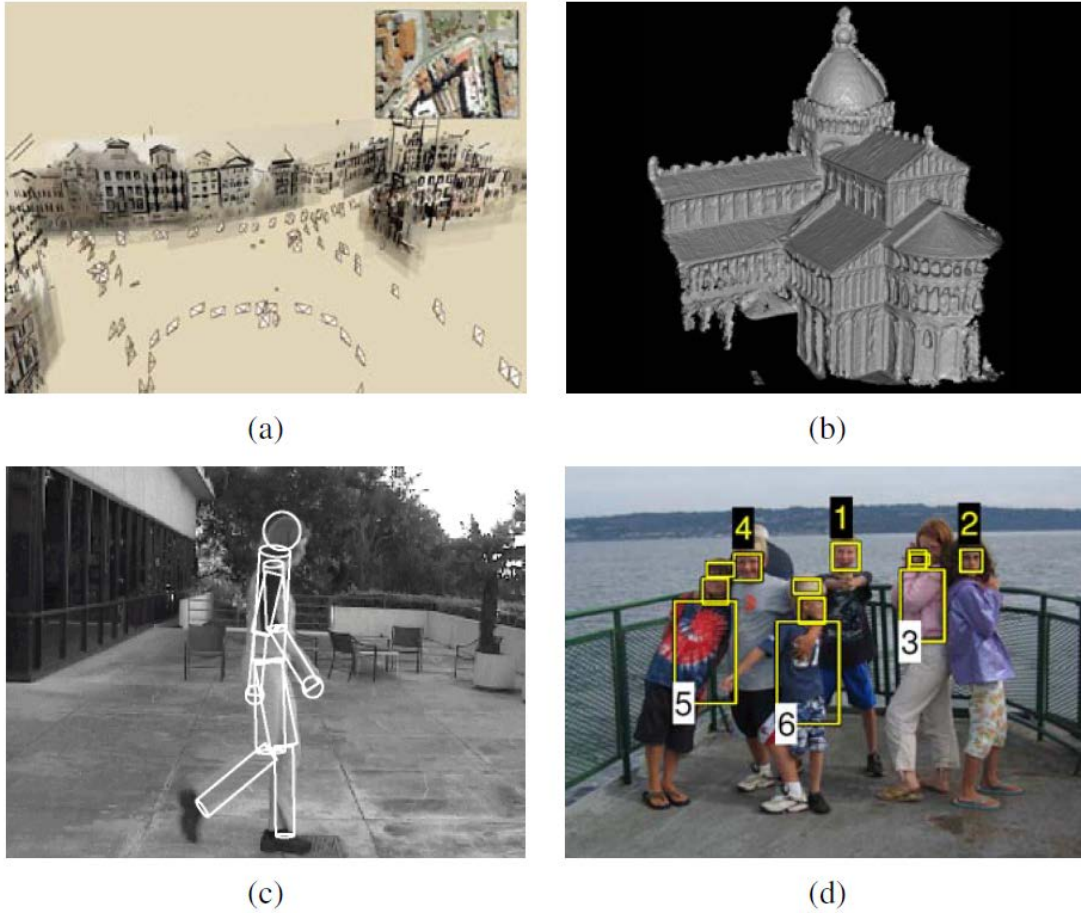
Computer vision is an extension and advanced level of image processing and refers to applying techniques related to emulating the human vision of objects and scenery, for example, the shape and translucency of each petal in Figure 2.38. The human visual system easily recognizes the subtle variations in translucency and shading in this photograph while computer vision aims to achieve it through *complex mathematical models to recognize the three-dimensional shape and appearance of objects in an image.*



**Figure 2.38** Petals of a flower are easily distinguished by human vision from the background

(Szeliski, 2010)

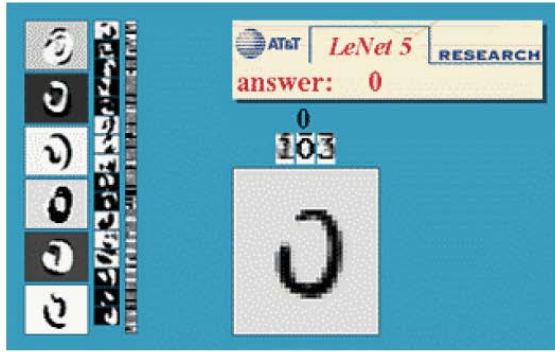
Some applications of computer vision are shown in Figure 2.39. A partial 3D model of an environment from thousands of partially overlapping photographs is shown in Figure 2.39 (a). An accurate dense 3D surface model using stereo matching is achieved in a large set of views of a particular object or façade in Figure 2.39 (b). A person's movement is tracked in Figure 2.39 (c) while the people are recognized by their face, clothing, and/or hair detection and recognition and labeled with their name in Figure 2.39 (d). However, detecting features or decrypting vision as close to humans using computer programming is not as simple as it is performed by humans. The computer vision models, therefore, adopt physics-based and probabilistic models to disambiguate between potential solutions (Szeliski, 2010).



**Figure 2.39** Some examples of computer vision algorithms and applications (Szeliski, 2010)

Computer vision has wide applications in real-world and has been summarized by (Szeliski, 2010) as follows:

- **Optical character recognition (OCR):** recognizing postal codes which are handwritten on mail (Figure 2.40a) and automatic number plate recognition (ANPR).
- **Machine inspection:** measure tolerances on aircraft wings or auto body parts employing stereo vision with specialized illumination for rapid parts inspection as part of quality assurance (Figure 2.40b) or use X-ray vision to find defects in steel castings.
- **Retail:** object recognition for automated checkout lanes (Figure 2.40c).



(a)



(b)



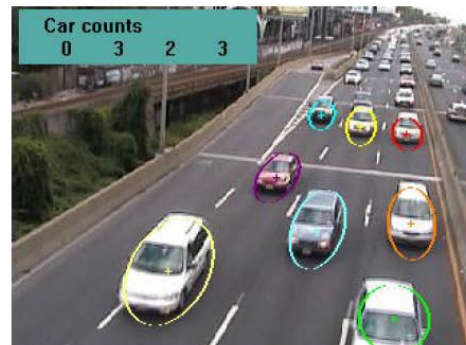
(c)



(d)



(e)



(f)

**Figure 2.40** Some industrial applications of computer vision (Szeliski, 2010)

- **3D model building (photogrammetry):** Utilizing aerial photographs to create 3D models which are fully automated and typically used in web mapping platforms like Bing Maps.
- **Medical imaging:** logging both intraoperative and preoperative images (Figure 2.40d) or conducting long-term research on aging people's brain morphology.

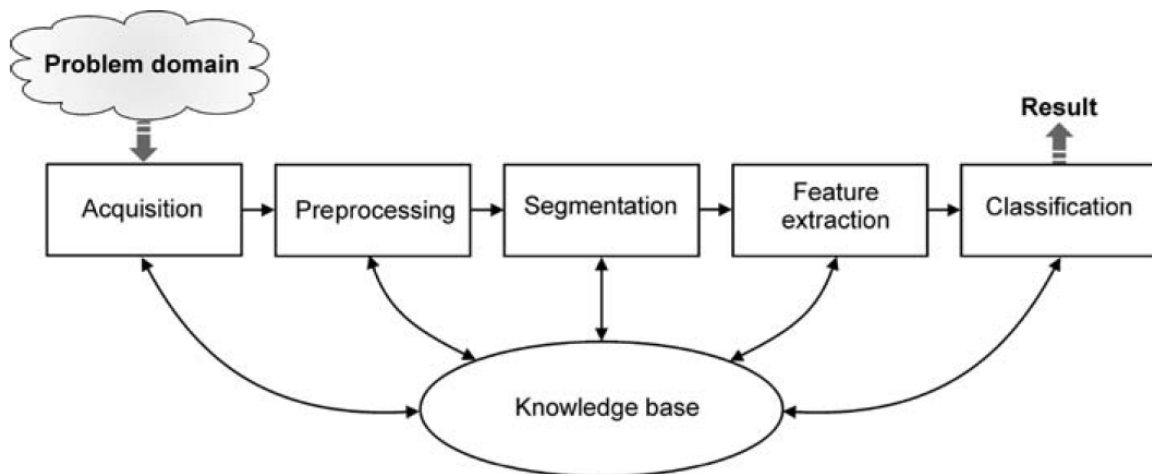
- **Automotive safety:** recognizing unforeseen obstructions, such as pedestrians on the road, in situations where active vision techniques like radar or lidar are ineffective (Figure 2.40e)
- **Match move:** combine computer-generated imagery (CGI) with live-action footage by tracking feature points to determine the 3D camera movements and environment shape (Figure 2.40f)

The main components of a computer vision system are explained using a practical example of recognizing license plates at a highway toll booth as shown in Figure 2.41 (Marques, 2011):

- **Problem Domain:** It represents the objective and in this example case, it is the automatic recognition of license plates. The exact alphanumeric contents of license plates of oncoming vehicles at a toll booth are to be identified in an automated and unsupervised way while considering the weather, speed of the vehicle, and acceptable success rate.
- **Acquisition:** It refers to acquiring one or more images of the license plate of a vehicle using a front or rear view of the vehicle, for example, using a CCD camera and controlling the lighting conditions to ensure that the image is suitable for further processing while considering various factors such as speed, choice of lens and others.
- **Preprocessing:** This step refers to applying techniques such as contrast improvement, brightness correction, and noise removal to improve the quality of the acquired image.
- **Segmentation:** It refers to partitioning an image into its main components: relevant foreground objects and background. The outputs are labeled regions of objects of interest and in this case, could be license plates segmented from the image, or characters segmented within a license plate.

- **Feature Extraction:** It refers to developing algorithms to encode the segmented image constituents in a concise and descriptive based on a measure of color, texture, shape, or most relevant features.
- **Classification:** The final stage after extracting and encoding objects of interest is pattern classification using techniques such as minimum distance classifiers, probabilistic classifiers, neural networks, and others. The ultimate objective, in this example, would be to produce a unique string as output containing the license plate contents.

All these modules are connected to a large block called the knowledge base which is meant for interconnecting them to successfully achieve the solution of recognizing license plates.



**Figure 2.41** Components of a computer vision system (Marques, 2011)

MATLAB provides a specialized tool for computer vision whose function can be utilized for edge detection, object detection, motion tracking, and others. Feature extracting through detection and recognition can be very useful in GPR data processing to identify hyperbolas contained within it and other anomalies. It can be further used for classifying such detected regions corresponding to

the corrosion levels in concrete. Thus, the application of image processing combined with computer vision could be a powerful tool for achieving the required objectives of this research.

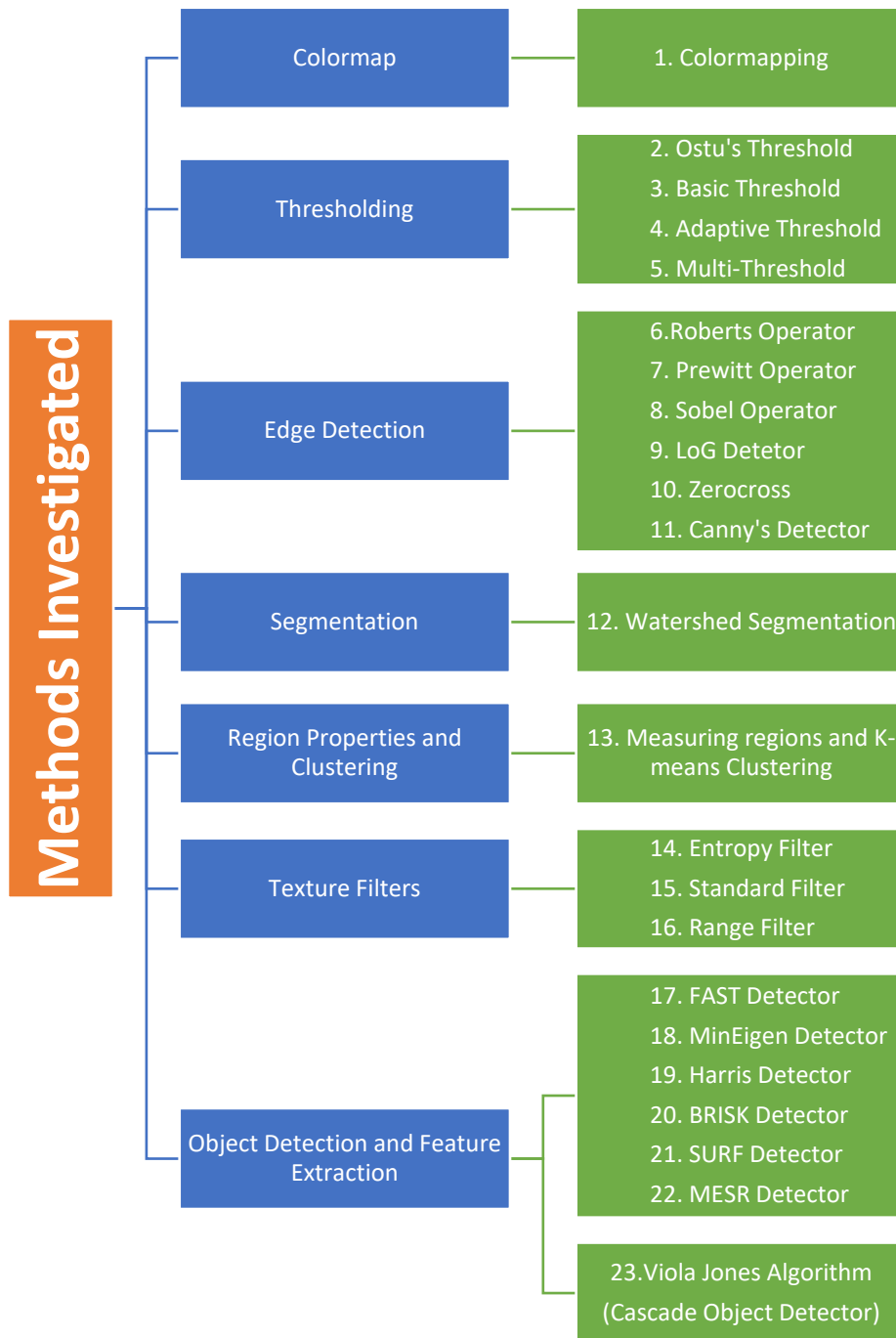
## **2.16 Methods Explored on GPR Data**

Based on the image processing & computer vision techniques delineated in the previous sections, the flowchart in Figure 2.42 shows all the methods investigated on sample GPR profiles. It has been classified into seven categories as shown. Each method has its own advantages and limitations. The objective of exploring multiple methods is to analyze the effects of various image processing techniques on GPR radar data and consequently, develop a robust methodology and model(s) by utilizing a combination of investigated approaches among others. Each of the seven categories is outlined along with a brief explanation of each method and their application on GPR profile(s).

### **2.16.1 Colormap**

A *colormap* is a sort of color filter in the form of a matrix that can be applied over GPR profiles to show variations of intensity in the image. It has a predefined command in MATLAB with the ability to define custom colormaps along with the standard colormaps feature available. The colormap matrix has only three columns but any number of rows. Each row represents a color in this matrix; the first element specifies the intensity of red, the second green, and the third blue. The function '*colormap (map)*' sets the colormap of a given indexed or grayscale image to the colormap specified by the *map*. The *map* is a built-in or custom colormap, specified as one of the built-in colormap functions or a three-column matrix of RGB triplets (The MathWorks, 2014).





**Figure 2.42** Methods investigated in this study with GPR profiles

Some of the built-in colormaps in MATLAB are shown in Table 2.8. A custom colormap can be defined as a three-column matrix of values in the range [0-1] where each row is an RGB triplet

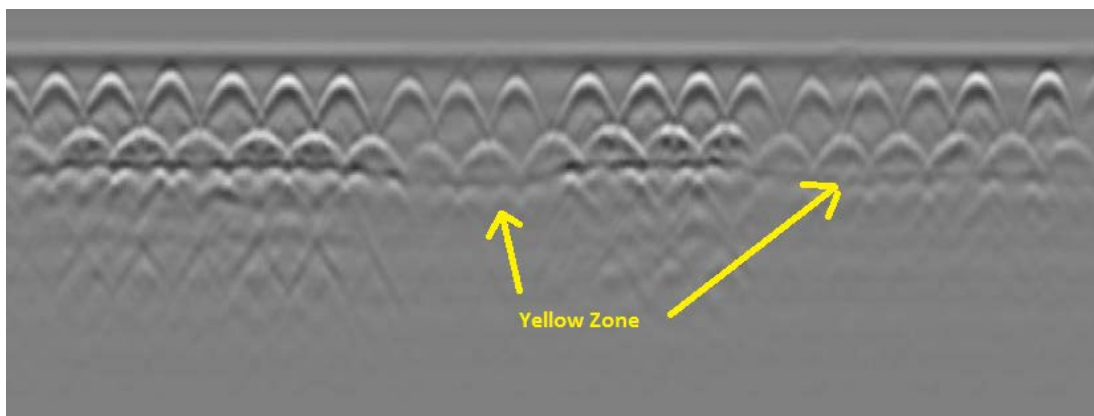
that defines one color of the colormap. A specific number of rows from the built-in colormap can also be used; for example, `colormap (summer (10))` uses 10 colors from the *summer* colormap. If the number of colors is not specified, the colormap contains all the colors within the built-in colormap. The colormap function is applied on a real-case bridge sample profile as shown in Figure 2.43. It was tested with various *maps* as shown in Table 2.8. The ‘*hsv*’ and ‘*jet*’ maps yielded satisfactory results which showed good distinction of the hyperbolas. The result of generating the *hsv map* is shown in Figure 2.44.

Hyperbolas which have greater intensity and representative of sound concrete have a more pronounced deep pink hue close to their vertex. Hyperbolas representative of moderately corroded concrete or bad concrete will not have such deep pink zones within due to lower intensity values. This distinction of color can be used to classify various zones of concrete. However, it has various limitations as discussed:

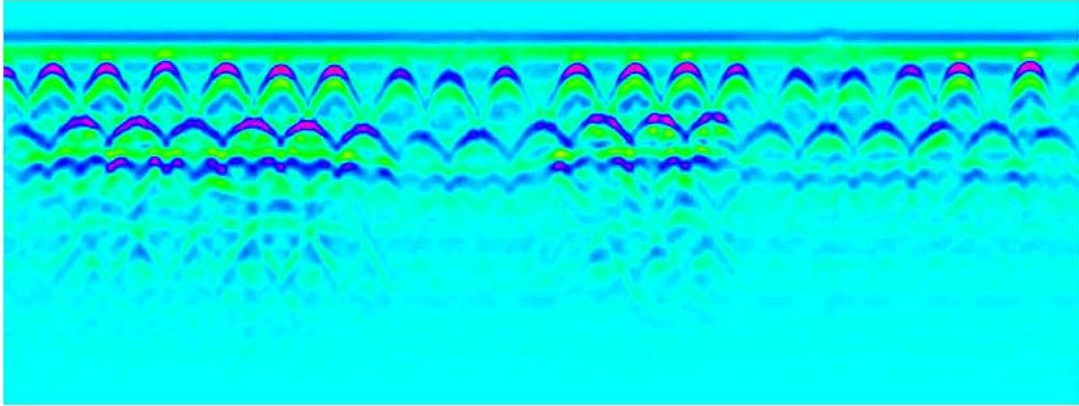
- a) It is difficult to extract absolute meaningful data from it because it is classified based on intensity alone and doesn’t distinguish hyperbolas.
- b) It was applied to various other GPR profiles, and it showed poor results with varying contrasts or profiles which have minor variances in intensities between sound and bad concrete and may give unreasonable results.
- c) It is hugely affected by noise and other anomalies and as such, anomalies that are not representative of good concrete may be considered as sound concrete by this analysis.
- d) Pre-processing is required for this method to successfully apply but it would have still several limitations as discussed earlier.

**Table 2.8** Built-in Colormaps in MATLAB (Marques, 2011)

Name	Description
hsv	Hue-saturation-value color map
hot	Black-red-yellow-white color map
gray	Linear gray-scale color map
bone	Gray scale with a tinge of blue color map
copper	Linear copper-tone color map
pink	Pastel shades of pink color map
white	All-white color map
flag	Alternating red, white, blue, and black color map
lines	Color map with the line colors
color cube	Enhanced color-cube color map
vga	Windows color map for 16 colors
jet	Variant of HSV
prism	Prism color map
cool	Shades of cyan and magenta color map
autumn	Shades of red and yellow color map
spring	Shades of magenta and yellow color map
winter	Shades of blue and green color
summer	Shades of green and yellow color map



**Figure 2.43** Sample GPR Profile - Yellow zones potentially indicate areas of moderate corrosion  
(Mohammed Abdul Rahman et al., 2016)



**Figure 2.44** Colormap (*hsv*) applied over the profile

### **2.16.2 Thresholding**

Thresholding refers to converting a greyscale image (a GPR Profile) which has intensity values ranging from 0 to 255 to a binary image which would have intensity values of 0 (black) and 1 (white) (Marques, 2011). Such a representation simplifies the data embedded in an image and helps in the easy identification and processing of variations contained within it. The thresholding of an image could distinguish the hyperbolas contained within the GPR image and its intensity levels and areas could be a good indicator of corrosion. The thresholding can be done manually but it has a big limitation of having different thresholds for each image and thus, negates the objective of automated image processing of GPR profiles. Therefore, thresholding is done with typically done with methods that automatically identify a threshold value, and the following four popular methods are described and implemented on GPR profiles: a) Otsu's Threshold; b) Basic Threshold; c) Adaptive Threshold and d) multi-Thresholding. MATLAB functions '*im2bw*' or '*imbinarize*' are used for converting a grayscale image to a binary image. In the output image, all pixels in the input image with luminance greater than a certain *level* are replaced with the value 1 (white), and all other pixels are replaced with the value 0 (black). The default *level* value is 0.5 if it is unspecified and can be used to convert any greyscale image to a binary image.

### *Image Thresholding by Otsu's Method*

Direct conversion of a grayscale image to a binary image using the above image type conversion function with a default value (0.5) yields transformed images that may not distinguish the hyperbolas in a GPR profile. However, the application of Global Image thresholding could produce images with distinct parabolas representing the top or bottom reinforcement embedded in an image. It is based on the concept that a grayscale image, based on its intensity or pixel values, can be differentiated into two zones, black and white, by introducing a single threshold value between 0 and 1 for the entire image. This value is calculated based on Otsu's method which automatically clusters the image into two zones while minimizing the intra-class variance using a predefined 'graythresh' function in MATLAB (MathWorks, 2017). To understand thresholding using this method, the histogram of a monochrome image needs to be defined. It is a graphical representation of the frequency of occurrence of each gray level in the image. The histogram data structure of an image stores the frequency values in a 1D array of numerical values,  $h$ , whose individual elements store the number (or percentage) of image pixels that correspond to each possible gray level (Marques, 2011). If the components of an image histogram can be denoted by Equation 2.5 (Gonzalez et al., 2010).

$$p_q = \frac{n_q}{n}; \quad q = 0, 1, 2, \dots, L - 1 \quad (2.5)$$

Where  $n$  is the total number of pixels in the image,  $n_q$  is the number of pixels that have intensity level  $q$ , and  $L$  is the total number of possible intensity levels in the image (intensity levels are always integer values). A threshold  $k$  is chosen such that  $C_1$  is the set of pixels with levels  $[0, 1, 2, \dots, k]$  and  $C_2$  is the set of pixels with levels  $[k+1, \dots, L-1]$ . The threshold value  $k$  is chosen such that it maximizes the between-class variance  $\sigma_B(k)$  defined as shown in Equation 2.6.

$$\sigma_B^2(k) = P_1(k)[m_1(k) - m_G]^2 + P_2(k)[m_2(k) - m_G]^2 \quad (2.6)$$

Where  $P_1(k)$  is the probability of  $C_1$  occurring and  $P_2(k)$  is given as in Equation 2.7 and 2.8.

$$P_1(k) = \sum_{i=0}^k p_i \quad (2.7)$$

$$P_2(k) = \sum_{i=k+1}^{L-1} p_i = 1 - P_1(k) \quad (2.8)$$

The terms  $m_1(k)$  and  $m_2(k)$  are the mean intensities of the pixels in sets  $C_1$  and  $C_2$  respectively.

The term  $m_G$  is the global mean (the mean intensity of the entire image) as shown in Equation 2.9.

$$m_G = \sum_{i=0}^{L-1} ip_i \quad (2.9)$$

The mean intensity up to level  $k$  is given by Equation 2.10.

$$m(k) = \sum_{i=0}^k ip_i \quad (2.10)$$

The equation of between-class can then be written as:

$$\sigma_B^2(k) = \frac{[m_G P_1(k) - m(k)]^2}{P_1(k)[1 - P_1(k)]} \quad (2.11)$$

The ratio of the between-class variance to the image intensity variance is given as:

$$\eta(k) = \frac{\sigma_B^2(k)}{\sigma_G^2} \quad (2.12)$$

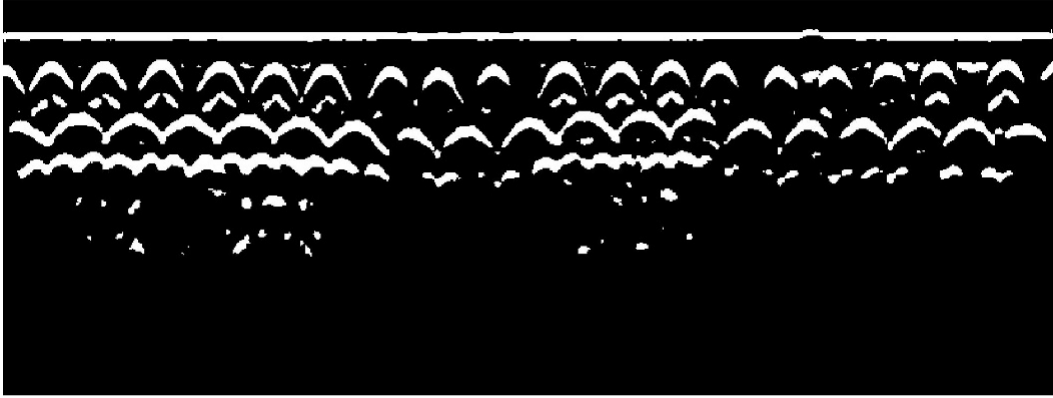
The *optimal threshold*,  $k^*$ , maximizes  $\eta$ , or equivalently maximizes  $\sigma_B^2$ , and is written as:

$$\sigma_B^2(k) = \max_{1 \leq k \leq L} \sigma_B^2(k); \quad 0 \leq \eta(k^*) \leq 1 \quad (2.13)$$

The concept of segmenting images based on maximizing the between-class variance is that the larger the variance is, the more likely it is that the threshold will *segment* the image properly. This

threshold is applied to a sample profile (Figure 2.43) to segment hyperbolic regions within the GPR Profile. Figure 2.45 shows the result of applying Otsu's threshold and the following inferences can be made visually: a) the hyperbolas areas are distinctly visible as white zones along with the thick asphalt layer in white; b) there is limited noise present in the image i.e., presence of many small regions along with insignificant hyperbolic areas; and c) Hyperbolas in strong concrete zones have larger areas than areas in the corroded (yellow) zone. The detected hyperbolic regions can be used to identify deterioration zones based on their shape and area. For further validation, it was applied to various GPR profiles of different bridges having differing image intensities, and the following were the major limitations found in using this method:

- a) The automatic threshold value generated is not suitable for all profiles as it yields profiles with either large noise or missing hyperbolas.
- b) Thresholding segmentation doesn't detect hyperbolas explicitly. It converts the greyscale image into a binary image and thus, further processing would be required to identify hyperbolas. However, in case of large noise or missing hyperbolas, it could lead to many false or missing detections.
- c) Thresholding could be a workable solution if all GPR profiles are similar in characteristics such as shape and intensity of hyperbolas. However, due to large variance in real case bridges GPR profiles, this method cannot be successfully applied for automation.
- d) The effect of change in illumination and reflectance will lead to differing results when this method is applied (Marques, 2011).



**Figure 2.45** Otsu's Threshold on GPR Profile Sample

### *Basic Global Thresholding*

A single global threshold value can also be obtained for an image by utilizing an iterative procedure until one produces a good result. This method is used to distinguish two peak areas in the histogram of an image, and it could be used on GPR profiles to distinguish hyperbolic areas similar to Otsu's method. The iterative procedure is as follows (Gonzalez et al., 2010):

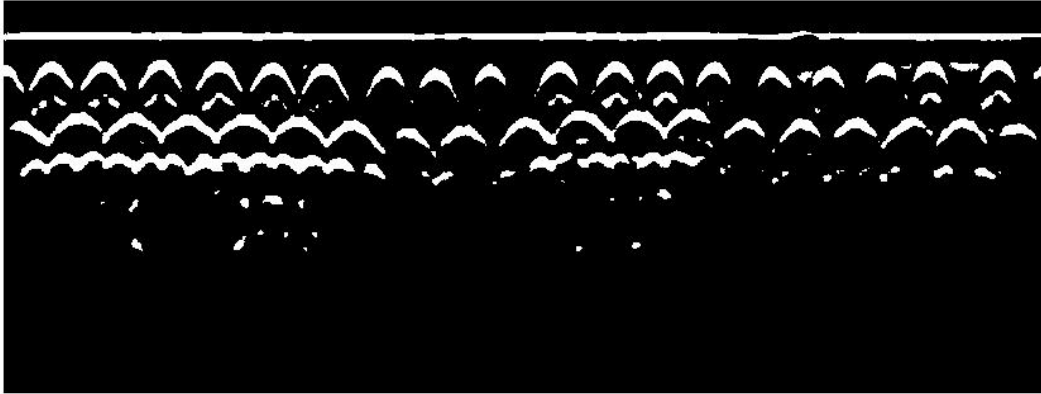
1. *“Select an initial estimate for the global threshold,  $T$ .*
2. *Segment the image using  $T$ . This will produce two groups of pixels:  $G_1$ , consisting of all pixels with intensity values greater than  $T$ , and  $G_2$ , consisting of pixels with values less than or equal to  $T$ .*
3. *Compute the average intensity values  $m_1$  and  $m_2$  for the pixels in regions  $G_1$  and  $G_2$ , respectively.*
4. *Compute a new threshold value:  $T = \frac{1}{2} (m_1 + m_2)$*
5. *Repeat steps 2 through 4 until the difference in  $T$  in successive iterations is smaller than a predefined value,  $\Delta T$ .*
6. *Segment the image using the function  $im2bw$ :*  
 *$BW = im2bw (I; T/den)$  where  $den$  is an integer (e.g., 255 for an 8-bit image) that scales the maximum value of ratio  $T/den$  to 1, as required by function  $im2bw$ . ‘ $I$ ’ is the original grayscale image while  $BW$  is the binary image after thresholding”.*



A global threshold is obtained by implementing the above algorithm logic on the sample GPR Profile (Figure 2.43). The threshold value 'T' obtained was '0.563' which is closer to Otsu's threshold, which was found to be '0.549'. Hence, the resultant image as shown in Figure 2.46 is close to Otsu's method and this method also suffers from similar limitations as described for Otsu's method.

### *Adaptive Thresholding*

Adaptive (or Local) Thresholding computes a locally adaptive threshold that uses block processing to threshold blocks of pixels, one at a time. The resultant matrix, T, applied over an image, I, is the same size as 'I' containing normalized intensity values in the range [0, 1]. It chooses the threshold based on the local mean intensity (first-order statistics) in the neighborhood of each pixel. The resultant matrix, T, is representative of the background information contained in an image. It is converted to an 8-bit unsigned integer values (uint8) image and subtracted from the original image to obtain an image that would contain areas of the image with higher intensities (Marques, 2011). If the GPR sample profile (Figure 2.43) undergoes adaptive thresholding, the resultant image after applying the process is shown in Figure 2.47. It contains less noise compared to other thresholding methods and hence, could be considered superior to other methods. However, this method suffers from similar major limitations as other thresholding methods, however, the results could be used as a preprocessing parameter in the identification of hyperbolic regions of an image.



**Figure 2.46** Basic Global Thresholding of Image

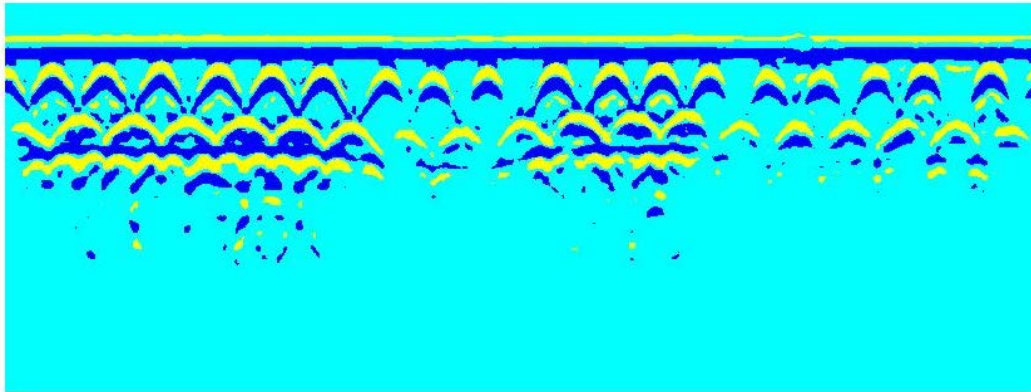


**Figure 2.47** Adaptive Thresholding of the sample GPR Profile

#### *Multi-thresholding by Otsu's Method*

Otsu's global thresholding method can be extended to find multiple thresholds in an image as explained in (Otsu, 1979). This can be used if there are multiple peak values in the image. In the case of segmenting the given sample GPR Profile (Figure 2.43) with two threshold values, three levels or areas are distinguished in RGB color zones as shown in Figure 2.48. The yellow areas correspond to the positive amplitude values and the blue zones correspond to negative amplitude values along with the noise present in the image. Higher thresholds can also be implemented but

it will have more noise levels. This method is good in separating positive and negative amplitudes of hyperbola but suffers from similar limitations of thresholding as discussed for Otsu's method.



**Figure 2.48** Multi-thresholding of the sample GPR Profile

### ***2.16.3 Edge Detection***

Edge detection refers to finding areas in an image where the intensity changes rapidly and it highlights an image contrast. It is insensitive to change in the overall illumination level and in detecting contrast, which is rapid change in intensity levels, it emphasizes the boundaries of features within an image. It is similar to how a human vision perceives the perimeter of an object since the object boundaries have rapidly changing intensity from its surroundings (Gonzalez et al., 2010). Therefore, it can be applied to evaluate if it would filter out the boundaries of hyperbolas within GPR profiles which usually have high varying contrast within the image. The most common classification of edge detectors is first-order and second-order edge detectors. The first-order edge detectors are equivalent to first-order differentiation while the second-order detectors are equivalent to second-order differentiation. Edge detection occurs along a path of rapid change in intensity based on following one of these two criteria: a) places where the first derivative of intensity is greater in magnitude than some threshold and ii) places where the second derivative of the intensity has a

zero crossing. The following are the six common edge detectors explained by (Marques, 2011) and applied over GPR profiles in this research and classified based on their order:

- a) First-Order Edge Detectors: Roberts, Prewitt, Sobel, and Canny
- b) Second-Order Edge Detectors: Laplacian of Gaussian (LoG), Zero-crossing

The gray-level gradient ( $g$ ) at a pixel, which can be approximated by the digital equivalent of the first-order derivative can be written for a pair of coordinates  $(x, y)$  with function value  $f(x, y)$  as shown in Equation 2.14 (Marques, 2011).

$$\begin{aligned}
 g_x(x, y) &\approx f(x + 1, y) - f(x - 1, y) \\
 g_y(x, y) &\approx f(x, y + 1) - f(x, y - 1)
 \end{aligned}
 \tag{2.14}$$

#### *Roberts Edge Detector*

Consider the 3 x 3 neighbor region of a pixel as shown in Figure 2.49a. The Roberts cross-gradient operator is one of the earlier attempts to use 2-D masks (Figure 2.49b) to digitally approximate the first derivatives as differences between adjacent pixels. It is based on implementing the following diagonal difference in the neighborhood as shown in Equation 2.15 (Gonzalez et al., 2010).

$$\begin{aligned}
 g_x &= \frac{\partial f}{\partial x} = (z_9 - z_5) \\
 g_y &= \frac{\partial f}{\partial y} = (z_8 - z_6)
 \end{aligned}
 \tag{2.15}$$

#### *Prewitt Edge Detector*

Masks of size 2 x 2 are not as useful for computing edge direction as masks that are symmetric about the center point, the smallest of which is of size 3 x 3. Such masks consider the nature of the data on opposite sides of the center point and thus carry more information regarding its edge. The simplest pair of kernels, known as the Prewitt edge detector (Figure 2.49c) is given by Equation 2.16 (Gonzalez et al., 2010).

$$\begin{aligned}
g_x &= \frac{\partial f}{\partial x} = (z_7 + z_8 + z_9) - (z_1 + z_2 + z_3) \\
g_y &= \frac{\partial f}{\partial y} = (z_3 + z_6 + z_9) - (z_1 + z_4 + z_7)
\end{aligned} \tag{2.16}$$

### *Sobel Edge Detector*

A slight variation to the Prewitt operators wherein the center pixel in each row or column is weighted by 2 to provide image smoothing gives the Sobel edge operator (Figure 2.49d) and is given by Equation 2.17 (Gonzalez et al., 2010).

$$\begin{aligned}
g_x &= \frac{\partial f}{\partial x} = (z_7 + 2z_8 + z_9) - (z_1 + 2z_2 + z_3) \\
g_y &= \frac{\partial f}{\partial y} = (z_3 + 2z_6 + z_9) - (z_1 + 2z_4 + z_7)
\end{aligned} \tag{2.17}$$

### *Laplacian of Gaussian (LoG) Detector*

The LoG detector first smoothens the image with a Gaussian low-pass filter and then applies a Laplacian edge detector to the result. The resulting transfer function (which resembles a Mexican hat) is shown in Figure 2.50a. The Gaussian function is given as in Equation 2.18 (Gonzalez et al., 2010).

$$G(x, y) = e^{-\frac{x^2+y^2}{2\sigma^2}} \tag{2.18}$$

Applying the Gaussian filter blurs an image as it's a smoothing filter. The degree of blurring is dependent on the standard deviation,  $\sigma$ . The Laplacian of the function is shown in Equation 2.19.

$$\nabla^2 G(x, y) = \frac{\partial^2 G(x, y)}{\partial x^2} + \frac{\partial^2 G(x, y)}{\partial y^2} = \left[ \frac{x^2+y^2-2\sigma^2}{\sigma^4} \right] e^{-\frac{x^2+y^2}{2\sigma^2}} \tag{2.19}$$

Z1	Z2	Z3
Z4	Z5	Z6
Z7	Z8	Z9

-1	0
0	1

0	-1
1	0

Roberts

-1	-1	-1
0	0	0
1	1	1

-1	0	1
-1	0	1
-1	0	1

Prewitt

-1	2	-1
0	0	0
1	2	1

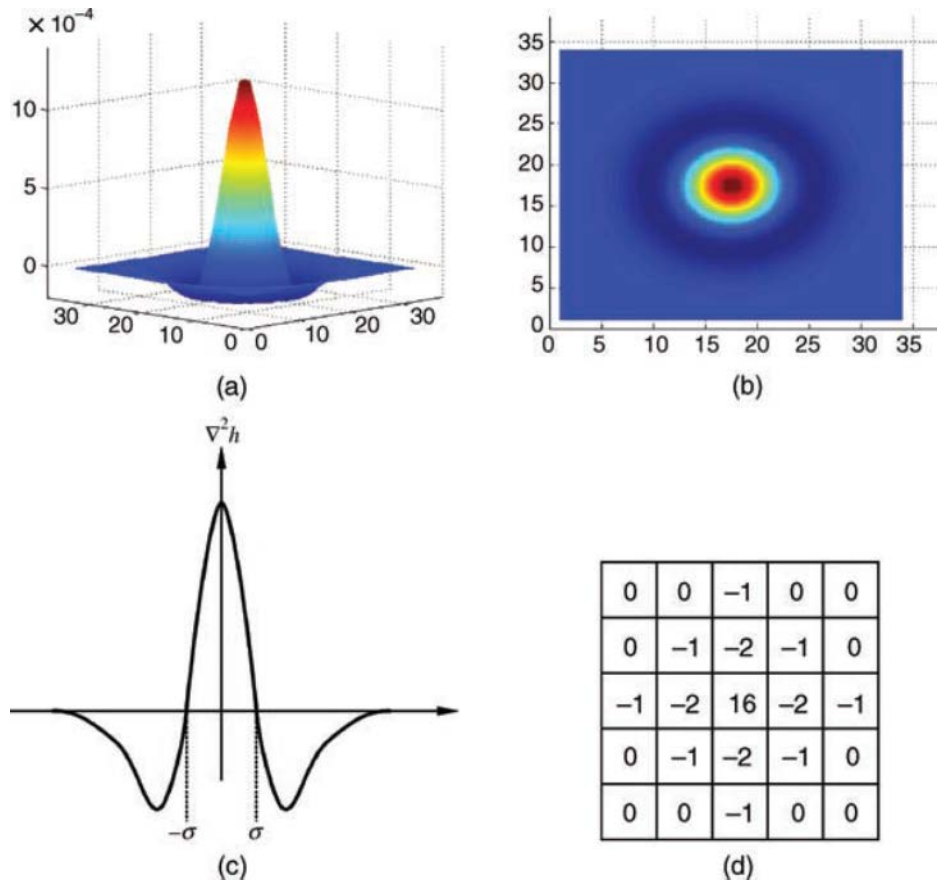
-1	0	1
-2	0	2
-1	0	1

Sobel

**Figure 2.49** Neighborhood of a pixel (a) and masks for Roberts (b), Prewitt (c) and Sobel, and (d) Edge Operators (top to bottom) (Gonzalez et al., 2010)

*Zero-Crossings Detector*

It is similar to the LoG detector, except that the convolution is carried out using a user-specified numeric matrix filter (The MathWorks, 2014).



**Figure 2.50** Laplacian of Gaussian (a) 3D Plot; (b) 2D intensity plot; (c) cross-section of (a); and (d) a 5x5 mask approximation to the shape in (a) from (Marques, 2011)

### *Canny Edge Detector*

The canny method is the most popular, powerful, and effective tool for edge detection as it has two different thresholds to identify strong and weak edges resulting in a very less noisy image.

The algorithm of this method is summarized by (Marques, 2011) as follows:

1. *“The input image is smoothed using a Gaussian low-pass filter, with a specified value of  $\sigma$ : large values of  $\sigma$  will suppress much of the noise at the expense of weakening potentially relevant edges.*
2. *The local gradient (intensity and direction) is computed for each point in the smoothed image.*

3. *The edge points at the output of step 2 result in wide ridges. The algorithm thins those ridges, leaving only the pixels at the top of each ridge, in a process known as nonmaximal suppression.*
4. *The ridge pixels are then thresholded using two thresholds  $T_{low}$  and  $T_{high}$ : ridge pixels with values greater than  $T_{high}$  are considered strong edge pixels; ridge pixels with values between  $T_{low}$  and  $T_{high}$  are said to be weak pixels. This process is known as hysteresis thresholding.*
5. *The algorithm performs edge linking, aggregating weak pixels that are 8-connected to the strong pixels”.*

#### *Application of Edge detectors in MATLAB*

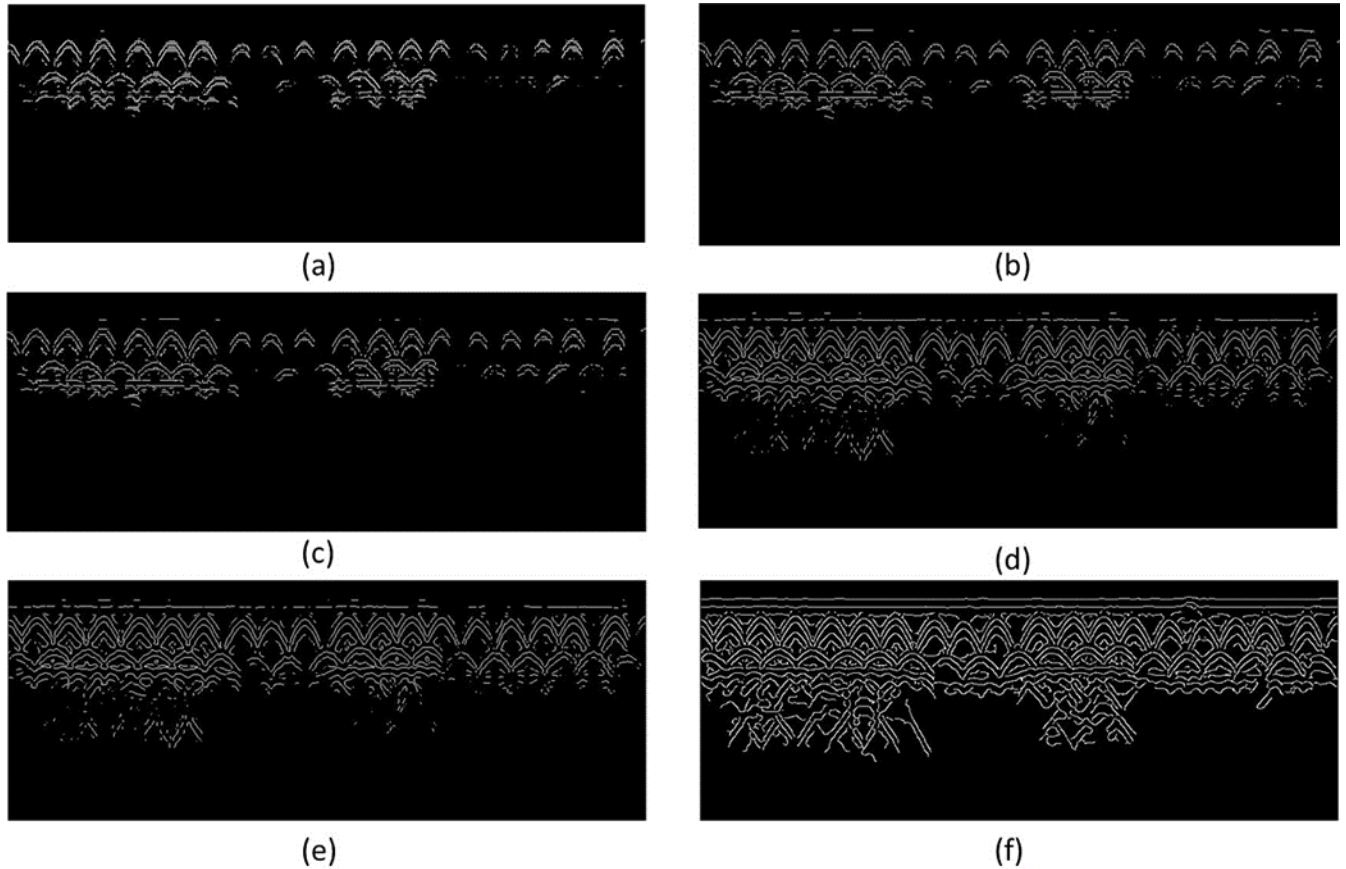
In MATLAB, the generic function used to detect edges (which converts it to a binary image) from a grayscale image is shown in Equation 2.20.

$$BW = \text{edge}(I, \text{'method'}, \text{'threshold'}) \quad (2.20)$$

The ‘method’ could be any of the methods described above and the convention to write each of the six methods is as follows: ‘roberts’, ‘prewitt’, ‘sobel’, ‘Log’, ‘zerocross’, and ‘Canny’. If the ‘threshold’ is specified, it chooses all edges above the specified point; else, the program chooses the threshold automatically. For Zerocross, the function is slightly different with a user-specified matrix, ‘h’ for convolution, and is written in MATLAB as in Equation 2.21.

$$BW = \text{edge}(I, \text{'zerocross'}, \text{'threshold'}, \text{'h'}) \quad (2.21)$$





**Figure 2.51** Application of edge detectors on sample GPR profile (a) Roberts; (b) Prewitt; (c) Sobel; (d) LoG; (e) Zerocross and (f) Canny

The sample GPR profile (Figure 2.43) is chosen to undergo all six edge detectors and the result is shown in Figure 2.51. If no threshold is specified, the result of the Prewitt and Sobel detector is similar, which means that image smoothing doesn't have much effect on the given GPR profile. Also, the results of 'LoG', 'Canny', and 'zerocross' are similar because the threshold value is not specified. The first three methods (Roberts, Prewitt, and Sobel) distinguish the hyperbola with their edges clearly while the last three methods (Canny, LoG, and Zerocross) have a lot of noise in them. When it was tested with other GPR profiles, the results were varying because of differing

intensities and automatic selection of the threshold. Following are the limitations of using edge detection techniques as described earlier:

- a) Variable inconsistent noises are present in the analysis of different GPR profiles and hence, meaningful data extraction is difficult.
- b) The threshold value is automatically chosen and hence, is not always optimal for differing GPR data sets.
- c) It detects the edges of hyperbolas, but the boundaries of hyperbolas are not stored in a data structure. However, further processing could lead to segmenting of individual hyperbolas.

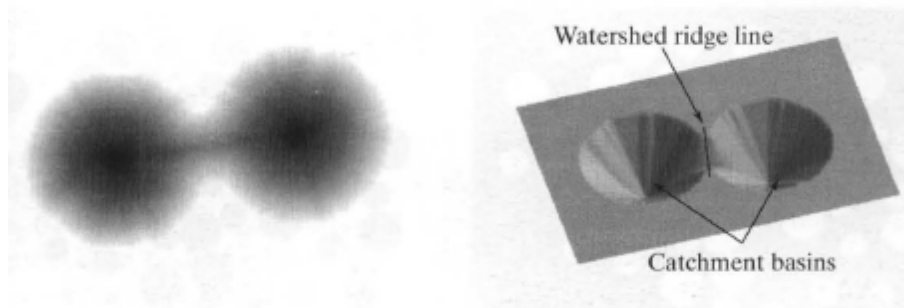
#### **2.16.4 Segmentation**

*Segmentation* refers to the process of portioning an image into nonoverlapping regions such that the regions correspond to desired meaningful objects. Essentially, thresholding an image and edge detecting implicitly segment an image too. However, explicit segmentation techniques partition an image explicitly into clear and concise regions or zones (Marques, 2011). Although there are many approaches for image segmentation, a popular technique called *watershed segmentation* has been investigated to understand the benefits of this approach for further exploration.

##### *Watershed Segmentation*

The term *watershed* is derived from geography, and it refers to a ridge that divides areas drained by different river systems. The geographical area that drains into a river or reservoir is called a *catchment basin*. The watershed segmentation is based on morphological image transformation that represents regions in a segmented image equivalent to catchment basins and the boundaries analogous to the ridge lines. The grayscale image is considered a topological surface, where the function values  $f(x,y)$  is interpreted as heights. For example, consider Figure 2.52(a) represents the grayscale image and it can be represented as a three-dimensional surface as shown in Figure 2.52

(b). If rain falls on this surface, water will collect in the areas labeled as *catchment basins* on the image and the water falling on the *ridge line* would equally divide into both catchment basins. Such ridge lines and catchment basins are found using this method and the image is segmented (Gonzalez et al., 2010).



**Figure 2.52** (a) Grey-scale image (left); and (b) Image viewed as a topological surface with ridge lines and catchment basins (Gonzalez et al., 2010)

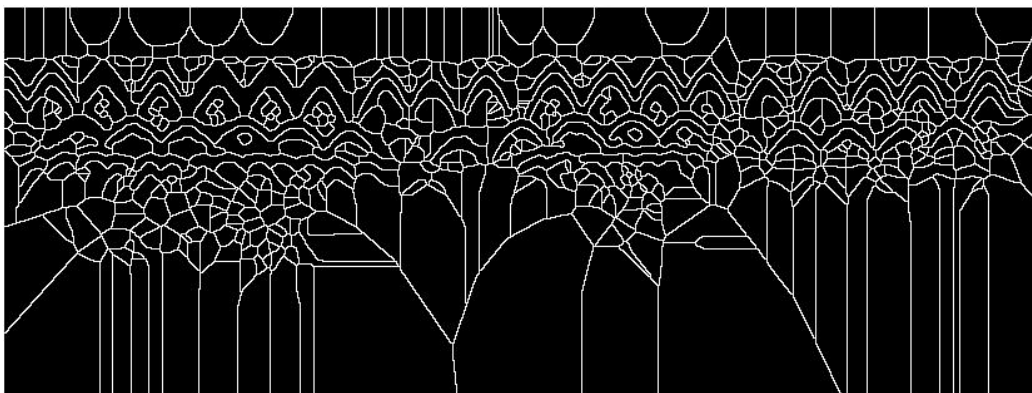
Applying a normal watershed segmentation approach could lead to the over-segmentation of an image. An approach called *Marker-Controlled Watershed Segmentation* is adopted to eliminate this problem. A marker is a connected component belonging to an image. An *internal* marker is a connected component inside each of the objects of interest, while an *external* marker is contained in the background. These markers are used to control the gradient image based on various methods chosen based on the original image such as linear filtering, non-linear filtering, and morphological processing to develop a segmented image. The following is the basic procedure for marker-controlled watershed segmentation (The MathWorks, 2014):

1. A segmentation function is evaluated wherein the dark regions in the image are to be segmented as *objects*.
2. Foreground markers are computed as connected blobs of pixels inside each object.

3. Identify background markers which are pixels that do not belong to any object.
4. Adjust the segmentation function so that the foreground and background marker positions are the only places where minima exist.
5. The modified segmentation function's watershed transforms should be evaluated.

The sample GPR profile (Figure 2.43) was applied with a marked controlled watershed segmentation method to visualize if it can identify and distinguish hyperbolic regions. The result is shown in Figure 2.53. The lines in the image show the ridgelines of the watershed and it separates zones of differing intensities in the image. Although the segmentation shows the edges of hyperbolic edges clearly, this method has the following limitations:

- a) It has too many ridgelines which is representative of noise.
- b) GPR profiles with slightly varying intensities produce lesser ridgelines.
- c) Although some of the ridgelines do represent hyperbolas, there is no clear distinction or detection based on a hyperbolic profile. The image could be employed with other processing approaches to distinguish hyperbolas.



**Figure 2.53** Watershed Segmentation of the Sample GPR Profile

### ***2.16.5 Region Properties and Clustering***

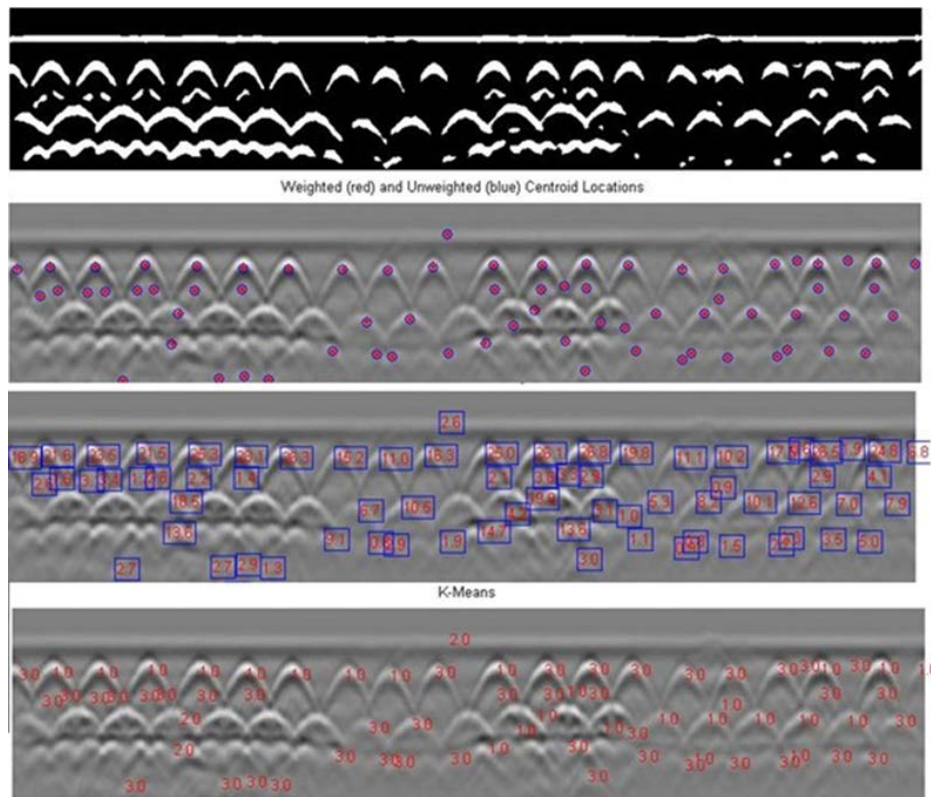
This approach is an extension of the segmentation method and essentially involves the following three steps: a) Segment the image by any of the techniques such as thresholding, edge detection, or watershed segmentation; b) measuring properties of segmented regions in the image such as centroid, the standard deviation of the regions; and c) cluster those segmented using K-Means clustering techniques based on measured property values.

#### *Measuring region properties and K-Means Clustering*

Based on the three-step philosophy, the sample GPR profile in Figure 2.43 has been processed. Firstly, Otsu's threshold image was adopted as the segmented image as it distinguished hyperbolas and had lesser noise for the given profile. To reduce noise and eliminate smaller regions, the detected regions were filled using the '*imfill*' MATLAB function to have closed loops of detected regions. Subsequently, the properties of these closed regions such as areas, centroid, orientation, perimeter, minimum and maximum values of intensities, weighted centroid, standard deviations, and others were extracted using the '*regionprops*' function in MATLAB. Finally, these regions were classified based on any of the region properties into three clusters using k-means. K-means clustering refers to the partitioning of a data set, of say 'n' observation into a certain 'k' number of mutually exclusive clusters (Jain, 2010) and would be explained in detail in Section 3.1.3. Figure 2.54 shows the GPR profile after each processing step (top to bottom): a) after filling gaps on Otsu's thresholded image; b) measuring weighted and unweighted centroid; c) Standard deviation values (chosen region property for classification) displayed at centroid locations; and d) K-means Clustered zones are marked from 1 to 3 where the lower value indicates regions with higher weighted centroid value. The following are the limitations of this method based on the obtained results:

- a) The regions detected are dependent on the method of transforming it into a binary image and would contain similar limitations as the method chosen. For example, if Otsu's method was chosen to binarize images, this method would also have its limitations.
- b) The weighted centroid locations do not correspond only to hyperbolic regions or peaks. There are many false and missing detections.
- c) The standard deviation values cannot be corroborated to define corrosion in the hyperbolic region due to poor correlation.
- d) Finally, the k-means clustering does not provide any meaningful clusters which could help distinguish deteriorated zones.

*Nevertheless, this three-step philosophy which includes identifying hyperbolic regions, measuring a meaningful property of detected regions, and clustering those regions with better image processing techniques can be used powerfully for GPR data analysis and has been adopted as part of research methodology.*



**Figure 2.54** Identifying region properties and K-means clustering of a GPR profile

### 2.16.6 Texture Filters

Texture analysis is defined by (The MathWorks, 2014) as follows: “*Texture analysis refers to the characterization of regions in an image by their texture content. Texture analysis attempts to quantify intuitive qualities described by terms such as rough, smooth, silky, or bumpy as a function of the spatial variation in pixel intensities. In this sense, the roughness or bumpiness refers to variations in the intensity values or gray levels. Texture analysis is used in a variety of applications, including remote sensing, automated inspection, and medical image processing. Texture analysis can be used to find the texture boundaries, called texture segmentation. Texture analysis can be helpful when objects in an image are more characterized by their texture than by intensity, and traditional thresholding techniques cannot be used effectively.*”

Texture refers to the “feel” of the image like for a fabric and is qualitatively as the smoothness or coarseness of the image itself (Manjunath & Ma, 1996). This could be a powerful tool for image analysis if intensity-based classification has various limitations as in the case of GPR profiles. The attempt to quantify this qualitative feel is what constitutes texture analysis. The texture of an image can be characterized by standard statistical measures because they provide information about the variability of the intensity values of pixels in an image (Tamura et al., 1978). For example, the range of values in the neighborhood around a pixel for a smooth textured area will have a small value when compared to a rough textured area. Similarly, the standard deviation could be a measure of the degree of variability of pixel values in that region and correlates with the texture of the image. While texture has been classified in the literature into various categories, texture analysis on GPR profiles has been limited to the following three functions in this section (Table 2.9) provided by MATLAB for initial examination:

**Table 2.9** MATLAB functions - Texture filters (The MathWorks, 2014)

<b>Function</b>	<b>Description</b>
<i>entropyfilt</i>	Calculates the local entropy of a grayscale image. Entropy is a statistical measure of randomness.
<i>stdfilt</i>	Calculates the local standard deviation of an image.
<i>rangefilt</i>	Calculates the local range of an image.

The texture filter is applied to a neighborhood around the pixel of interest by calculating the statistics for that neighborhood, and this statistical value is used as the pixel of interest in the output image. To demonstrate with an example, if the *rangefilt* function is applied on the matrix A shown below:

A = [ 1 2 3 4 5; 6 7 8 9 10; 11 12 13 14 15; 16 17 18 19 20 ]



A is written in MATLAB output as Equation 2.22.

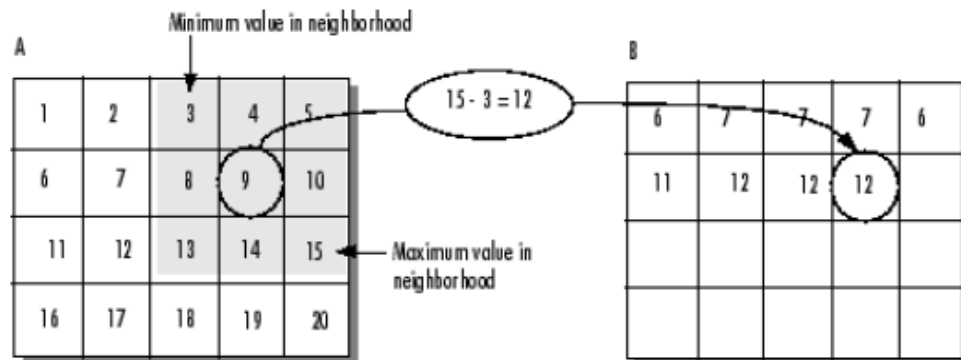
$$A = \begin{bmatrix} 1 & 2 & 3 & 4 & 5 \\ 6 & 7 & 8 & 9 & 10 \\ 11 & 12 & 13 & 14 & 15 \\ 16 & 17 & 18 & 19 & 20 \end{bmatrix} \quad (2.22)$$

Then, the output matrix utilizing the function (Equation 2.23) is given as in Equation 2.24.

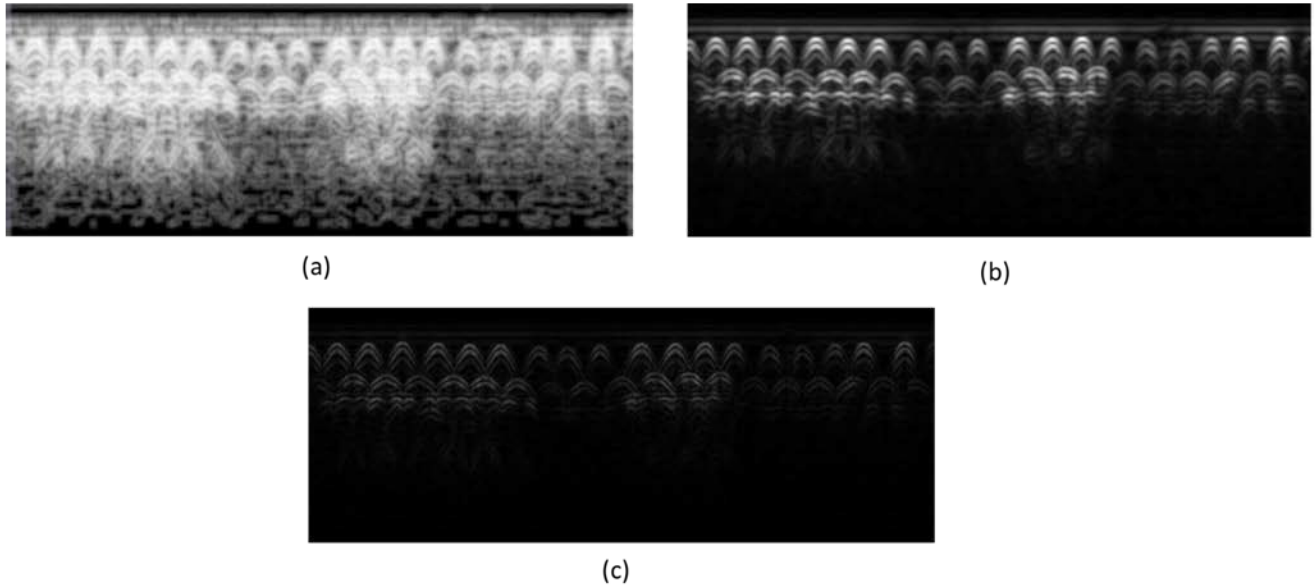
$$B = \text{rangefilt}(A); \quad (2.23)$$

$$B = \begin{bmatrix} 6 & 7 & 7 & 7 & 6 \\ 11 & 12 & 12 & 12 & 11 \\ 11 & 12 & 12 & 12 & 11 \\ 6 & 7 & 7 & 7 & 6 \end{bmatrix} \quad (2.24)$$

Figure 2.55 shows how the value of element B (2, 4) was calculated from A (2,4). The default neighborhood for functions is 3x3; however, users can specify neighborhoods of different shapes and sizes.



**Figure 2.55** Determining Pixel Values in Range Filtered Output Image (The MathWorks, 2014)



**Figure 2.56** Texture Filters (a) entropy filter; (b) standard filter and (c) range filter

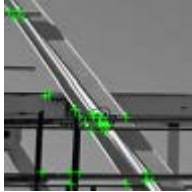

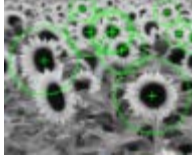

The three filters were applied to the sample GPR profile (Figure 2.43), and the results obtained are shown in Figure 2.56. The entropy filters have lots of noise while the standard and range filters distinguished hyperbolas with reduced noise. The resultant output gives the “feel” or “roughness” of the image and can be a good indicator of the deterioration of concrete based on the “roughness” of the texture. In the absence of any irregularities, it can be concluded that *a higher roughness in the texture measurement indicates a better concrete condition, with less signal loss*. Although these methods are superior to methods based on intensity classification for GPR profiles, it suffers from two major limitations: a) Noise and b) Hyperbolas are not distinguished. However, *employing hyperbolic detections along with texture filters* could be a better approach for generating deterioration maps as adopted in the *research methodology of the developed models which is discussed in the next chapter*.

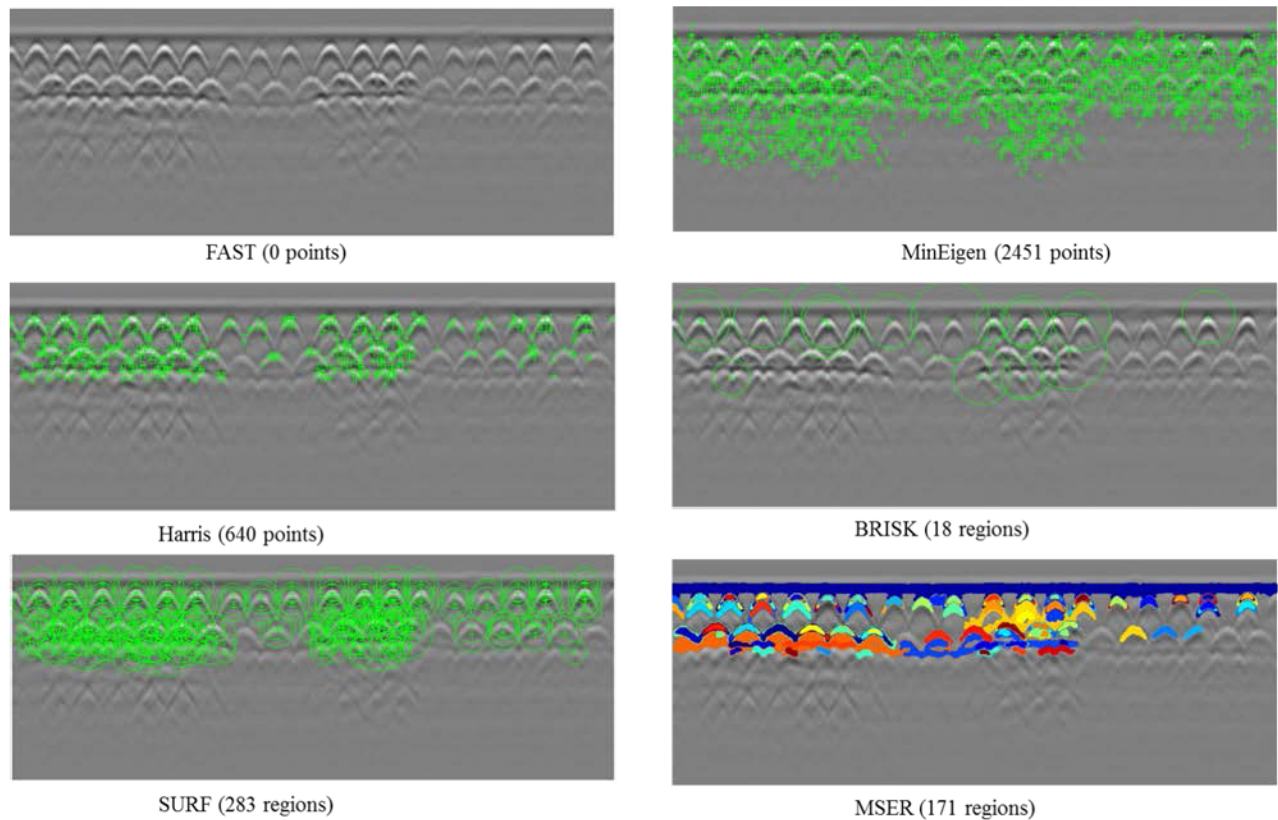
### ***2.16.7 Object Detection and Feature Extraction:***

All the previous methods focused on processing the GPR profile were based on finding thresholds, edges, image segmentation, and/or applying texture filters. One of the key components or objects of interest which directly relates to the corrosion in concrete is analyzing reflected signals at the rebar level which have a hyperbolic shape in a GPR profile. The shape, intensity, and texture of the hyperbola are critical factors in deducing the corrosion level present at the rebar layer based on the GPR-IBA. Therefore, this section delineates efforts explored in detecting hyperbolic regions to later analyze them for determining the corrosiveness level. *In a GPR profile, the object of interest is either “hyperbolas” or it could be other anomalies*, and feature extraction refers to the process of detecting certain features of interest within an image related to an object of interest for further processing. It is part of computer vision and image processing solutions and can be effectively used for detecting objects based on feature extraction and matching (Shapiro & Stockman, 2001). Initially, readymade algorithms which detect local features based on distinct patterns or structures found in an image (such as corners, blobs, and edge pixels) are applied to GPR profiles to evaluate if such algorithms can differentiate hyperbola from its immediate surroundings based on its texture, shape, or intensity. If the functions corresponding to local feature detection do not distinguish the hyperbolas, a customized algorithm could be developed for hyperbola detection.

Table 2.10 shows the methods investigated with a brief overview showing classification based on local features.

**Table 2.10** Local Feature Detectors - MATLAB functions (The MathWorks, 2014)

Points Object	Returned By	Type of Feature
cornerPoints	<p><b>detectFASTFeatures</b> Features from the accelerated segment test (FAST) algorithm Uses an approximate metric to determine corners.</p>	 <p>Corners Single-scale detection Point tracking, image registration with little or no scale change, and corner detection in scenes of human origin, such as streets and indoor scenes.</p>
	<p><b>detectMinEigenFeatures</b> Minimum eigenvalue algorithm Uses minimum eigenvalue metric to determine corner locations.</p>	
	<p><b>detectHARRISFeatures</b> Harris-Stephen's algorithm More efficient than the minimum eigenvalue algorithm</p>	
BRISKPoints	<p><b>detectBRISKFeatures</b> Binary Robust Invariant Scalable Keypoints (BRISK) algorithm</p>	 <p>Corners Multiscale detection Point tracking, image registration, handling changes in scale and rotation, corner detection in scenes of human origins, such as streets and indoor scenes</p>
SURFPoints	<p><b>detectSURFFeatures</b> Speeded-up robust features (SURF) algorithm</p>	 <p>Blobs Multiscale detection Object detection and image registration with scale and rotation changes</p>
MSERRegions	<p><b>detectMSERFeatures</b> Maximally stable extremal regions (MSER) algorithm</p>	 <p>Regions of uniform intensity Multi-scale detection Registration, wide baseline stereo calibration, text detection, and object detection. Handles changes to scale and rotation. More robust to affine transforms in contrast to other detectors.</p>



**Figure 2.57** Detections of points and regions (local features) using multiple algorithms

These methods were applied to the sample GPR Profile (Figure 2.43) to assess if any of the methods can automatically detect the hyperbolic regions or their points with little or no noise. The resulting images after these algorithm applications are shown in Figure 2.57. The FAST algorithm (Rosten & Drummond, 2006) doesn't detect any points while *MinEigen* features (Shi & Tomasi, 1994) yield too many points to make sense. The *Harris* features algorithm (Harris & Stephens, 1988) showed promising results as the points were located mostly in hyperbolic regions. Moreover, higher *Harris* points were detected in hyperbolic regions of higher intensity and vice versa. The number of *BRISK* regions (Leutenegger et al., 2011) was limited and do not always correspond to hyperbolic regions. The regions based on *the SURF* algorithm (Bay et al., 2008) had lots of

outliers that were not representative of hyperbolic zones. The *MSER* algorithm (Matas et al., 2002) yielded 171 detections and most of them corresponded to the hyperbolic regions. However, it has some false and missing detections along with some connected hyperbolas. Conclusively, detections based on such feature-extracting algorithms could be utilized in combination with others and further investigated for detecting and classifying hyperbolic regions.

While the algorithms employed earlier could detect hyperbolic features, more robust and wholesome methods found in the literature (Table 2.7) for detecting hyperbolic regions are based on applying multiple steps with advanced ML and deep-learning algorithms such as CNN and CSVM. A popular ML method based on the *Viola-Jones algorithm* (Viola & Jones, 2004) was chosen as part of this *research methodology* to create a custom classifier for detecting hyperbolas in GPR profiles. A brief background of this algorithm, its reasons for its adoption, and its complete application for holistic hyperbola detections have been described in the next chapter.

### 3 RESEARCH METHODOLOGY

Based on the methods identified in the literature review (Section 2.8.2) and the research investigation (Section 2.16), this research has developed three models in a progressive approach, with each subsequent model surpassing its predecessor in terms of performance and effectiveness. In this chapter, the complete methodology of these models has been discussed, following a phased approach that improves sequentially. Each phase builds upon the previous one, resulting in an enhanced methodology for the development and implementation of these models. This chapter encompasses the complete modus operandi and flowchart of the models. However, the application of these models on real case bridge decks or slabs has been reserved for the next chapter, where the practical implementation and results on actual structures will be presented. The first model termed the “X-Sim” Method (M Abdul Rahman & Zayed, 2016), attempts to generate a condition map without detecting hyperbolic regions while utilizing a standard filter and K-means clustering approach. The drawbacks of this method are subsequently discussed, the apparent one being not detecting hyperbolas leading to inaccurate zoning of corrosion zones. The second model employed the *three-step philosophy* outlined in Section 2.16.5, which involved the following processes: a) Pre-processing of profiles, followed by hyperbola detections utilizing the Viola-Jones Algorithm and statistical analysis, b) Evaluation of detected objects using a texture-based factor, specifically entropy, and c) Utilization of the K-means algorithm to cluster the evaluated factors and establish a deterioration scale for each profile. In most cases, this model generates reasonable condition maps primarily because of the pre-processing steps and statistical analysis. These steps significantly reduce false and missing detections. However, it is important to note that in instances where hyperbolas exhibit complex or heavily distorted shapes, the model may encounter challenges and may not be as accurate in those specific cases. The final model also follows the *three-step*

*philosophy*, with the last two steps similar to the second model. However, for more robust hyperbolic detections, a novel algorithm has been developed in this model. This algorithm incorporates concepts borrowed from pixel-based approaches such as OSCA (Zhou et al., 2018) and (Mertens et al., 2016), as shown in Table 2.6. Additionally, the final model includes a user-interactive approach that takes into account the structure information being inspected and considers anomalies to generate reliable condition maps. The assumptions and limitations of each developed model are outlined in the following chapter.

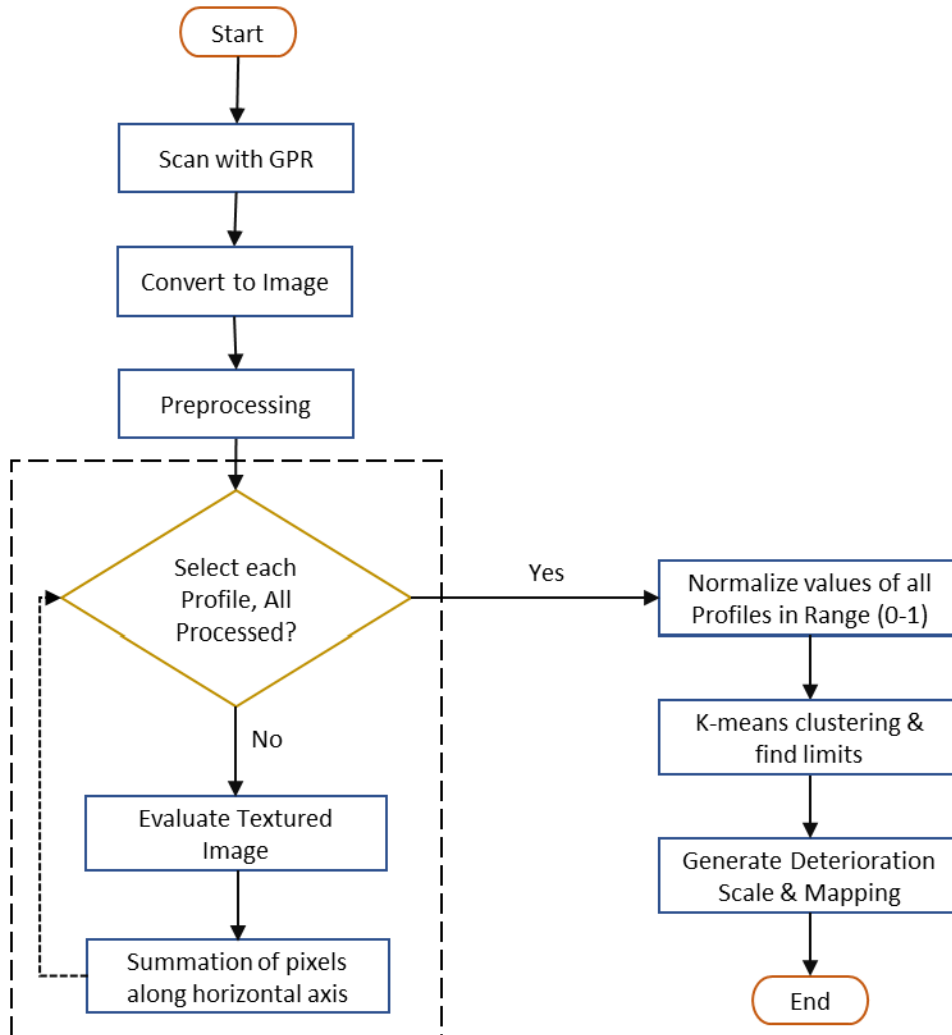
### **3.1 X- Sim Method**

The first model in this thesis aims to develop an approach that generates condition maps without explicitly detecting hyperbolas. The objective is to investigate the reliability of such a strategy. The flowchart for analyzing GPR data based on this model is shown in Figure 3.1, and it has been explained stepwise, outlining the sequential process involved in generating the condition maps using this approach.

#### ***3.1.1 Image Conversion and Preprocessing***

The first step is obtaining GPR profiles of a reinforced structure such as a bridge deck or any reinforced structural element either by scanning it using GPR equipment or utilizing available data as explained in Section 2.8.1. After acquiring these B-scans, they are converted into grey-scale images and imported into the MATLAB environment. In these greyscale images, the intensity values range from 0 to 255 pixels. Lower pixel values correspond to darker shades of grey, while higher pixel values correspond to lighter shades of grey. Additionally, an absolute black color is represented by a pixel value of 0. Conversely, an absolute white color is represented by a pixel value of 255 (M Abdul Rahman & Zayed, 2016).





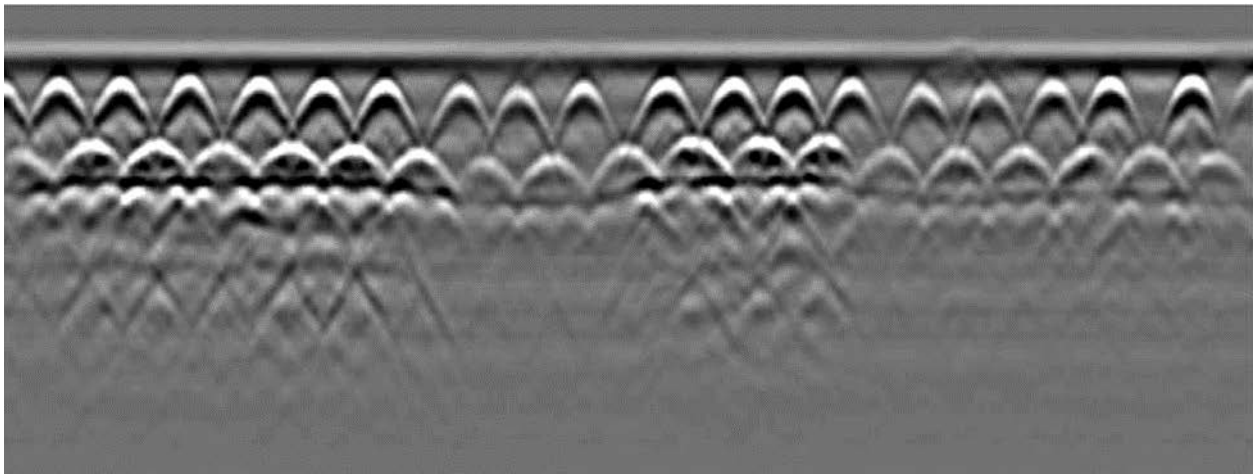
**Figure 3.1** Flowchart for the X-Sim method

Subsequently, the images undergo preprocessing using the following two steps. Firstly, all GPR profiles, which have been scanned with a uniform tracing distance, are cropped on both sides to have an equal number of columns and rows. Typically, since the scan depth is the same, the number of rows in all profiles remains equal. However, the number of columns is adjusted for easier processing of profiles using this method. This step can also be performed in the proprietary GPR software such as RADAN 7 if scanned using GSSI® equipment. Secondly, the intensity values of all profile images are adjusted using the MATLAB function as in Equation 3.1.

$$J = \text{imadjust}(I); \quad (3.1)$$

I – Input GPR profile image; J- Processed GPR image.

This function increases the contrast of a greyscale image by saturating the top and bottom 1% of all pixel values. Essentially, it brightens the lighter pixels and darkens the black pixels of the GPR profile, and eliminates noise in the image to some extent (The MathWorks, 2014). Figure 3.2 shows the result of applying this filter over the sample image shown in Figure 2.43.



**Figure 3.2** Image Preprocessing - Applying a contrast filter.

### **3.1.2 Evaluate standard filter and summation.**

The subsequent step involves applying a texture filter to all preprocessed profile images. The texture filters, as described in Section 2.16.6, take into account the "feel" of an image and provide a more "human-like" qualitative factor rather than relying solely on crisp numeric intensity-based factors. The *standard texture filter*, among the three texture filters, was able to distinguish hyperbolas and reduce sufficient noise in a typical GPR profile as shown in Figure 2.56. The processed image resulting from this approach displays the internal features of a GPR profile, effectively distinguishing hyperbolic regions. It bears a resemblance to X-ray images, revealing subsurface

structures and anomalies. As a result, this approach has been aptly named the X-sim method, signifying its similarity to X-ray imaging in terms of the processed image appearance. In an image, the standard filter determines the neighborhood local standard deviation of each pixel. Using the MATLAB function "*stdfilt*", the local standard deviation of an image is determined with the syntax shown in Equation 3.2 (M Abdul Rahman & Zayed, 2016).

$$g = \text{stdfilt}(f, \text{nhood}) \quad (3.2)$$

where  $f$  is the input image and  $\text{nhood}$  is an array of zeros and ones where the nonzero elements denote the neighbors required to calculate the local standard deviation (Gonzalez et al., 2010). While the default value of  $\text{nhood}$  is  $\text{ones}(3)$ , specified as an odd array always, it is set as  $\text{ones}(9)$  in this model to account for a wider range of nearby pixels for computing standard deviation. If a random variable,  $z$ , represents intensity, then the corresponding histogram is denoted by  $p(z_i)$ , where  $i = 0, 1, 2, 3, \dots, L-1$ ;  $L$  is the number of distinct intensity levels (for example, 256 levels in a grayscale 8-bit image). Then, the  $n$ th moment of  $z$  about the mean can be written as:

$$\mu_n(z) = \sum_{i=0}^{L-1} (z_i - m)^n p(z_i) \quad (3.3)$$

The mean,  $m$ , is the average intensity of the image or region and is evaluated as:

$$m = \sum_{i=0}^{L-1} z_i p(z_i) \quad (3.4)$$

Finally, the standard deviation, a texture descriptor that measure the average contrast, is evaluated as the square root of the second moment in Equation 3.3:

$$\sigma = \sqrt{\mu_2(z)} = \sqrt{\sigma^2} \quad (3.5)$$

Consequently, all profile images are sequentially converted into the 'X-Sim' type images. Finally, a summation scale is calculated for each processed image by summing the pixel values along the horizontal axis (X-axis). This scale for each profile would be a vector linear scale having an equal number of columns equal for all profiles. *In the absence of any anomalies, the high range of values across hyperbolas is indicative of good areas while areas with less distinct or no hyperbolas have a lower range of values.*

### **3.1.3 K-means clustering and condition mapping**

After evaluating the summation scale for all profile images in a GPR scan of a structural element, these values are normalized within the range of 0 to 1. Normalization ensures that the values are standardized and fall within a consistent and comparable range, irrespective of the specific magnitudes of the original summation scale values. Corollary, each profile image would be represented by a single-row scale with an equal number of columns, resembling a one-dimensional frequency signal with peaks and troughs. The values in these scales of all profiles are then classified into zones via data-clustering methods (unsupervised learning). Given that GPR datasets of scanned elements exhibit variable data ranges that correspond to varying conditions of concrete quality, data classification or supervised learning techniques may not be the preferred approach in this context (Mohammed Abdul Rahman, Zayed, et al., 2022). Data classification approaches can be employed based on extensive datasets acquired under similar GPR survey parameters and environmental conditions. For example, a study aimed to improve depth-amplitude effects was conducted by analyzing a large dataset from bridge decks showed a strong correlation between the

variation in rebar reflection amplitudes and the thickness of the concrete cover (Kien Dinh et al., 2016).

However, data clustering approaches are preferred and a widely accepted framework for categorizing such techniques is as follows: (a) hierarchical clustering, in which data is divided into multiple sequences, ranging from one cluster containing all individuals to  $n$  clusters containing each individual; and (b) partitional clustering, in which data are divided into predetermined zones in a single step without any hierarchical structure (Everitt et al., 2001). A partitional clustering approach has been used because the number of zones or clusters is typically *known* when generating condition maps. Since its creation 50 years ago, *K-means* is a commonly applied data-partitioning technique (Jain, 2010). For GPR data interpretation, K-means have been used to cluster amplitude values and generate condition maps by (Kien Dinh et al., 2015) and (Alsharqawi et al., 2020). It has also been used by (Alsharqawi et al., 2018) for rating conditions of bridges, and for corrosion quantification by image processing in concrete slabs by (Zaki et al., 2020). Therefore, K-means has been used in the developed models of this research as the maps generated would show good correspondence with actual concrete conditions. Using K-means, a set of data can be clustered as shown as follows (Jain, 2010):

If  $X = \{x_i\}$ ,  $i = 1, 2, \dots, n$ ; where  $X$  represents a set of  $n$  data points needed to cluster into a set of  $K$ -partitions,  $C = \{c_k, k = 1, 2, \dots, K\}$ .  $C$  represents a set wherein  $c_k$  is a set of data points of the  $k$ -th cluster and let  $\mu_k$  represents its mean. The data set is clustered using the K-means algorithm in a way that minimizes the squared error between the points in each cluster and their respective means. Equation 3.6 evaluates the squared error between  $c_k$  and  $\mu_k$ .

$$J(c_k) = \sum_{x_i \in c_k} \|x_i - \mu_k\| \quad (3.6)$$

As shown in Equation 3.7, K-means seeks to minimize the sum of this squared error over all K-clusters.

$$J(C) = \sum_{k=1}^K \sum_{x_i \in c_k} \|x_i - \mu_k\|^2 \quad (3.7)$$

(Xu & Wunsch, 2005) summarize the iterative steps of the K-means algorithm as follows:

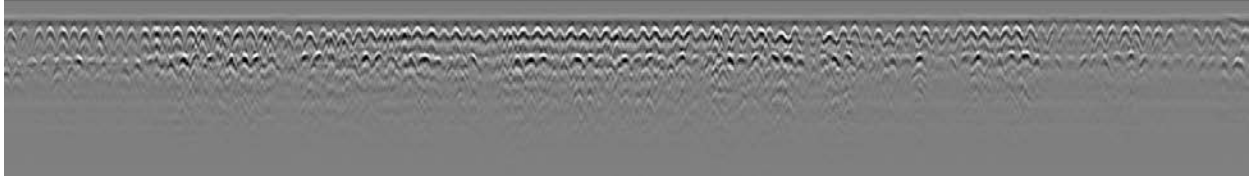
1. First, distribute K-partitions at random or according to some prior information. If  $M$  represents the centroid mean, it can be written in a set form:  $M = \{\mu_k, k = 1, 2, \dots, K\}$
2. If  $c_\omega$  represents the nearest cluster of a data point in the data set  $X$ , it is allocated to its nearest cluster as follows:

$$x_i \in c_\omega; \|x_i - \mu_\omega\| < \|x_i - \mu_k\|; i = 1, 2, \dots, n; i \neq \omega; k = 1, 2, \dots, K$$

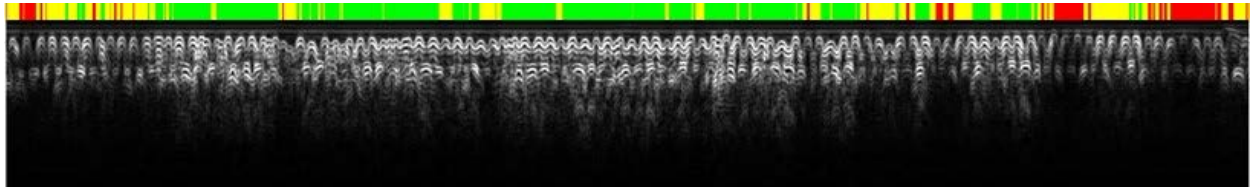
3. Based on the current partition set,  $C$ , the centroid matrix  $M$  is reevaluated.
4. Steps 2–3 are repeated until each cluster shows no change.

The normalized summation (n-s) values in scales of all GPR profile images are clustered using K-means into three *colored* zones. If  $k_1$  and  $k_2$  are limits obtained after clustering and considering that the range of values lies between 0 and 1, the following is the classification of concrete condition at pixel level depending upon the n-s value: a) if it lies between 0 to  $k_1$ : corresponding zone (pixel or group of pixels across the length of scan) is classified as concrete in bad condition and represented with the color red, b)  $k_1$  to  $k_2$ : corresponding zone is classified as concrete in moderate condition and represented with color yellow, and c)  $k_2$  to 1: corresponding zone is classified as

concrete in good condition and represented with the color green. Based on these principles, a deterioration scale can be generated for each profile individually, considering the cluster classification of the n-s value for each pixel across the length of the scan. This deterioration scale utilizes the three aforementioned colors (red, yellow, and green) to identify different concrete conditions. For example, a GPR profile taken from a case study has been shown in Figure 3.3 (a). This figure was taken from a case study of a bridge deck which shows the application of this developed model in Section 4.1. Figure 3.3(b) depicts the textured image of the profile after applying a standard filter, along with the deterioration scale represented by three colors indicating the concrete condition at each pixel value. The profile is generally in good condition (green) while it is in moderate to bad condition (yellow to red) at end zones on either side. Finally, these deterioration scales of all GPR profiles of a data set are stacked together with *uniform width which is representative of the tracing distance to generate a condition map*. Such a map shows a complete picture of the condition level of a bridge deck or a structural element in general.



(a)



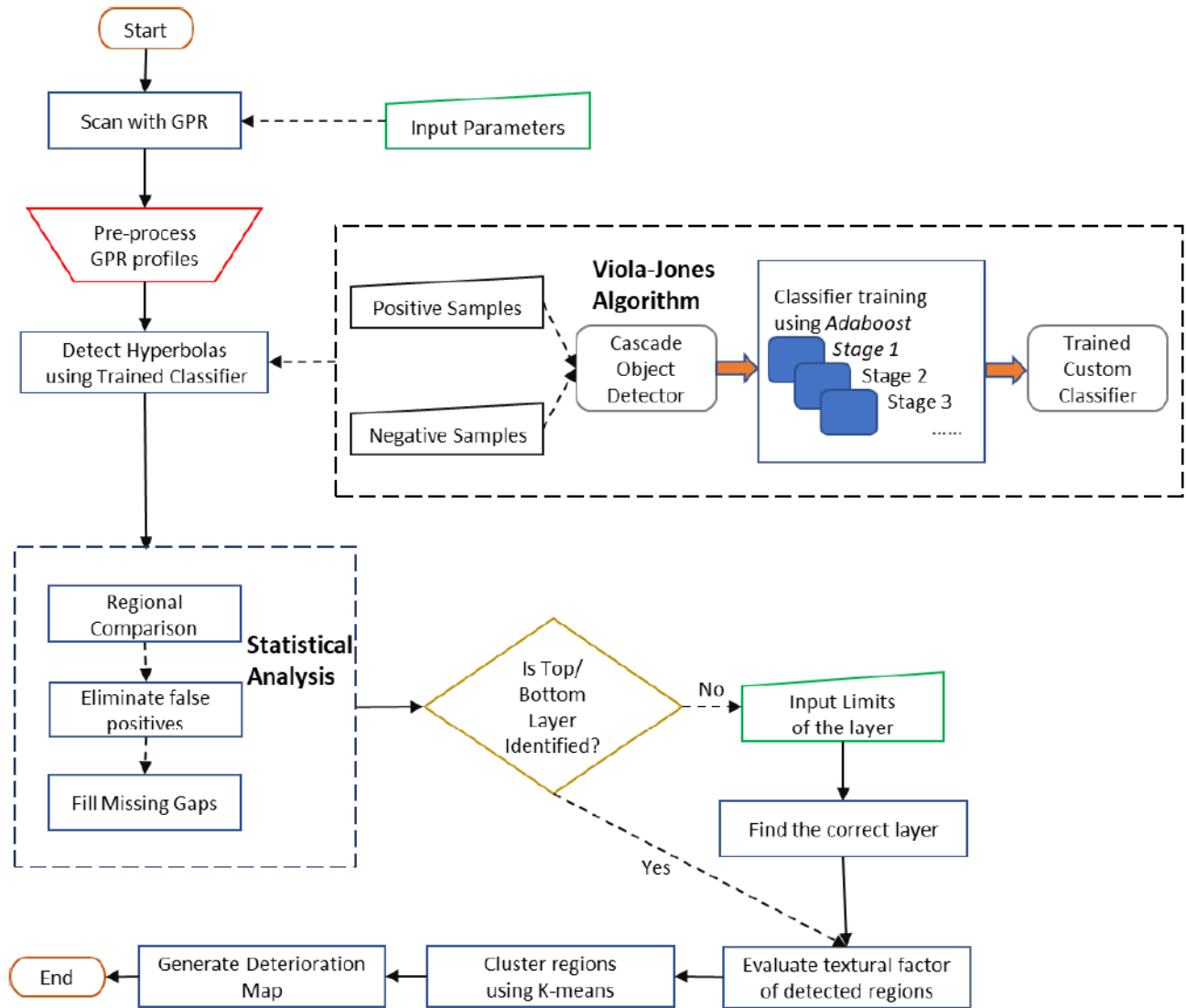
(b)

**Figure 3.3** (a) Sample GPR Profile; and (b) Output image with deterioration scale (Mohammed Abdul Rahman et al., 2016)

The limitations of this model have been discussed in detail in Section 4.1.4 after investigating the results of the condition map for a real-case bridge deck. Essentially, the deterioration scale of profiles has numerous impractical small-size zones which could falsely indicate the actual state of concrete and this model does not detect objects of interest which include hyperbole and other anomalies. To overcome these shortcomings, a better approach has been proposed in the next section which involves detecting hyperbolas based on the Viola-Jones algorithm and other improved steps.



### 3.2 Viola-Jones Algorithm-based Model (V-JAM)



**Figure 3.4** Methodology of V-JAM to generate condition maps

Figure 3.4 presents the flowchart of the developed model, outlining its comprehensive methodology. The initial stage involves data acquisition, which can be done by either utilizing existing scans or performing a new scan on the element requiring inspection. Commercially available GPR equipment from reputable firms such as Geophysical Survey Systems, Inc. (GSSI®, Nashua, NH, USA),

Ingegneria Dei Sistemi (IDS) Georadar (Pisa, Italy), MALÅ GPR (Malå, Sweden), among others, is employed for this purpose. Parameters like traverse spacing, antenna frequency, number of samples per scan, and other relevant factors, as mentioned in Section 2.8.1, must be predetermined and considered during the scanning process (Varnavina et al., 2015).

To prevent erroneous scans, the GPR antenna must be dragged at an optimal pace while considering scan spacing and sweep rate. Additionally, the scans should be taken perpendicular to the location of the rebars either in a grid pattern or a single direction. In the case of a bridge deck, it is recommended to position the antenna in such a way that it intersects the reinforcing layer at an angle as close as possible to  $90^\circ$  along the longitudinal direction, which is parallel to the deck's centerline (ASTM D6087, 2015). Large air or water gaps in the scanned element must be considered, as they significantly affect penetration depth and transmission velocity during the scanning process (Utsi, 2017). Subsequently, the GPR data which are obtained as B-scans must be pre-processed to improve the detection rate of hyperbolas.

### ***3.2.1 Pre-process GPR profiles***

The raw GPR B-scans must be pre-processed using the proprietary software provided by a GPR equipment manufacturer, such as RADAN® 7 from GSSI® (Nashua, NH, USA). The algorithm being adopted in this model, *Viola–Jones*, is sensitive to the aspect ratio, or the proportion of the width to the height of detected boxes containing hyperbolic regions (Rahman & Zayed, 2018). As a result, *if necessary*, these steps are employed on GPR profiles sequentially:

1. *If required*, the initial step is *horizontally stacking or stretching all the GPR profiles* of the structural element to be examined to keep the aspect ratio closer to the computed average value of the trained classifier, which is 1:1.68 (explanation of this algorithm along with the

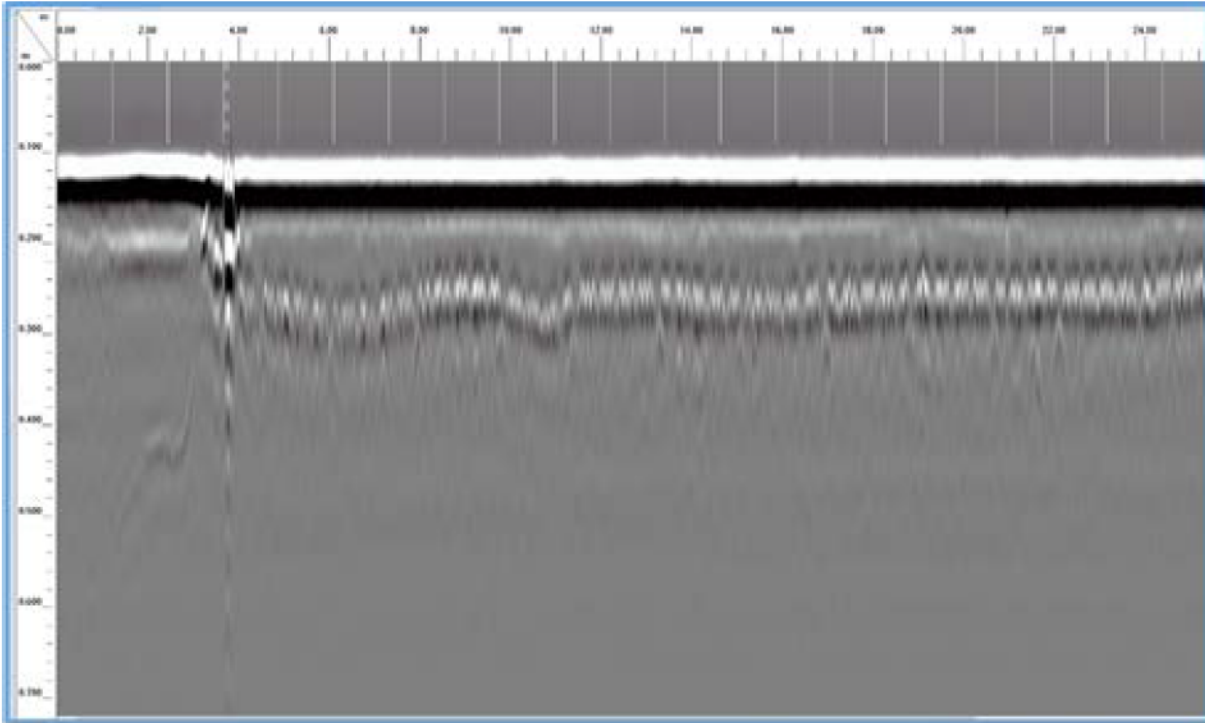
trained classifier is discussed in the following section). This step is adopted to *improve the hyperbola detection rate* and the process entails the following steps: (a) determine the aspect ratio of the raw B-scans by selecting a random small sample representative of hyperbolas with the highest frequency of occurrence in all of the profiles; and (b) if needed, horizontally stack, or stretch all profiles by a factor so that the aspect ratio of the chosen samples is closer to the aforesaid classifier value. Figure 3.5 displays a section of a GPR profile as an example of a bridge deck with a large span whose hyperbolas require horizontal stretching due to their dense stacking.

2. To improve the contrast of the GPR B-scans, the second phase of pre-processing entails *increasing "display" or "range" gain, if required*. The application of gain adjustment becomes necessary either due to horizontal stretching in the preceding stage or if the contrast of the raw GPR data is inherently low. By manually applying an optimal gain visually, the analyst can ensure that the gain is neither too low nor too high, improving the detection rate of the algorithm. While the process is subjective, employing this approach enhances the accuracy and effectiveness of the detection algorithm.
3. The last phase involves *removing background signals from the B-scans*, which lowers the high contrast of reflections from asphalt/concrete and/or concrete/air level and, inadvertently, enhances the contrast of hyperbolic regions. A full-pass automatic horizontal background removal option available in GSSI® RADAN 7 software is applied on GPR profiles of reinforced structural members as the reflections due to hidden objects are primarily due to rebars (hyperbolas) which are not eliminated due to this step application. In case of geotechnical, archeological, or other investigations where primary object detections are buried pipes, bones, or other objects, care must be taken to ensure proper application of this

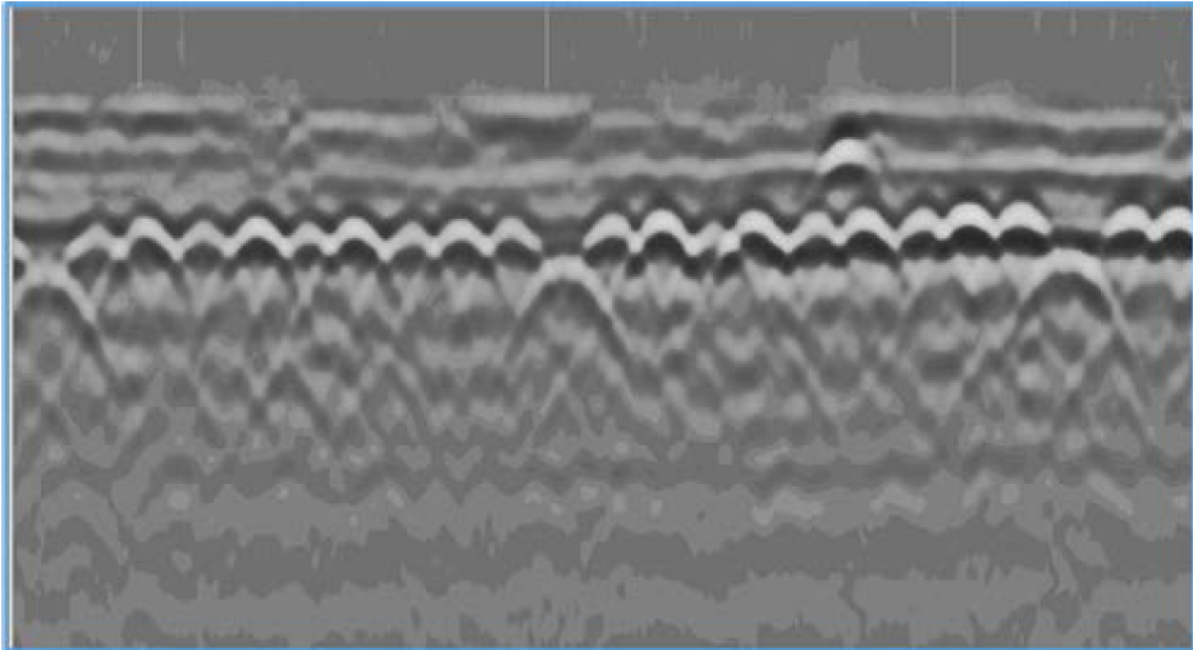
filter i.e., either a manual filter is applied or completely avoided depending on the type of investigation and the data profiles obtained (Leach, 2019). However, since this research is focused on hyperbolic detections from rebar reflections of reinforced members only, full-pass background removal is employed.

The outcome of pre-processing the GPR profile shown in Figure 3.5 is depicted in Figure 3.6 which included the following steps: It was first stretched horizontally by a factor of "8" to keep an aspect ratio at 1:1.49 closer to the classifier, then the display gain in RADAN® was increased to "20," and finally, the background signals were removed to clearly show the top layer of rebar reflections for accurate and fast detections.

These pre-processing steps, if applicable, are *extremely vital* and must be applied to all GPR profiles of an element being inspected. Through empirical observation, it has been noted that conducting pre-processing using proprietary software yields superior results compared to applying image processing techniques using tools like MATLAB® R2019b, even though these steps could be automated by exporting raw GPR profiles. Despite taking only a few minutes to apply these pre-processing steps, they significantly enhance the detection rate of hyperbolas, thereby mitigating the limitations associated with using a ML approach (Mohammed Abdul Rahman, Zayed, et al., 2022).



**Figure 3.5** A GPR profile section of a large bridge deck (Rahman & Zayed, 2018)

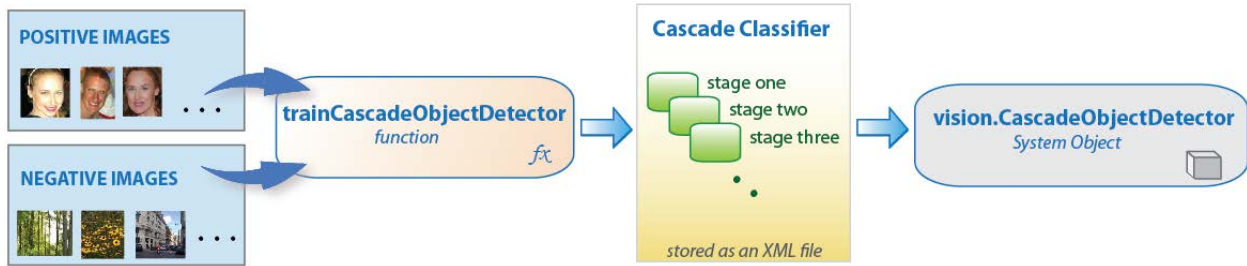


**Figure 3.6** A sub-section of the GPR profile after applying pre-processing steps including horizontal stretching, range gain, and background removal (Rahman & Zayed, 2018)

### 3.2.2 Trained Classifier and Hyperbola Detections

The next stage is to convert the pre-processed GPR profiles into image files (.jpeg, .tiff, etc.) and apply a trained custom classifier for hyperbolic detections using MATLAB® software (Rahman & Zayed, 2018). The *Viola-Jones (V-J) algorithm* is briefly described, and the data that was used to train the classifier is also explained subsequently. It was initially proposed as a framework for the fast processing of images with high detection rates for facial features (Viola & Jones, 2004). The implementation of the V-J algorithm for face detection along with its comprehensive development and analysis has been described in (Viola & Jones, 2004), (YQ Wang, 2014), and (Chaudhari et al., 2015). It originally used “Haar-like” features to detect faces, but it was later expanded to train and detect any facial feature or object employing these feature extractors: Local Binary Pattern (LBP) (Ojala et al., 2002), Histogram of Oriented Gradients (HOG) (Dalal & Triggs, 2005), and “Haar”. (Dang & Sharma, 2017) compared prominent face-detection algorithms and deduced that *V-J* has the best precision and recall rate. The following benefits led to the adoption of this algorithm in this model to find hyperbolic features in GPR profiles: (a) scale-invariance, i.e., ability to detect hyperbolas of different sizes that have a similar aspect ratio, (b) the algorithm assumes that the features to be detected are in *full-view upfront position* similar to hyperbolas in B-scans, (Rahman & Zayed, 2018) and (c) rapid and precise with low false-detection rate (Gupta & Sharma, 2014). While there are other ML and deep-learning algorithms employed for hyperbola detections (Section 2.10) , this algorithm has been preferred due to the following two-step approach in detecting hyperbolic regions: a) the classifier used to detect hyperbolas based on V-J algorithm is *lighter and speedily* detects maximum hyperbolic regions in GPR profiles, and b) the top/ bottom layer in GPR profiles is identified based on regional comparison, and

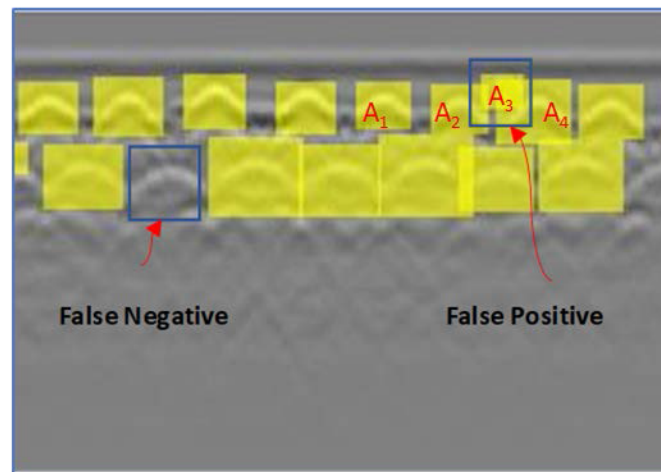
subsequently, false detections are eliminated and missing gaps are filled based on statistical analysis (discussed as the next step) for *accurate* detections.



**Figure 3.7** Framework of Cascade Object Detector (MathWorks, 2016)

Firstly, the cascade object detector in MATLAB® is utilized to train a custom classifier with GPR data. Figure 3.7 shows the generalized framework for training custom classifiers and detecting objects based on this classifier. Initially, training is done in multiple stages after supplying the classifier with a set of positive samples (image boxes of GPR profiles with hyperbolas present) and negative samples (images or image boxes with non-hyperbolic regions in GPR profiles). The HOG feature type is used to typically identify objects without fine-scale details, such as people and cars. In their study on detecting hyperbolic reflections in bridge decks, (Kaur et al., 2015) conducted a thorough comparison of various feature descriptors, including HOG, direct gradient-orientation histogram, maximum gradient orientation, edge pixels, intensity values, and intensity histogram, among others. Among these descriptors, HOG exhibited the best performance in terms of accuracy, precision, sensitivity, and specificity. As a result, it has gained significant popularity among researchers, as mentioned in Section 2.10, and will be employed in this model. A *boosting technique* enhances the training process in each stage by eliminating negative samples and processing positive samples to the next stage (Mohammed Abdul Rahman, Zayed, et al., 2022). The recommended boosting algorithm proposed in the literature which has been adopted in this model

is called *Adaboost* since the classifier is trained to categorize just the hyperbolic regions from the background of a GPR profile i.e., a case of binary categorization (Freund & Schapire, 1997). To create a strong classifier, it combines several weak learners by averaging the decisions taken at each stage, as explained in detail by (Viola & Jones, 2004). After all the stages are executed by the classifier, the identified objects can be categorized as follows: (a) *true positives* are positive samples that were accurately detected; (b) *false positives* are negative samples that were incorrectly labeled as positive; and (c) *false negatives* are positive samples that were incorrectly identified as negative. For example, Figure 3.8 shows the three types of detections based on a trained classifier on a sample GPR profile: true positives are labeled as filled yellow rectangles, whereas a false negative is labeled as an empty blue box and a false positive ( $A_3$ ) is marked as a filled yellow rectangle enclosed in a blue box. For cascade training, two additional parameters must be stipulated in addition to the total number of stages: (a) *the false positive rate*, which is the ratio of total false positives to the sum of all false positives and true negatives; and (b) *true positive rate*, which is the ratio of total true positives to the sum of all false negatives and true positives.



**Figure 3.8** A sample GPR profile showing true positives and false detections (Mohammed Abdul Rahman, Zayed, et al., 2022)



**Table 3.1** Condition and Considerations for the training set (MathWorks, 2016)

<b>Condition</b>	<b>Consideration</b>
A large training set (in the thousands).	Increase the number of stages and set a higher false positive rate for each stage.
A small training set.	Decrease the number of stages and set a lower false positive rate for each stage.
To reduce the probability of missing an object.	Increase the true positive rate. However, a high true positive rate can prevent you from achieving the desired false positive rate per stage, making the detector more likely to produce false detections.
To reduce the number of false detections	Increase the number of stages or decrease the false alarm rate per stage.

Table 3.1 shows the general conditions and considerations employed in choosing these parameters. The selection of the number of stages is also a trade-off between more stages with a higher false positive rate or fewer stages with a lower false positive rate. A greater number of weak learners exist when a lower false positive rate is specified and vice versa (MathWorks, 2016). During each stage of training, a region classified as *negative* indicates detection is finished (no hyperbola present) while a region labeled as *positive* is processed to the following stage. To reject negative samples as quickly as possible during the stages, the classifier is trained to assume that the vast majority of windows do not contain the object of interest (Rahman & Zayed, 2018). For the classifier to function well, the false negatives should be lower as once a region is falsely detected as negative, the classifier stops analyzing that region. Therefore, the false positive rate is generally specified higher as the detector incorrectly labels those regions as positive, which could be corrected in subsequent stages. The overall false positive rate is  $f^s$ , where  $f$  is the false positive rate per stage in the range (0 1) and  $s$  is the number of stages. The overall true positive rate is  $t^s$ , where

' $t$ ' is the true positive rate per stage in the range (0 1]. Thus, adding more stages reduces the overall false positive rate while reducing the true positive rate, and therefore, a proper trade-off must be done for accurate and faster detection (MathWorks, 2016). After training a custom classifier with chosen parameters on a GPR data set (bridge deck), it can be used to identify objects (hyperbolas) in any given image (GPR profile).

A bridge deck in Sumner, Iowa, labeled O2, was inspected as one of the nine bridges comprehensively assessed for bridge deck deterioration mapping, and its data was used to train the classifier (Gucunski et al., 2011). The reasons for choosing this deck, its cross-section, and the scanning parameters utilized for its GPR survey are discussed in detail as part of the case study in Section 4.1. This bridge has two-lane roadways with a total width of 48 ft and a total of 24 scans (GPR profiles) were obtained at 2 feet of uniform inter-scan distance. The cascade object detector was utilized in two consecutive phases for training. In the first phase, a total of 167 positive samples (hyperbola enclosed boxes) and negative samples (profile with hyperbola deleted) were provided for training from just one B-scan (first swab). These input parameters were used: *number of cascade stages: 20; per-stage false alarm rate: 0.5; and per-stage true positive rate: 0.995*. In the next phase, the classifier, which was trained using one profile, was utilized to identify hyperbolas in all 24 profiles. The results were as follows when compared to the manually counted ground truth of 3843 hyperbolas as shown in Appendix A: *true positives - 3400 (88.5%), false positives -14 (0.4%), and false negatives - 443 (11.5%)* (Rahman & Zayed, 2018). Lastly, the classifier was trained again using the same input parameters, and the aforesaid obtained true positives and false negatives. *The resulting trained classifier obtained could be used for detecting hyperbolas in GPR profile scans of any RC structural or bridge element, assuming the profiles were pre-processed as described earlier in Section 3.2.1.*

### 3.2.3 Regional comparison and Statistical analysis

Although the custom classifier can successfully identify most hyperbolas in B-scans, in real cases, there may be a few false detections. Automated *regional comparison and statistical analysis* can remove such false positives and false negatives, shown in Figure 3.8 as an example (Rahman & Zayed, 2018). The fundamental premise for this analysis is that the reinforcement bars are layered in a single or double layer with uniform spacing, typically in the case of RC bridge components, slabs, or parking lots. By employing the following *three principles stepwise*, the potential false positives and false negatives can be eliminated.

#### *Principal 1- Regional Comparison*

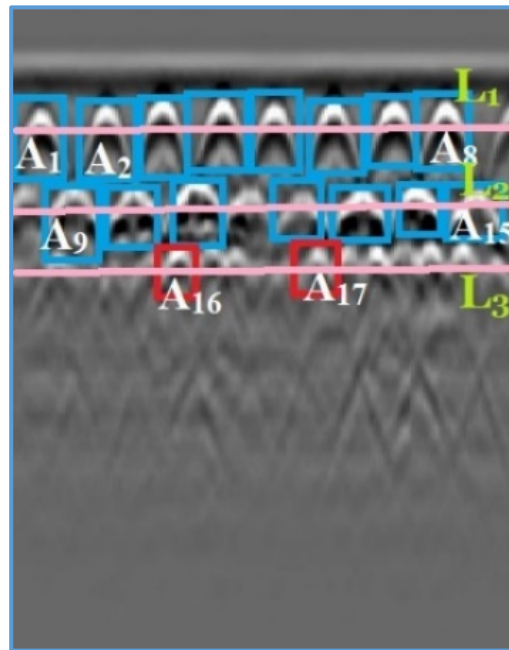
Due to their regional position in the B-Scan, the detections, *if present*, - whether true or false - that do not occur along the chosen layer i.e., either top or bottom, are regarded as false positives and removed. The developed code identifies and eliminates these false positives as follows:

1. Firstly, arrange all detected hyperbolas (boxes) in *horizontal layers* based on their regional position. To illustrate with an example, please consider a section of a GPR profile in Figure 3.9. It has 8 hyperbolas identified as  $\{ A_1, A_2, \dots, A_8 \}$  in top layer, marked L<sub>1</sub>; 8 other hyperbolas identified as  $\{ A_9, A_{10}, \dots, A_{15} \}$  in the bottom layer of reinforcement, marked L<sub>2</sub>; and lastly, let's assume that two false positives have been identified in the bottom deck reflections of the bridge deck by the classifier, identified as A<sub>16</sub> and A<sub>17</sub>; marked in layer L<sub>3</sub>. To identify these layers  $\{ L_1, \dots, L_m \}$ ; where  $m = 3$  i.e., the total number of layers; the hyperbolas A<sub>1</sub> to A<sub>n</sub> are first arranged in an ascending order based on the closest distance between the top-left edge of the detected boxes (which is closer to the apex of the hyperbola) and the top-leftmost edge of the complete GPR profile as follows:

$$\{ A_1, A_2, \dots, A_n \}, n=17.$$

The first hyperbola  $A_1$  is assumed to lie in the first layer,  $L_1$ . The next hyperbola  $A_2$  would lie in this layer  $L_1$  if the vertical edges of  $A_1$  &  $A_2$  overlap. If not,  $A_2$  will lie on a new layer,  $L_2$ . This process is iterated until all hyperbolas are exhausted. If a hyperbola lies on two layers, which rarely occurs, it is assumed to lie on the layer whose vertical distance is closest to the two. If there are overlapping hyperbolas (two or more) in the same layer, both are considered valid and the false positive among them would be eliminated in the next step.

The developed code based on the above principle would yield the following results:  $\{A_1, A_2, \dots, A_8\}$  would lie in layer  $L_1$  as  $A_2$  left-edge overlaps with the box of  $A_1$ ,  $A_3$  overlaps with  $A_2$ , and so on. Similarly, the second layer,  $L_2$ , starts with  $A_9$  as it does not overlap with  $A_8$  and ends with  $A_{15}$ . The last layer,  $L_3$ , has hyperbolas  $A_{16}$  and  $A_{17}$ .



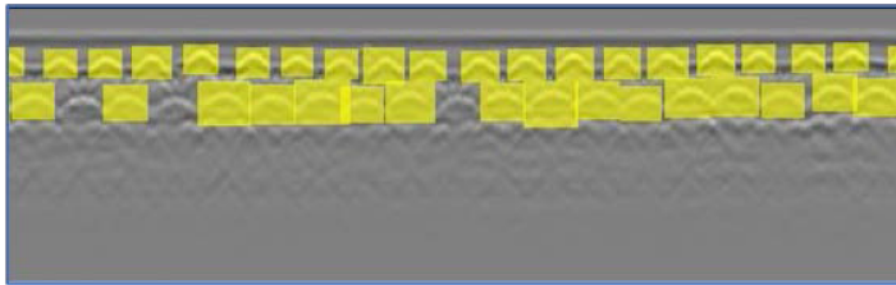
**Figure 3.9** Regional Comparison – Identifying horizontal layers and eliminating false positives

2. Lastly, the top/bottom layer is identified as it generally lies on the top with the greatest number of hyperbolas. After identifying the required layer for analysis, all other hyperbolas are eliminated. So, in the case of Figure 3.9, if the analysis is performed based on the top layer,  $L_1$ , hyperbolas  $A_9$  to  $A_{17}$  are discarded as false positives. However, if the analysis is performed based on the bottom layer,  $L_2$ , hyperbolas  $\{A_1, A_2, \dots, A_8\}$  &  $\{A_{16}, A_{17}\}$  would be eliminated. In the cases of thin decks, slabs, or pavements, condition mapping can be done based on either the top layer or bottom layer as both the layers are typically visible. Nevertheless, data analysis typically focuses on the top layer, as corrosion often initiates from this layer in North America due to the presence of de-icing salts (Coleman & Schindler, 2022). In certain instances, even when employing high-frequency radar, the top layer may remain obscured due to factors like excessive moisture, high chloride content, or an exceptionally thick concrete cover. Under such circumstances, GPR may not be a viable option, and it is advisable to explore alternative NDT methods (Utsi, 2017).
3. In most cases, the top/bottom layer is detected correctly by the developed model. However, in the presence of GPR profiles with severely disoriented rebar layers and/or complex hyperbolic reflections, the automatic identification of the required layer may not be accurate.

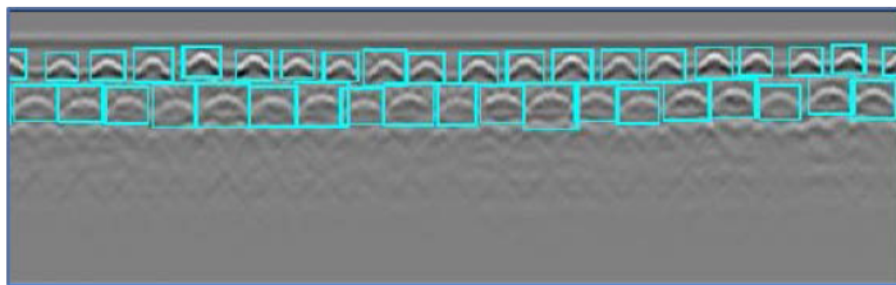
#### *Principal 2- Statistical Analysis: Eliminating false positives*

After eliminating false positives which do not lie along the top/bottom layer, the next step is to eliminate false positives in the form of overlapping detections present along the chosen layer. These overlapping hyperbolas are typically present due to the following reasons: a) stronger reflections cause a ripple effect in which the classifier identifies the weaker reflections present beneath the true positives as false positives; and b) reflections from other rebars present due to repair

work or other reasons. When such overlapping reflections occur, typically one of them is a true positive, and the other(s) are false. To identify and discard the false detections, the location (predominant factor) and the average size of all the overlapping detections are compared with the non-overlapping neighboring true positives. For example, Figure 3.8 shows two overlapping detections,  $A_2$  &  $A_3$ , present in-between two neighboring true positives:  $A_1$  &  $A_4$ . Hyperbola  $A_3$  is a false positive and eventually eliminated as the true positive is  $A_2$  due to the following reasons: a) location i.e., the vertical distance of the top-left edge of  $A_2$  (taken as reference) is closer to both,  $A_1$  &  $A_4$ , and b) the size of  $A_2$  is also closer to its neighbors.



**Figure 3.10** A sample cut-out of a GPR profile after applying a custom classifier (Mohammed Abdul Rahman, Zayed, et al., 2022)



**Figure 3.11** A sample cut-out of a GPR profile after complete detections (Mohammed Abdul Rahman, Zayed, et al., 2022)

*Principal 3- Statistical Analysis: Missing gaps*

There could be gaps missing along the chosen top/bottom layer due to the following reasons:

- a. false negatives i.e., an undetected clear-shaped hyperbola
- b. zones with highly distorted hyperbolas
- c. zones with an absence of hyperbolas; possibly due to severe corrosion.
- d. *Anomalies*

In this step, the missing gap width, denoted as ' $w$ ' is compared with the minimum width of all the detected hyperbolic regions, denoted as ' $gm$ ', for classification. The gap can occur in three possible scenarios: between any two detected hyperbolic regions, before the first hyperbolic region detected along the top layer from the left, or after the last hyperbolic region along the top layer. Firstly, the pixels of the missing gap are summed and normalized along the horizontal axis. Secondly, this summation of pixels is transformed into a 1-D signal by utilizing the cubic spline fitting function in MATLAB. This function is based on the popular spline interpolation technique as described in the book by (De Boor, 1978). The reason for converting *a gap along the top layer* into a signal is that the local highest peaks *can* represent corresponding hyperbolic peaks while the local lowest peaks *can* represent the dividing gap between two hyperbolas in a GPR profile. It can help split the gaps based on *reasonable accuracy* and the following three cases occur which are dealt with accordingly:

1.  $w < gm$ : If the width is too small, i.e., smaller than the minimum width, it is assumed that the gap is too small to contain any object of interest within it. Therefore, if the gap lies between two hyperbolic regions, the lowest peak in its corresponding 1-D signal is found using the proprietary '*findpeaks*' function in MATLAB. This function is based on the modified form of the widely utilized '*PeakUtils*' algorithm (Negri & Vestri, 2017) for

identifying signal peaks. Subsequently, the width of the detected region box on the left side of the gap is extended up to the identified lowest peak pixel. Likewise, the width of the detected region box on the right side is extended to start immediately after the left side, effectively closing the gap. However, if the gap is located at either end of the profile, it is closed by extending the detected region box to start from the first pixel or to end at the last pixel, depending on the specific side of the gap. Figure 3.12 shows a GPR profile section with all three cases of missing gaps for demonstration purposes. In Figure 3.13, the small gaps at both ends of the profile are filled with yellow boxes, which are marked as Case I. These yellow boxes are used to fill in the gaps and ensure a continuous profile of detections along the top layer. Additionally, all the other red boxes in the figure are extended on either side, if necessary, to maintain the aforesaid continuity.

2.  $gm \leq w < (2 \times gm)$ : Under this circumstance, it is assumed that the gap encompasses a single object of interest, regardless of whether it is a false positive or any other scenario. Thus, to fill the gap between two hyperbolic regions, the function identifies the two lowest peaks in the signal closer to the gap's boundaries. Subsequently, the bounding boxes on either end are extended to encompass these lowest peaks, while a *new* single box is formed between the two lowest peaks. This process effectively fills the gap by incorporating the relevant data within the identified regions. Similarly, when the gap is present at either end of a profile, a new single box is created on the respective side (start or end) of the profile. This is accomplished by identifying the lowest peaks that are closer to the detected region boxes. These lowest peaks serve as the boundary for enclosing the new single box and effectively closing the gap. In Figure 3.13, the green box labeled as Case II represents a potential object of interest that has been identified through the application of this step.



3.  $w \geq (2 \times gm)$ : In this case, the gap is assumed to contain 2 or more objects of interest. *An optimal number of cuts is required to split the gap irrespective of its width.* Let 'O' represent the total number of cuts needed. If there are 'N' number of lowest peaks identified in the corresponding 1-D signal of the gap, then the value of 'N' is typically much greater than 'O'. Each 'O' is identified using an iterative process as shown below:

Let  $N_1$  represent the first peak in consideration in ascending order across the top layer. Let  $N_{1c}$  be its column value. Let  $N_2$  be the next peak. Thus,  $N_{2c} > N_{1c}$ .

If the value of  $(N_{2c} - N_{1c}) < gm$ ; then  $N_2$  becomes the first 'possible' optimal cut *only* if its 'row' value ( $N_{2r}$ ) is lower than  $N_{1r}$ . Otherwise,  $N_1$  becomes the 'possible' first optimal cut.

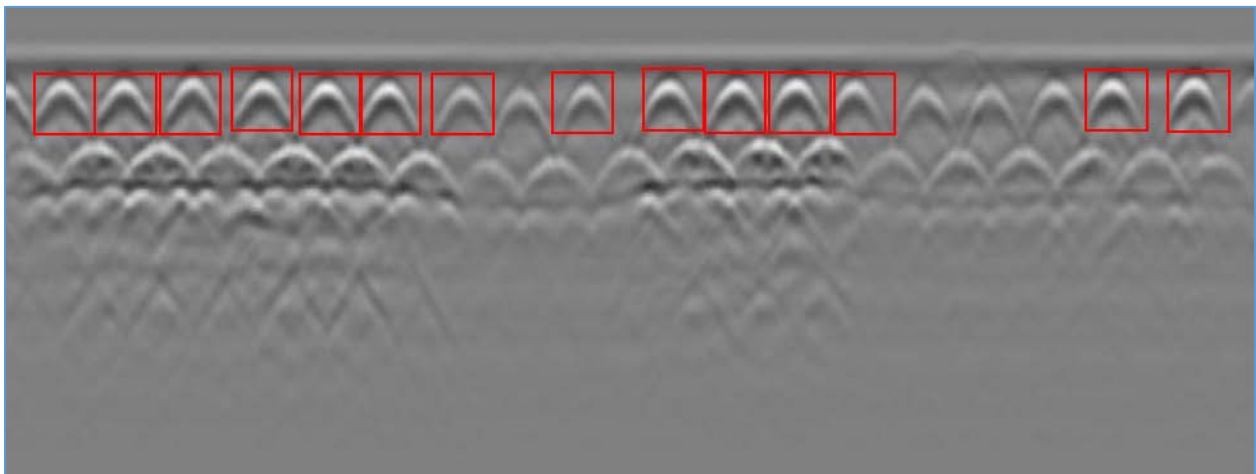
However, *If*  $(N_{2c} - N_{1c}) > gm$ ; then  $N_1$  becomes the first 'definitive' optimal cut which is recorded, while  $N_2$  becomes the 'possible' first optimal cut.

Then, the 'possible' optimal cut ( $N_2 / N_1$ ) is compared with the next peak ' $N_3$ '.

This is repeated until each of the lowest peaks, 'N', is checked in ascending order of its column values to find a complete list of complete optimal cuts 'O'. **(3.8)**

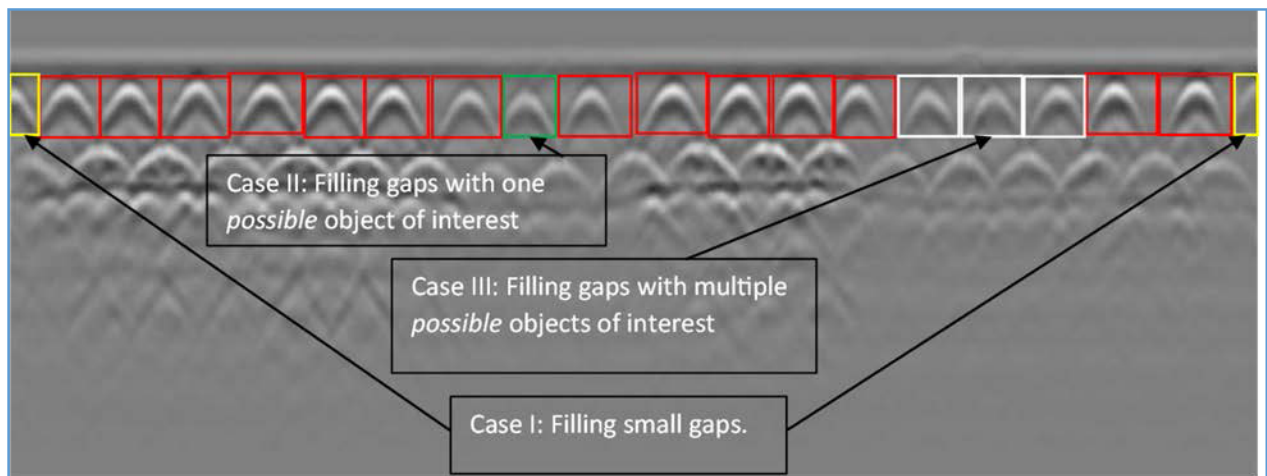
Subsequently, the list of definitive optimal cuts is used to bind *new surrounding boxes* and extend the detected region boxes on either side, if applicable. This iterative process is utilized for all three gap locations accordingly such that the missing gaps have new boxes while the existing boxes on either end are extended, if applicable and needed, to effectively close the gap across the top layer. In Figure 3.13, after applying this step, four optimal cuts were obtained between the two red-detected hyperbolic boxes. Two of these cuts are positioned closer to the boxes on both ends. As a result, three white boxes, labeled Case III, are shown, representing potential objects of interest in the figure.

Finally, this process is repeated for each of the missing gaps identified across the top layer. The new surrounding boxes *can* contain an anomaly since it's not a detected region. Lastly, the suggested model employs a user-interactive approach which prompts the user to confirm if the necessary layer has indeed been successfully recognized (*Yes/No*). If the user response is negative, a further prompt asks the user to draw a surrounding box with a typical hyperbola along the required (top/bottom) layer in a GPR profile. This information is used to record the upper and bottom limits of the required layer for analysis and the width of this box is considered as the minimum width 'gm'. Subsequently, the new limits of the top layer are assumed to be a *complete gap* and the steps of the aforesaid third case are applied to determine optimal cuts and bound the complete layer with new surrounding boxes. The identification of such a layer in case of incorrect detection of the required layer is explained with an example in Section 4.4. Hence, the adoption of a user-interactive approach guarantees the selection of the appropriate layer, which is vital in the development of reliable maps.



**Figure 3.12** The sample GPR profile is shown with missing detections.

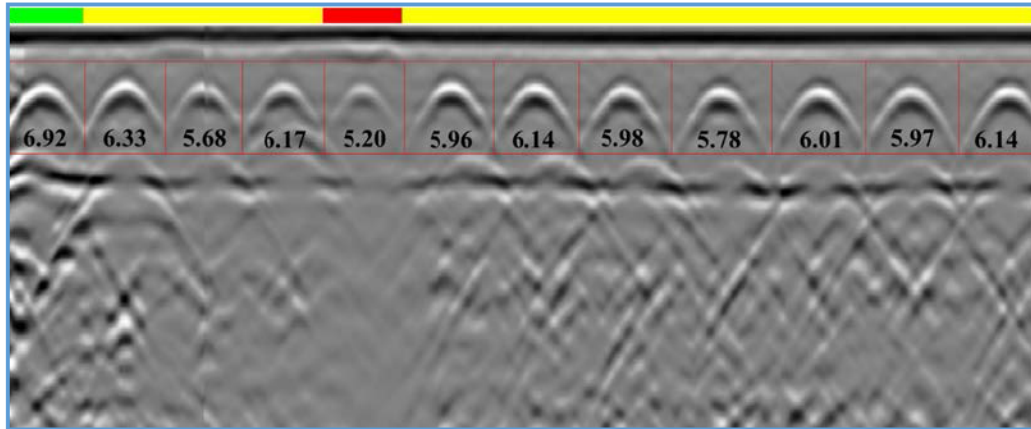
The *user-labeled anomalies module (ULAM)* discussed in Section 3.3.4 can be incorporated into this model wherein the user marks anomaly regions in missing gaps, if present, based on aided tools. Otherwise, this model assumes that there are no anomalies present in its GPR profiles. In case of no anomalies, it is assumed that the missing gaps contain either hyperbolic regions which could not be detected by the model or severely corroded regions. While it has the potential to yield erroneous results, proper marking of anomaly regions by the user using ULAM can mitigate this limitation and ensure accurate marking of regions. After applying the aforesaid principles, the missed false negatives are correctly labeled in boxes as shown in Figure 3.13. Consequently, *detections are complete* in all GPR profiles after employing the V-J algorithm along with these *three* principles and processed towards the next phase of evaluating a textural factor for all the detected regions which are bounded in rectangular boxes along the top layer. Figure 3.11 shows another example after detections are completed over the Figure 3.10.



**Figure 3.13** Missing gaps in a GPR profile filled for varying cases.

### 3.2.4 Condition Mapping

A condition rating relative to the deterioration level of detection regions must be assigned along the user-selected top (or bottom) layer. In the GPR-IBA approach, it is achieved qualitatively as an expert analyst labels the regions using his visual perception and judgment (Tarussov et al., 2013). The *texture* would be an equivalent parameter to differentiate regions in a GPR profile. Even though the human visual system can intuitively distinguish and segment various textures, automating it with computer vision is challenging (Tatu & Bansal, 2015). Texture describes both an object's tactile nature, i.e., its tangible "feel", and visual or optical nature, i.e., its shape or contents (Manjunath & Ma, 1996). Coarseness, contrast, directionality, line-likeness, regularity, and roughness are six mathematical metrics that relate textural features to visual perception (Tamura et al., 1978). The texture in image processing terminology indicates the spatial distribution of intensities in a greyscale image (Shapiro & Stockman, 2001). Therefore, a textural factor has been chosen in this model for assessing detected regions because it can distinguish subtle nuances in patterns of GPR images while traditional intensity-based methods may prove rather ineffective (Mohammed Abdul Rahman, Zayed, et al., 2022).



**Figure 3.14** A sample GPR profile with detections in red boxes, entropy values enclosed, and deterioration scale in color on top (Mohammed Abdul Rahman, Zayed, et al., 2022)

(Shapiro & Stockman, 2001) states there are two broad approaches for classifying textures: structural and statistical. A structural approach is employed for evaluating fairly regular or repeated textures like a brick wall. However, GPR profiles, which are based on quantitative measurements of intensity variations within a region, are best analyzed using a statistical approach. Entropy, a statistical measure of an image's variability or randomness, has been employed in this model (Gonzalez et al., 2010). Although the standard filter reduces noise and distinguishes areas in a GPR profile as discussed in Section 2.16.6, entropy is a better factor for the detected regions as it can better differentiate slight variance's among them due to higher sensitivity. *In essence, the entropy values of two detected regions that are similar to each other would have closer values, whereas two dissimilar regions would have a significant difference in their entropy values.* Accordingly, entropy can effectively differentiate areas of deterioration as good vs. bad based on its values. There are no units for entropy, and its mathematical evaluation is done by examining the grayscale pixels of a given area or image (Gonzalez et al., 2010): If a random variable,  $z$ , represents intensity, then the corresponding histogram is denoted by  $p(z_i)$ , where,  $i = 0, 1, 2, 3, \dots, L-1$ ;  $L$  is

the number of distinct intensity levels (for example, 256 levels in a grayscale 8-bit image). Then, the entropy is given by Equation 3.9.

$$\mathbf{Entropy} = - \sum_{i=0}^{L-1} p(z_i) \log_2 p(z_i) \quad (3.9)$$

For GPR profiles of a structural element being inspected, entropy is evaluated for all the detected regions across the single layer (usually at the top reinforcement level). The *K-means* data-clustering algorithm is then used to grade these (entropy) values into zones. The reasons for using K-means in analyzing GPR data have been explained in Section 3.1.3. Subsequently, K-means is used to cluster detected regions based on entropy values into a pre-assigned number of zones, typically three or four. *Zones with higher entropy levels indicate better concrete conditions, and vice versa, as entropy values are strongly correlated with the deterioration level of the concrete.* A color-coding convention is used for condition mapping to correlate each identified region with its deterioration level. If three zones are used, the green color indicates good concrete (regions associated with highest values of entropies), the yellow color indicates moderate corrosion, and the red color indicates severely corroded zones (regions associated with lowest values of entropies). Similarly, if four color-convention is utilized, the blue zone indicates very good concrete condition, the green zone implies good condition of concrete, the yellow zone refers to moderately corroded concrete and the red zone indicates concrete in bad condition. Corollary, a *deterioration scale* is developed based on clustered zones for each GPR profile. This is demonstrated using a GPR profile taken from a case study in Section 4.2 with the deterioration scale shown on its top in Figure 3.14. In this example, K-means has clustered the detection regions into zones based on the entropy values as follows: one region (hyperbola) is in good condition (indicated by green color),

one region is in severe condition (red) while others are moderately corroded (yellow). In the GPR-IBA, an analyst examines such profiles individually and could label a yellow region as red or vice versa (incorrectly), especially in cases of large profiles. *However, since this model uses crisp entropy values based on all profiles, the automated assignment is consistently robust and accurate.* Lastly, the developed deterioration scales of all GPR profiles of a data set are stacked together in the order in which they were scanned to generate the *condition map* (Mohammed Abdul Rahman, Zayed, et al., 2022). The application of this model using a complete case study with condition or deterioration mapping used interchangeably, and its comparison is discussed in the next chapter in Section 4.2. The major limitations of the V-JAM method after its application have been stated in the aforesaid section and these include the inability to detect ill-shaped hyperbolas and anomalies and not considering information relating to the structural element being inspected. To overcome these limitations, a robust user-interactive model has been proposed which strives to generate reliable condition maps for reinforced structural elements for wholesome condition assessment.

### **3.3 Robust User-Interactive Model (RUIM)**

One of the main limitations of the numerical ABA method is that by considering only amplitude values, it majorly ignores information relating to the structural element being inspected such as the presence of structural elements or anomalies present within the structure (Tarussov et al., 2013). The GPR-IBA method considers these factors and to incorporate such information, the developed RUIM method aims to achieve a holistic approach through the following two steps: a) a user-interactive approach of condition mapping in which the GPR analyst inputs relevant known information about the scanned element such as the age, severity of corrosion in profiles, and

anomalies; b) a *user-labeled anomalies module* which assists in identifying anomaly regions that can be tagged by the user for accurate analysis. Besides, the RUIM method also detects hyperbolic variations in GPR based on a novel algorithm utilizing concepts from OSCA (Zhou et al., 2018) and (Mertens et al., 2016) so that ill-shaped hyperbolas are also accounted for extensive robust detections. The complete flowchart of this model is shown in Figure 3.15 and has been explained stepwise.

### **3.3.1 Obtain GPR scans, pre-processing, and User-Assisted input**

The first stage involves obtaining GPR scans either by scanning the structural element such as a bridge deck or utilizing previously scanned GPR data as described in Section 2.8.1. The next stage involves pre-processing GPR profiles using the proprietary software of the GPR equipment used for scanning, such as Geophysical Survey Systems, Inc. (GSSI®, Nashua, NH, USA), Ingegneria Dei Sistemi (IDS) Georadar (Pisa, Italy), MALÅ GPR (Malå, Sweden), and others. This process includes similar steps as explained in detail in Section 3.2.1

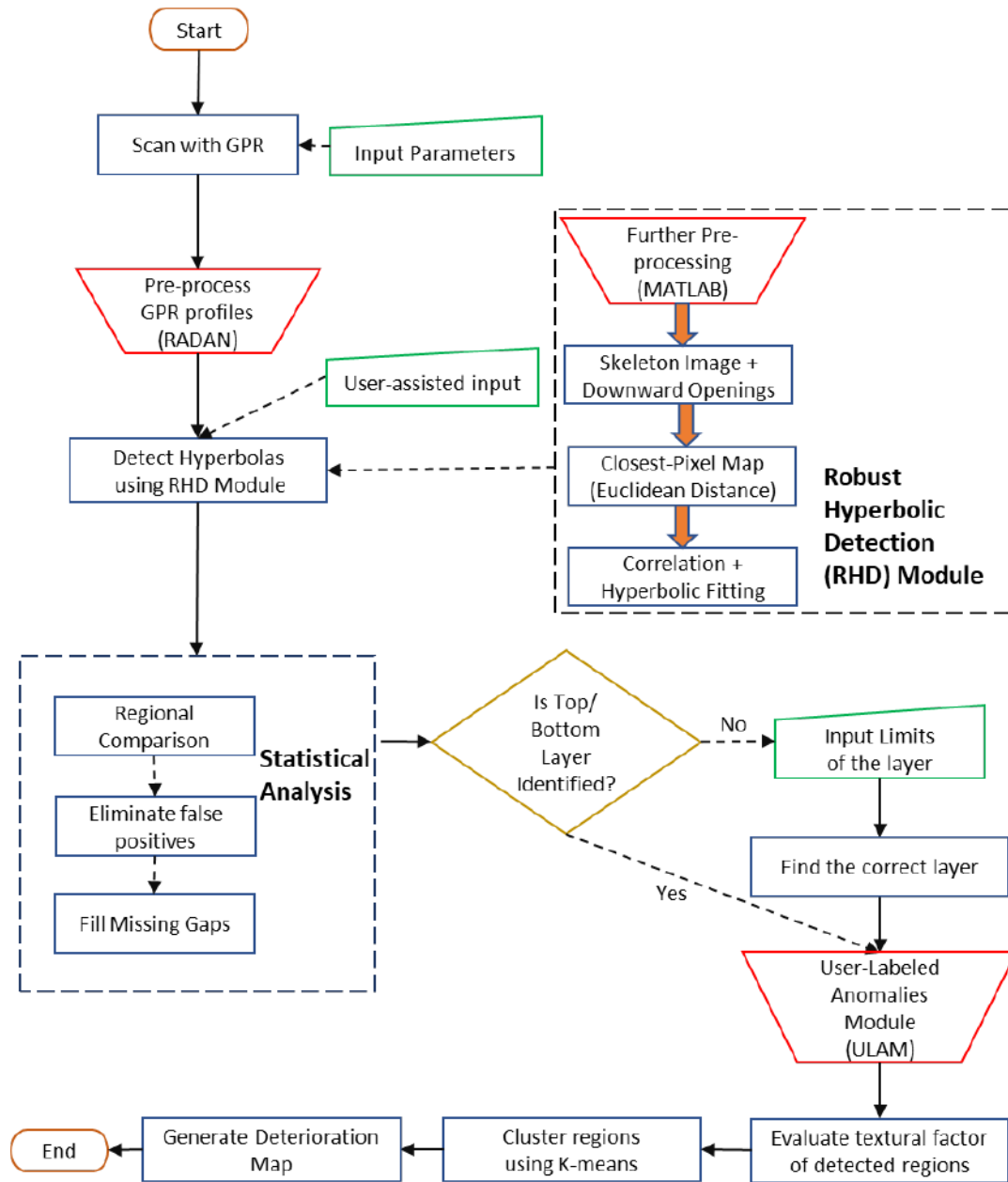
- a) Horizontally stretching or stacking of all GPR profiles, *if necessary*, to reasonably separate the hyperbolic legs - ensuring they are not too close to each other or too far apart. However, maintaining a specific aspect ratio (1:168) like in the case of V-JAM for this model input is not required.
- b) Adjusting the "range gain", *if needed*, to enhance the contrast of the obtained GPR scans. This adjustment is useful in scenarios involving horizontal stretching or when the original contrast is inherently low. The range gain improvement is easily adjustable by a GPR analyst and consumes minimal time (typically seconds or a few minutes), but significantly enhances the detection rates of hyperbolic regions.



- c) The final pre-processing step is the automatic removal of the background signals during a full-pass scan. It typically reduces the stronger surface reflections, such as those at the asphalt/concrete and/or concrete/air interface, from the GPR profiles. It is *necessary* because the hyperbolic reflections (objects of interest) beneath the surface reflections typically have lower intensities. By applying this step, the reflections from hidden objects, such as rebars, are highlighted, resulting in higher intensities.

In the next stage, the GPR profiles are converted into image formats such as .png, .jpeg, .tiff, etc., and imported into the MATLAB® environment for further processing. This model prompts the user to select the folder containing all the GPR profile images of the inspected element. Therefore, it is crucial to store all the GPR profile images in a dedicated folder without any other images or files present. The files should be named in ascending order based on the scanning sequence. If the total number of files is in two digits (10s) or more, a zero (0) should be prefixed to the numeric filenames. Here are some examples of file naming conventions:

- i. 01, 02, 03, ..., n (assuming 'n' is the total number of GPR profiles)
- ii. A, B, C, ..., P (where P = n)
- iii. File001, File002, File003, ..., File0'n'



**Figure 3.15** Flowchart of the RUIIM

The RUIIM method offers a key advantage by being a user-interactive approach, aiming to generate reliable condition maps by seeking input from the GPR analyst regarding the element being inspected. It emphasizes gathering as much information as possible to enhance the accuracy and

effectiveness of the analysis. This model assumes that the scanning direction is primarily longitudinal. If scanning was also performed in the transverse direction, the files pertaining to the transverse scans must be stored in a separate folder to generate condition maps specific to that direction. After selecting the designated folder, the GPR analyst is prompted to enter the following information:

- 1) Length of the scanned element? : \_\_ m.
- 2) Traverse spacing? : \_\_ m.
- 3) Age of the element? : \_\_ years/ Unknown.
- 4) Any visual signs of (moderate/severe) corrosion in profiles? : Yes/No/Not sure
- 5) Any visual signs of *severe* corrosion in profiles? : Yes/No/Not sure
- 6) The number of zones for condition mapping? : Three/Four (default is *three*)
- 7) The layer of analysis? : Top/ Bottom (default is *top*, if not specified)

Questions 1-2 are *compulsory* (length & traverse spacing) for the user to input as it assists in scaling the condition map to be generated. Questions 3-5 are *optional but highly recommended* to input for determining the *optimal number of clusters* for the condition map based on this user information and methodology delineated in (Kien Dinh et al., 2015). The selection of this optimal cluster value is discussed in detail in Section 3.3.5. The GPR analyst (user) is asked to rapidly inspect GPR profiles visually, *if possible*, and to answer these questions based on his/her experience, i.e., if the user sees (any) signs of moderate or severe corrosion in the profiles (Question 4); and if the user sees signs of severe corrosion specifically (Question 5). Questions 6-7 are *optional* as these have *default* values that the model recommends i.e., a) three (color) zones as this number is typically used in practice; and b) as mentioned previously in Section 3.2.3, the top layer is typically

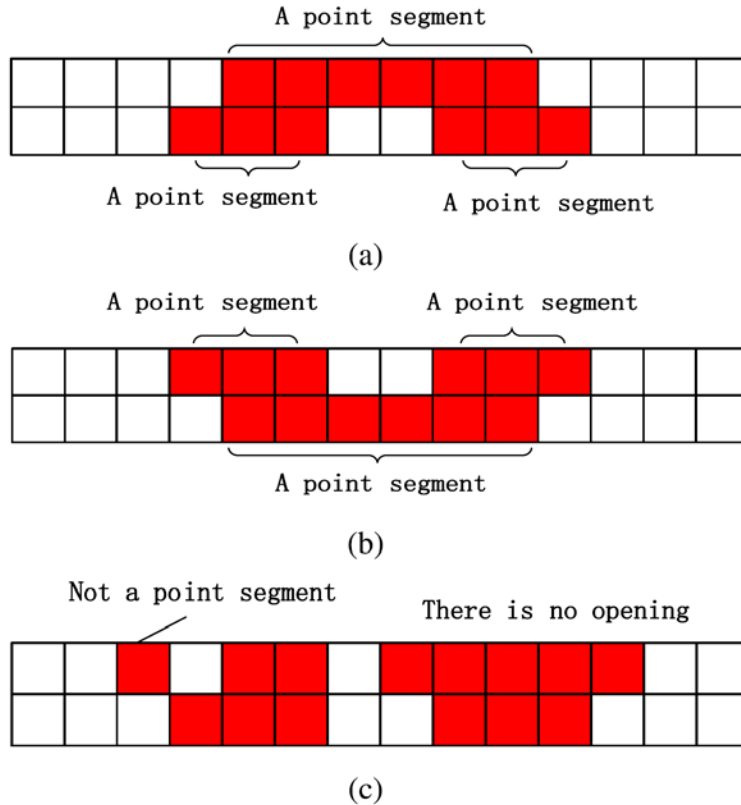
prioritized for profile analysis, as corrosion processes commonly initiate from the top surface. Moreover, the upper layer tends to exhibit better reflections in comparison, owing to lower signal loss. Consequently, the detection of hyperbolic regions becomes relatively easier for the model when focusing on the upper layer.

### **3.3.2 Robust Open-Scan Clustering Algorithm (OSCA) (Zhou et al., 2018)**

The recent methods for hyperbola detections are majorly based on applying Machine Learning (ML) and deep-learning algorithms (Table 2.7) and have generated results with a higher degree of accuracy on real-time GPR data including the developed V-JAM method in this report. However, the reliance on training datasets is a limiting factor for these methods, especially considering the lack of an open-source representative GPR library encompassing multiple images from various real environments (Martoni et al., 2022). Algorithms based on training datasets often yield better results when the GPR element being inspected is similar in type and environment to the training dataset used for detections. To achieve robust detections of hyperbolic regions in GPR profiles without relying on training data, a method called the open-scan clustering algorithm (OSCA) has been proposed by (Zhou et al., 2018). OSCA detects hyperbolas based on identifying *downward openings (DOs)* in GPR images. In this proposed robust model, the methodology for hyperbola detections is also based on identifying DOs. However, it employs a different approach for faster and more efficient detections. Firstly, a brief background on the OSCA algorithm is delineated along with relevant explanations of utilized terms.

A GPR profile is first pre-processed before applying OSCA that includes the following steps: a) filter image noise based on the standard median filter (Olhoeft, 2000); b) a non-linear time-varying gain applied to the GPR signal (Strange et al., 2002); and finally c) a thresholding algorithm based on gradient information to convert it into a binary image (Zhou et al., 2018). The OSCA algorithm

is applied to the resulting binary thresholded GPR image. Before explaining the algorithm in detail, it is essential to define a few concepts that are relevant to the process.



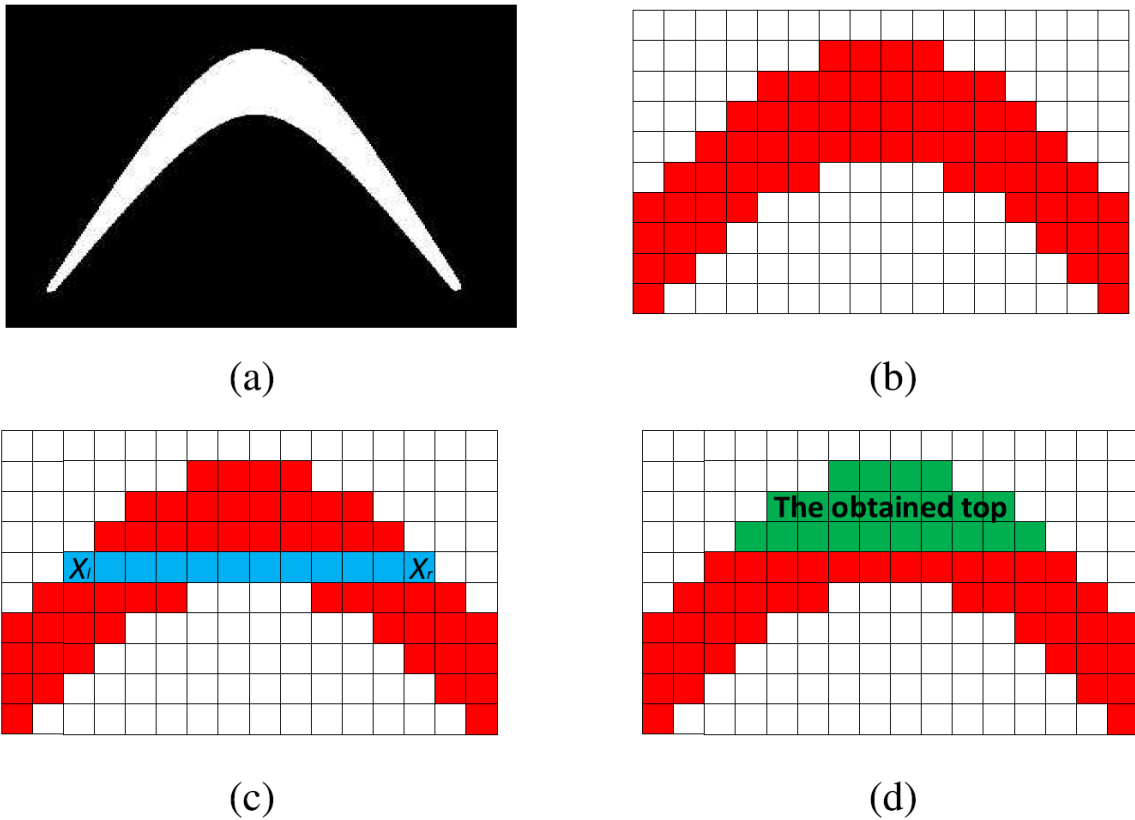
**Figure 3.16** (a) Three-point segments with a downward opening; (b) Three-point segments with an upward opening; and (c) Two examples that can't be defined as openings (Zhou et al., 2018)

*Point Segment:* A set of three or more consecutive pixels (white) in a row in the binary image.

*Downward opening (DO):* A set of three connected point segments such that one of its point segments on top has horizontal overlap with the other two on the bottom with a gap in between those two.

*Upward opening:* A set of three connected point segments such that one of its point segments on the bottom has horizontal overlap with the other two on top with a gap in between those two.

Figure 3.16 shows examples of point segments with downward/upward openings.



**Figure 3.17** (a) A hyperbolic feature in binary form; (b) pixels of the hyperbola with a downward opening; (c) the main top point-segment of the opening  $X_l$  to  $X_r$  and (d) the obtained *top* in green along with *tails* in red (Zhou et al., 2018)

The OSCA algorithm initially scans for all such downward and upward openings in the binary image of a given GPR profile. Subsequently, hyperbolic point clusters from the DO are found if they satisfy the following conditions:

- i) the connected points segments above the top point segment of DO are found to have narrower point segments with lengths less than or equal to the point segment below - this set forms the *top* of the hyperbola.

- ii) the bottom part of the hyperbola called *tails* can be found by finding overlapping points segments below the two bottom point segments of a DO along the left and right sides as shown in *Figure 3.17*.

The upward openings are typically intersections of two hyperbolas and this algorithm identifies and separates them. Eventually, OSCA identifies all such hyperbolic signatures in an image, and further steps which include the parabolic fitting-based judgment (PFJ) method, and restricted algebraic-distance-based fitting (RADF) are performed to confirm the presence of rebars/ anomalies in a GPR profile. The algorithm was further modified by (Lei et al., 2019) to include some different variants of hyperbolic signatures and exclude some anomalies unidentified by OSCA. The main advantage of this algorithm is that identifies hyperbolas based on their fundamental characteristics in a GPR profile *i.e., point-based clusters containing downward openings*. This algorithm does have the following factors which could affect the detection rate: a) OSCA identifies DOs in a binary image (BI) rather than the raw image and thus, its results depend heavily on this threshold (numeric) factor which may not be always optimal for each set of GPR data leading to false or missing detections; and b) While it is true that all hyperbolic regions have DOs, the vice versa is not true. Since OSCA identifies all DOs (the parabolic feature is judged later and eliminated using PFJ), it could pick up many false detections leading to excess processing time, especially in the case of large profiles. Nevertheless, OSCA is a powerful approach in detecting hyperbolic regions especially compared to other ML approaches as it does not depend on any trained data. Therefore, an alternative approach has been proposed in this model which identifies *parabolic DOs with improved processing times and accurate number of detections*.

### ***3.3.3 Robust Hyperbolic Detections***

The complete methodology for robust hyperbolic detections (RHDs) adopted in RUIM is explained based on the steps delineated in Figure 3.15.

#### *Preprocessing in MATLAB*

The preprocessing steps applied in proprietary software serve to clean GPR data by reducing surface reflections, thereby emphasizing reflections from concealed targets in GPR profiles. However, caution should be exercised when applying the standard background removal technique, particularly in cases where profiles exhibit varying transmission velocities due to huge fluctuations in cover thickness or in the presence of large voids. In such cases, it may be necessary to apply filtering techniques selectively to different sections of a GPR profile (Utsi, 2017). These filtering techniques, often referred to as signal processing, are commonly employed to reduce noise. It can be applied directly to individual A-scans or to B-scans (as these are A-scans stacked along the length of the scan), prior to image processing. While the earlier V-JAM approach exclusively depended on standard background removal, this method incorporates an innovative filtering technique applied to B-scans.

Preprocessing requires an optimal solution because if a GPR profile is heavily preprocessed i.e., if excess noise is removed, it causes missing hyperbolic detections in images while under-preprocessing cause excess noise in images leading to false detections. Some preprocessing algorithms employed in literature for noise removal of GPR profiles include Otsu's threshold (Otsu, 1979), standard mean filter (Olhoeft, 1984), maximum entropy thresholding (Kapur et al., 1985), Canny edge-detection filter (Canny, 1986), unimodal thresholding (Rosin, 2001), gaussian filter (Singh & Nene, 2013), median subtraction (Sagnard & Tarel, 2016), adaptive threshold based on gradient information (Zhou et al., 2018), among others. While these methods have shown promising results



on real-case GPR profiles, there is a need to develop an approach that reduces *optimal noise in varying GPR data sets with differing intensities and input parameters*. The developed preprocessing approach reduces significant noise without compromising reflections from hidden objects in GPR profiles of varying datasets. Since background removal significantly reduces horizontal noise of surface reflections, preprocessing in MATLAB involves the following three steps which are explained in brief subsequently: a) amplifying higher intensity values as these are indicative of hidden objects (hyperbolic detections in reinforced members) majorly and anomalies, if present; and b) reducing noise by adaptive threshold subtraction; and c) image binarization with Otsu's multi-threshold to eliminate noise associated with low-intensity pixels and lastly, applying morphological operations.

Firstly, a MATLAB function which brightens low-light areas in a RGB or greyscale image has been adopted to improve higher-intensity pixels in a GPR image to enhance the contrast of hyperbolic detections. The algorithms associated with this function are part of image dehazing approaches and their detailed explanation along with their application is shown in (Dong et al., 2011) and (Park et al., 2014). A single haze removal technique is employed and the primary equation to recover a dehazed image, let's say,  $\mathbf{J}$ , is written as:

$$\mathbf{J}(\mathbf{x}) = \frac{\mathbf{I}(\mathbf{x}) - \mathbf{A}}{r(\mathbf{x})} + \mathbf{A} \quad (3.10)$$

$\mathbf{I}$  - original intensity;  $\mathbf{x}$  - spatial location in the image;  $\mathbf{A}$  - atmospheric light;  $r$  - medium transmission describing the portion of the light that is not scattered.

The method uses a per-pixel dark channel to estimate haze i.e., transmission  $r$  and quadtree composition to estimate the atmospheric light,  $\mathbf{A}$  based on equations proposed in (Dong et al., 2011).

Since the primary function of the MATLAB function being applied, ‘*imlocalbrighten*’ is to increase low-pixel intensities in an image, a GPR profile is first inverted i.e., each pixel value is subtracted from the maximum pixel value supported by the class such that the dark areas become lighter and light areas become darker. The complement of the image (i.e., inverted image) is then processed with the aforesaid function and the image is re-inverted to obtain *an output image that distinguishes brighter areas while keeping areas with lower intensities, typically noise, relatively unchanged*. If H is an image imported into MATLAB, the output image, I, can be obtained using the following code in MATLAB:

$$\begin{aligned}
 Hc &= imcomplement(H); \\
 I &= imlocalbrighten(Hc); \\
 I &= imcomplement(I)
 \end{aligned}
 \tag{3.11}$$

After brightening areas with higher intensities, the next step of preprocessing is to evaluate the noise present in an image. It is achieved based on Bradley’s method which computes an adaptive threshold at each pixel using local mean intensity (Bradley & Roth, 2007). In this algorithm, an *integral image*, wherein every pixel is the summation of the pixels above and to its left, is initially computed as follows represented by  $I(x,y)$  at each pixel.

$$I(x, y) = f(x, y) + I(x - 1, y) + I(x, y - 1) - I(x - 1, y - 1)
 \tag{3.12}$$

Wherein,  $f(x,y)$  - original intensity at each pixel location  $(x,y)$ .

Subsequently, an adaptive threshold value at each pixel location is evaluated by taking an average of an  $s \times s$  window of pixels on all sides over the integral image, wherein  $s$  is given by:

$$s = 2 * floor\left(\frac{size(I)}{16}\right) + 1
 \tag{3.13}$$

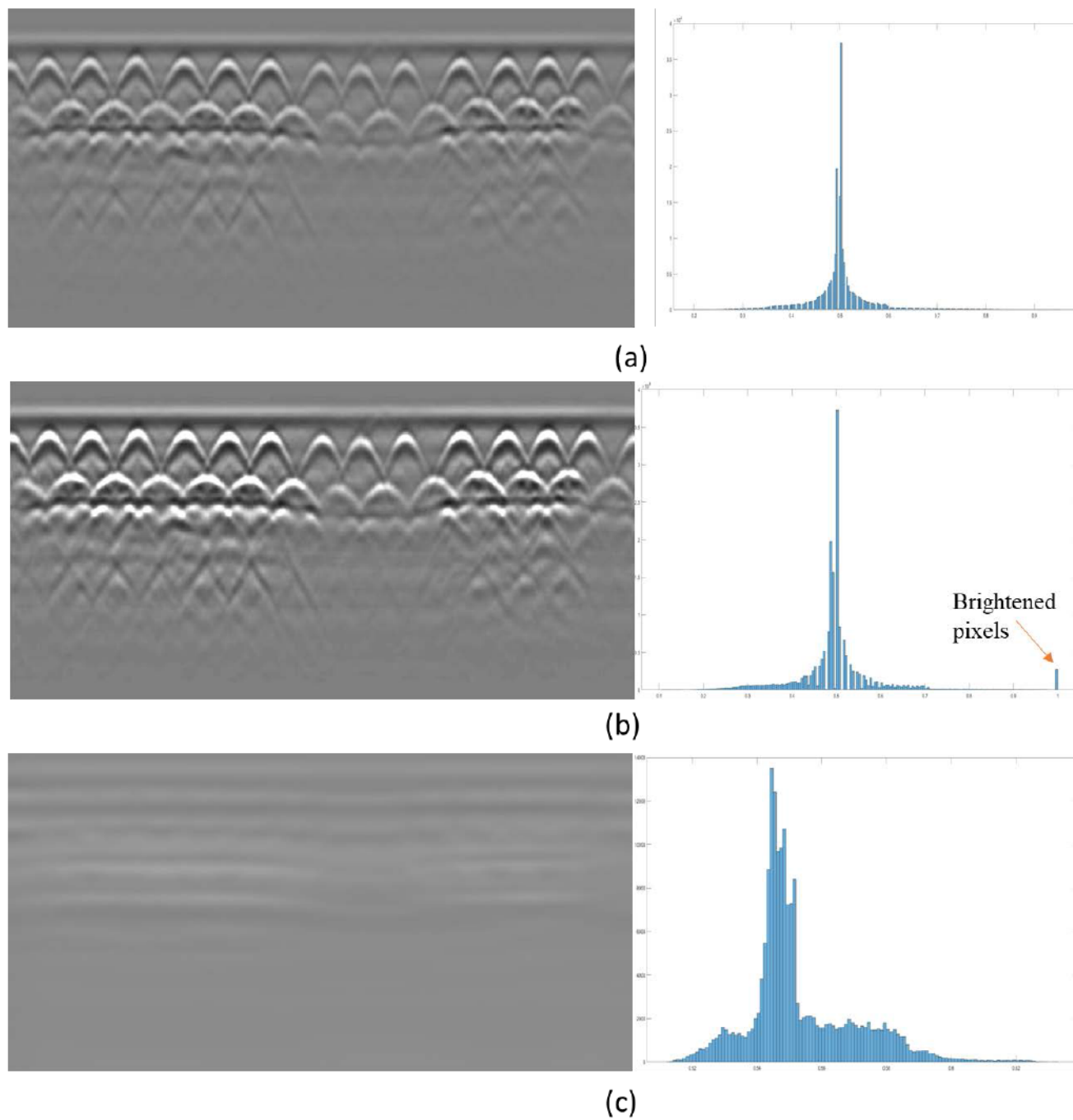
The pseudocode to evaluate adaptive threshold is given in (Bradley & Roth, 2007). MATLAB evaluates these two steps using a single function as follows, let  $\mathbf{I}$  be the preprocessed image after local brightening, then  $I_{at}$  represents the output image with the adaptive threshold at each pixel location:

$$I_{at} = \text{adaptthresh}(I); \quad (3.14)$$

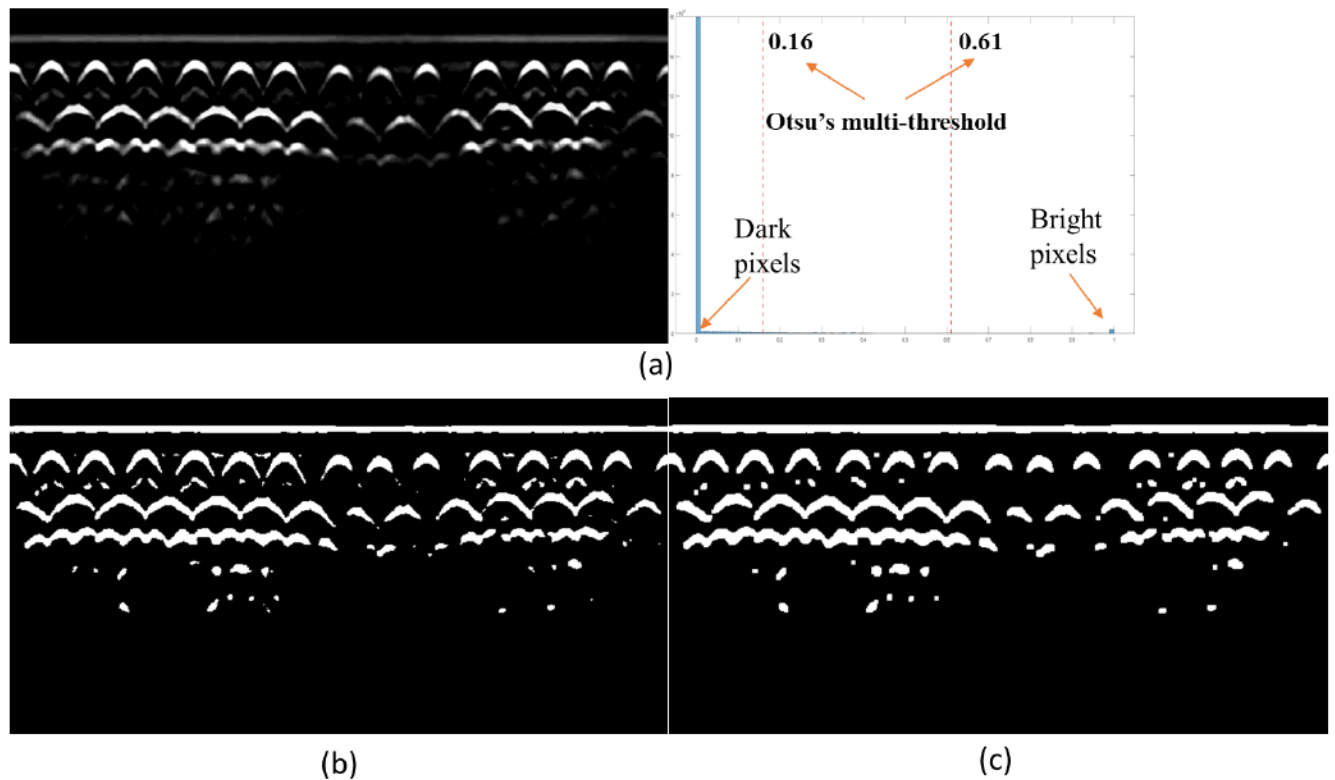
The output image,  $I_{at}$ , represents major noise in a GPR image and is eventually subtracted from the original image ( $\mathbf{I}$ ) while improving its contrast utilizing the *imadjust* function (described in Section 3.1.1) to compute a cleaner image such that the majority of the noise is removed. The command in MATLAB is written as:

$$I = \text{imadjust}(I - I_{at}); \quad (3.15)$$

To illustrate the application of the preprocessing steps, consider a sample GPR profile, labeled ‘ $H$ ’ after it has been imported into MATLAB as shown in Figure 3.18(a) along with the image’s histogram aside. The image type has been converted to double precision i.e., the values of dark to white pixels range from 0 (black) to 1 (white). The majority of the pixels are spread in the middle region as shown in the histogram. After applying the algorithms based on brightening higher pixel values, the resulting image is shown in Figure 3.18(b). The hyperbolic regions are visibly brightened in the image with the highest pixel value, i.e., white (1), and this is also reflected in the image histogram shown aside. Figure 3.18 (c) shows the image containing adapted threshold values applied over the integral image of (b). Image (c) is also representative of the noise of image (a) with its histogram shown aside. Figure 3.19(a) shows the output image after subtracting the images shown in Figure 3.18(b) from Figure 3.18(c). Importantly, the resulting figure has a majority of noise eliminated as it shows the *hyperbolic detections clearly*.



**Figure 3.18** (a) *H* - GPR profile sample imported into MATLAB with its histogram (Mohammed Abdul Rahman et al., 2016); (b) Profile after brightening of lighter pixels with its histogram; (c) Profile showing noise of image (a) with its histogram



**Figure 3.19** (a) Profile after removing noise with histogram; (b) Profile image binarized after Otsu's multi-threshold; and (c)  $BW_p$  - Final preprocessed image after morphological operations

The next step after eliminating a majority of the noise is to *binarize* the preprocessed image as a precursor to robust detections. This is accomplished by applying a multi-thresholding algorithm based on Otsu's algorithm (Otsu, 1979). The reason for choosing this approach can be understood by analyzing the histogram of the resulting image in Figure 3.19(a) shown aside. It shows that the majority of the pixels in the image either have *dark pixels* (0) or *white pixels* (1) while the remaining few pixels lie in between. This disparity of majorly dark and light pixel peaks on either end indicates good image segmentation and that the image can be binarized by selecting an optimal threshold anywhere between 0 and 1. In the process of binarizing the image, Otsu's multi-threshold technique is employed, which divides the image into three distinct regions. The lower threshold,

positioned closer to the darker region, is selected for binarization. This choice is made to preserve certain remaining noise in the image, as it can be crucial for GPR images where the noise may represent false negative regions. Simultaneously, the method eliminates very low-pixel dark regions. Given that the majority of the noise has already been eliminated, the adoption of this multi-threshold approach ensures the retention of the maximum number of remaining lighter pixels, enhancing the accuracy and effectiveness of subsequent processing steps.

Otsu's is a widely popular algorithm that evaluates a threshold such that the weighted variance between the foreground and background pixels is kept minimum. Section 2.16.2 delineates the procedure to evaluate a single optimal threshold,  $k^*$ , (Equation 2.13), based on Otsu's algorithm, and it could be extended to find multi-thresholds as explained in (Otsu, 1979). If  $k_1$  and  $k_2$  are two thresholds [ $1 < k_1 < k_2 < L$ ];  $L$ - total number of intensity levels an image (=1 for double type gray-scale image), then these thresholds separate the range into three classes,  $[1, \dots, k_1]$ ,  $[k_1, \dots, k_2]$ , and  $[k_2, \dots, 1]$ . The between-class variance,  $\sigma_B^2$ , becomes a function of two variables,  $k_1$  and  $k_2$ , and the optimal set of thresholds,  $k_1^*$  and  $k_2^*$ , are selected by maximizing  $\sigma_B^2$  using Equation 3.16.

$$\sigma_B^2(k_1^*, k_2^*) = \max_{1 \leq k_1 \leq k_2 \leq L} \sigma_B^2(k_1, k_2) \quad (3.16)$$

This algorithm was applied to find these two thresholds  $\{0.16, 0.61\}$  for the sample GPR image in Figure 3.19(a) as highlighted in its histogram. Subsequently, the image was binarized, as shown in Figure 3.19(b), by assigning all pixels below this lower threshold value (0.16) as black (0) while assigning all pixels above this value as white (1).

Lastly, a morphological *opening* is performed on the binarized image using a structural element through combined operations of image *erosion followed by dilation*. A structural element is a basic

neighborhood structure represented typically by a small matrix, whose shape and size, impact the morphological operation being performed on an image (Marques, 2011). Erosion is a morphological operation that “shrinks” or “thins” objects in a binary image, and it is used to *eliminate tiny clutter noises* in a GPR image. Erosion of a GPR image, A, by a structural element, B, is defined mathematically in set form using Equation 3.17 (Gonzalez et al., 2010).

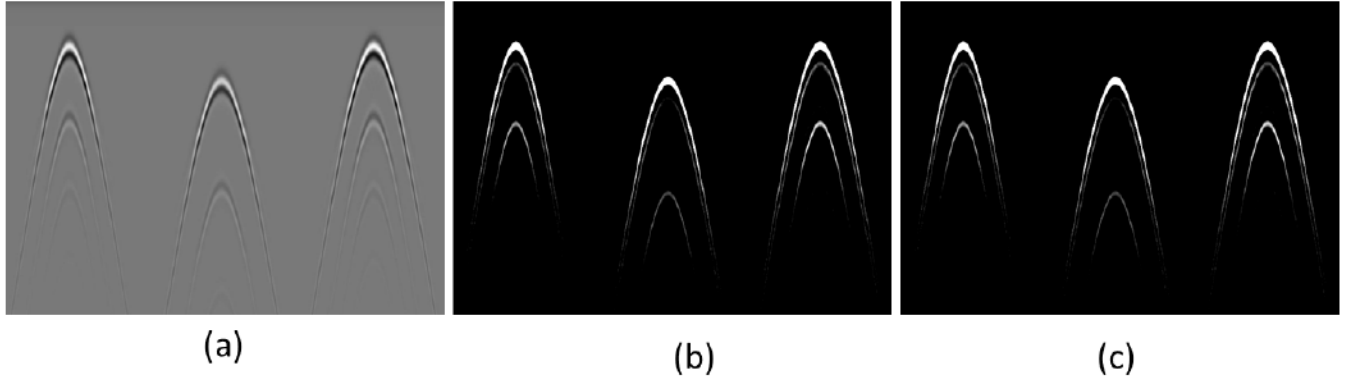
$$A \ominus B = \{ z | (\hat{B})_z \cup A^c \neq \emptyset ; \emptyset \text{ is an empty set} \} \quad (3.17)$$

Dilation operation causes objects in an image to “grow” or “thicken” and it is applied on a binarized GPR image to thicken the objects contained within it for *slight magnification* of possible hyperbolic curves, which is useful for their detection. Dilation of a GPR image, A, by a structural element, B, is defined mathematically in set form using Equation 3.18 (Gonzalez et al., 2010). Figure 3.19(c), labeled  $BW_p$ , shows the *final preprocessed image* after applying morphological opening using a structural element matrix of *ones(3)* on the image shown in Figure 3.17(b).

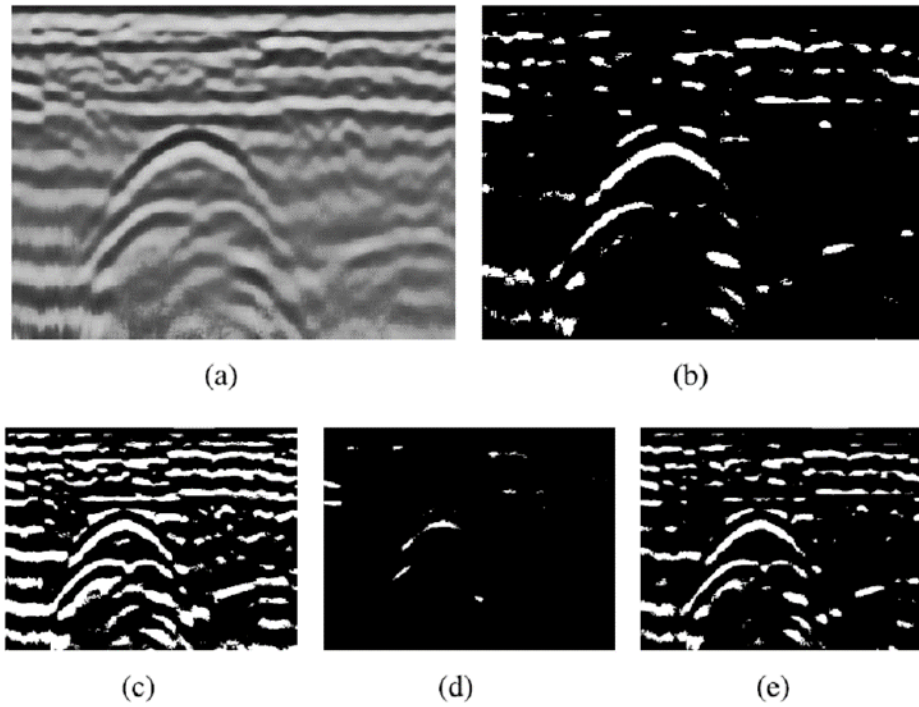
$$A \oplus B = \{ z | (\hat{B})_z \cap A \neq \emptyset ; \emptyset \text{ is an empty set} \} \quad (3.18)$$

Figure 3.20 shows a GPR image sample taken from (Zhou et al., 2018) along with the preprocessing results which demonstrate the removal of noise using the applied methodology and clear identification of hyperbolic curves. Figure 3.21 shows a GPR also taken (Zhou et al., 2018) along with the results obtained using different thresholding algorithms. Figure 3.22 shows the results obtained using the developed model. Although the hyperbolic curves in the preprocessed images are present with significant clarity, there is some noise horizontal noise present in this image as *background removal* was not performed on this profile. Therefore, it is essential to remove surface reflections based on background subtraction before applying the proposed preprocessing steps in MATLAB. Figure 3.23 is an additional GPR image from (Zhou et al., 2018) and the preprocessed

image obtained from the proposed model was able to eliminate significant noise while retaining all the hyperbolic curves present within the GPR profile.

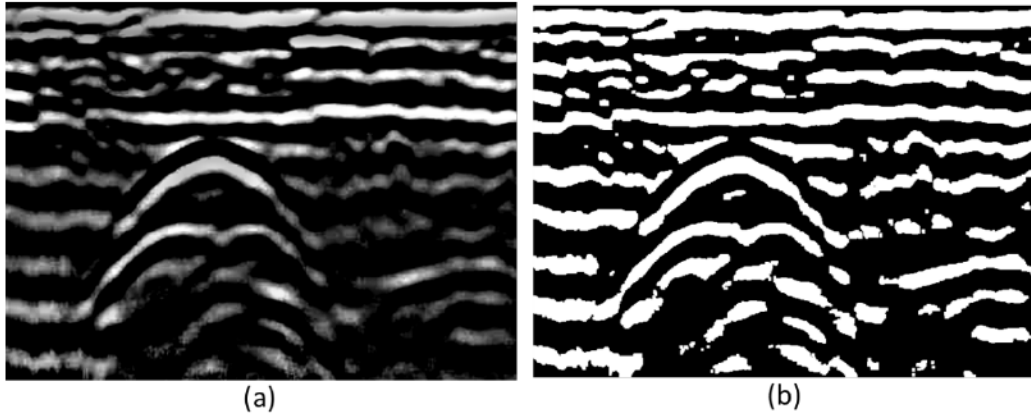


**Figure 3.20** (a) GPR Image (Zhou et al., 2018); (b) Image preprocessed after noise removal; (c) Preprocessed binarized image

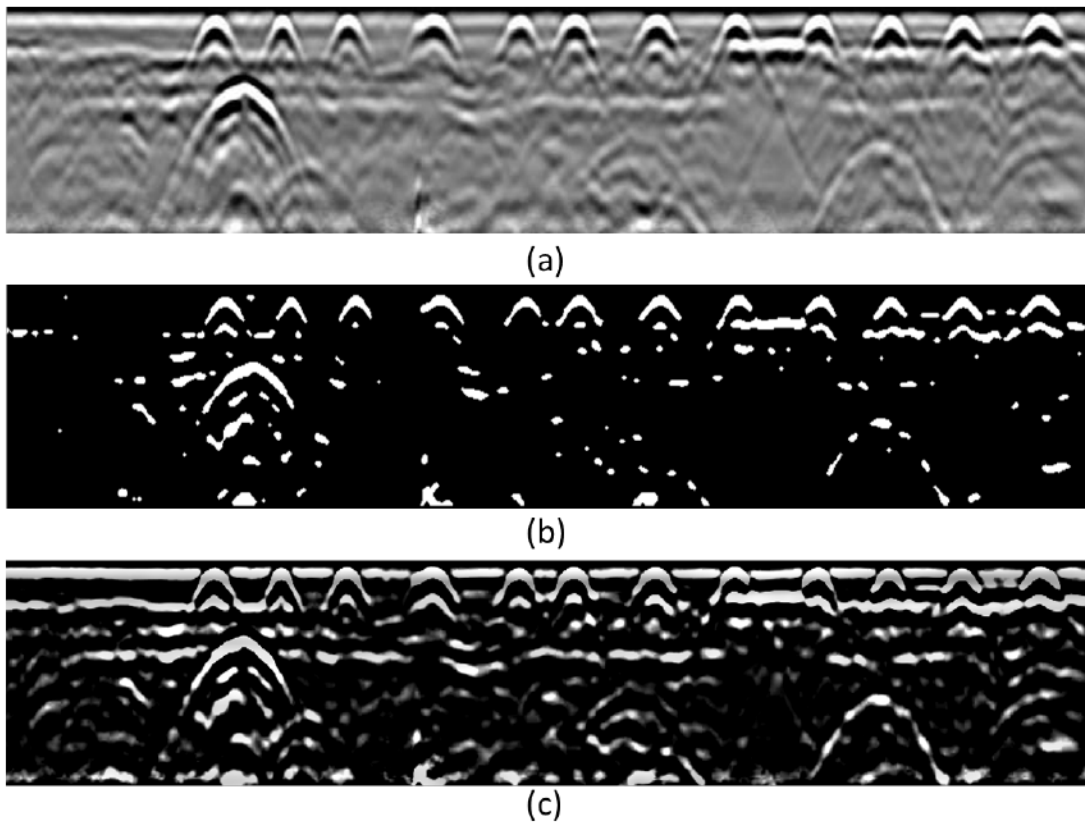


**Figure 3.21** (a) GPR Image (Zhou et al., 2018), (b) Image thresholded based on gradient information (Zhou et al., 2018), (c) Image thresholded based on (Otsu, 1979), (d) Image thresholded based on maximum entropy (Kapur et al., 1985); (e) Unimodal thresholding (Rosin, 2001)





**Figure 3.22** (a) Image preprocessed after noise removal; (b) Final preprocessed image



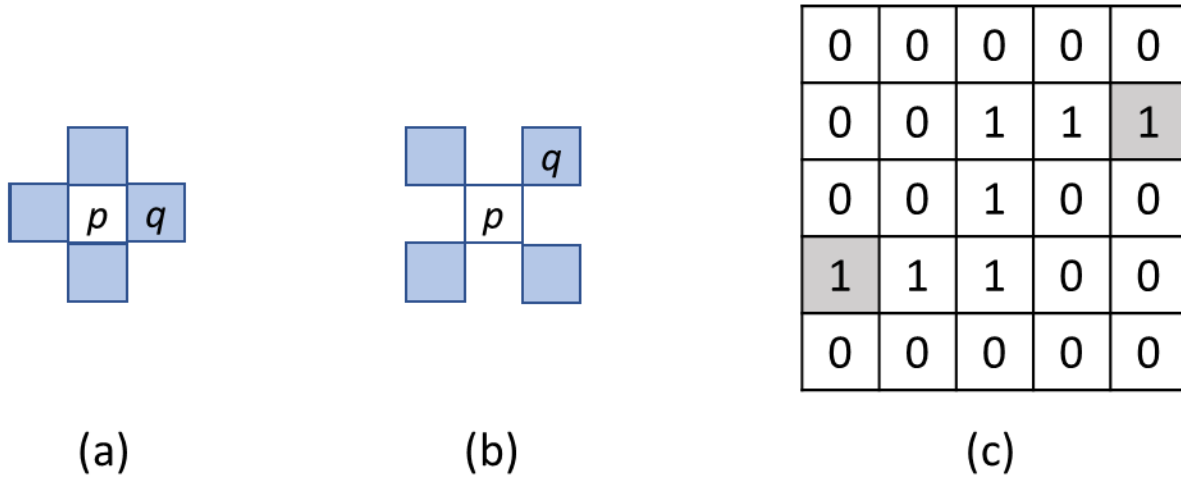
**Figure 3.23** (a) GPR image (Zhou et al., 2018); (b) Image thresholded based on gradient information (Zhou et al., 2018), (c) Image preprocessed (noise removal) based on the proposed model

### *Hyperbola Detections*

After binarizing the image based on a robust preprocessing approach applicable to GPR profiles, the next step is to identify downward openings (DOs). While the original OSCA (Zhou et al., 2018) algorithm identifies these DOs on the preprocessed binary image, the proposed method adopts a different approach for faster and more efficient detections as follows: a) firstly, boundary pixels are identified for the binary image; b) an exhaustive downward openings search for DOs (which could include false positives); and c) eliminating incorrect detections based on hyperbolic characteristics by applying *constraints* or limitations. Essentially, the hyperbolas are identified utilizing a *constraint satisfaction sequencing problem-solving* strategy. Initially, hyperbolic curvatures are found based on a single constraint (DOs), and then true detections are narrowed down sequentially by incorporating additional hyperbolic characteristics (constraints). The sequential steps of this methodology, along with its application on a sample GPR profile, has been delineated to demonstrate the process and highlight how the constraints are used to refine and validate the hyperbolic detections.

*Boundary pixels:* Initially, a morphological operation is applied to identify boundary pixels of the binarized image with the purpose of image size reduction and faster, exhaustive search. A binary image contains either foreground pixels (1, white) or background pixels(0, black). The concept of *connected components* or objects is first introduced to find the boundary pixels. A pixel  $p$  with coordinates  $(x,y)$ , in a binary image, has two horizontal and two vertical neighbors with coordinates  $(x + 1, y)$ ,  $(x - 1, y)$ ,  $(x, y + 1)$ , and  $(x, y - 1)$  as shown in Figure 3.24(a) with shaded blue boxes, denoted as  $N_4(p)$ . Two pixels,  $p$  and  $q$ , are said to be *4-adjacent* if  $q$  lies on either of these neighbors i.e.,  $q \in N_4(p)$ . Figure 3.24(a) also shows a pixel  $q$  that is 4-adjacent to  $p$ . The pixel  $p$  has four *diagonal* neighbors with coordinates  $(x+1,y+1)$ ,  $(x+1,y-1)$ ,  $(x-1,y+1)$ , and  $(x-1, y-1)$  as shown in

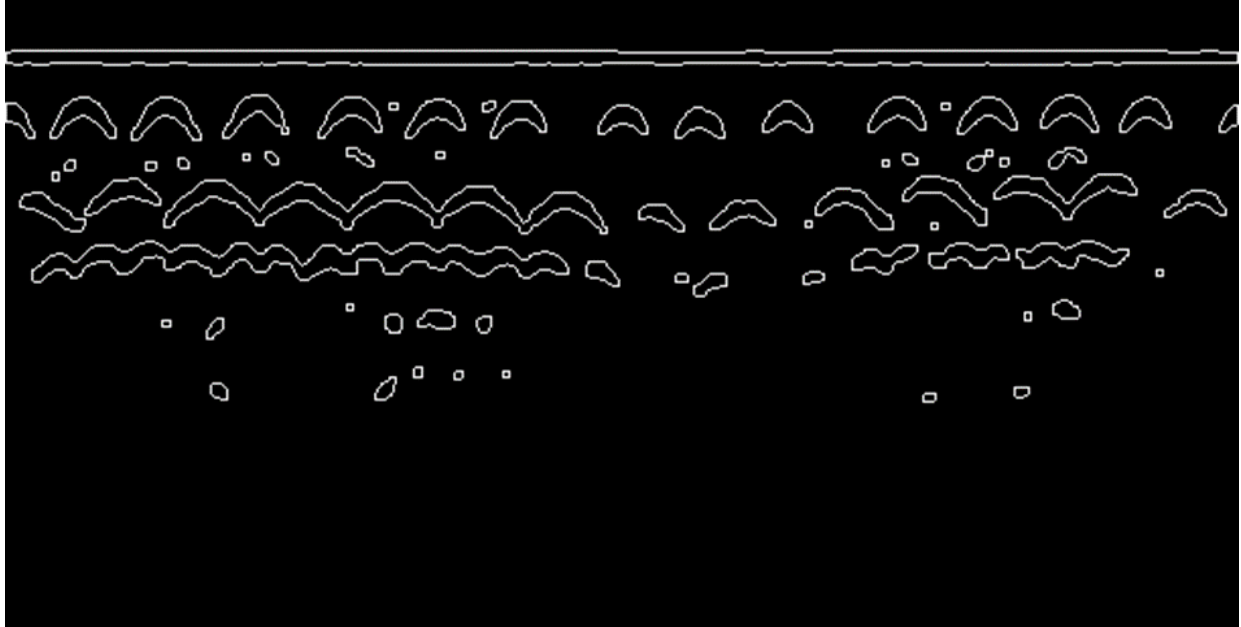
Figure 3.24(b) with its top-right diagonal neighbor ‘q’. Corollary, two pixels,  $p$ , and  $q$  are said to be *4-connected* if there exists a 4-connected path consisting of all foreground pixels between them (Gonzalez et al., 2010). Figure 3.24(c) shows two pixels, shaded in grey, are 4-connected wherein the first is located at (4,1) while the other is located at (2,5).



**Figure 3.24** (a) pixel  $p$  with its 4 adjacent neighbors,  $p$  & pixel  $q$  are *4-adjacent*; (b) pixel  $p$  with its 4 diagonal neighbors including  $q$ ; (c) Grey-shaded foreground pixels are 4-connected (Gonzalez et al., 2010)

The boundary pixels have at least one background pixel as zero in its 4-adjacent neighbors. Therefore, the boundary pixels are identified in a binary image containing objects as follows: *foreground pixels with all its 4-adjacent pixels as unity are set to 0 as these are interior pixels while all other remaining pixels are not eliminated as these are all boundary pixels*. Figure 3.25, denoted as  $BW_b$ , displays the boundary pixels that have been identified on the preprocessed final image,  $BW_p$ , (Figure 3.19(c)), for the sample GPR profile,  $H$  (Figure 3.18(a)). The boundary pixels in the  $BW_b$  image trace the outer and inner boundaries of the hyperbolas. The objective is to identify *inner boundaries as these are DOs and could be potential hyperbolic detections* while the outer boundaries are

not preferred as the hyperbolic arms may not be complete for detections that are closer to each other.



**Figure 3.25**  $BW_b$  -Boundary pixels of a binarized GPR sample

*Inner boundaries:* To identify inner boundaries, the next step is to find valid *point segments*; wherein a point segment, in this method, is either a single unity pixel in a row (or) a set of two or more consecutive (white) pixels in a row. The *constraint* applied to identify required point segments is that only those are detected which have *bottom-left and bottom-right diagonal adjacent neighbors only* as shown in Figure 3.26. Let  $s(i, j:k)$  represent any point segment having width 'k-j+1' and be located at the  $i^{\text{th}}$  row and from the  $j^{\text{th}}$  to the  $k^{\text{th}}$  column. The valid point segments are selected based on these constraints applied over the GPR image with boundary pixels ( $BW_b$ ):

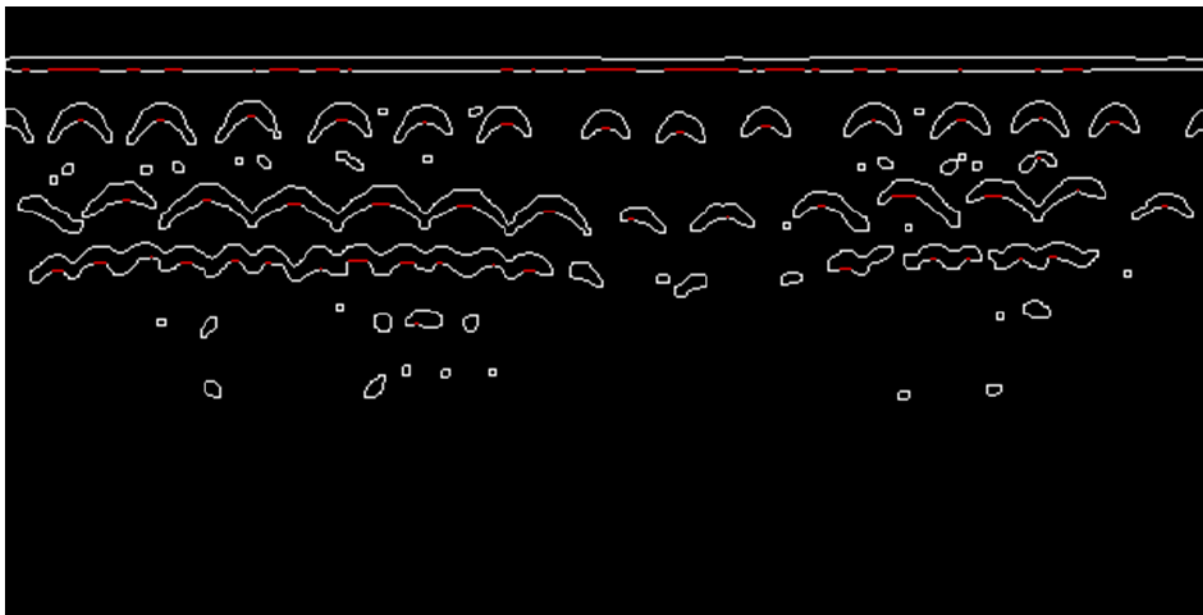
- a) Each pixel on the top row of this point segment is zero:  $\sum (s(i-1, j:k)) = 0$
- b) Each pixel on the bottom row of this point segment is zero:  $\sum (s(i+1, j:k)) = 0$
- c) Top-left diagonal adjacent pixel is zero:  $s(i-1, j-1) = 0$

- d) Top-right diagonal adjacent pixel is zero:  $s(i-1, k+1) = 0$
- e) Bottom-left diagonal adjacent pixel must be one:  $s(i+1, j-1) = 1$
- f) Bottom-right diagonal adjacent pixel must be one:  $s(i+1, k+1) = 1$
- g) The top adjacent pixel of the binarized image ( $BW_p$ ) is zero to identify if it's an inner boundary point segment:  $BW_p(i-1, j) = 0$

			column →	$j^{\text{th}}$		$k^{\text{th}}$		
	0	0	0	0	0	0	0	0
	0	0	0	0	0	0	0	0
$i^{\text{th}}$ row	0	0	0	1	1	1	0	0
	0	0	1	0	0	0	1	0
	0	1	0	0	0	0	0	1
	1	0	0	0	0	0	0	0

Point segment

**Figure 3.26** A valid point segment in the  $i^{\text{th}}$  row.



**Figure 3.27**  $BW_{ps}$  - Image overlaid with valid point segments in red

Figure 3.27, labeled as  $BW_{ps}$ , shows all the valid point segments identified in the  $BW_b$  image of the GPR profile,  $H$ , as overlaid in red color after applying the aforesaid constraints.

Subsequently, the inner boundaries of all the valid point segments are found by tracing valid points on both sides. If  $BW_b(i,j)$  represents the bottom-left adjacent pixel of a point segment  $s$ , the valid points on the left side are found using a *while* loop until the adjacent pixel at either of the location coordinates in the image  $(i+1,j)$ ,  $(i,j-1)$ ,  $(i+1,j-1)$  is unity. The pseudocode is written as follows:

```

while  $BW_b(i+1,j)==1 \parallel BW_b(i,j-1)==1 \parallel BW_b(i+1,j-1)==1$ 
if  $BW_b(i+1,j)=1$ ;  $BW_i(i+1,j)=1$ ;  $i=i+1$ ; end
if  $BW_b(i,j-1)=1$ ;  $BW_i(i,j-1)=1$ ;  $j=j-1$ ; end
if  $BW_b(i+1,j-1)=1$ ;  $BW_i(i+1,j-1)=1$ ;  $i=i+1$ ;  $j=j-1$ ; end
repeat until the 'while' condition is not met
end
where  $BW_i$ : resulting image with inner boundaries traced on the left side. (3.19)

```

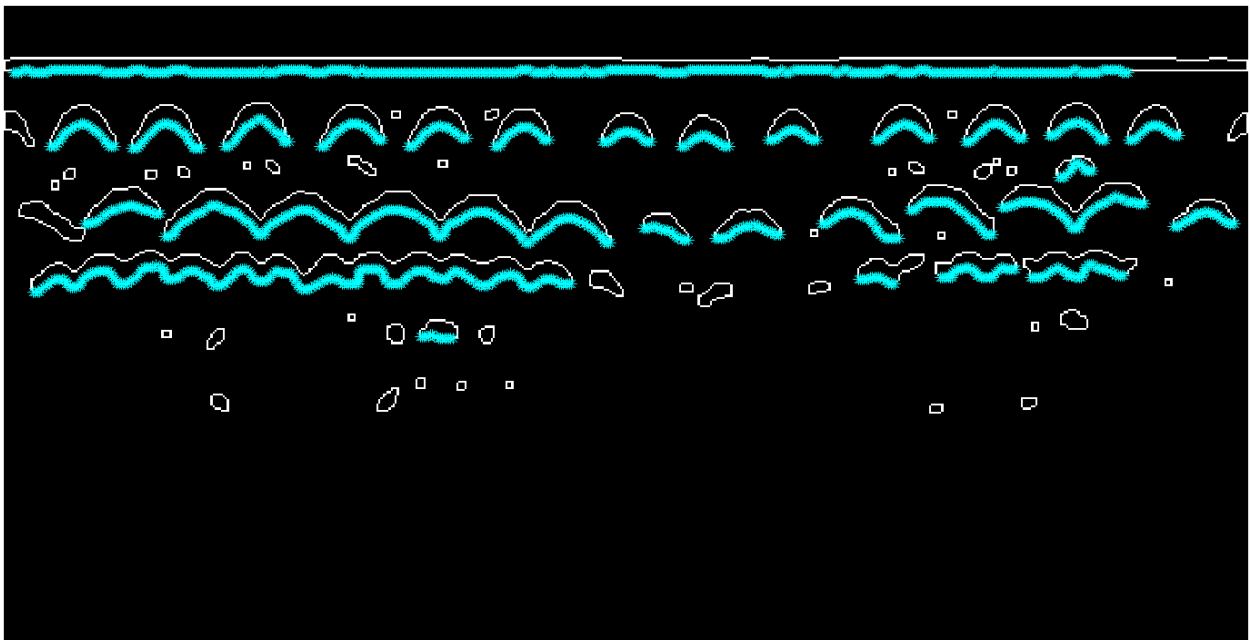
Similarly, if  $BW_b(i,j)$  represents the bottom-right adjacent pixel of a point segment  $s$ , the valid points on the right side are found using a *while* loop until the adjacent pixel at either of the location coordinates in the image  $(i+1,j)$ ,  $(i,j+1)$ ,  $(i+1,j+1)$  is unity. The pseudocode is written as follows:

```

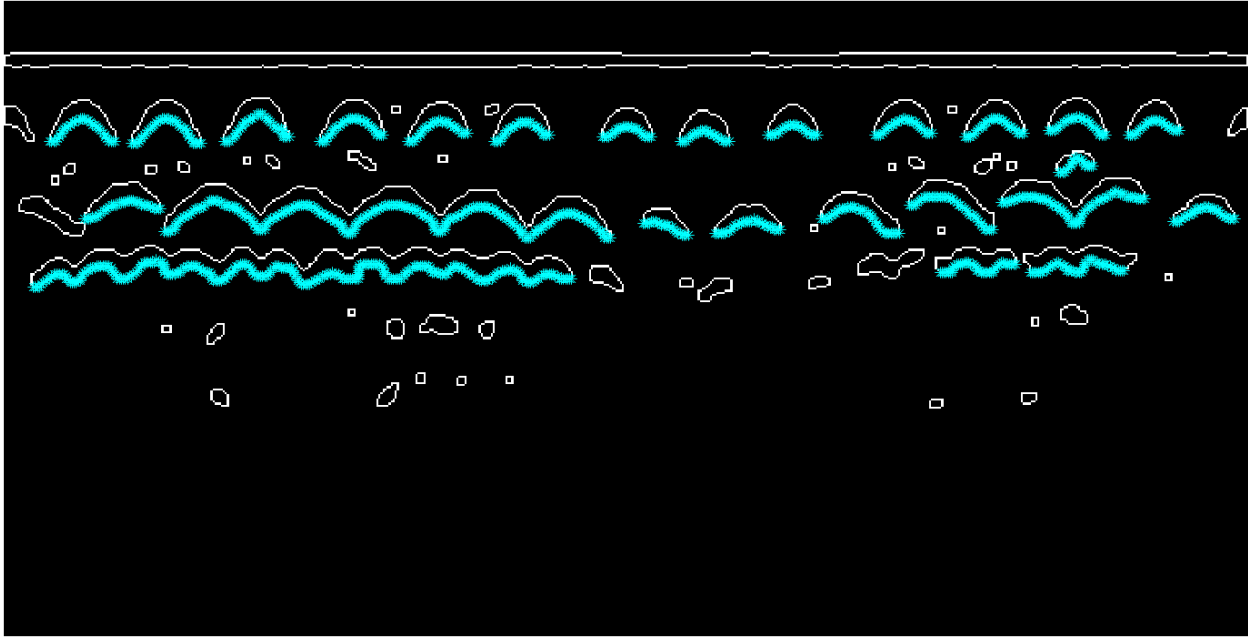
while  $BW_b(i+1,j)==1 \parallel BW_b(i,j+1)==1 \parallel BW_b(i+1,j+1)==1$ 
if  $BW_b(i+1,j)=1$ ;  $BW_i(i+1,j)=1$ ;  $i=i+1$ ; end
if  $BW_b(i,j+1)=1$ ;  $BW_i(i,j+1)=1$ ;  $j=j+1$ ; end
if  $BW_b(i+1,j+1)=1$ ;  $BW_i(i+1,j+1)=1$ ;  $i=i+1$ ;  $j=j+1$ ; end
repeat until the 'while' condition is not met
end
where  $BW_i$ : resulting image with inner boundaries traced on the right side. (3.20)

```

Figure 3.28, labeled as  $BW_i$ , shows all the inner boundaries traced (overlaid in cyan color with asterisk marker) by applying both the pseudocodes *only* upon the valid point segments in the image  $BW_b$  for the profile,  $H$ . However, such a resulting image ( $BW_i$ ) may typically contain inner boundaries of surface reflections and other non-hyperbolic objects. To refine these inner boundaries, the following *constraint* is applied: only those inner boundaries are filtered out which have at least three or more rows with valid points on either side of each point segment of the identified inner boundaries. The number *three* is taken empirically taken from (Mertens et al., 2016) to consider even the smallest of possible hyperbolic detections while eliminating surface reflections. Therefore, this constraint typically removes such surface reflections as can be visualized in Figure 3.29, labeled as  $BW_{ir}$ , after the filtering process.



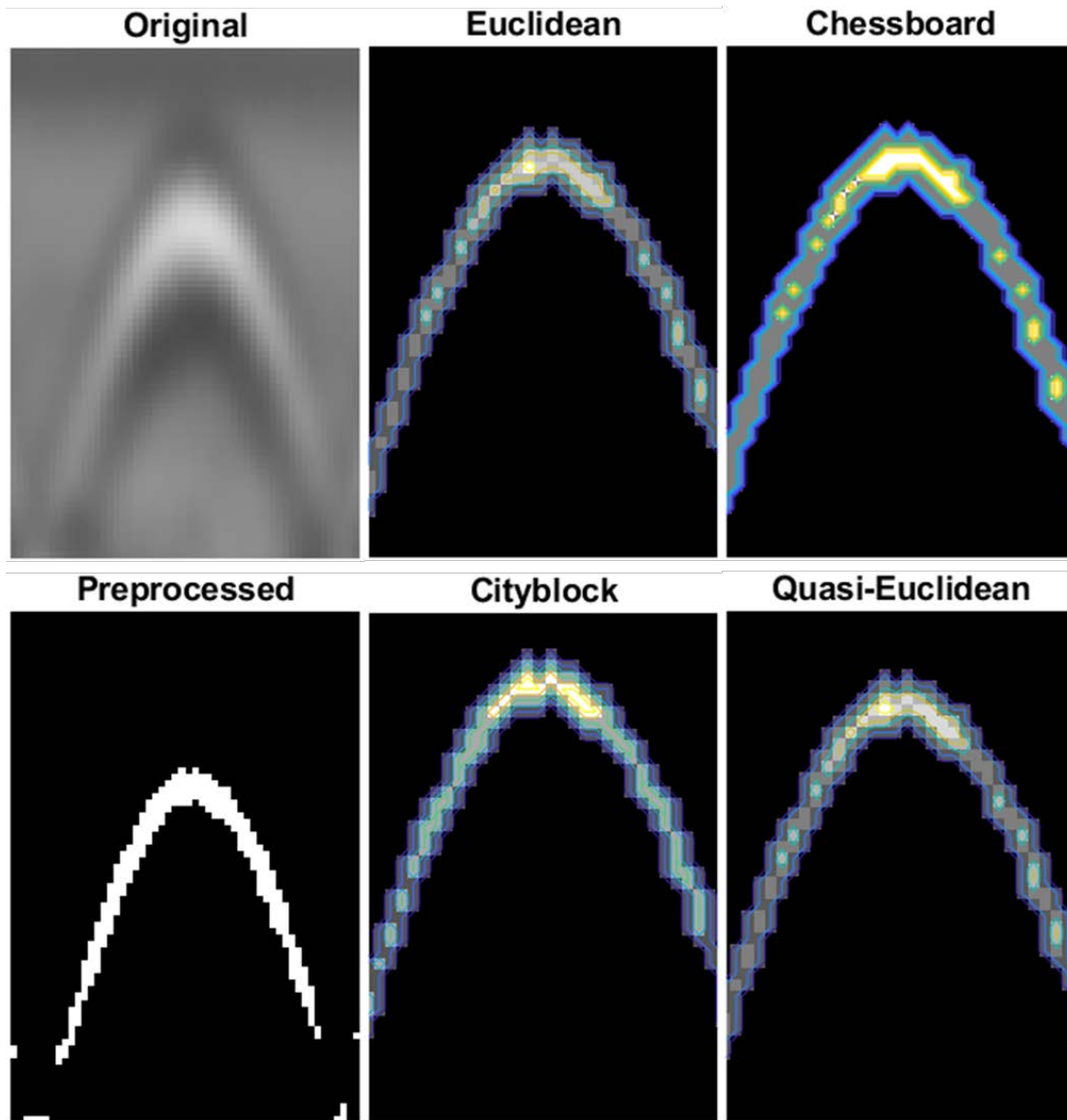
**Figure 3.28**  $BW_i$  - boundary pixel image with inner boundaries overlaid.



**Figure 3.29**  $BW_{ir}$  - boundary pixel image with filtered inner boundaries overlaid.

*Distance Transform:* After detecting inner boundaries based on identifying DOs, the next step is to identify hyperbolic cluster points of each possible true detection. It is achieved by applying *distance transform*, which is an operation that converts a binary image into a greyscale image such that each pixel is replaced with the distance between that pixel and its closest nonzero pixel (Paglieroni, 1992). While there are numerous methods found in the literature to evaluate distance metrics (Borgefors, 1986), the four common metrics to include their range are *Euclidean*, *city block*, *chessboard*, and *quasi-Euclidean*. If  $(x_1, y_1)$  and  $(x_2, y_2)$  are two points, then the aforesaid distance metrics between them are evaluated using equations shown in Table 3.2. Since the distance transform calculates the distances from the nearest *white* pixel, it is applied on the *complement* image of a preprocessed binary GPR profile ( $\sim BW_p$ ). Consequently, the highest distance values could align with the peak values in the hyperbolic detections.





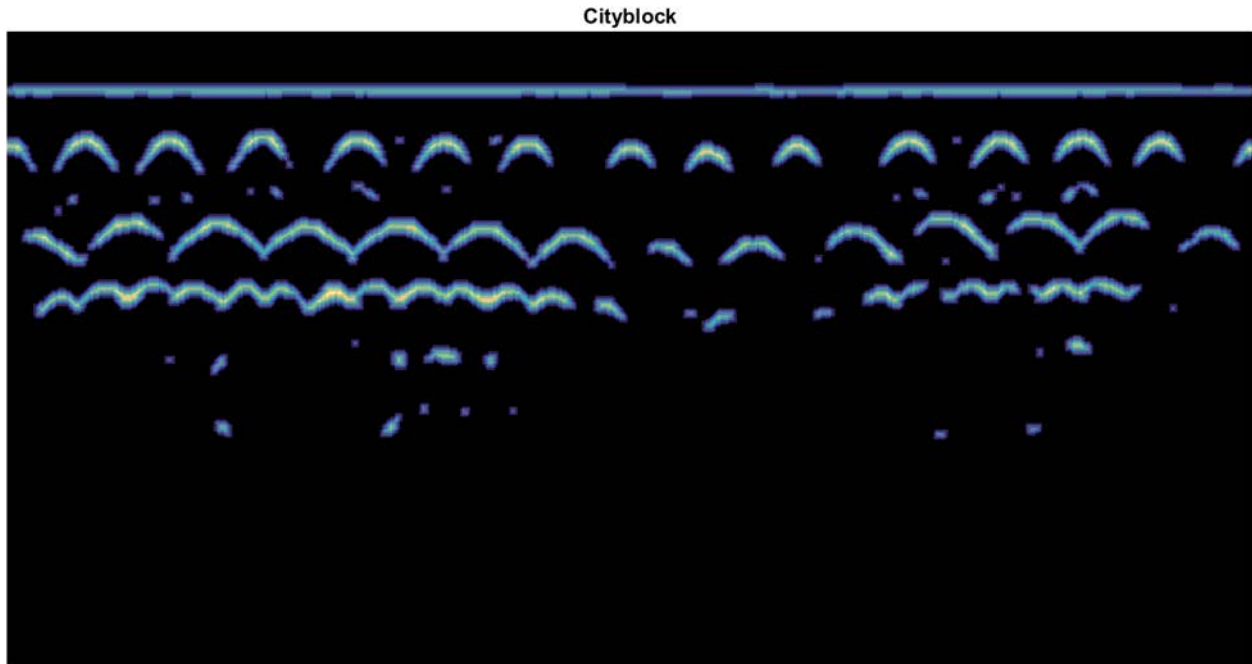
**Figure 3.30** A hyperbolic detection with its preprocessed image and 4 distance transformations

Figure 3.30 shows a hyperbolic detection in a GPR profile with its preprocessed image. It also shows (slightly zoomed) contour maps after applying the four distance transformations on its preprocessed image. The *city block* distance metric has been chosen because it appropriately identifies possible hyperbolic point clusters for the following reasons:

- a) The city block distance metric displays a relatively higher number of hyperbolic cluster points with higher indexes, as shown in the figure. This indicates that it effectively captures and represents the clustering patterns in the hyperbolic detections.
- b) The city block distance metric measures the path between pixels based on a 4-connected neighborhood, where edge-touching pixels are considered 1 unit apart, and diagonally touching pixels are considered 2 units apart. This metric aligns with the characteristics of hyperbolic structures, allowing for accurate measurement of distances between pixels in the cluster and preserving the spatial relationships between them.

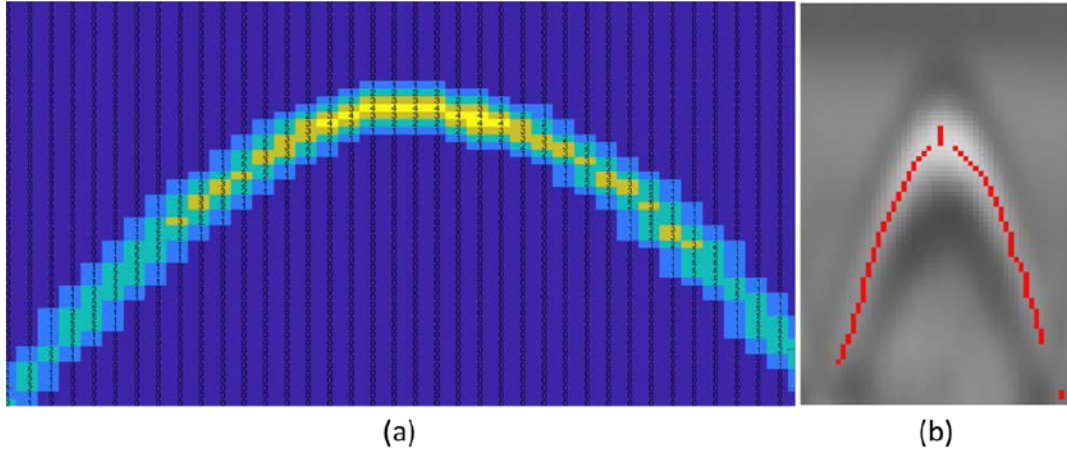
**Table 3.2** Equations for measuring distance metrics (The MathWorks, 2014)

Sl.	Distance metric	Equation
1	<i>Euclidean</i>	$\sqrt{(x_1 - x_2)^2 + (y_1 - y_2)^2}$
2	<i>city block</i>	$ x_1 - x_2  +  y_1 - y_2 $
3	<i>chessboard</i>	$\max( x_1 - x_2 ,  y_1 - y_2 )$
4	<i>quasi-Euclidean</i>	$\text{If }  x_1 - x_2  >  y_1 - y_2 ;  x_1 - x_2  + (\sqrt{2} - 1) y_1 - y_2 $ $\text{Else; } (\sqrt{2} - 1) x_1 - x_2  +  y_1 - y_2 $



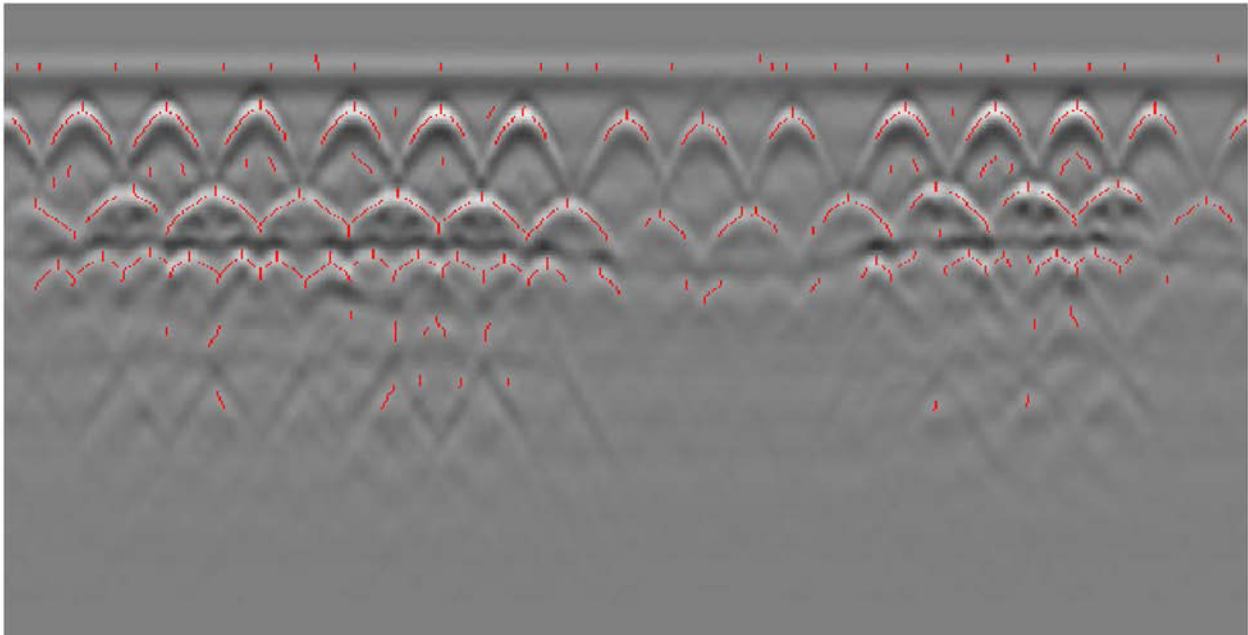
**Figure 3.31** Distance transform of the preprocessed image

*Local maximums:* Figure 3.31 shows the *city block* distance transform contour map of the complement of the preprocessed image ( $\sim BW_p$ ). The resulting map contains *greyscale* point segments with the highest index values in the innermost region while these values gradually decline to have the lowest index values lie along the edge pixels. To illustrate with an example, Figure 3.32(a) shows the hyperbolic arc *section* of the *city block* distance transform with index values (ranging from 1 to 4) of the *original* image shown in Figure 3.30. This image contains higher values (4, 3, or 2) in the innermost section of the hyperbolic arc (point segments) while these values gradually decline to have the lowest value (1) to *always* lie along the edges. It is similar to greyscale hyperbolic reflections in a GPR profile wherein the highest pixel values lie in the interior of most regions while these values gradually decline to have relatively lower pixel values along the edges. Therefore, *locations of local maximums of each point segment of the distant transform image are extracted to identify possible hyperbolic clusters.*



**Figure 3.32** (a) A hyperbolic arc section of the distance transform with index values; (b) Local maximums overlaid in red color on the original image

Figure 3.32(b) shows these local maximums' locations overlaid in red color on the *original* image shown in Figure 3.30. Figure 3.33, labeled as  $BW_c$ , shows the possible hyperbolic cluster points overlaid in red color on the original GPR profile,  $H$ , which are identified by filtering out locations of local maximums of the distance transform image shown in Figure 3.31.



**Figure 3.33**  $BW_c$  - Possible hyperbolic clusters overlaid on the original image,  $H$

*Correlation:* The point clusters in the image,  $BW_c$ , do not all correspond to hyperbolic signatures as seen in the figure. The next step is to group these clusters into individual hyperbolic signatures while filtering out the noise which is not representative of valid signatures. To achieve this objective, the processed image,  $BW_c$ , is correlated with the inner boundaries identified based on the DOs in the image,  $BW_{ir}$ . If  $s(i, j:k)$  is represented as the point segment of an inner boundary in  $BW_{ir}$ , then, let  $r(a,b)$  and  $t(c,d)$  represent the leftmost and rightmost points of that inner boundary respectively. The following constraints are applied to identify valid hyperbolic clusters by checking each inner boundary identified in  $BW_{ir}$  (using a *for* loop):

- a) Since  $s(i,j)$  is the left-most (first) pixel of the point segment, identify the first hyperbolic cluster point in  $BW_c$ , if present, along the same row on the left side of  $s(i,j)$ . Let this point found be represented as  $BW_c(i, y_1)$ . Check if this point lies within the limits of the inner boundary as follows i.e.,

$$\text{If } y_1 > b; \quad (3.21)$$

If the above condition is *true*, trace all 4-connected points of  $BW_c(i, y_1)$  along its left-bottom side using a *while* loop until the adjacent pixel at either of the location coordinates in the image  $(i+1, y_1)$ ,  $(i, y_1-1)$ ,  $(i+1, y_1-1)$  is unity. The pseudocode is written as follows:

```

while  $BW_c(i+1, y_1) == 1 \parallel BW_c(i, y_1-1) == 1 \parallel BW_c(i+1, y_1-1) == 1$ 
if  $BW_c(i+1, y_1) == 1$ ;  $i = i + 1$ ; end
if  $BW_c(i, y_1-1) == 1$ ;  $y_1 = y_1 - 1$ ; end
if  $BW_c(i+1, y_1-1) == 1$ ;  $i = i + 1$ ;  $y_1 = y_1 - 1$ ; end
repeat until the 'while' condition is not met
end

```

(3.22)

Let the last point identified after applying the *while* loop be represented as  $BW_c(i_{last}, y_{last})$ .

A final check is performed to see if the last point identified lies within the limits of the inner boundary as follows:

$$\text{If } i_{last} < a; \&\& \text{If } y_{last} > b; \quad (3.23)$$

- b) Similarly, since  $s(i,k)$  is the right-most (last) pixel of the point segment, identify the first hyperbolic cluster point in  $BW_c$ , *if present*, along the same row on the right side of  $s(i,k)$ . Let this point found be represented as  $BW_c(i, y_1)$ . Check if this point lies within the limits of the inner boundary as follows i.e.,

$$\text{If } y_1 < d; \quad (3.24)$$

If the above condition is *true*, trace all 4-connected points of  $BW_c(i, y_1)$  along its right-bottom side using a *while* loop until the adjacent pixel at either of the location coordinates in the image  $(i+1, y_1)$ ,  $(i, y_1+1)$ ,  $(i+1, y_1+1)$  is unity. The pseudocode is written as follows:

```

while  $BW_c(i+1, y_1) \neq 1 \parallel BW_c(i, y_1+1) \neq 1 \parallel BW_c(i+1, y_1+1) \neq 1$ 
if  $BW_c(i+1, y_1) = 1$ ;  $i = i + 1$ ; end
if  $BW_c(i, y_1+1) = 1$ ;  $y_1 = y_1 + 1$ ; end
if  $BW_c(i+1, y_1+1) = 1$ ;  $i = i + 1$ ;  $y_1 = y_1 + 1$ ; end
repeat until the 'while' condition is not met
end

```

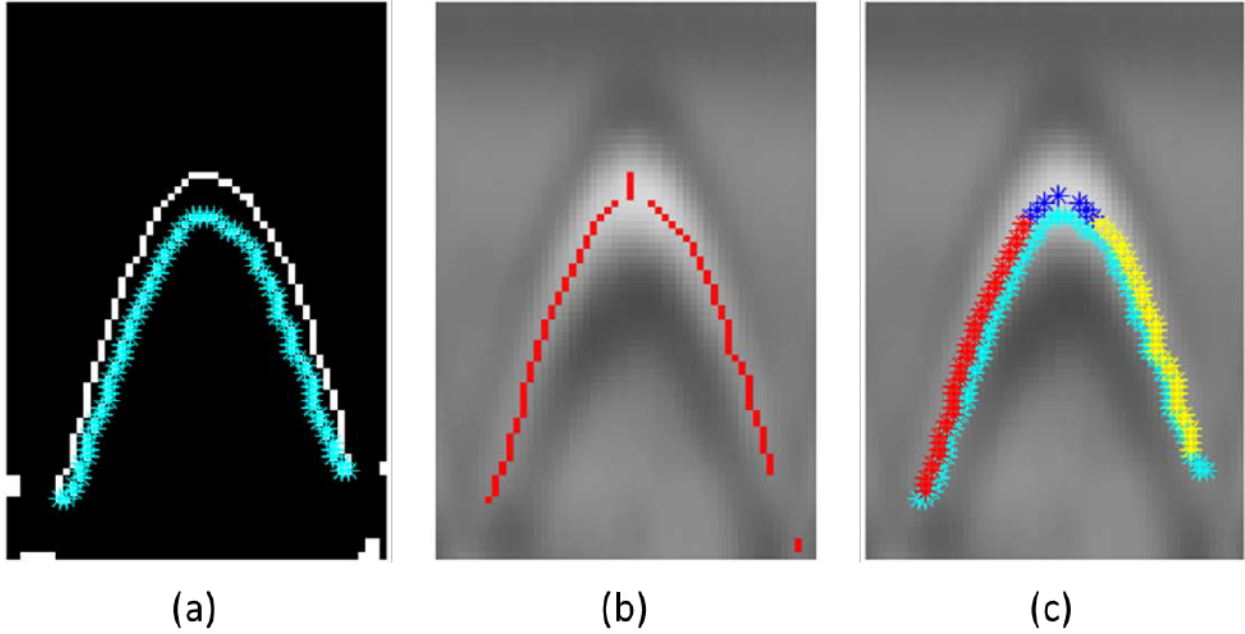
**(3.25)**

Let the last point identified after applying the *while* loop be represented as  $BW_c(i_{last}, y_{last})$ .

A final check is performed to see if the last point identified lies within the limits of the inner boundary as follows:

$$\text{If } i_{last} < c; \&\& \text{If } y_{last} < d; \quad (3.26)$$

- c) Subsequently, if all the conditions of (a) & (b) are satisfied for an inner boundary, then the *hyperbolic point clusters identified on both sides of the point segments are classified as valid*. The points clusters identified on the *left side* of the point segment are saved as *rising legs* as these clusters of 4-connected points follow an ascending stairs pattern towards the top of the hyperbola. Similarly, the points clusters identified on the *right side* of the point segment are saved as *trailing legs* as these clusters of 4-connected points follow a descending stairs pattern away from the top of the hyperbola.
- d) After identifying *rising legs* and *trailing legs* point clusters, the next step is to identify the top of the hyperbola at and above the point segment level called the *apex*. The *apex* point clusters are searched by identifying the valid point clusters in  $BW_c$  by following the *rising leg* trail towards the right side upwards and the *trailing leg* towards the left side upwards while *interpolating* missing points such that these points are *4-connected adjacent neighbors* until the peak (topmost) point is reached.
- e) The three points clusters of *apex*, *rising legs*, and *trailing legs* together form a complete *individual hyperbolic signature cluster*.
- f) The procedure (a-e) is repeated for all inner boundaries in  $BW_{ir}$  while retaining sets of all valid individual hyperbolic signature clusters.

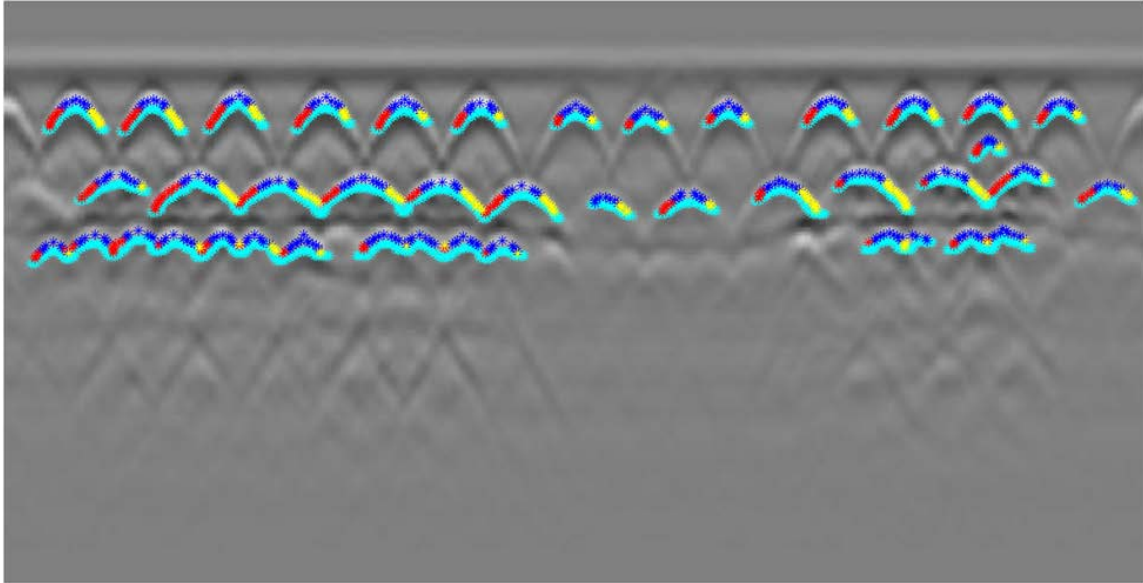


**Figure 3.34** (a) Inner boundary of the hyperbola; (b) local maximums overlaid on the hyperbola; (c) hyperbolic cluster with inner boundary overlaid.

To illustrate with an example, the above-mentioned constraints were applied to the original image in Figure 3.30. Figure 3.34(a) shows the *inner boundary* identified in cyan color overlaid on the boundary pixels of the preprocessed image. Figure 3.34(b) shows the *local maximums* of the distance transform on the complement of preprocessed image overlaid in red color traced upon the *original* image. Figure 3.34(c) shows the *complete hyperbolic point cluster* as overlaid on the *original* image along with the inner boundary shown in cyan color as follows: *apex* in dark blue color, *rising* leg in red color, and *trailing* leg in yellow color. Similarly, Figure 3.35, labeled as  $BW_{pc}$ , shows sets of individual hyperbolic point clusters utilizing the same color convention in the aforesaid statement. It detected a total of 42 hyperbolic signatures as follows: 13 in the top layer of reinforcement, 13 in the bottom layer of reinforcement, a duplicate signature from a strong



reflection of the top layer (present in between the top and bottom layer), and 15 other detections from the slab bottom as shown in the figure.



**Figure 3.35**  $BW_{pc}$  - Hyperbolic point clusters with inner boundaries overlaid on the GPR profile,  $H$

*Hyperbolic fitting:* Corollary, the hyperbolic point clusters are identified based on *correlating inner boundaries of the downward openings with the local maximums of distance transform* of a preprocessed GPR image. A final check is performed to eliminate false positives by verifying if the cluster points conform to a fitting algorithm of hyperbolas. The fitting algorithms for conic sections which include hyperbolas can be broadly classified into two categories: a) clustering algorithms such as RANSAC (Fischler & Bolles, 1981) and b) optimization algorithms such as (Fitzgibbon et al., 1996), (O’Leary & Zsombor-Murray, 2004), (Yan et al., 2008), and (Y Liu & Dong, 2010). Although clustering algorithms are robust against outliers, such algorithms are slow, less accurate, and require large memory (Y Liu & Dong, 2010). However, optimization algorithms are preferred as these fit better accurately to a given set of points with fast computation time

(Fitzgibbon et al., 1996). Therefore, the direct, specific fitting algorithm of (O’Leary & Zsombor-Murray, 2004) has been adopted in this model as it imposes quadratic constraints on scattered data points of a cluster to identify its hyperbolic equation with improved computational efficiency and better fit. The complete procedure has been described in the paper, but it has been summarized as follows:

1. If  $(x_i, y_i)$  represent a set of  $n$  data points, then let  $(\bar{x}, \bar{y})$  be the centroid coordinates. Then a scaled, mean-free set of data points are evaluated as follows:

$$mx_i = m(x_i - \bar{x}) \text{ and } my_i = m(y_i - \bar{y})$$

$$m = \sqrt{\frac{2n}{\sum_{i=1}^n (x_i^2 + y_i^2)}} \quad (3.27)$$

2. Linear regression is performed on the mean-free data  $(mx_i, my_i)$ , and if the residual is too small, the set of points is best described by a line (not a conic section).
3. The equation of a conic section can be represented as a product of vectors as follows, wherein, design “**d**” and coefficient “**z**” are the dual-Grassmannian and Grassmannian coordinates of the conic coordinates respectively:

$$\mathbf{dz} = [x^2 \ xy \ y^2 \ x \ y \ 1][a \ b \ c \ d \ e \ f]^T = 0; a - f \text{ are real coefficients} \quad (3.28)$$

4. The design matrices are partitioned into quadratic, linear, and constant groups as follows:

$$D_2 = \begin{bmatrix} x_1^2 & x_1y_1 & y_1^2 \\ \vdots & \ddots & \vdots \\ x_n^2 & x_ny_n & y_n^2 \end{bmatrix}; D_1 = \begin{bmatrix} x_1 & y_1 \\ \vdots & \vdots \\ x_n & y_n \end{bmatrix}; D_0 = \begin{bmatrix} 1 \\ \vdots \\ 1 \end{bmatrix} \quad (3.29)$$

5. Then, the scatter matrix, **M**, is computed with linear predication removed from the quadratic terms:

$$\mathbf{M} = S_{22} - S_{21}S_{11}^{-1}S_{21}^T = D_2^T(I_n - D_1D_1^+)D_2;$$

$$D_1^+ \text{ is pseudo - inverse matrix of } D_1; I_n - \text{identity matrix} \quad (3.30)$$

6. For hyperbolas (and ellipses), the eigenvectors of the matrix,  $C^{-1}M$  are determined to fit the required conic with a quadratic constraint as follows:

$$\text{wherein, } C = b^2 - 4ac (> 1 \text{ for a hyperbola})$$

Lastly, the following *constraints* are executed stepwise on each of the hyperbolic point clusters identified ( $BW_{pc}$ ) in a GPR profile as follows:

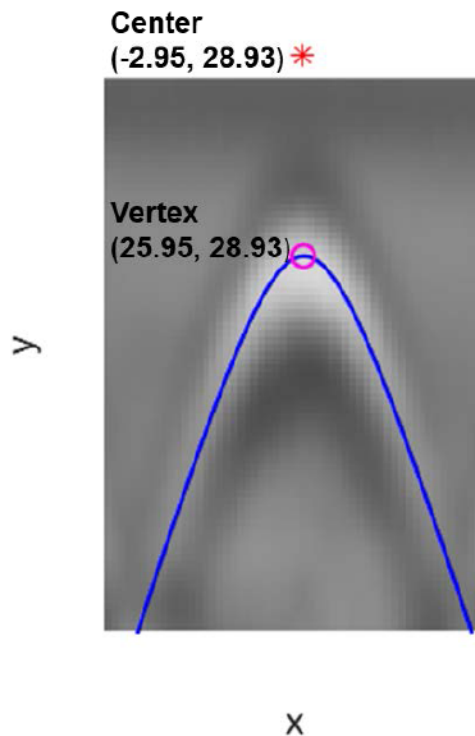
- a) The aforementioned procedure based on the (O’Leary & Zsombor-Murray, 2004) algorithm is applied and the hyperbolic equation is obtained while ensuring *eccentricity* is real and greater than 1 (if the set of points does not fit, then such point clusters are eliminated).
- b) Additionally, since *the hyperbolic signatures in GPR profiles are always downwards*, the center of the hyperbola, let’s say,  $C(a,b)$  must be above the vertex of the points clusters, let’s say  $V(c,d)$ , i.e.,

$$a > c \quad (3.31)$$

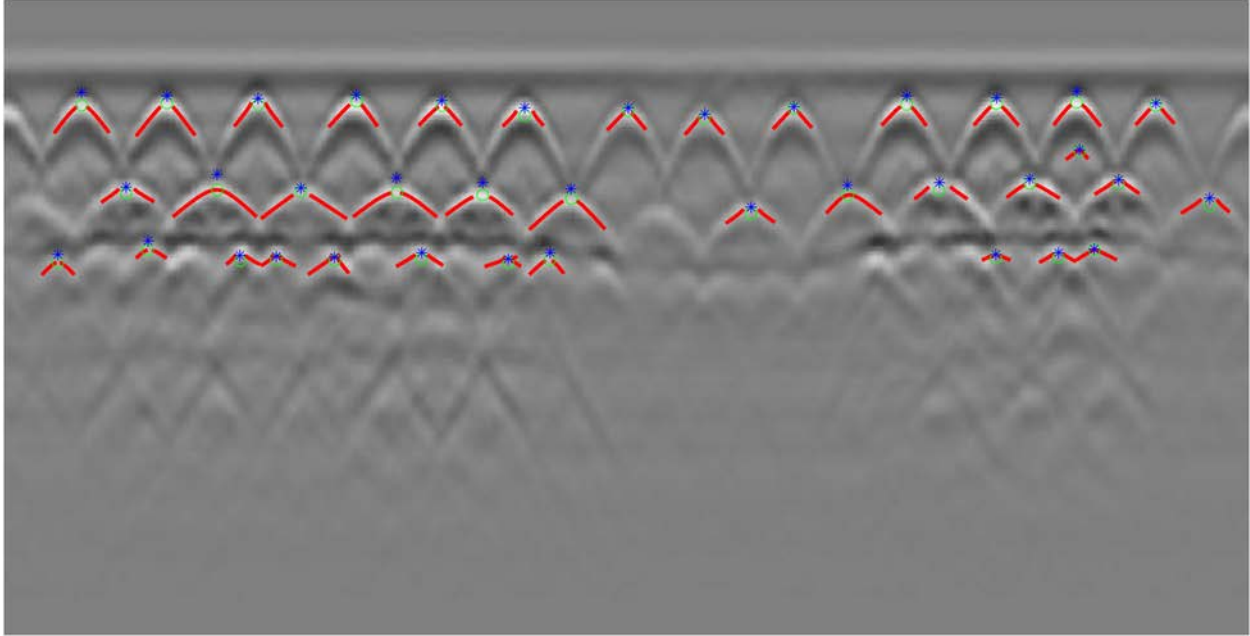
- c) The hyperbolic equation obtained is *theoretical* for each set of point clusters as all the points would not lie exactly along the curve. Ideally, the axis of symmetry of this theoretical hyperbola should align perfectly parallel to the vertical axis of a GPR profile in case of well-defined hyperbolic reflections. However, (Mertens et al., 2016) state that complex hyperbolic signatures in real GPR profiles could be *misshaped* and thus, this axis may not always align (perfectly) with the vertical axis. Therefore, a *buffer zone* must be considered for the angle of deflection of the axis of symmetry with respect to the vertical axis of a GPR profile. Based on the empirical evaluation of data sets of varied GPR profiles and for a conservative estimation, the angle of deflection of the axis of symmetry of the theoretical

hyperbola of a hyperbolic point cluster *must be less than  $30^\circ$*  on either side of the vertical axis.

Figure 3.36 shows the curve of the hyperbolic equation obtained utilizing the hyperbolic point clusters in Figure 3.34(a) while applying the aforesaid constraints. The figure also displays the vertex ('o') and the center ('\*') of the hyperbola along with its coordinates. Similarly, Figure 3.37, labeled as  $BW_{hc}$ , shows the identified hyperbolic curves (red color) along with vertex 'o' and centroid '\*' of each curve overlaid on the profile,  $H$ . This step completes the RHD module of this proposed approach.



**Figure 3.36** Hyperbolic curve plotted with vertex and center

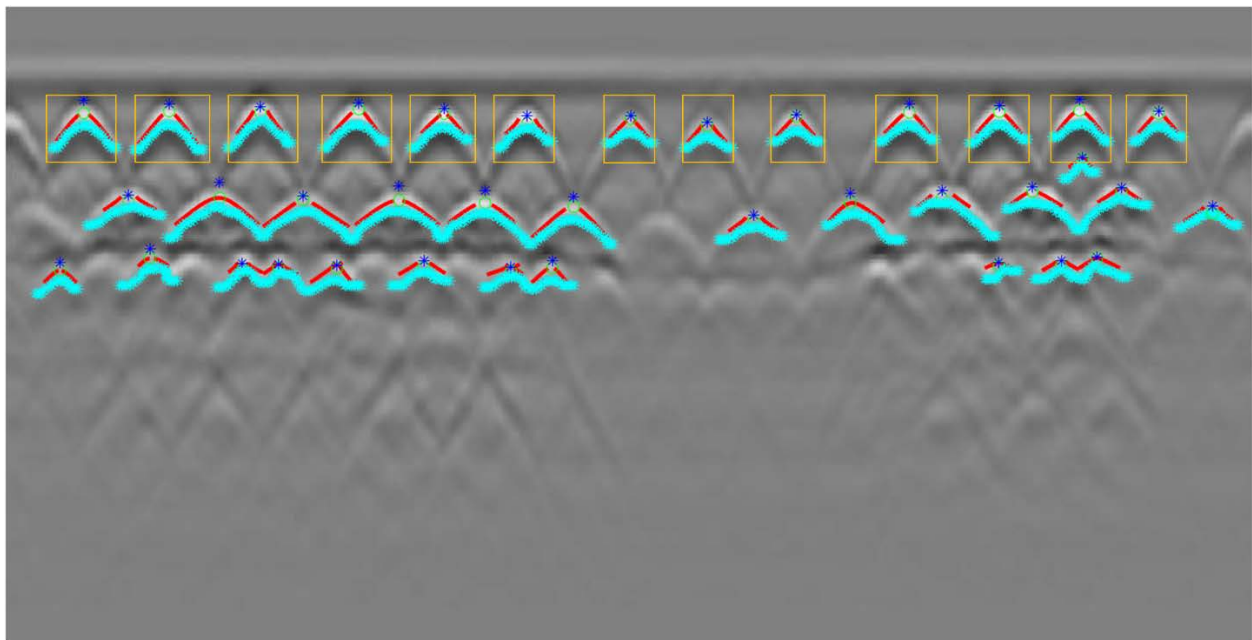


**Figure 3.37**  $BW_{hc}$  – Hyperbolic curves with vertex and center overlaid on the profile,  $H$

### 3.3.4 Regional comparison, statistical analysis, and user-labeled anomalies module

After identifying exhaustive hyperbolic clusters in a GPR profile based on the RHD module, the detected hyperbolic regions in  $BW_{hc}$ , are bounded in surrounding boxes based on the following: a) the *width* (vertical sides) of each bounding box is either equal to the width of that cluster's inner boundary, b) the top horizontal side of each bounding box is taken a few pixels above the vertex of that cluster such that the corresponding pixel in the image,  $BW_p$ , is equal to the first zero-pixel value while moving upwards away from the vertex, and c) similarly, the bottom horizontal side is taken corresponding to the lowest row value of its inner boundary. Subsequently, the necessary layer (either top or bottom) is determined while eliminating false positives and filling gaps by applying the principles outlined in Section 3.2.3. Figure 3.38, labeled as  $BW_{tl}$ , shows the top layer identified after regional comparison in orange boxes along with the hyperbolic clusters (red color)

and inner boundaries (cyan color) overlaid over the GPR profile image,  $H$ . The model identifies such a layer and prompts the user to verify its accuracy. In case of an incorrect detection, the procedure described in the same section is further employed. It utilizes the cubic spline fitting and peaks' detection algorithms to enclose the required layer within surrounding boxes while utilizing the information provided by the user. Finally, the user is prompted to provide anomalies information present in the GPR profiles in the missing gaps.

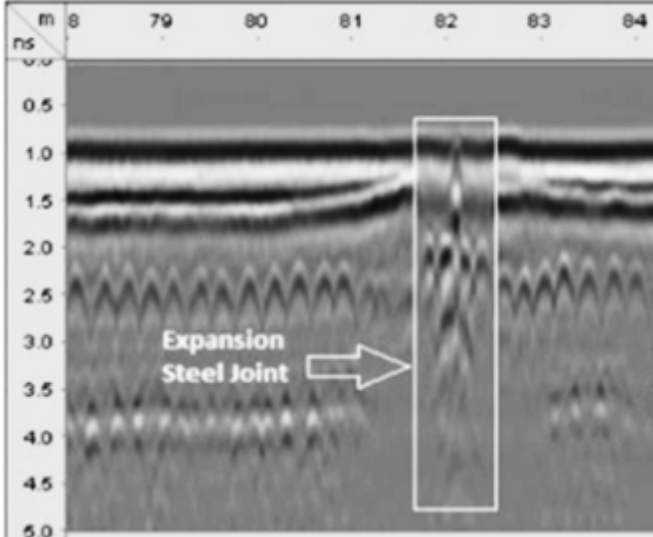
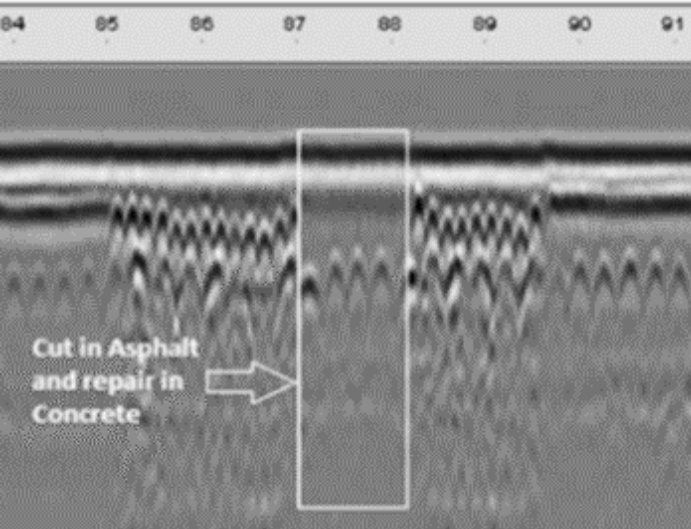
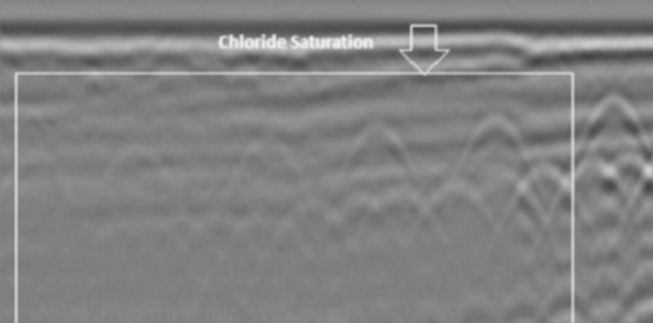


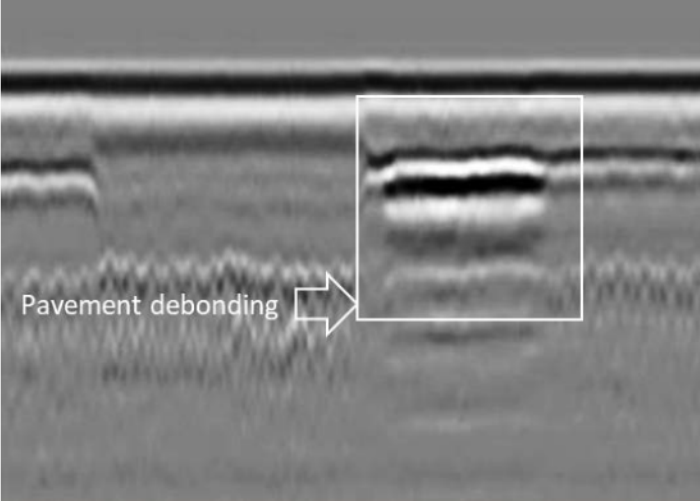
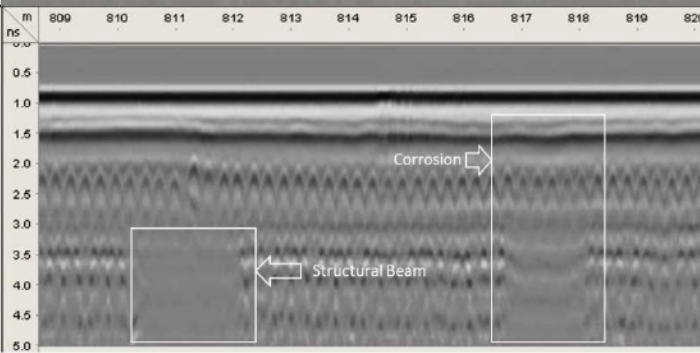
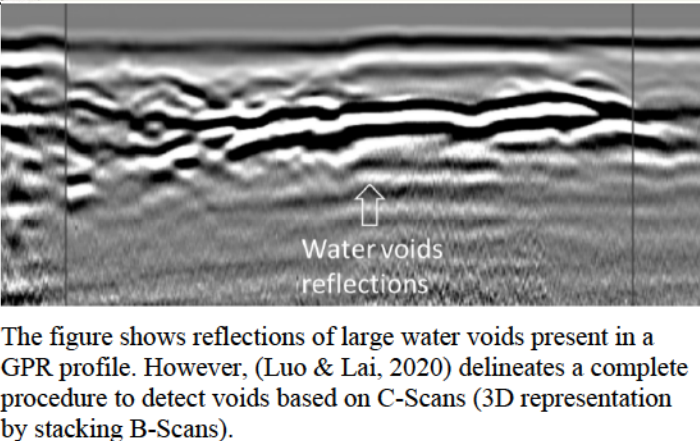
**Figure 3.38**  $BW_{it}$  -Top layer identified based on regional comparison

*User-Labeled Anomalies Module (ULAM)*

As stated earlier, the RUIIM method takes a comprehensive approach to analyzing GPR data, which involves considering and incorporating the anomaly regions in the analysis. The presence of anomalies in GPR data can be categorized as either known or unknown to the user.

**Table 3.3** Anomalies Detections based on the characteristic features in GPR Profiles

Name of anomaly	Characteristics	Example
<p><b>Expansion Joint</b></p>	<p>Reverberated (ringing) effects from the surface until the bottom of the profile.</p> <p>Surface disturbances: <i>Yes</i>.            Variances at rebar level: <i>Yes</i>.            Variance below rebar level: <i>Yes/No</i>.</p>	
<p><b>Repair and cut</b></p>	<p>Stacking of hyperbolas on the sides and Surface level displaced.</p> <p>Surface disturbances: <i>Yes</i>.            Variances at rebar level: <i>Yes</i>.            Variance below rebar level: <i>Yes/No</i>.</p>	
<p><b>Chloride Saturation</b></p>	<p>High level of attenuation from the surface to the bottom</p> <p>Surface disturbances: <i>Yes</i>.            Variances at rebar level: <i>Yes</i>.            Variances below rebar level: <i>Yes</i>.</p>	

<p><b>Pavement debonding</b></p>	<p>Heavy loss of energy signals at the surface leads to lower reflections at the rebar level.</p> <p>Surface disturbances: <i>Yes</i>.          Variances at rebar level: <i>Yes</i>.          Variances below rebar level: <i>Yes</i>.</p>	
<p><b>Structural Member (Beam)</b></p>	<p>Complete loss of signal compared to a corroded region. Typically, staggered rebars are also present on the sides.</p> <p>Surface disturbances: <i>No</i>.          Variances at rebar level: <i>Yes</i>.          Variances below rebar level: <i>Yes</i></p>	
<p><b>Void (Air/ Water)</b></p>	<p>The detection of voids is a complex detection process. If the voids are large, a reverberation or ringing effect is observed.</p> <p>Surface disturbances: <i>Yes/ No</i>, varies based on void size.          Variances at rebar level: <i>Yes</i>.          Variances below rebar level: <i>Yes/No</i>, varies based on void size.</p>	 <p>The figure shows reflections of large water voids present in a GPR profile. However, (Luo &amp; Lai, 2020) delineates a complete procedure to detect voids based on C-Scans (3D representation by stacking B-Scans).</p>

Known anomalies are typically identified by the analyst through various means such as examining construction drawings, referring to previous inspection reports, or visually inspecting GPR profiles. In such cases, the analyst can label these specific regions along the detected layer accordingly. For anomalies that do not require further inspection, such as an expansion joint or a structural



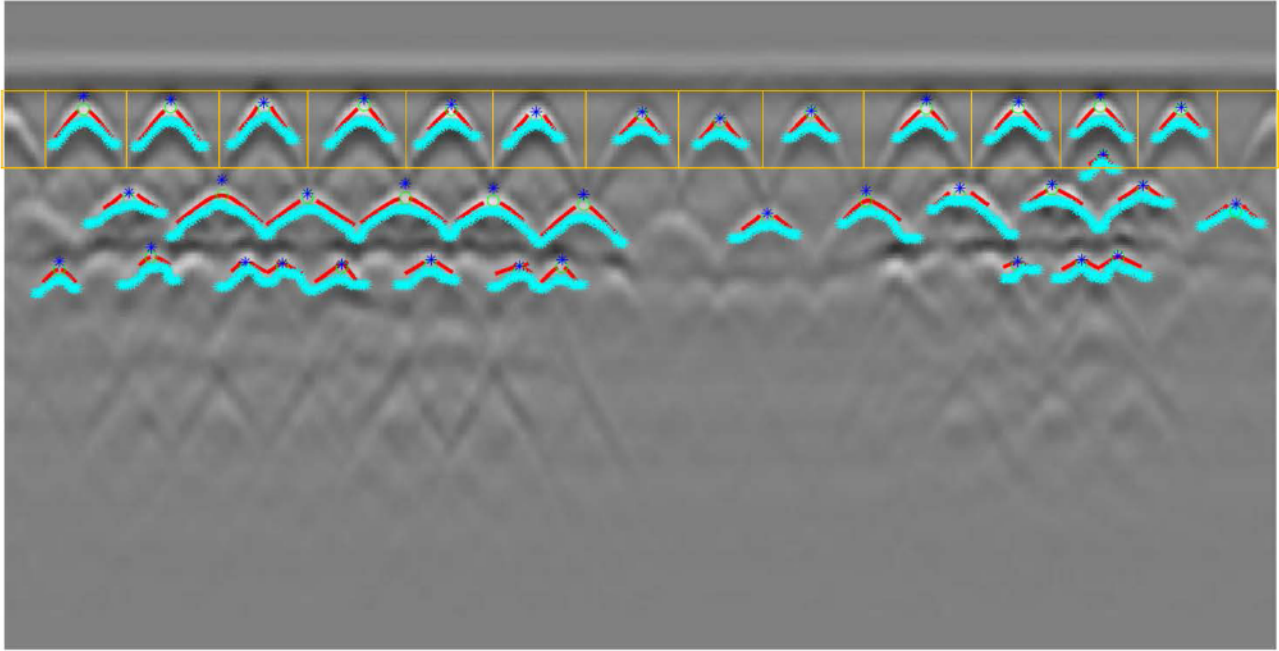
member, the user can label them as "green," indicating that the condition of the concrete is considered good. Conversely, if an anomaly requires immediate inspection during repair and maintenance, such as voids or surface anomalies, the user can label it as "red." Lastly, for anomalies that may not require immediate attention or need to be marked with a unique color on condition maps, the analyst can assign them a "white" color tag.

Table 3.3 presents a comprehensive overview of typical anomalies encountered in bridge elements, along with their defining characteristics. Additionally, it indicates whether each anomaly affects different levels: a) disturbances at the surface above the detected layer, b) variations at the rebar level where the anomaly typically differs from a regular hyperbolic region, and c) variations below the rebar level, with a width equal to that of the detected region at the rebar level. By carefully analyzing and understanding these variances, the user can make informed decisions and appropriately label the anomalies.

When dealing with unknown anomalies, this model offers two assistance tools for the user. Let's consider a scenario where hyperbolic regions are detected in the top layer, along with enclosed missing gaps that may potentially contain anomalies. The first tool available is a similarity matrix colormap that encompasses the three regions (surface, rebar level, and level below rebar) discussed earlier. This matrix is generated by comparing the HOG features of all the detected regions in the top layer using the normalized Euclidean (EUC) distance. The choice of HOG features stems from their superior performance in distinguishing hyperbolic regions in bridge elements, as highlighted earlier in the study by (Kaur et al., 2015). The normalized EUC distance metric was chosen based on a comparison study conducted by (Montiel-Zafra et al., 2017) which evaluated various metrics such as cosine similarity and the Kullback-Leibler (KL) divergence. The study revealed that it

outperformed other metrics in distinguishing hyperbolic regions from the background. Therefore, this model utilizes the normalized EUC metric as it can effectively discriminate hyperbolic regions from anomalies based on the HOG features. The second tool available is the visualization of the GPR profile using a ‘jet’ colormap as discussed in Section 2.16.1. This visual tool aids the user in identifying anomaly regions within the enclosed missing gaps. By leveraging these two figures - the similarity matrix colormap and the GPR profile visualization - the user can accurately mark anomaly regions using the color convention previously discussed.

ML approaches, such as ANNs, can be employed to create a database for benchmarking various anomalies. While this can enable automated anomaly detection, establishing such a database can be a challenging task. For instance, the identification of expansion joints is relatively straightforward due to reverberation effects, but when it comes to the detection of voids, the task becomes complex due to their varying sizes and unique characteristics. Moreover, the computational cost associated with automatically detecting all types of anomalies can be high. To address these challenges, this model adopts a different approach. It involves the analyst manually labeling the anomaly regions by scanning *only* the enclosed boxes of missing gaps. The analyst is facilitated with tools or figures to accurately mark the anomaly regions. By combining manual input from the analyst and the assistance provided by the model, more efficient and accurate analysis of the anomaly regions can be achieved. The software implementation of the developed model is demonstrated in Section 4.4, where examples are provided to showcase the ULAM application. Figure 3.39, labeled as  $BW_j$ , shows the final processed image with automated detection (no anomalies) enclosed in orange boxes along the top layer.



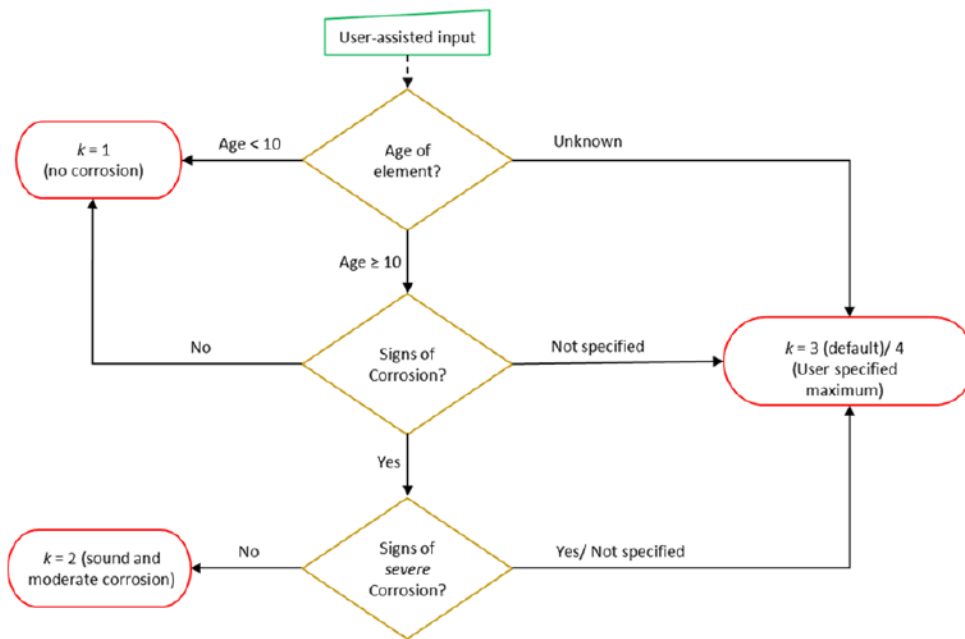
**Figure 3.39**  $BW_f$ – Final processed image after automated detections

### 3.3.5 Condition mapping

The final stages of the RUIM methodology for generating a condition map closely follow a similar path as described in Section 3.2.4 for the V-JAM approach. These steps have been summarized for the RUIM method as follows:

1. The entropy values are computed for all detected boxes from the processed image ( $BW_f$ ) of each profile within a complete GPR dataset of a scanned element. However, the regions which are assigned as anomalies, *if any*, are excluded.
2. Subsequently, the entropy values are clustered using *K-means* to generate a deterioration scale for each profile of the GPR data set being inspected. The maximum number of clusters (zones) is specified by the user (three/four). Additionally, based on the information provided by the user regarding the age of the element and visual signs of corrosion, the flowchart in Figure 3.40 shows the philosophy adopted by the model in determining

optimal clusters. The justification of using visual examination data and other information from an analyst in determining optimal clusters has been proposed by (Kien Dinh et al., 2015) such as if the age of the element (bridge deck) is less than ten years, it is inferred that corrosion hardly initiates based on numerous studies. Similarly, if the age of the element is greater than 10 years, and it shows signs of corrosion without any *severe* signs, the optimal cluster value is *two* i.e., sound concrete and moderate corrosion zones. As previously stated, if anomalies were detected, their respective regions on deteriorated scales are assigned appropriately.



**Figure 3.40** Flowchart to determine the number of optimal clusters ( $k$ ) based on user-information

3. Finally, a *condition map* is generated by stacking the deterioration scales of all GPR profiles of a given data set.

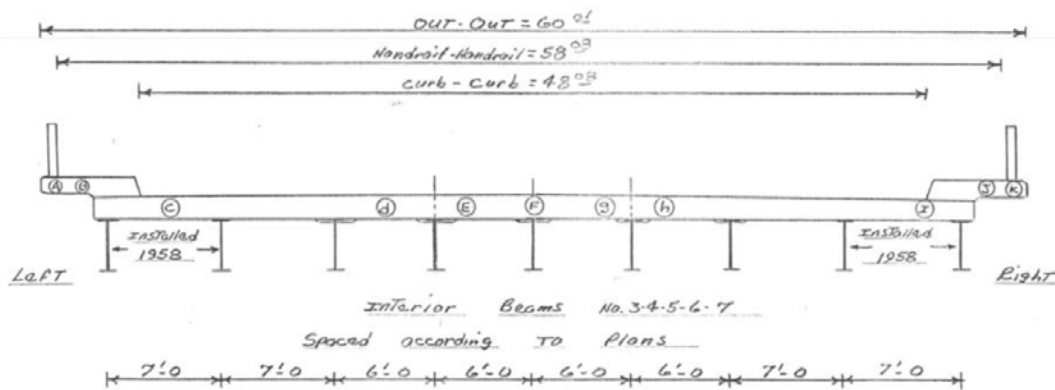
The application of this model using three case studies with developed condition maps and their comparative evaluation has been discussed in Section 4.3, Section 5.2, and Section 5.3.

## 4 CASE STUDIES FOR THE DEVELOPED MODELS

This chapter focuses on the application of the three developed models, with each model being applied to a separate case study. For the first and third case studies, GPR data of bridge decks were obtained from previously acquired scanned data. On the other hand, the second case study involved the physical scanning of a concrete slab in Montréal, Quebec. The condition maps obtained from the developed models are compared with the existing ABA approach and GPR-IBA analysis and inferences are drawn for each model subsequently based on their application. Lastly, a state-of-the-art software tool developed based on the RUIIM methodology is showcased, highlighting its capabilities and features through various examples.

### 4.1 Case Study A – Condition mapping based on the X-Sim Method

A case study has been presented to demonstrate the implementation of the model utilizing the methodology described in Section 3.1.



**Figure 4.1** Deck O2 cross-section with 60 ft clear span (Gucunski et al., 2011).

#### **4.1.1 Data Collection of GPR data**

A bridge deck called O2 was inspected as part of the comprehensive bridge deck deterioration mapping of nine bridges in the state of Iowa, US (Gucunski et al., 2011). This specific case study was chosen in this study for the following reasons:

- 1) The deck O2 underwent examination using four non-destructive testing (NDT) techniques, namely Half-Cell Potential, GPR, Impact-Echo (IE), and Electrical Resistivity Method. The results obtained from each of these techniques correlated with each other and were further validated by comparing them with the findings from in-situ coring samples.
- 2) It serves as an interesting case as this bridge deck had small, corroded zones spread across its subsurface.
- 3) The comparison of the map generated by the developed model with multiple NDTs could prove its stronger reliability for further assessment of other structures.



**Figure 4.2** Deck O2 Data Collection with multiple NDTs – Grid pattern at 2 ft apart (Gucunski et al., 2011)

The total span of deck O2 is 63 feet, and the clear span length is approximately 60 feet. It was originally constructed in 1936 and reconstructed in 1960 with a total width of 48' ft. and currently has two-lane roadways besides two 5' sidewalks. It is built over a small natural stream in Sumner, Iowa (Nashua, NH, USA), and carries the national highway #93 in the east-west direction. *Figure 4.1* shows the original and reconstructed cross-section of the deck with a 48' ft. and 60' ft. clear span respectively. To cover the entire width of 48 feet, 24 swabs were collected, spaced 2 feet apart, along the grid arrangement as shown in *Figure 4.2*. These are the given input parameters for the survey performed:

- Radar Equipment System: GSSI® SIR-20
- Frequency antenna: 1500 MHz
- Scans/m: 197 (60 scans/foot)
- Samples/Scan: 512
- Bit/Sample: 16
- Scans/sec: 346
- FIR Filter, Vertical, High Pass: 250 MHz
- FIR Filter, Vertical, Low Pass: 3050 MHz
- Depth Range: 1.2m
- Range Gain: 0

#### ***4.1.2 Maps generated with ABA and analysis by other NDTs***

The results generated based on ABA mapping and Half-Cell (HC) Potential Cores have been shown in *Figure 4.3*. The scans were taken along the eastbound traffic direction (left to right) of Highway #93 and the origin (start of the first scan) is located on the west approach expansion joint-

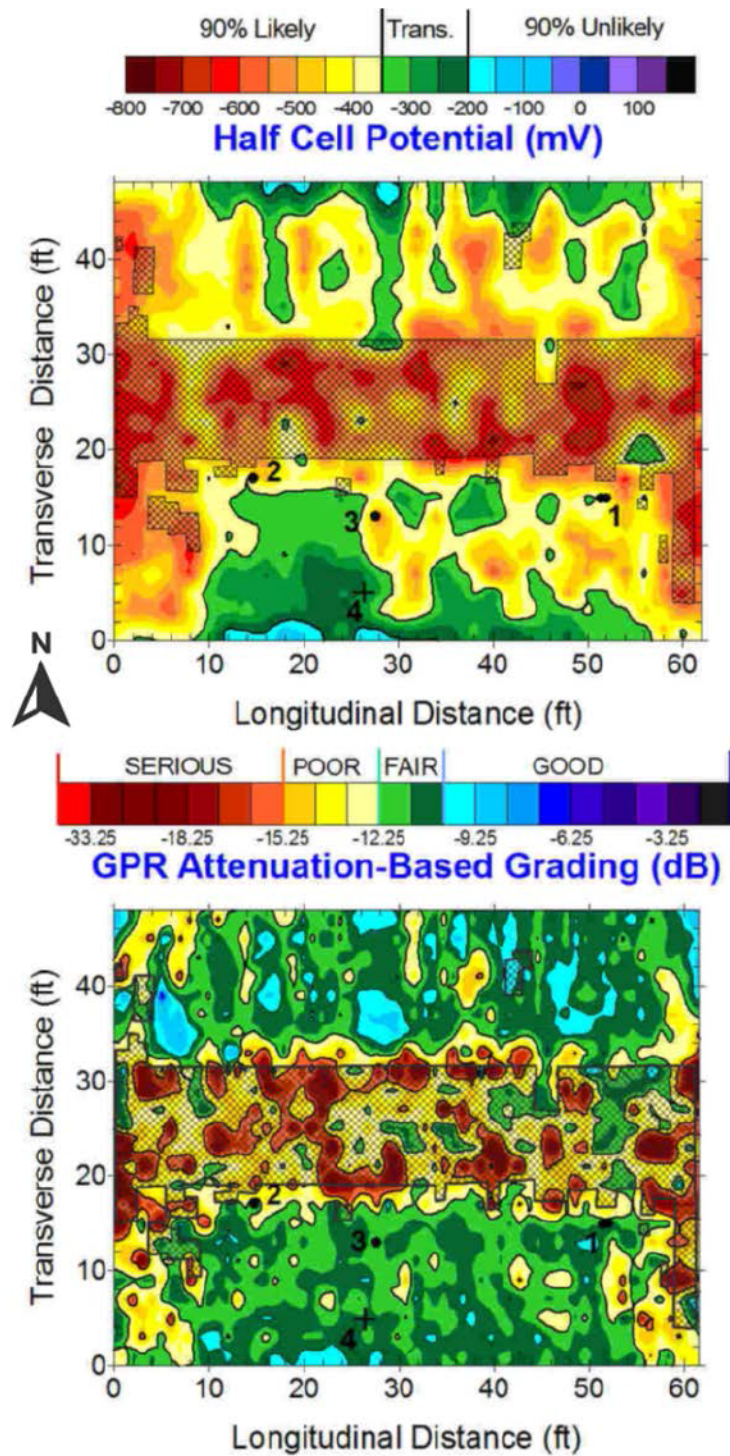
curb intersection. This origin is represented at the left-bottom (SW) corner on condition maps while the first profile scan has been mapped at the bottom i.e., 0-2 ft., and the last scan has been mapped on top at 46-48ft. while the other scans are in-between along the transverse distance axis (Y-axis). The cores extracted for HC Potential mapping are marked from 1-4 and the GPR attenuation map is rated from “serious”, “poor”, and “fair” to “good” concrete based on the amplitude values picked. According to the report by (Gucunski et al., 2011), the actual condition of the concrete, as determined from the extracted cores, was found to be consistent and validated with the respective locations on the GPR attenuation map. *Figure 4.4* shows the map generated based on IE & Electrical Resistivity methods. The IE map was similarly graded from “serious” to “poor” while the electrical resistivity was scaled from 0-100 kOhm\*cm (higher values indicating good concrete/low-level corrosion). This deck was subsequently repaired, and these repair zones are shown overlaid in the figures (in mesh shape) on these NDE maps. It was reported that all four condition maps had *extremely good correlation* areas among each other as shown in both figures. The likely cause of the deterioration and such correlation for this type of bridge deck is corrosion.

#### ***4.1.3 Maps Generated based on GPR-IBA and developed X-Sim Method***

Based on the philosophy discussed in Section 2.9, a condition map is generated for this bridge deck based on the GPR-IBA by manually marking the areas as “green”, “yellow” or “red” across all the twenty-four profiles in the RADxpert® software. Since this analysis is prone to human errors, the analyst took extreme care in marking attenuated areas and cross-examined the profiles repeatedly. *Figure 4.5* shows the map generated based on the GPR-IBA and it showed good correspondence with the maps generated based on other NDTs as the deck is heavily corroded in its middle section.



Finally, based on the model developed in Section 3.1, all the profiles are initially converted to image files and imported into a MATLAB environment. Subsequently, all the profile images are preprocessed by equalizing profile sizes and adjusting their contrast. The X-Sim image of each profile is generated by applying the standard filter and n-s values are evaluated and clustered using K-means for each profile. These were the cluster limits obtained after applying K-means: {0.117,0.468}. Therefore, the deterioration scale for each profile is generated as follows: If the pixel value lies between (0, 0.117), it is zoned as red; if the pixel value lies between (0.117,0.468), it is zoned as yellow; and if pixel value lies between (0.468,1), it is zoned as green. Eventually, a condition map is generated by stacking the deterioration scale of each profile with uniform width and a color scale indicating the condition of the concrete. The origin and mapping direction is consistent with the other NDE maps. *Figure 4.6* shows the condition map generated based on the developed model. If this map is compared with the GPR-IBA map (*Figure 4.5*) visually, it can be inferred that there is generally close correspondence between deteriorated concrete zones (yellow and red) and good concrete (green) zones in these maps. The middle and top deck is severely corroded compared to the bottom deck as seen in both maps while the left section of the deck is relatively more corroded than the middle and right section.



**Figure 4.3** Map Generated based on HC Potential and GPR along with Cores 1-4 marked with repairs overlaid (Gucunski et al., 2011)

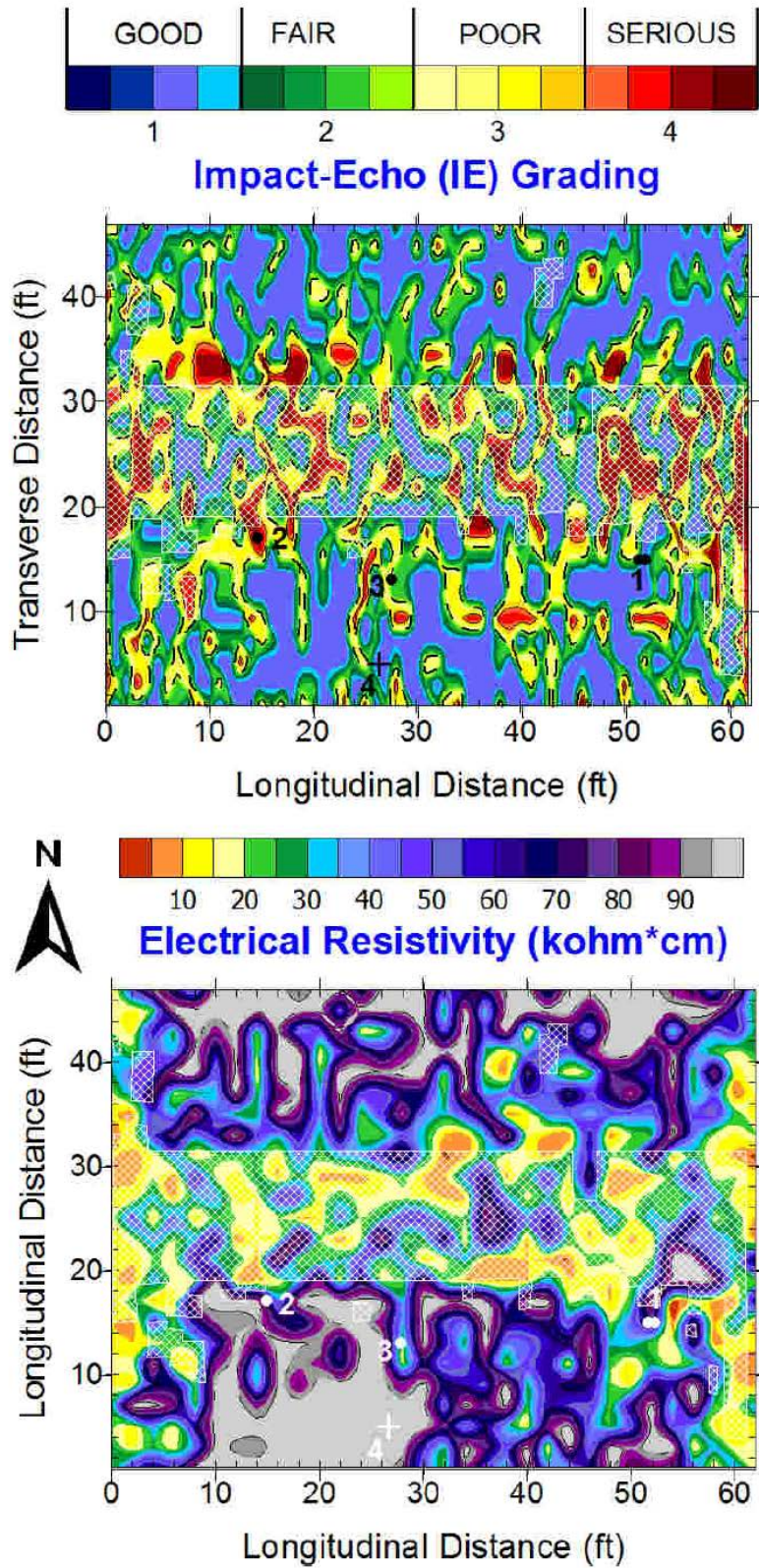
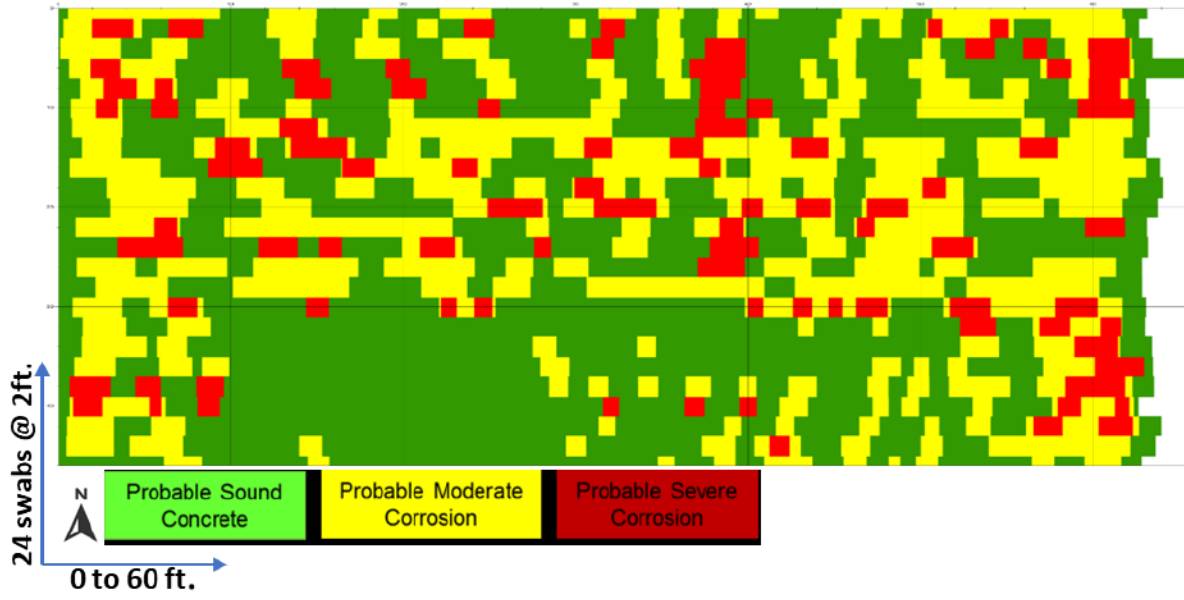
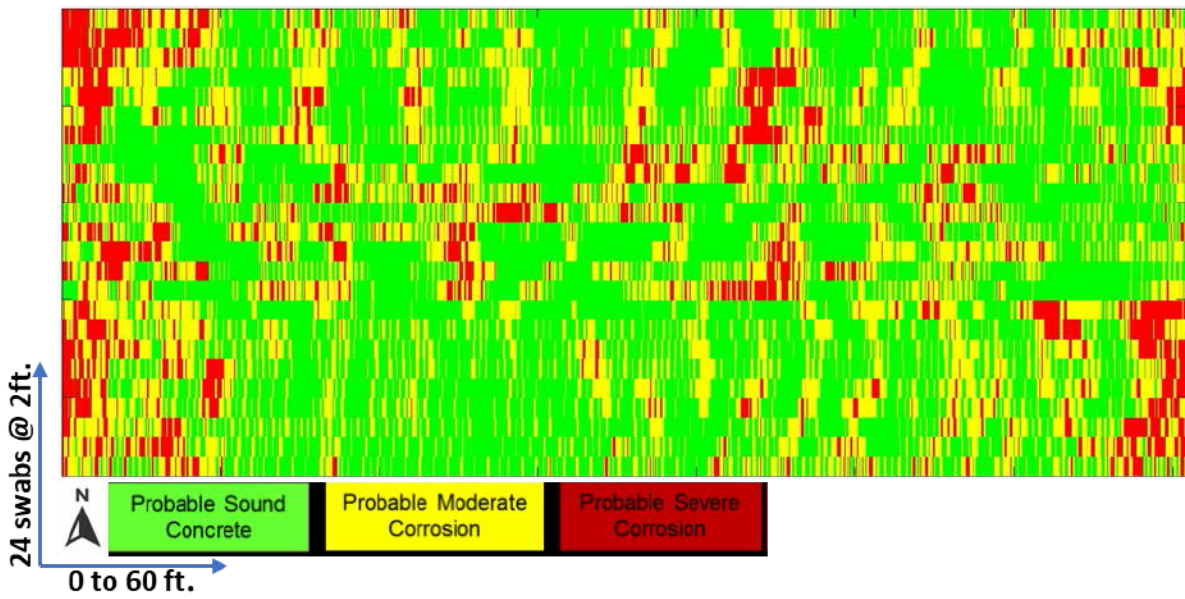


Figure 4.4 IE & Electrical Resistivity maps with repairs overlaid (Gucunski et al., 2011)





**Figure 4.5** Condition maps based on GPR-IBA (M Abdul Rahman & Zayed, 2016)



**Figure 4.6** Condition map based on X-Sim Method (M Abdul Rahman & Zayed, 2016)

**Table 4.1** Quantitative Comparison of deteriorated areas (M Abdul Rahman & Zayed, 2016)

Deterioration Map Type	% Green pixels	% Yellow pixels	% Red pixels
GPR-IBA ( <i>Figure 4.5</i> )	<b>54%</b>	<b>34.5%</b>	<b>11.5%</b>
X-Sim Method ( <i>Figure 4.6</i> )	<b>53.6%</b>	<b>35.6%</b>	<b>10.8%</b>

A quantitative comparison between both the maps (GPR-IBA and developed model) has been done by calculating the total percentage areas of red, yellow, and green pixels as shown in Table 4.1. The total sound concrete condition area (% green pixels) in the developed model map (53.6%) is similar to the GPR-IBA map (54%). Additionally, total areas of concrete with moderate corrosion indicated by the percentage of yellow pixels and total areas of concrete with severe corrosion (% red pixels) are also similar. This greater correlation of the developed model map with GPR-IBA map both visually and quantitatively shows this model identifies general corrosion zones accurately due to the following two reasons: a) the GPR-IBA shows greater correlation with the other NDE maps while these NDEs have also shown good correspondence with the coring samples (Gucunski et al., 2011); and b) GPR-IBA approach itself shows greater correspondence with the ground-truth as validated and compared by cores (Tarussov et al., 2013) in general although it has some of its limitations.

#### **4.1.4 Limitations**

The condition maps generated by this model have various limitations and have been tabulated in an effort to develop a more robust model:

1. Due to its saturation of the top and bottom 1% of pixel values, the contrast-enhancing filter proves less effective when applied to diverse GPR profiles.

2. It does not detect hyperbolas and thus, does not identify the characteristic object(s) in GPR images which could lead to inappropriate zoning of deterioration areas.
3. Since the normalized summation values across the horizontal axis are at each pixel level in this model, the final map generated by the model has numerous very-short condition zones (green, yellow, or red) sometimes equal to a single pixel. This is not true in real-case and thus, the condition map has an inaccurate representation of such areas. Such smaller areas could be neglected by adopting the summation of a strip or block of pixels approach. However, identifying the hyperbolas and considering them as blocks would be more appropriate.
4. It does not detect anomalies and it is difficult to distinguish the deteriorated areas based on this model.
5. It does not always generate accurate maps when it was investigated on other bridge decks especially with complex hyperbolic signatures and with the presence of anomalies in GPR profiles.

## **4.2 Case Study B – Condition Mapping based on V-JAM**

### **4.2.1 Data Collection**

A case study carried out on a reinforced concrete slab of a parking lot in Côte-des-Neiges, Montréal, illustrates the application of V-JAM based on the methodology explained in Section 3.2. A hand-held GPR equipment, available at Concordia University, Montréal, was used to scan the slab surface along both directions with the following parameters:

- Radar Acquisition System: GSSI® SIR 4000 with Model 615 handcart
- Antenna frequency: 1600 MHz
- Depth Range: 55 cm

- Dielectric constant: 7.0 (concrete)
- Samples/Scan: 256
- Scan/m: 400
- Scans/sec: 260
- Bits/Sample: 32
- FIR Filter, Vertical, High: 480 MHz
- FIR Filter, Vertical, Low: 3295 MHz
- Range Gain: 0

The slab's scanned dimensions were 3.5 m by 2.9 m. (approximately). In Figure 4.7, the scanning grid pattern is illustrated on the parking lot with white chalk and the traverse spacing between each scan was 20 cm. It also depicts the sequence in which the 31 swabs were collected across both directions: first, 14 scans were obtained along the X-direction to cover the slabs longitudinal direction (3.5 m), and then, 17 scans were performed along the Y-direction to cover the transverse direction (2.9 m) (Mohammed Abdul Rahman, Zayed, et al., 2022).



**Figure 4.7** Parking lot scanned using GPR across both directions of the slab surface  
(Mohammed Abdul Rahman, Zayed, et al., 2022)

#### **4.2.2 Data Processing**

The RADAN® software was used to pre-process the raw GPR scans and it involved only applying a full-pass background subtraction. No range gain was required as the profiles have good contrast. Additionally, no horizontal stretching or stacking was needed as the aspect ratio (1:1.44) of a typical hyperbola in these profiles is closer to the trained classifier. After pre-processing, these scans were transformed into image files and imported into the MATLAB® environment. Then, the trained classifier (Section 3.2) based on the V-J algorithm was used to detect hyperbolas in all profiles. The three principles of regional comparison and statistical analysis were applied to eliminate false positives along the top layer and identify false negatives respectively. There were no anomalies identified in the slabs to be considered for condition mapping. Entropy values were evaluated for detected regions in all profiles. Subsequently, a deterioration scale was generated



using K-means clustering with *three* and *four* color-coded conventions for each profile across X and Y directions respectively. For example, Figure 3.14 depicts swab #6 taken along the Y-direction with its deterioration scale (three colored zones). Lastly, deterioration scales were stacked to develop separate condition maps along both X and Y directions and with both color-coded conventions. The maps based on the developed model were compared with two approaches: the commonly adopted numerical ABA described in (ASTM D6087, 2015) and the GPR-IBA. It has been observed that there is good general correspondence of concrete condition zones when amplitude-based results are compared to the GPR-IBA, particularly in cases of relatively ideal GPR profiles with no anomalies (Tarussov et al., 2013), (Abouhamad et al., 2017). Therefore, the resulting maps based on the V-JAM should have a good resemblance with maps based on the numerical ABA. Additionally, since the developed model aims to automate the GPR-IBA, the resulting maps should correspond relatively better with the maps based on it. Finally, attenuated areas based on GPR-IBA were labeled very carefully to eliminate human errors as much as possible (Mohammed Abdul Rahman, Zayed, et al., 2022).

#### **4.2.3 Results and their discussion**

The comparison between various methods along each direction is explained separately, and the condition maps generated along the X and Y directions are graphically illustrated with figures.

##### *X-direction*

The four condition maps of swabs 1 through 14 taken along the X-direction with the following methods are shown in Figure 4.8: a) numerical-ABA method; b) GPR-IBA method; c) V-JAM method with three clusters (green, yellow, and red); and d) V-JAM method with four clusters (blue, green, yellow, red). Entropy values for each zone of maps c) and d) in the aforesaid figure range

from 7.21 to 4.27, as shown in Table 4.2. When using four cluster zones, the additional blue zone (very good) and green zone (good) primarily fill the green zone (good) of the three-cluster-based map, while the moderate and severely deteriorated zones remained largely unchanged. The percentages of green, yellow, and red zones were measured for maps based on amplitude (map-a), GPR-IBA (map-b), and V-JAM method (map-c) as these three maps reveal an identical number of concrete condition zones (good, moderate, and bad). This quantitative comparison is shown in Table 4.3.

**Table 4.2** Range of entropy values in generated deterioration maps (Mohammed Abdul Rahman, Zayed, et al., 2022)

Map-Direction	Zone	Color (Entropy Values)			
		Blue	Green	Yellow	Red
X-direction	3 Clusters	-	7.21–6.28	6.28–5.44	5.44–4.27
	4 Clusters	7.21–6.34	6.34–5.76	5.76–5.16	5.16–4.27
Y-direction	3 Clusters	-	20.86–11.28	11.28–5.94	5.94–2.22
	4 Clusters	20.86–14.49	14.49–9.92	9.92–5.56	5.56–2.22

First off, the amplitude-based map (map-a) and the developed model (map-c) share certain visual resemblances as both have upper regions that are either severely or moderately corroded. Contrary to map-a, map-c reveals that the slab is overall more corroded because its bottom part is also moderately corroded. In terms of percentage, map-c has 84.3% of its surface covered in yellow and red zones as opposed to 40.7% in map-a. Likewise, Map-a estimates (59.6%) that the slab's concrete state is four times better than map-c (15.7%). The map based on the GPR-IBA (map-b) exhibits higher similarity to map-c because of the visual resemblance of all corrosion zones along with extensive corrosion of the middle part of the slab. In terms of percentage, the overall amount of corroded concrete (yellow and red) in map-b (77.9%) is comparable to map-c (84.3%). Map-b (33.4%), on the other hand, estimates the slab is slightly more corroded than Map-c (29.6%).

**Table 4.3** Quantitative comparison of maps based on the color distribution (concrete condition)  
(Mohammed Abdul Rahman, Zayed, et al., 2022)

Map-Direction	Type of Analysis	Percentage of Color Distribution in Maps		
		Green (Good)	Yellow (Moderate)	Red (Bad)
<b>X-direction (3-clusters)</b>	(a) Amplitude-based	59.6	25.7	14.7
	(b) GPR-IBA	22.1	44.5	33.4
	(c) Developed model	15.7	54.7	29.6
<b>Y-direction (3-clusters)</b>	(a) Amplitude-based	22.6	41.7	35.7
	(b) GPR-IBA	46.1	15.1	38.7
	(c) Developed model	18.2	35.9	45.9

*Y-direction*

The four condition maps of swabs 15–31 generated along the Y-direction using methods similar to the X-axis are displayed in Figure 4.9. The range of entropy values for each colored zone in maps-c and map-d of the aforesaid figure varies from 20.86 to 2.22 and is also shown in Table 4.2. The spread of entropy values is greater along the Y-direction than the X-direction, but these ranges cannot be standardized because the survey data is unique to each scanned element. There is some visual similarity between map-c and map-a because both maps show moderate to severe corrosion on the right side and heavy corrosion in the center of the slab. In terms of numbers, map-c (81.3%) is closer to map-a (77.4%) in terms of the overall amount of corroded concrete (yellow and red). The center and right sections of the slab display excellent visual correspondence in map-b and map-c, however, the left section of map-c, in contrast to map-b, showed some areas of moderate

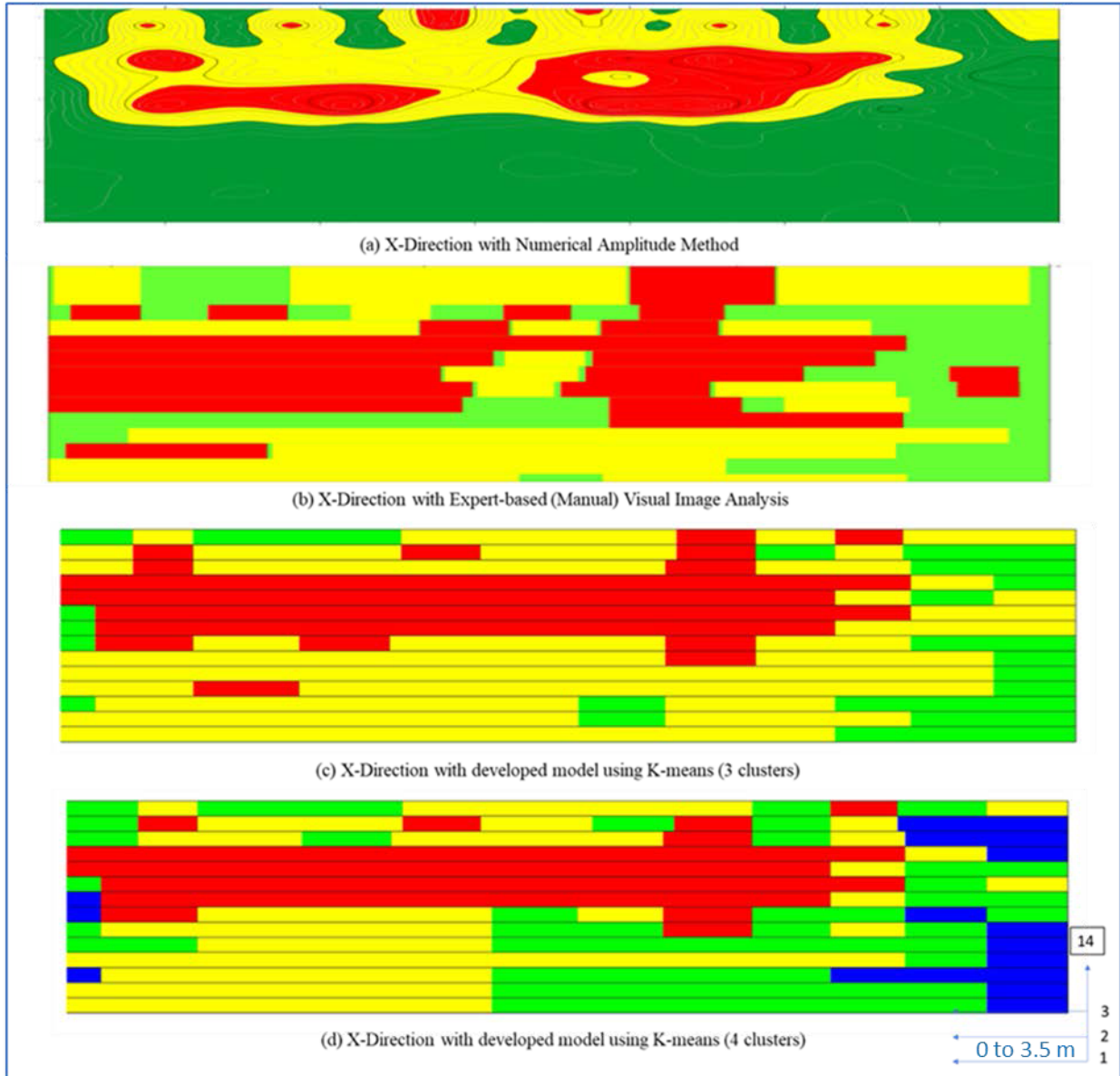
corrosion. This disparity is possibly due to an analyst manually labeling regions of each profile separately to generate map-b while V-JAM clusters all profiles of a data set together and thus, detect zones more accurately. According to map-c (81.3%), the slab is substantially more corroded compared to that in map-b (53.6%). Additionally, map-b (46.1%) estimates that the slab is roughly 2.5 times in better condition than map-c (18.2%). It can be concluded by comparing maps along both directions that the slab is heavily corroded (~80%), and that *map-c is better able to estimate the overall condition of the slab* (Mohammed Abdul Rahman, Zayed, et al., 2022).

#### **4.2.4 Limitations**

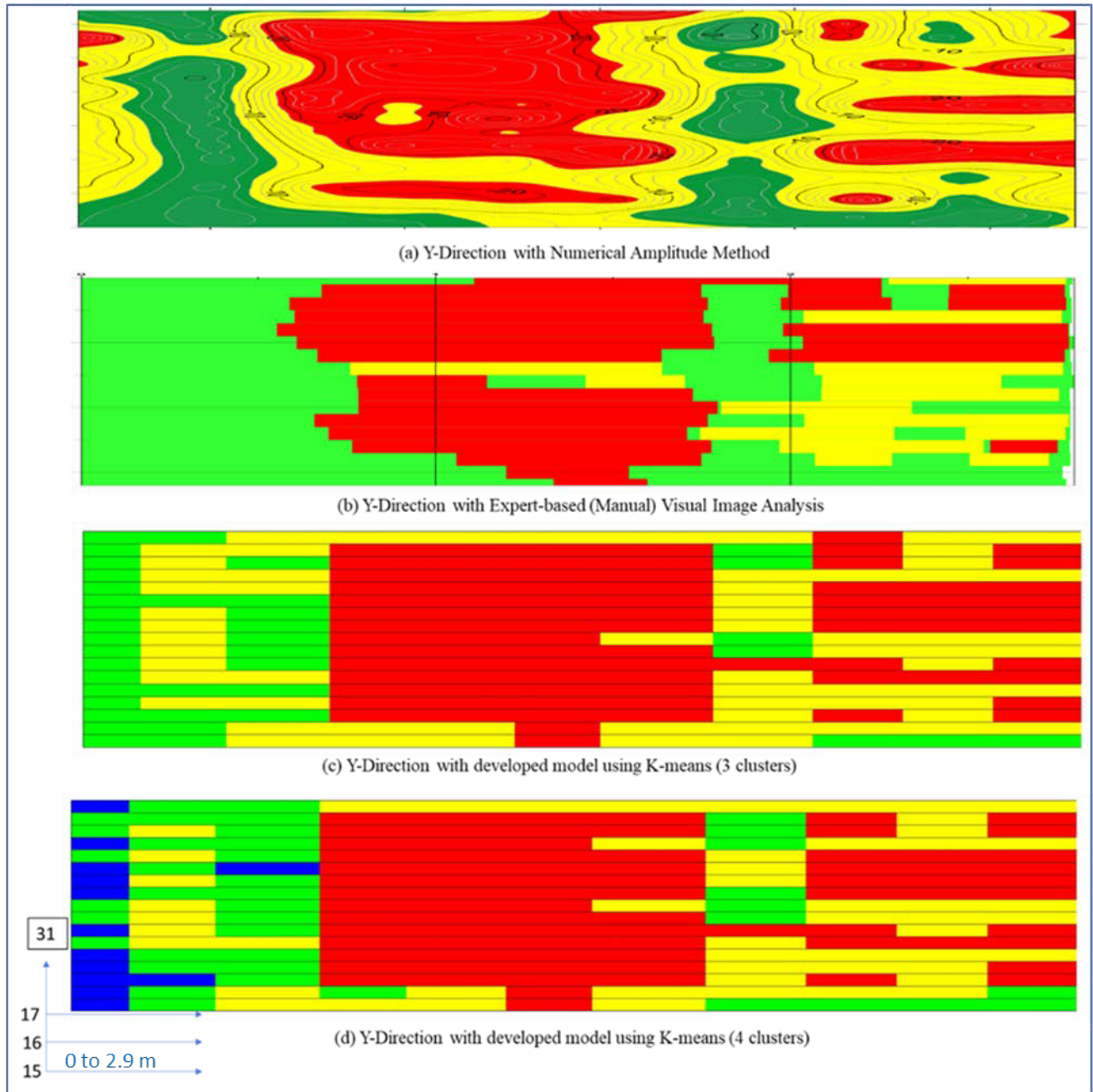
A model has been developed to generate reliable condition maps using GPR B-scans for structural elements with uniformly spaced rebars. The proposed V-JAM method is superior to existing amplitude-based methods and aims to reduce the subjectivity of the GPR-IBA through automation and scientific analysis. The following few limitations can be inferred based on the developed methodology and demonstrated case study:

1. It does not consider various anomalies. This slab did not have any anomalies and thus, the results generated were reliable. However, the *ULAM* of the RUIM method (Section 3.3.4) can be incorporated into this model to overcome this limitation.
2. The hyperbolas in B-scans of scanned elements must be fairly visible with their aspect ratio closer to the trained classifier. In case of the presence of majorly ill-shaped hyperbolas, the detection rate would be very low. Additionally, if the top layer is heavily disoriented, the results would not be reliable as the depth variance is not accounted.
3. Lastly, this model does not take important structural information from the user for the scanned element based on the drawings, natural conditions, and other factors such as the

presence of anomalies, geolocation, and repair work. If such pre-existing information is considered by the model, the results generated would be more robust and reliable.



**Figure 4.8** Condition maps comparison along X-direction (Mohammed Abdul Rahman, Zayed, et al., 2022)



**Figure 4.9** Condition maps comparison along the Y-direction (Mohammed Abdul Rahman, Zayed, et al., 2022)

### **4.3 Case Study C – Condition Mapping based on RUIM**

#### **4.3.1 Data Collection**

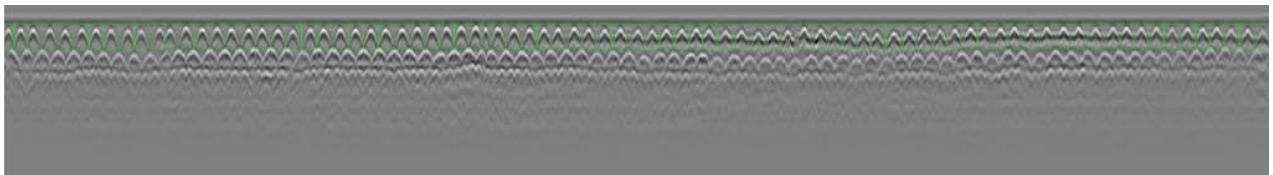
The bridge deck, O2, inspected as part of a comprehensive bridge decks evaluation (Gucunski et al., 2011) and employed in the first case study (Section 4.1) has been utilized in this section to generate a condition map based on the developed Robust User-Interactive Model (RUIM) delineated in Section 3.3 and results were compared with other NDE techniques. The main reasons for using this specific case study, as stated earlier, are the correlation of results of various NDE techniques and in-situ coring samples, whose results would be compared with the map based on RUIM. The input parameters for the GPR survey have been delineated in Section 4.1 and the user-assisted input for RUIM is as follows: *a) Length of deck: 60 feet; b) Traverse spacing: 2 feet; c) Age (when the inspection was performed): 49 years; d) 4) Any visual signs of corrosion in profiles: Yes; e) Any visual signs of severe corrosion: Yes; f) Number of zones for condition mapping: Three; and g) Layer of analysis: Top.* Since the age of the bridge deck is more than 10 years and it has signs of severe corrosion, the number of clusters determined as per the flowchart shown in Figure 3.40 is equal to the total number of zones specified by the user, i.e., *three*.

#### **4.3.2 Results and discussion**

##### *Comparison of NDE maps*

As discussed in Section 4.1.2, Figure 4.3 shows the condition mapping results based on Half-Cell potential and GPR while Figure 4.4 shows the condition mapping results based on Impact Echo (IE) and Electrical resistivity techniques. The location of four cores (1-4) taken for destructive evaluation and comparison have been marked in these maps. The repairs performed after the evaluation of this bridge deck have been overlaid on the condition maps and it indicates that the deck is *heavily corroded majorly in the middle section* (Gucunski et al., 2011).

After importing files and entering user-assisted information, the RUIM method detected all the hyperbolic clusters in each of the twenty-four profiles based on the RHD module. The top layer was correctly identified by RUIM (verified by the user), and no anomalies were detected. Subsequently, false positives were eliminated while missing gaps due to heavy corrosion or ill-shaped hyperbolas were enclosed in boxes for further analysis. Figure 4.10 shows the first profile of the bridge deck with the automated detections enclosed in green boxes. Finally, entropy was evaluated for these boxed regions and a deterioration scale was generated for each of the 24 profiles which were stacked together to generate a condition map. The map generated based on the GPR-IBA method has been redrawn in Figure 4.11(a) along with the location of four cores. Correspondingly, the map generated based on the RUIM method with three cluster zones (good, moderate, and severe) is shown in Figure 4.11(b) along with the location of four cores marked 1-4.

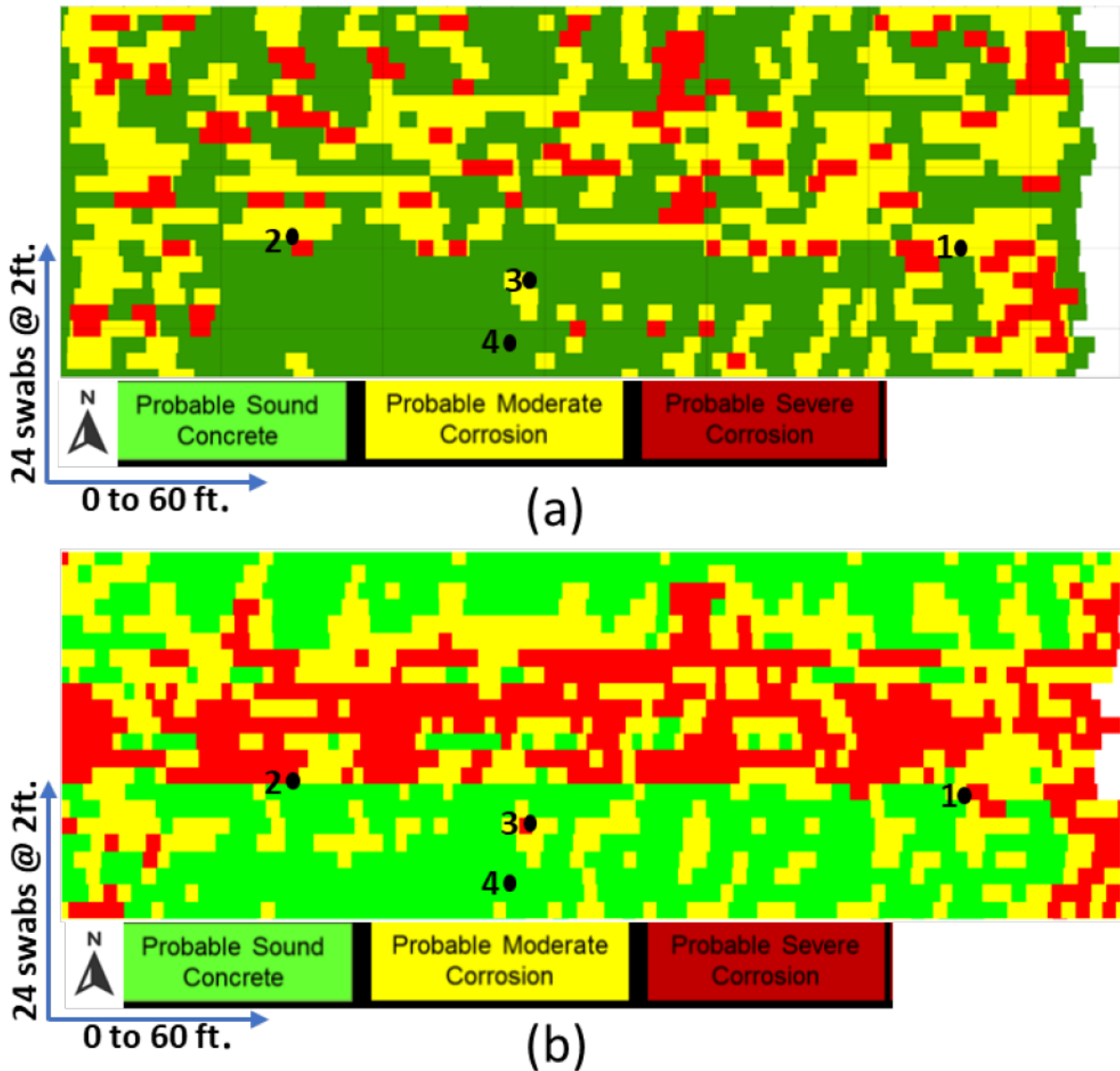


**Figure 4.10** A GPR profile of Bridge deck, O2, with automated detections enclosed

Table 4.4 shows a quantitative comparison of deteriorated areas in corresponding zones based on the GPR-IBA and RUIM. The map based on the RUIM estimates (34.17%) that the total percentage of the area of concrete with moderate corrosion is similar to the area estimated (34.5%) by GPR-IBA. However, RUIM estimates that the bridge deck (23.77 %) is *more* heavily corroded, especially in the middle region, when compared to the estimate (11.5%) of the GPR-IBA approach. Nevertheless, the condition map based on RUIM *corresponds* closely with the maps based on other



NDE techniques including the GPR-IBA as there is a general resemblance of all maps showing that the deck is heavily corroded in the middle section.



**Figure 4.11** (a) Condition map based on GPR-IBA with core locations (1-4); (b) Condition map based on developed RUIIM with core locations (1-4)

**Table 4.4** Quantitative comparison of deteriorated areas

Condition Map	% Green - Good	% Yellow - Moderate	% Red - Severe
GPR-IBA; Figure 4.11(a)	54%	34.5%	11.5%
RUIM; Figure 4.11(b)	42.06%	34.17%	23.77%

*Validation with core samples*

Four cores were extracted at locations shown in all maps for *validation* i.e., to verify if the deterioration level obtained from cores correlated with the field NDE results (condition maps). While the complete analysis of field data for the on-site selection of cores, field procedures, and detailed interpretation of results are described in (Gucunski et al., 2011), the reports also state the core samples validate the results obtained from the four NDE maps (Half-Cell, GPR: numerical-ABA, IE, & electrical resistivity) by revealing expected results of deterioration at those locations. However, to validate the results for the GPR -IBA and the developed model, RUIM, Table 4.5 shows the deterioration level obtained from cores (ground-truth) and compared it to the deterioration level (identified by zone color) at those specific locations in respective condition maps. *Core#1* showed a moderate corrosion level with the presence of delamination and this result was validated with the condition obtained from both maps. However, the results obtained from *Core # 2-3* validated better with the developed RUIM method (high corrosion) when compared to the GPR-IBA approach (moderate). Finally, *Core #4* results were consistent and valid in both maps (sound concrete).

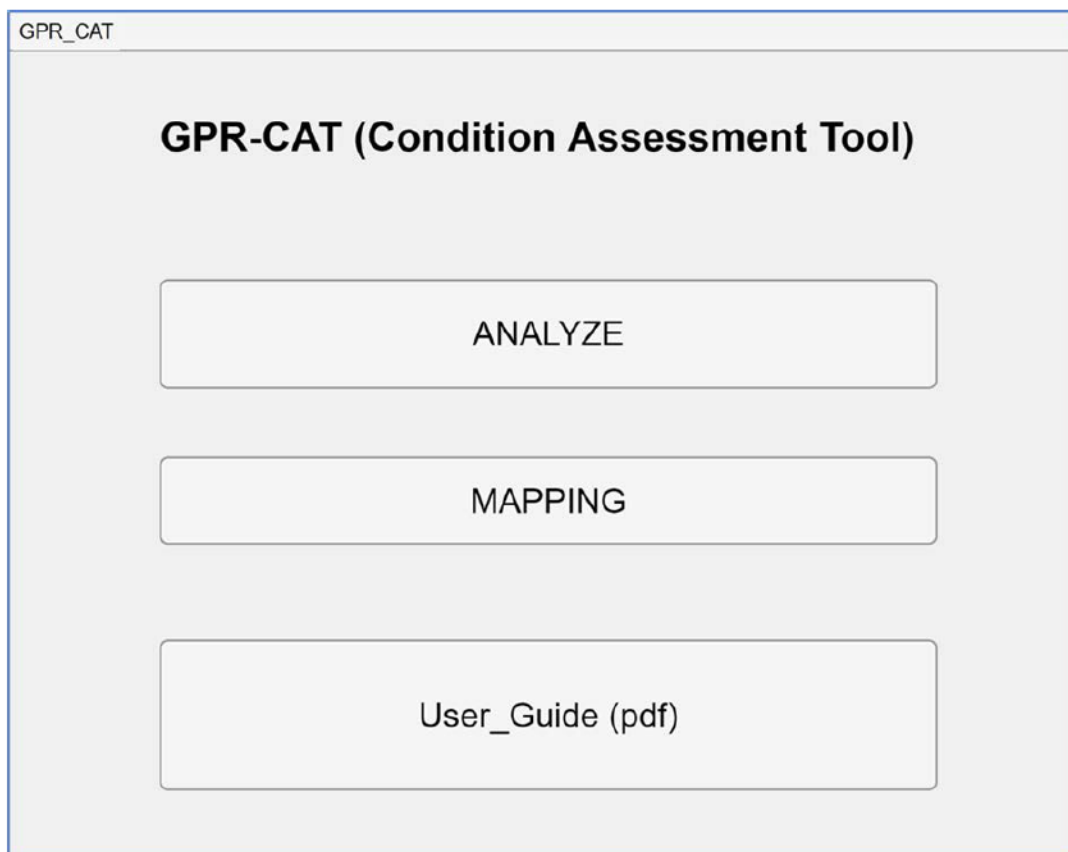
**Table 4.5** Validation of ground truth with GPR-IBA and RUIM condition maps

Core #	Ground-truth deterioration level	GPR-IBA	RUIM
1	Moderate Corrosion with delamination	Moderate	Moderate/High
2	High corrosion with delamination	Moderate	High
3	High corrosion	Moderate/Good	High/Moderate
4	Sound Concrete	Sound Concrete	Sound Concrete

In summary, *greater map correlation for both methods, V-JAM and RUIM, with the GPR-IBA approach suggests that the proposed approaches can identify the zones of deterioration accurately because the results of the GPR-IBA method have been validated to be closer to the actual ground truth (Tarussov et al., 2013), (Abouhamad et al., 2017) and (Dawood et al., 2020). The user-assisted input and ULAM in the RUIM can also be incorporated into V-JAM to identify optimal clusters and detect anomalies. Nevertheless, the RUIM method can detect better hyperbolic clusters (compared to V-JAM) in varied GPR data sets because of its robustness. Importantly, both developed models yield consistent results that are easily reproducible due to scientific analysis.* The (destructive) coring results of the bridge deck, O2, *compared better with the RUIM method compared to the GPR-IBA approach. However, further laboratory testing and in situ, destructive techniques in the field need to be carried out for better validation of the developed model(s) and improved reliance on GPR as an NDE technique. Lastly, the developed models can localize deteriorated areas effectively and can be used by structural inspectors with confidence for repair and rehabilitation purposes (Mohammed Abdul Rahman, Zayed, et al., 2022). Additionally, the results maps are also beneficial in modeling a deteriorated structure to assess its remaining capacity (Ghodoosi et al., 2018).*

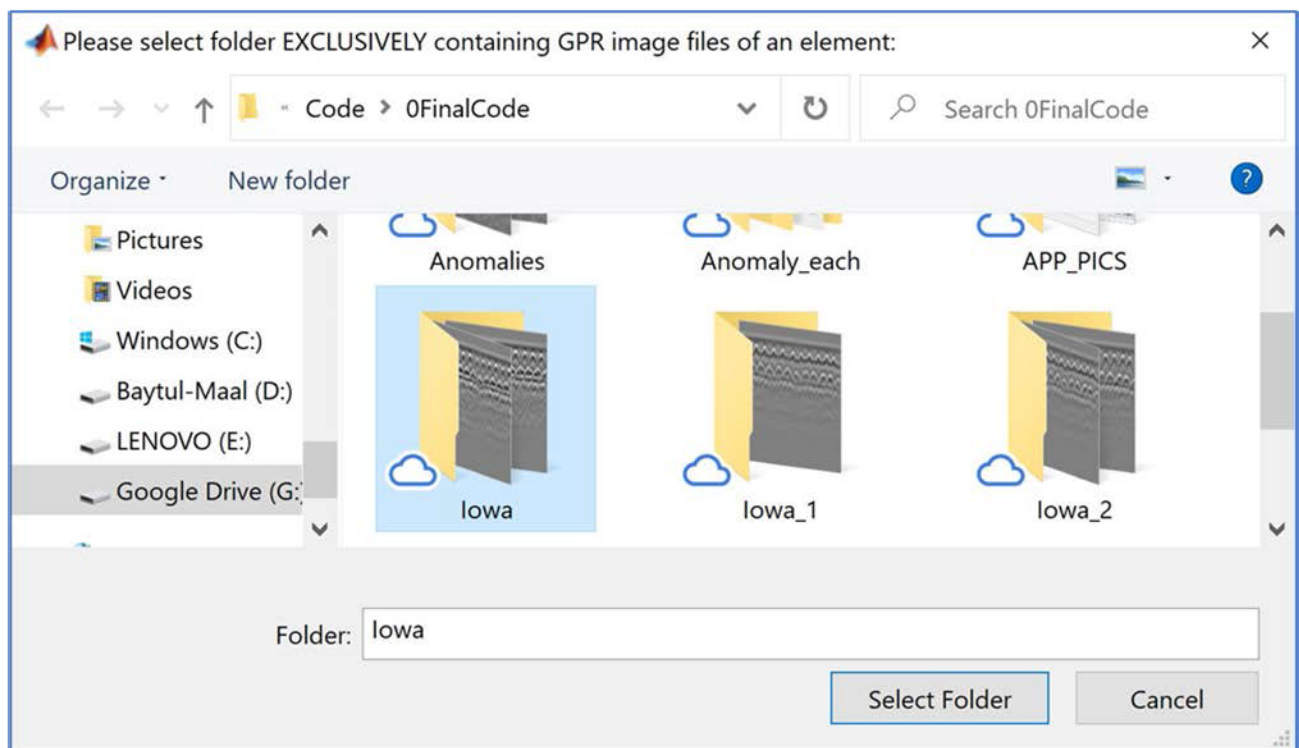
#### 4.4 GPR-CAT (GPR-based Condition Assessment Tool)

A user-friendly software tool has been created using the 'MATLAB App Designer features to develop condition maps of structural elements scanned with GPR. The tool implements the RUM method and is specifically designed to analyze structural elements, such as bridge decks, pavements, and slabs, that often have uniformly spaced reinforcement rebars. It offers a graphical interface to enhance usability and ease of interaction. The application has been given the name '**GPR\_CAT**' and uses a '*.mlapp*' extension. The acronym GPR\_CAT refers to the GPR-based Condition Assessment Tool. Its primary interface includes three pushbuttons, as depicted in Figure 4.12.



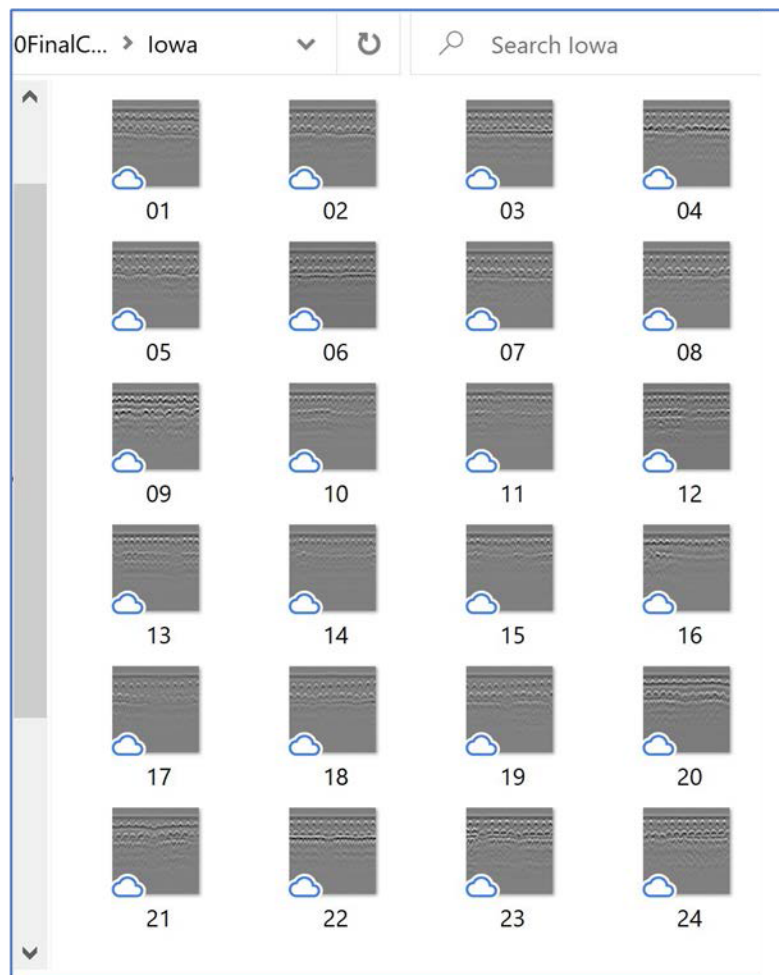
**Figure 4.12** User-Interface of the designed app termed as GPR\_CAT

To obtain a condition map based on GPR scans, you need to click the first two buttons in sequence: a) "ANALYZE" and b) "MAPPING." The implementation of GPR\_CAT is shown stepwise and illustrated with figures based on the developed graphical user interface (GUI) for analyzing the bridge deck, O2, in Case Study C. When the first button, "ANALYZE," is clicked, the user will be prompted to select a folder that exclusively contains all the saved image files of a GPR-scanned element. Figure 4.13 depicts a prompt that appears to the user, requesting them to choose a folder (named 'Iowa') containing all the profiles of GPR images for the bridge deck, O2.



**Figure 4.13** User-Prompted to select a folder containing GPR image files.

In accordance with the guidelines outlined in Section 3.3.1, the files within the separate folder that contain all the GPR images of a scanned element must be named in ascending order. Specifically, for the deck labeled as 'O2', the 24 obtained scans in the '.png' format have been named from '01' to '24'. Figure 4.14 illustrates these named scans, which are contained within the 'Iowa' folder.



**Figure 4.14** Folder 'Iowa' containing all its 24 profiles.

Subsequently, the user will be prompted to provide information about the inspected element, including the length of the scan, traversing spacing, age of the element, and other relevant details. Figure 4.15 illustrates the user's input for the Iowa bridge deck, based on the information presented

in Section 4.3.1. If the user is aware of the age of the scanned element and selects the "Yes" button, an additional input prompt appears, requesting the user to enter the element's age. The software then evaluates an optimal cluster based on this user-provided information, following the methodology described in Section 3.3.5. Once the user completes the 'user input' form, it is necessary to click the 'Save' button to store this data. A confirmation message box is then displayed to acknowledge the successful saving of the data.

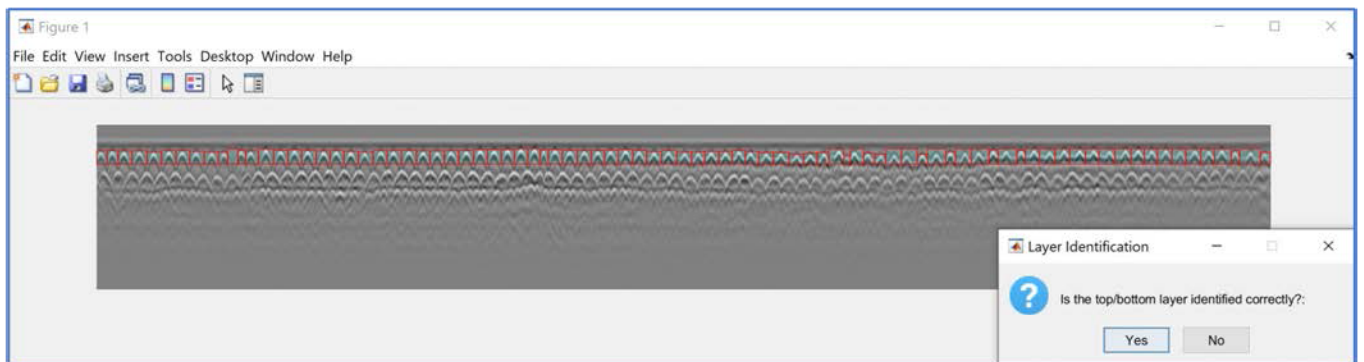
The image shows a software window titled "USER INPUT" with a menu bar (File, Edit, View, Insert, Tools, Desktop, Window, Help) and a toolbar. The main area contains the following form elements:

- Title: PLEASE INPUT INFO ABOUT THE GPR SCANNED ELEMENT
- Length of each scan in (m/ft):
- Traverse spacing in (m/ft):
- Is age of the Element known?:  Yes  Unknown
- Enter age (in years):
- Any visual signs of (moderate/severe) corrosion in profiles?:  
 Yes  No  Not sure
- Any visual signs of SEVERE corrosion in profiles?:  
 Yes  No  Not sure
- No. of Zones/ Clusters for condition mapping (default is 3)?:  
 3  4
- Select the layer for analysis (default is top)?:  
 Top Layer  Bottom Layer
- Note: For last 2 questions, please DE-SELECT the default value & then, select the other option.
- Save button

An overlaid "Success" dialog box contains the text "Data saved successfully." and an "OK" button.

**Figure 4.15** User-assisted Input for the GPR scanned deck.

After the user information is saved, the tool initiates the sequential evaluation of each profile. Starting with the first profile of the deck O2, the tool performs preprocessing on the profile, identifies hyperbolic detections using the RHD module, and encloses these detections within boxes. Then, the user is prompted to confirm if the top layer has been correctly identified, as this is crucial for an effective analysis. Figure 4.16 illustrates the detected hyperbolas for the first profile, accompanied by a user prompt to confirm the accurate identification of the top layer.

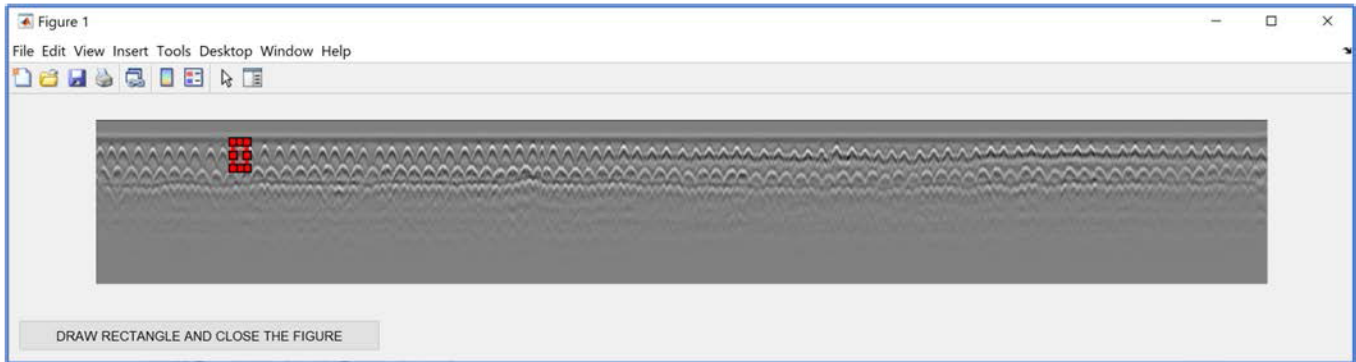


**Figure 4.16** User is prompted to confirm if the specified layer is identified correctly.

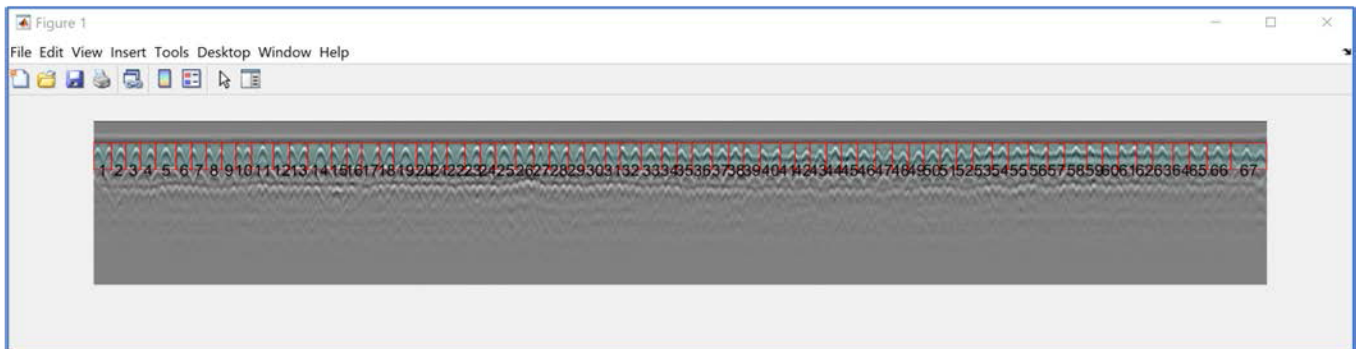
If the tool fails to correctly identify the specified layer, the user should respond with "No" to the layer identification prompt. While the program generally identifies the layer accurately in cases of uniformly spaced rebars, there may be instances where it is unable to detect it correctly. This can happen due to the presence of highly complex hyperbolic variations or extremely undefined hyperbolas across the entire profile. Next, the user is asked to manually draw a minimum-width hyperbola within the correct layer. This allows the tool to automatically detect all hyperbolic boxes associated with this layer using the cubic spline fitting and peak detection algorithms, following the approach explained in Section 3.2.3. As an example, if the tool fails to accurately detect hyperbolic regions and the user presses "No" for the scenario depicted in Figure 4.16, the user can manually draw a rectangle around a hyperbolic region in the top layer of the deck O2, as



demonstrated in Figure 4.17. In response, the tool automatically divides the regions into potential hyperbolic regions along the top layer with a reasonable level of accuracy as shown in Figure 4.18, facilitating further analysis. Although the accuracy of detections may not be correct for all regions along the top layer, the splitting process is carried out optimally to ensure the reliability of the generated condition map. It is important to acknowledge that difficulties in detecting the hyperbolic layer can arise in real cases of GPR profiles, but the developed tool effectively addresses these limitations through automatic detections.

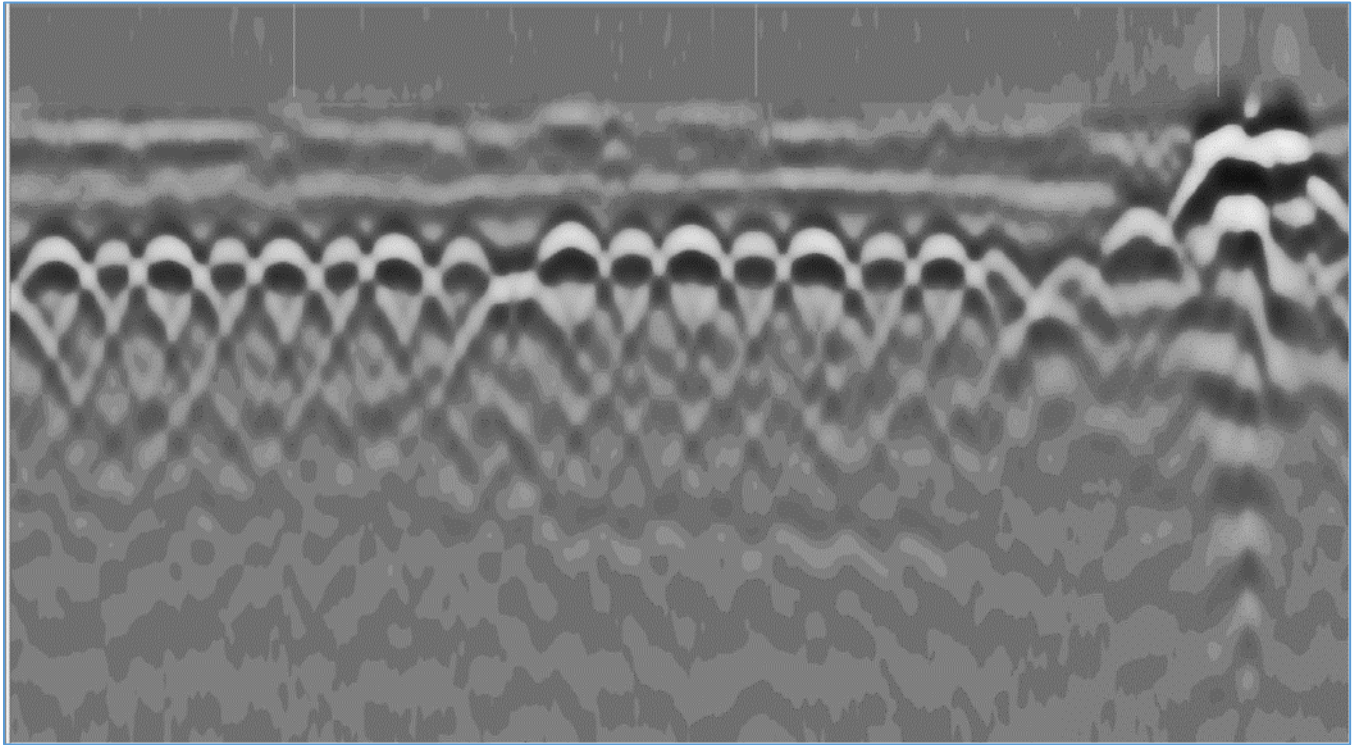


**Figure 4.17** User is prompted to enclose a hyperbolic region at the required layer of analysis.



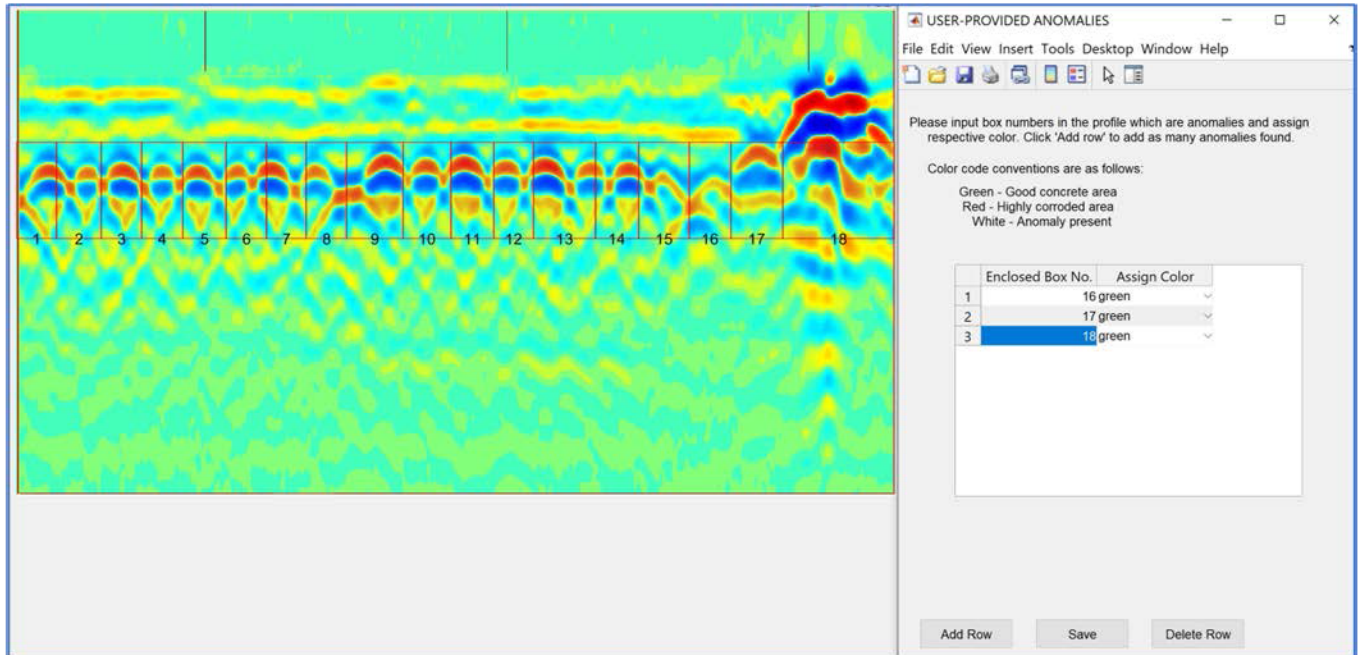
**Figure 4.18** The tool automatically splits into possible hyperbolic regions along the top layer with reasonable accuracy.

After enclosing the detected hyperbolic areas in profiles, the tool prompts the user to assign anomaly regions based on their knowledge and provides figures to assist in this process. As the Iowa deck does not contain anomalies, another example is utilized to illustrate this step. Figure 4.19 displays a profile section featuring an expansion joint.



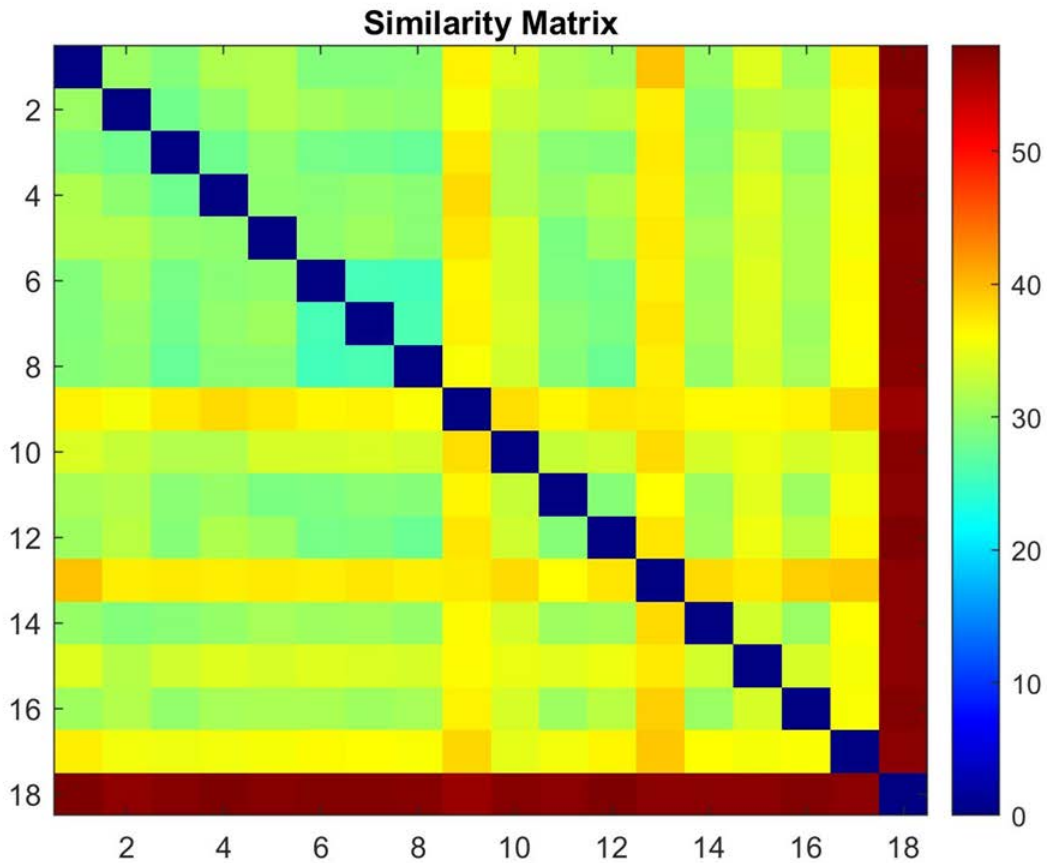
**Figure 4.19** GPR profile with an expansion joint

The first figure of assistance, Figure 4.20, presents a jet colormap that aids in visually distinguishing anomaly areas. The user can specifically examine those boxes that do not have automated detections. It is evident from the colormap that boxes 16 to 18 exhibit differences from other hyperbolic regions due to the presence of the joint. Figure 4.20 also displays a dialog box where the user can enter this information and assign an appropriate color. In this case, the color 'green' has been chosen based on the convention that such regions typically do not require further inspection.



**Figure 4.20** Colormap of the profile with a user-input dialog box to assign anomalies.

The second figure of assistance, Figure 4.21, displays the normalized EUC similarity matrix map of HOG features for all boxes ranging from 1 to 18. In this map, box 18 demonstrates a clear distinction, indicating the potential presence of an anomaly to the user. This map provides additional information to aid in the analysis of the detected regions. When the user inputs anomaly regions, the generated map accurately classifies these zones, thereby preventing errors in the analysis.

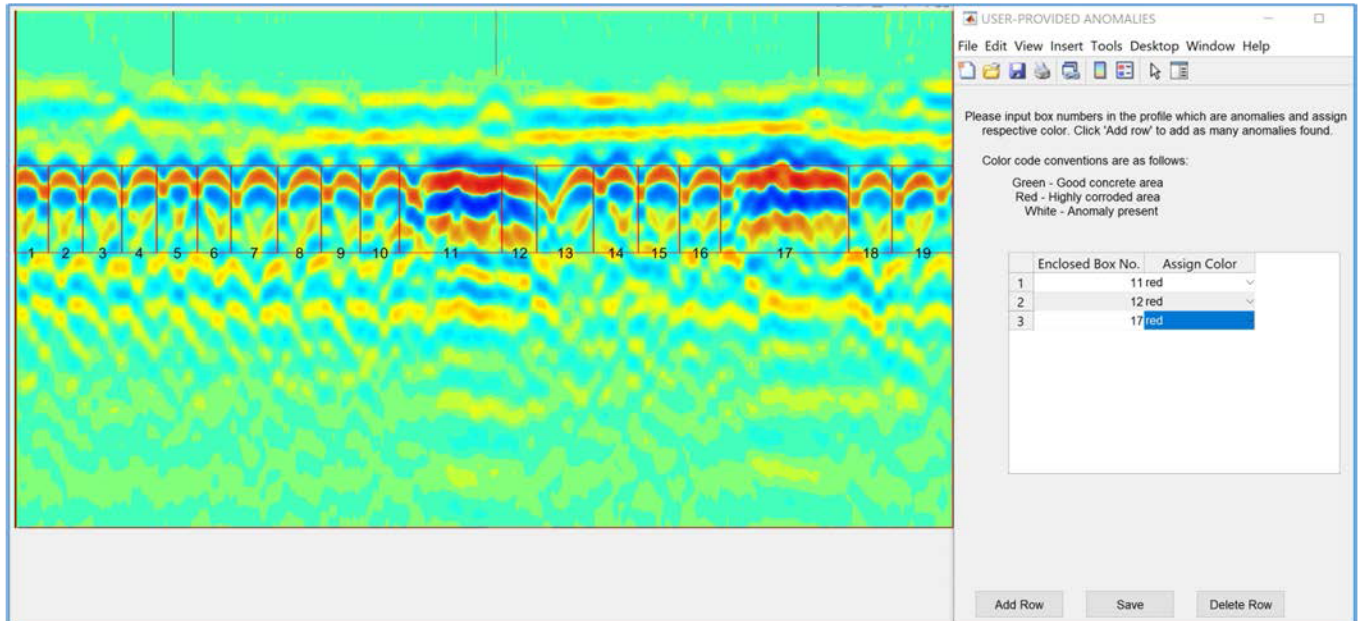


**Figure 4.21** Normalized EUC similarity matrix map of HOG features for all regions.

Figure 4.22 presents another example of a profile with two anomaly regions, which are likely caused by debonding and/or the presence of voids. In this scenario, the user assigns the relevant boxes, specifically boxes 11, 12, and 17, based on the similarity matrix map shown in Figure 4.23. The similarity matrix map highlights boxes 12 and 17, indicating their distinctiveness. To signify that these regions may require immediate inspection, the user assigns the color ‘red’ to these boxes. This enables proper classification and identification of the anomaly regions within the profile. To streamline the process of identifying anomaly regions, the tool offers an option to utilize previous profile anomaly data. This feature eliminates the need for repeatedly assigning the same anomaly regions for each profile, as anomalies tend to be present in similar locations across a set of GPR

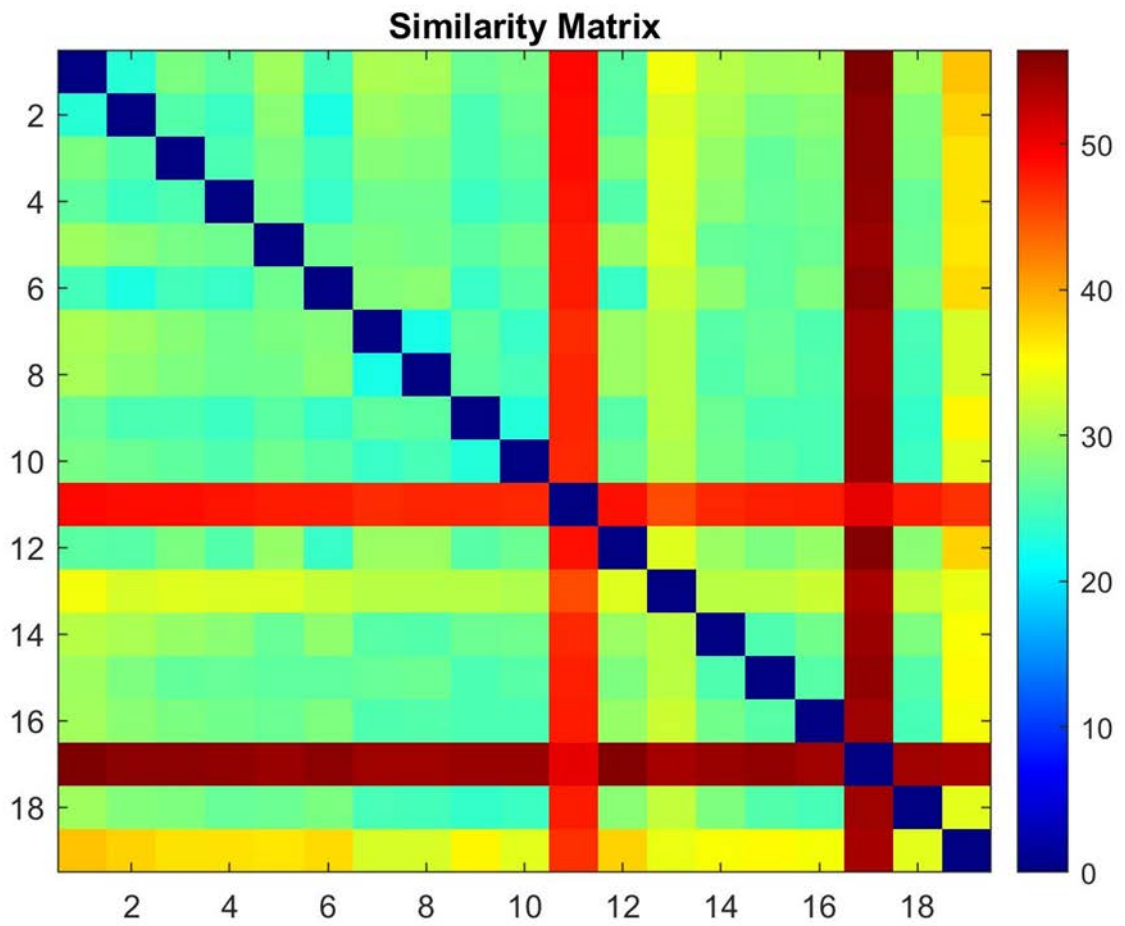


profiles. While this user-interactive approach, which involves assistance from the user, may require additional time during the analysis, it enhances reliability.



**Figure 4.22** Colormap of a GPR profile with a user-input dialog box to assign anomalies.

Upon completion of the necessary steps, the user can click the "MAPPING" button to generate a condition map, as depicted in Figure 4.11(b), specifically for the Iowa deck. Additionally, a "USER-GUIDE" button is available, offering a concise user manual in PDF format that explains the execution steps for the developed tool, GPR\_CAT. To ensure accessibility, the code of the developed tool can be ported to open-source software like *Octave*. This eliminates the need for users to purchase MATLAB or its compiler licenses for GPR-based condition assessment, providing more flexibility in utilizing the tool.



**Figure 4.23** Normalized EUC similarity matrix map of HOG features for all boxes.

## 5 LAB TESTS AND FURTHER CASE STUDIES

### 5.1 Laboratory Testing – Entropy evaluation of subsurface objects in Concrete Slabs

The developed models, RUIM and V-JAM, assessed GPR data utilizing the following three main steps: *a)* automated detections of hyperbolic regions, and user-labeled anomalies, if present; *b)* evaluating a textural factor, *entropy*, for hyperbolic regions; and *c)* classifying regions based on K-means, generating deterioration scale for each profile, and stacking them to generate a condition map. To improve the efficacy of GPR data analysis, a series of laboratory experiments are being conducted in the structural lab of Concordia University, Montréal, along with some possible field tests. Since *entropy* is the primary factor used for detecting hyperbolic regions, tests were conducted to evaluate this factor for GPR B-scans of concrete slabs with varying materials and differing depths, and its comparison was done with respective amplitude values as part of initial laboratory experiments (Donda et al., 2021), (Mohammed Abdul Rahman, Donda, et al., 2022).

#### 5.1.1 Experimental Setup



**Figure 5.1** GPR antenna mounted on a Model 615 handcart (Donda et al., 2021)

The lab experimental setup for this study has been described briefly while complete details can be found in (Donda et al., 2021). The GPR scanning was performed on plain concrete slabs with the following parameters:

- Radar Acquisition System: GSSI® 51600 S model, SIR-4000 control unit, and Model 615 handcart as shown in Figure 5.1
- Antenna Frequency: 1600 MHz
- Pulse Duration: 0.7 ns
- Samples/scan: 256
- Bits/sample: 16
- Dielectric constant: 6.0 (concrete)
- Depth range: 35 cm
- Range Gain: 0

As illustrated in Figure 5.2(a), three plain cement concrete slabs with in-plan measurements of 25 x 50 cm and depths of 5 cm, 10 cm, and 20 cm, respectively, were cast with a high early strength commercial-grade concrete mix called Quikrete 5000. These three slabs were placed in various configurations to acquire GPR scans for each interfacing material (rebar, air, and water). Slab 1 and Slab 3 were layered on top of one another in the *first configuration*, with the interface material sandwiched in between. It was utilized to assess GPR scans with the material placed at a 5 cm depth of concrete. In the *second configuration*, Slab 2 was stacked over Slab 3 to examine profiles at a 10 cm depth. In the *third configuration*, all three slabs were employed. Slabs 1 and 2 were stacked together, and the interfacing material was tested at a total depth of 15 cm, with Slab 3 at the bottom (Donda et al., 2021),.





(a)

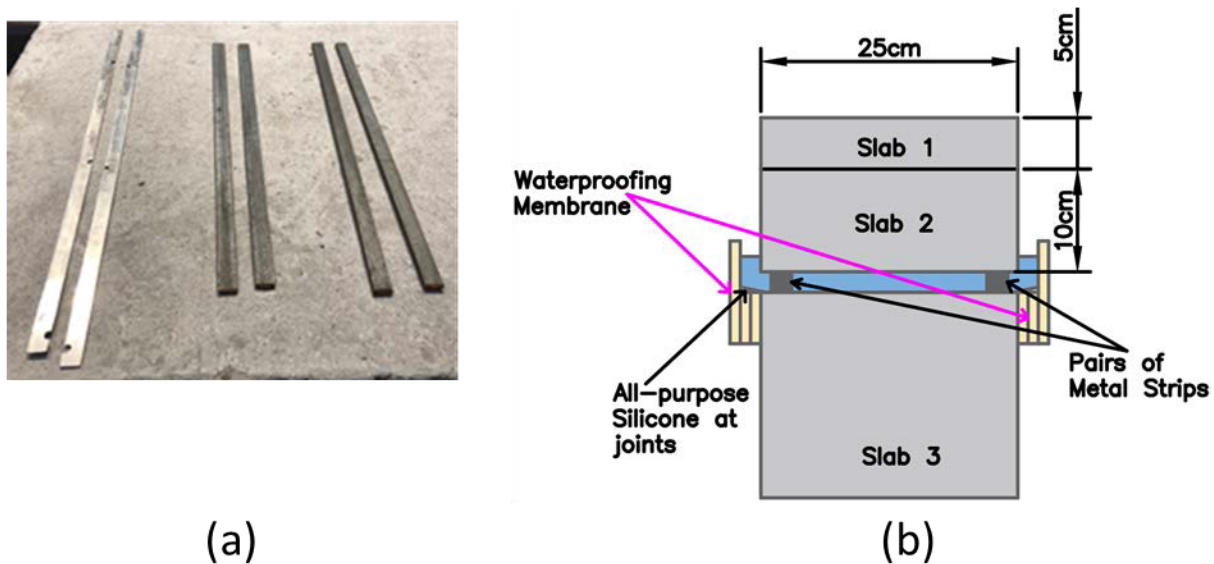


(b)

**Figure 5.2** (a) Three slabs were cast in the laboratory with dimensions shown; (b) Various sizes of rebars used for testing Used (Left to Right; 6 mm, 10 mm, 18 mm, 20 mm, & FRP 21.8 mm) (Donda et al., 2021)

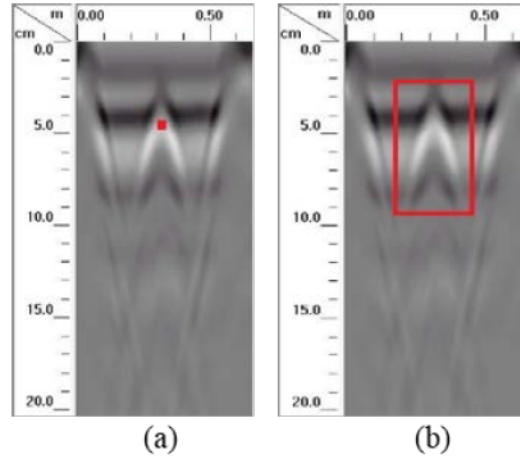
This study used four rebars with diameters of 6 mm, 10 mm, 18 mm, and 20 mm as well as a FRP bar with a diameter of 21.8 mm to evaluate reflections from the *rebars*, as shown in Figure 5.2. (b). A single bar was positioned between slabs for scanning during each test because the slab dimensions were small, and this ensured that a complete hyperbolic reflection was obtained with no overlaps. In order to imitate the *air gaps* and study their impact on signal attenuation, pairs of metal strips of various sizes were edge-positioned along the length of the GPR scan (to prevent GPR signal interference) for each slab configuration. The concrete could have air gaps formed inside it for a variety of reasons, such as cracks that normally appear during the summer due to deterioration which are then filled with air and other impurities. Figure 5.3(a) illustrates the sizes of the metal strips used to represent the thickness of the air gaps: 3 mm, 4 mm, 4.8 mm, 5.8 mm, and 8.8 mm. The experiment was carried out for each of the three slab configurations to examine attenuation at different depths (5 cm, 10 cm, and 15 cm) caused by various air gap widths. *Water*

*gaps* may develop inside the concrete for a variety of reasons, such as drainage water seeping into tunnels, penetration due to rainwater runoff, or melted snow caused by salts, usually in colder climates. In order to replicate water gaps, similar arrangements to those used for air gaps were utilized, but to prevent water leakage at membrane joints, a multipurpose waterproofing membrane and an all-purpose silicone were additionally applied to ensure water tightness. A schematic diagram of the special configuration used to simulate a water gap for the third configuration (15 cm depth) can be seen in Figure 5.3(b) (Donda et al., 2021),.



**Figure 5.3** (a) Various sizes of metal strips used (Left to Right; 1 mm, 3 mm, & 4.8 mm thickness); (b) Schematic diagram to simulate water gap at 15 cm depth (Donda et al., 2021)

Figure 5.4 displays a sample scan of a 20 mm rebar placed at a depth of 5 cm between two plain concrete slabs (first configuration) to demonstrate the evaluation of amplitude and entropy from GPR scans. Figure 5.4(a) illustrates the calculation of the amplitude value based on the explanation in Section 2.8.3, and Figure 5.4(b) illustrates the computation of the entropy value for the image region enclosed by a red box based on the explanation in Section 3.2.4.

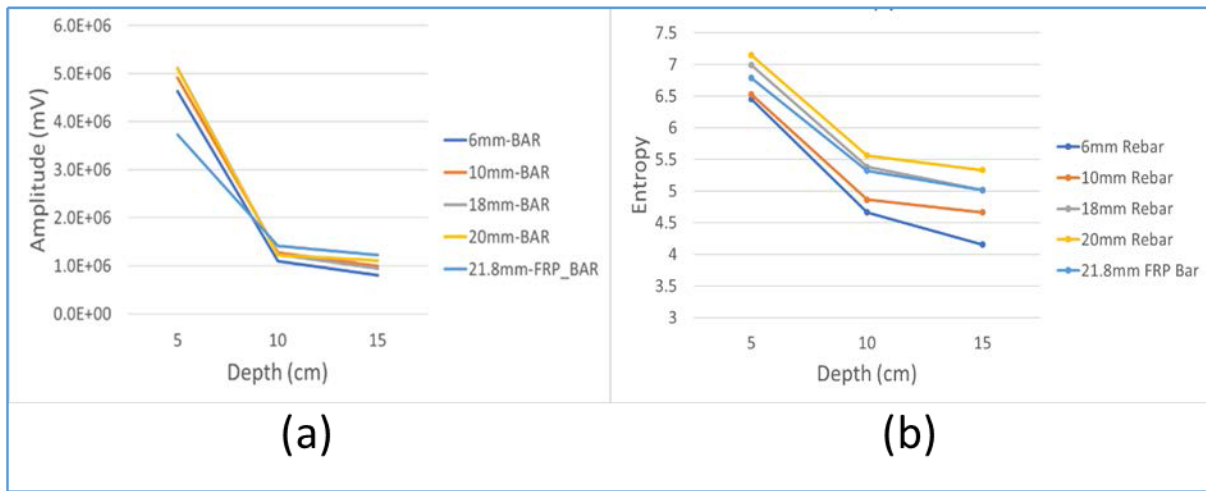


**Figure 5.4** (a) Measuring amplitude at peak (red dot); and (b) Measuring Entropy for the bounded region (red box) (Mohammed Abdul Rahman, Donda, et al., 2022)

### 5.1.2 Comparative analysis for rebars

GPR scans were repeated thrice for each case of rebar size (6 mm to 21.8 mm) at all depths (5 cm, 10 cm, and 15 cm) to ensure lab test conformity and consistency. Therefore, amplitude values were measured at hyperbolic peaks, and values were averaged over three scans unless an anomaly was identified which was discarded. Similarly, the entropy values for a rectangular region enclosing the hyperbolic reflection were evaluated and averaged. For all rebar diameters, including 6 mm, 10 mm, 18 mm, and 20 mm rebar as well as a 21.8 mm FRP bar, Figure 5.5(a) displays the amplitude of reflection vs depth graph and Figure 5.5(b) displays the entropy values vs depth graph. The values of both these factors (amplitude and entropy) increase across all depths as rebar diameter increases. For instance, at a depth of 5 cm, the amplitude value increased by 10.9% from  $4.6 \times 10^6$  mV for 6 mm rebar to  $5.1 \times 10^6$  mV for 20 mm rebar. Similarly, for the same depth, the entropy value exhibited a good correlation as it increased from a value of 6.45 for a 6 mm rebar to 7.15 for a 20 mm rebar (10.9% increase). However, the 21.8 mm FRP bar was the outlier in the results due to its different dielectric characteristics. The signal attenuation values decreased as depth increased

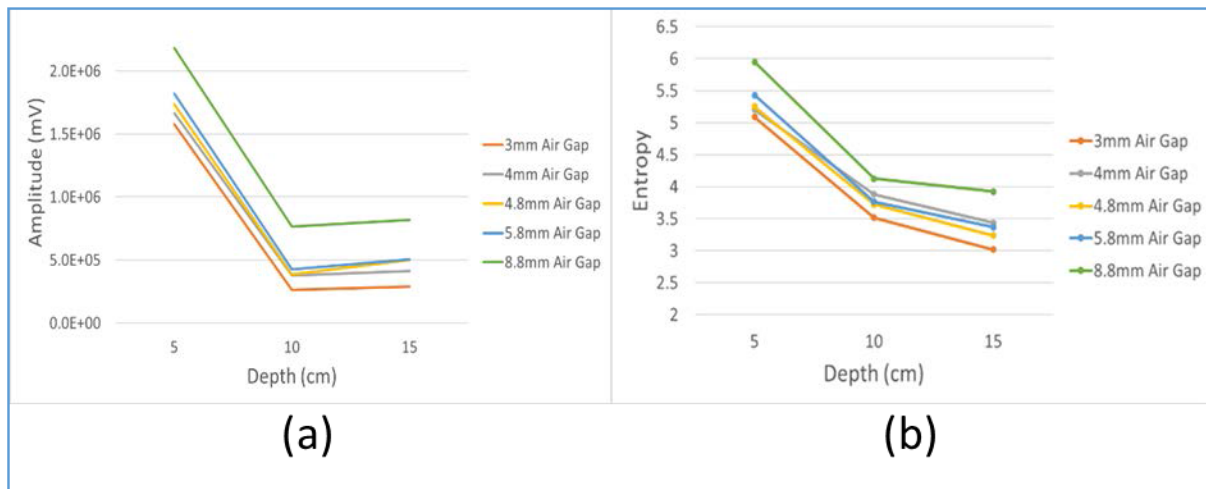
because greater penetration results in more signal loss. To draw inferences, an average value was taken for all rebars (6 mm to 20 mm, except the FRP bar) at each depth. From a depth of 5 cm to 10 cm, amplitude values for each rebar significantly decreased; the average value decreased by 76%, from  $4.9 \times 10^6$  mV to  $1.2 \times 10^6$  mV. Additionally, the averaged amplitude values noticeably declined from a depth of 10 cm to 15 cm by 20% ( $1.2 \times 10^6 - 0.96 \times 10^6$  mV). The averaged entropy value also decreased from a depth of 5 cm to 10 cm by 24.5% (6.8 - 5.1), and from 10 cm to 15 cm by 6.4% (5.1 - 4.7). Entropy numbers had a smaller range than amplitude values, hence the overall drop percentage was lower but comparable. Two conclusions can be drawn from the measured values of amplitude and entropy for rebars: a) for all rebar sizes, a sharp decrease in both factors is seen with depths, but b) it is difficult to discriminate between different rebar sizes in real-case scenarios since an increase in rebar size has a minor impact on the increase in both factors (Mohammed Abdul Rahman, Donda, et al., 2022).



**Figure 5.5** (a) Amplitudes for rebars of varying sizes (Donda et al., 2021); (b) Entropies for rebars of varying sizes (Mohammed Abdul Rahman, Donda, et al., 2022)



### 5.1.3 Comparative analysis for air gaps

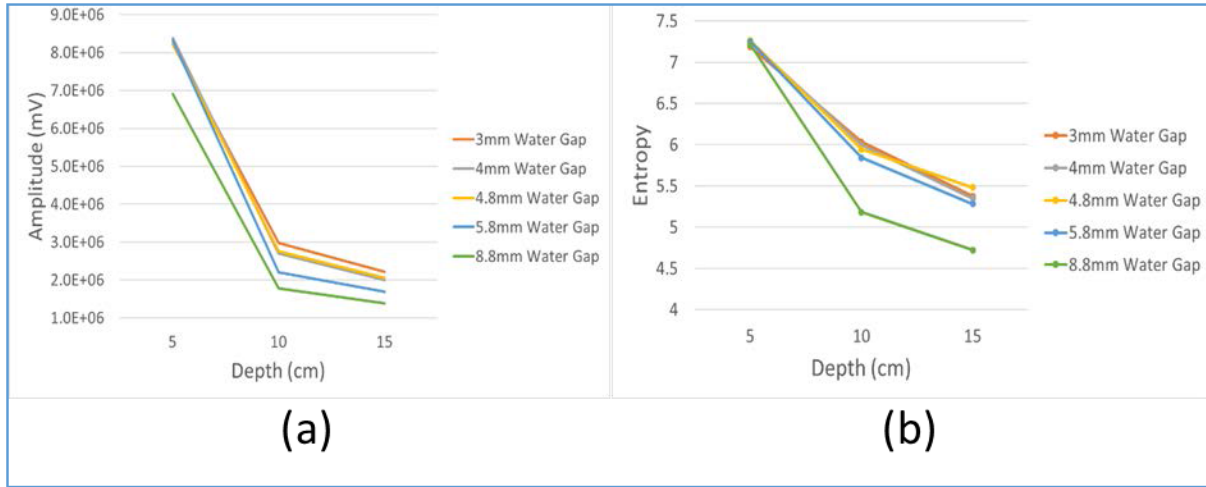


**Figure 5.6** (a) Amplitudes for varying thicknesses of air (Donda et al., 2021); (b) Entropies for varying thicknesses of air gaps (Mohammed Abdul Rahman, Donda, et al., 2022)

To ensure lab conformity, the tests were similarly repeated three times for each experiment on air gaps. For all gap sizes, Figure 5.6(a) plots amplitude values vs depth, and Figure 5.6(b) plots corresponding entropy values. The values of both factors for air gaps increased along with an increase in gap size across all depths. For instance, at a depth of 5 cm, the amplitude value increased from a 3 mm gap ( $1.6 \times 10^6$  mV) to an 8.8 mm gap ( $2.2 \times 10^6$  mV) by 38%, while the entropy value increased by 17%. (5.09 - 5.95). From a depth of 5 cm to 10 cm, all sizes of air gaps exhibited a significant decrease in both factors. For instance, when averaged for all gaps from 5 cm to 10 cm depth, there was a 75% decrease in amplitude value ( $1.8 \times 10^6$  mV -  $0.44 \times 10^6$  mV) and a 29% decrease in entropy values (5.39 - 3.80). When the depth was increased from 10 to 15 cm, there was an inconsistent average increase in amplitude of 14% ( $4.44 \times 10^5$  mV -  $5.06 \times 10^5$  mV), but the entropy values were consistent with an average drop of 11%. (3.8 - 3.4). The relatively weak reflections observed at greater depths are the cause of these skewed amplitude values, but this

limitation is circumvented by using the ‘entropy’ image processing factor (Mohammed Abdul Rahman, Donda, et al., 2022).

#### 5.1.4 Comparative analysis for water gaps



**Figure 5.7** (a) Amplitudes for varying thicknesses of water gaps (Donda et al., 2021); (b) Entropies for varying thicknesses of water gaps (Mohammed Abdul Rahman, Donda, et al., 2022)

Results from the water gap analysis were considerably different from those from other materials. For all gap sizes, Figure 5.7(a) plots amplitude values against depth while Figure 5.7(b) plots corresponding entropy values. For water gaps ranging from 3 mm to 5.8 mm in depth, it was noted that the amplitude and entropy values remained relatively similar across all depths. However, across all depths from a gap of 5.8 mm to 8.8 mm, an average decrease in amplitude value of 18% ( $1.22 \times 10^7$  mV -  $1.01 \times 10^7$  mV) an average decrease in entropy value of 7% (18.3 - 17.11) were observed. The entropy value at an 8.8 mm gap for a 5 cm depth was anomalous because it was closer to a 5.5 mm gap. The discrepancy can be explained by the significant impact of moisture and/or water content on GPR signals. Higher amplitude values suggested that the attenuation was less for small water gaps (3 mm to 5.8 mm). However, lower values of 8.8 mm gaps indicate

reflections become weaker as the water gap widens. This suggests that to detect variation in the examined factors, the water gap size difference must be significant. Nonetheless, a consistently significant average drop in both factors was seen with increasing depth throughout all water gaps. For depths of 5 cm to 10 cm, an average decrease in amplitude values of 69% ( $8.02 \times 10^6$  mV -  $2.48 \times 10^6$  mV) and an average decrease in entropy values of 20% (7.23 - 5.8) were observed. Similar but relatively minor decreases in averaged amplitude values of 25% ( $2.48 \times 10^6$  mV -  $1.87 \times 10^6$  mV) and 10% (5.8 - 5.24) in all water gaps were seen at depths from 10 cm to 15 cm (Mohammed Abdul Rahman, Donda, et al., 2022).

#### ***5.1.5 Comparative analysis for different materials***

A comparative analysis of signal attenuation has been done based on amplitude and entropy values for different materials (rebars, air, and water). Since rebars and gaps varied in size, an average value for both factors (amplitude or entropy) was taken at each depth for each material for suitable comparison. For example, a single representative amplitude value for varying rebar sizes (6 mm to 20 mm) was calculated to be  $4.94 \times 10^6$  mV, which is the average amplitude value for all rebar sizes at 5 cm depth. The FRP rebar values were omitted because they are an outlier. The averaged amplitude values for all materials are shown in Table 5.1, and the corresponding averaged entropy values are shown in Table 5.2. The trend should *ideally* be consistent across all materials because an increase in depths results in higher attenuation of signals. It holds true for amplitude values of rebars and water gaps as there was a consistent decrease with depth. However, the amplitude values did not produce reliable results for air gaps. *But the trend remained reliable with entropy values for all materials across all depths.* The results also reveal that, at a given depth, reflections from water gaps are the strongest, followed by those from rebars, and finally, those from air gaps. Using GPR, the range of these values could be used to differentiate between various subsurface materials.

Additionally, the loss in signal reflection is greater across all materials from a depth range of 5 cm to 10 cm than it is at a depth range of 10 cm to 15 cm. It indicates that much of the energy of the reflected signals is lost closer to the surface.

**Table 5.1** Comparison of Amplitudes for different materials (Donda et al., 2021)

<b>Amplitude (mV)</b>			
<b>Depth↓</b>	Rebars	Air Gaps	Water Gaps
<b>5 cm</b>	$4.94 \times 10^6$	$1.80 \times 10^6$	$8.02 \times 10^6$
<b>10 cm</b>	$1.21 \times 10^6$	$4.44 \times 10^5$	$2.48 \times 10^6$
<b>15 cm</b>	$7.12 \times 10^5$	$5.06 \times 10^5$	$1.87 \times 10^6$

**Table 5.2** Comparison of Entropies for different materials (Mohammed Abdul Rahman, Donda, et al., 2022)

<b>Entropy Values</b>			
<b>Depth↓</b>	Rebars	Air Gaps	Water Gaps
<b>5 cm</b>	6.78	5.39	7.23
<b>10 cm</b>	5.12	3.80	5.80
<b>15 cm</b>	4.79	3.40	5.24

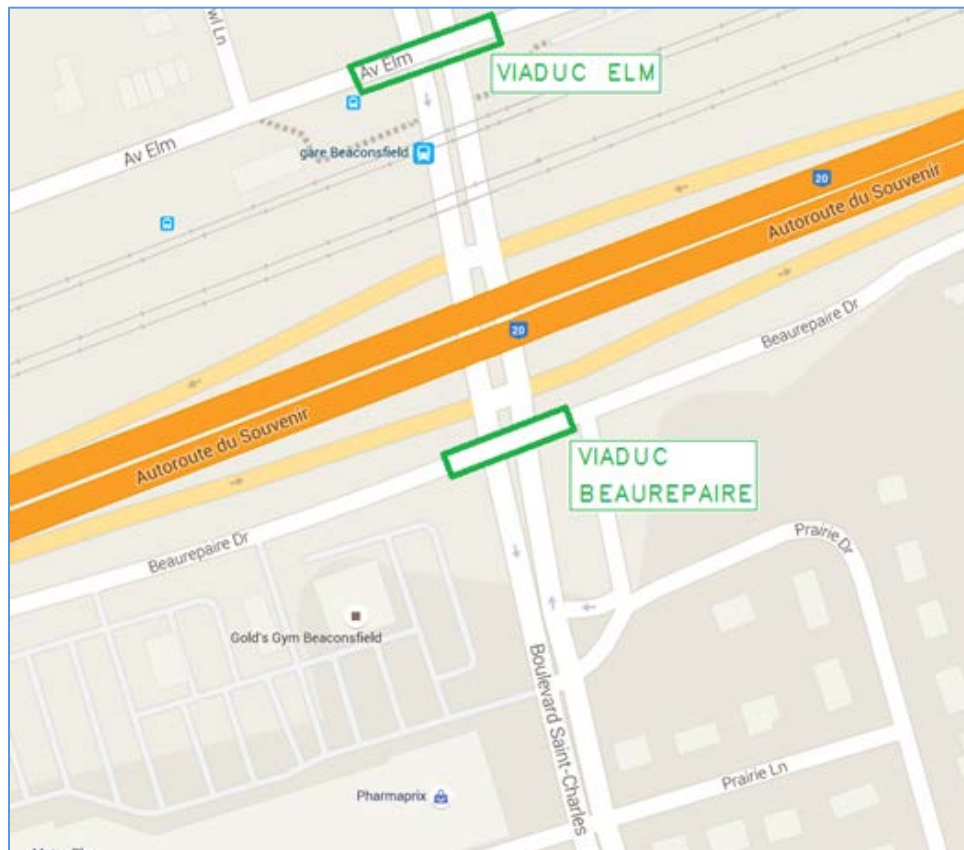
In conclusion, a GPR study was carried out in a controlled laboratory setting using concrete slabs with varying materials and differing depths and the evaluated entropies and respective amplitude values were compared. If the interface material is rebar, increasing the rebar size at any depth causes an increase in both evaluating factors. A decrease in amplitude and entropy values also occurs as depth increases. An increase in both factors was observed with an increase in air gap sizes but a decrease was observed with an increase in water gaps across all depths. Additionally, only entropy values consistently decrease as depth increases. Lastly, the study indicates that GPR can be successfully used to detect and distinguish various subsurface objects at differing depths based on evaluated factors while entropy yielded *consistently reliable* results.



## 5.2 Case Study D – Viaduct Elm P-13486-02

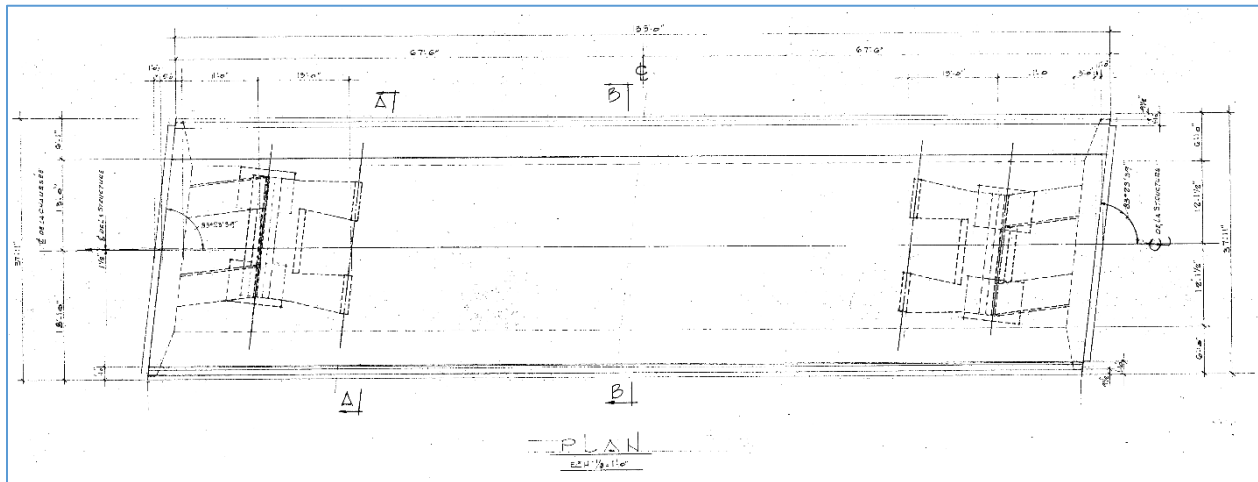
The application of the developed model with the RHD module (for detections) in generating condition maps has been demonstrated further with two additional case studies of bridge decks located in Quebec. The bridge data has been provided by *Radex Detection Inc.*, a georadar company headquartered in Montreal. These decks were scanned using GPR and investigated by this company for condition assessment which included corrosion mapping. The GPR data of these decks were analyzed based on the developed model and compared with the GPR-IBA analysis along with coring samples.

### 5.2.1 Data Collection



**Figure 5.8** Location of Elm and Beaurepaire overpass in Beaconsfield, QC

The Viaduct Elm (overpass) along with the Viaduct Beurepaire (presented as the next case study) was scanned in September 2015 using GPR to analyze rebar corrosion and detect upper reinforcement covering. Additionally, three cores were taken in each Viaduct to determine chloride content and verify with the generated maps. These viaducts are located adjacent to the crossing of Auto-route du Souvenir (A. 20) and Boulevard Saint-Charles in Beaconsfield, QC as shown in Figure 5.8. It facilitates two-way traffic traveling with one traffic lane along the East and West directions.



**Figure 5.9** Viaduct Elm Plan

The Viaduct Elm has a length of 135' ft. (41.15m) and the total width of the deck is 35' 11'' (11.56m) with 1'6'' (0.46m) curbs on either side as illustrated in Figure 5.9. The data was collected along the longitudinal direction and eighteen swabs were taken each 0.5m apart to cover the whole width. The road was closed during the data collection and GPR scans were taken along with three extracted cores. The GPR equipment used for the survey was SIR 3000 GSSI® Structure Scan with a 1600 MHz antenna mounted on a GSSI Utility Cart Model No. 623.

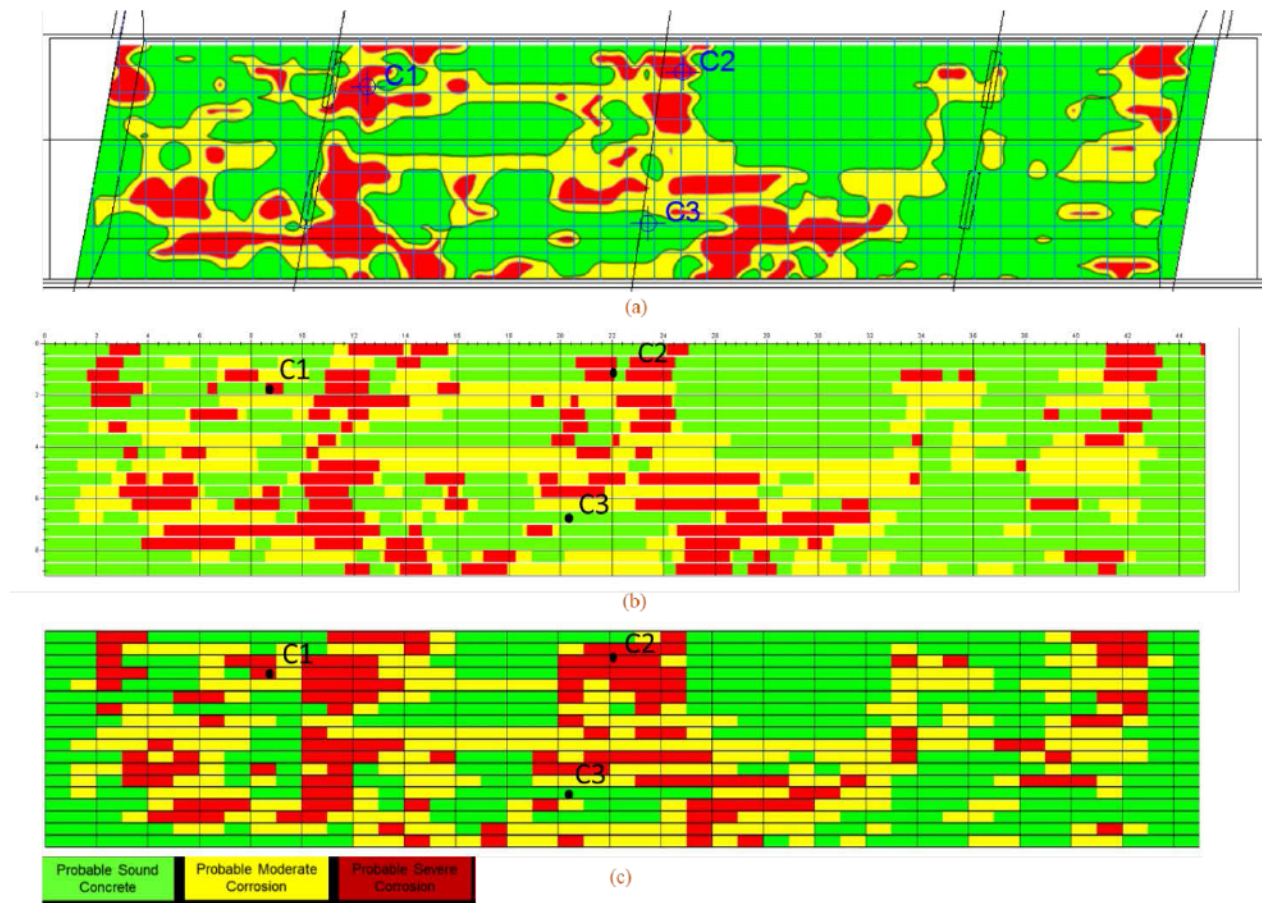
These are the input parameters for the survey performed:

- Antenna frequency: 1600 MHz

- Scans/m: 100
- Samples/scan: 256
- Bits/sample: 16
- Range Gain: 0
- FIR Filter, Vertical, High 470 MHz
- FIR Filter, Vertical, Low: 1930 MHz

### 5.2.2 Condition mapping

The condition map generated based on GPR-IBA drawn in the Surfer® model is shown in *Figure 5.10(a)*. It is mapped at an angle to simulate its overlay over the actual bridge deck plan. As stated in earlier sections, the GPR-IBA involves manually marking the areas by an analyst as probable “green”, “yellow” or “red” corresponding to the condition of hyperbolas and the areas in the GPR profile. *Figure 5.10(b)* shows the actual map generated based on this approach using RADxpert® 2019 software. The condition map based on the developed model is shown in *Figure 5.10(c)* and it involved the following user-assisted input: a) Length of deck: *41.2 m*; b) Traverse spacing: *0.5 m*; c) Age (when the inspection was performed): *46 years*; d) 4) Any visual signs of corrosion in profiles: *Yes*; e) Any visual signs of severe corrosion: *Yes*; f) Number of zones for condition mapping: *Three*; and g) Layer of analysis: *Top*. Since the age of the bridge deck is more than 10 years and it has signs of severe corrosion, the number of clusters determined as per the flowchart shown in *Figure 3.40* is equal to the total number of zones specified by the user, i.e., *three*.



**Figure 5.10** Viaduct Elm maps with the location of Cores marked as C1-C3 including (a) GPR-IBA in Surfer®; (b) GPR-IBA in Radex and (c) RUIM-based map

In general, the maps in *Figure 5.10* showed high resemblance and great correlation as the corroded zones lie primarily in similar areas in all of them. The bridge deck has a total corroded area of about 40~45% while severely corroded areas in all the maps are about 15~20%. The figure also shows the three cores extracted from the bridge deck taken for additional testing in all maps. Core C1 and C2 were taken from possibly a severely corroded area on the site (before complete GPR data analysis) while Core C3 was taken from a sound concrete region. The coring results *corroborated* with the deteriorated regions marked respectively in all the maps.

### 5.3 Case Study E – Viaduct Beaurepaire P-13486-03

#### 5.3.1 Data Collection

The Viaduct Beaurepaire was scanned along with the Viaduct Elm using the same GSSI equipment, survey input parameters, and user-assisted information for RUIIM. This deck is also similar in length (41.15m) and width (11.56m) and therefore, an equal number of scans (18) were taken along the longitudinal direction with each swab 0.5 apart. Figure 5.11 shows the bridge deck plan which was scanned using GPR between expansion joints (sidewalks excluded).

#### 5.3.2 Condition mapping

*Figure 5.12(a)* shows the GPR-IBA map as overlaid on the actual bridge deck using Surfer®. The GPR-IBA map in Radex software is shown in *Figure 5.12(b)* while the map based on the developed model as discussed in the Elm case is shown in *Figure 5.12(c)*. The corroded areas have a high correlation between the maps similar to the Elm case. The total corroded area in the Viaduct Beaurepaire is lesser than Elm in all the maps as it is evaluated at around 35 ~ 40%. However, the percentage of severely corroded area in Viaduct Beaurepaire in all the maps is evaluated to be around 25~30%, which is relatively higher than Viaduct Elm. The extracted cores taken from this Viaduct are also shown in all maps. While Core C1 was taken from an estimated zone to be severely corroded and the result corroborated in maps, Core C2 was also estimated to be in a severely corroded zone. However, C2 was found to be located just outside the corroded area in the GPR-IBA maps while it lay in a moderately corroded zone in the RUIIM-based map i.e., showing a relatively better correlation. The Core C3 corroborated with the estimated zone in all maps as being in a sound concrete region.

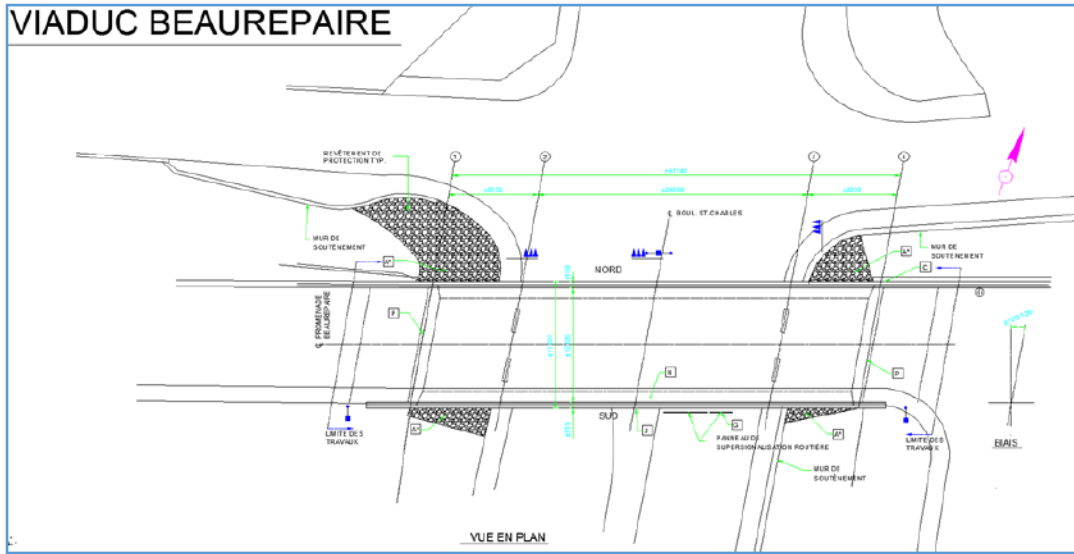


Figure 5.11 Viaduct Beaurepaire Plan

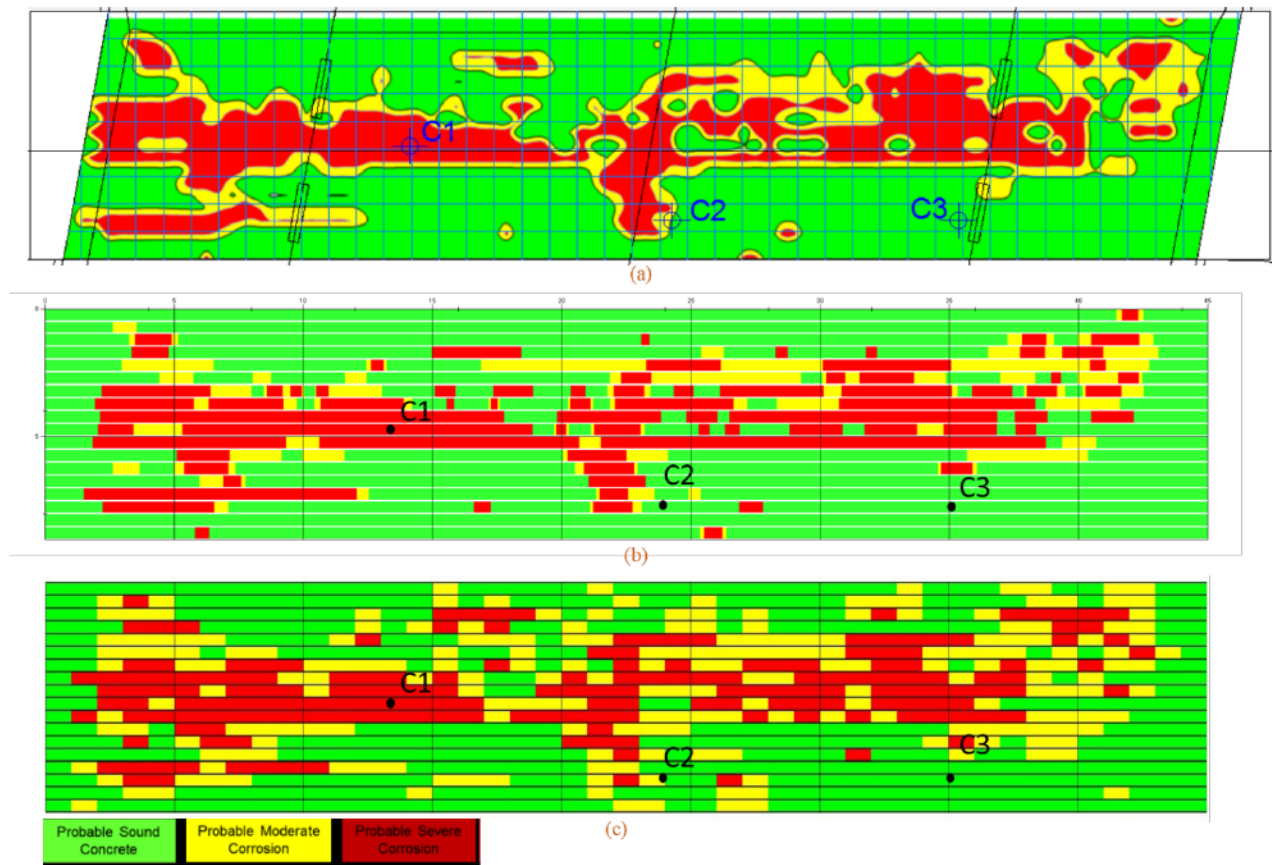


Figure 5.12 Viaduct Beaurepaire maps with the location of Cores marked as C1-C3 including (a) GPR-IBA map in Surfer®; (b) GPR-IBA map in Radex and (c) RUIM-based map

## 6 CONCLUSIONS AND LIMITATIONS

### 6.1 Research Summary and Conclusions

GPR is a powerful NDE technique utilized for condition assessment of reinforced concrete structural elements, especially bridge decks and pavements due to its ability to detect major subsurface defects in a short span of time. However, the interpretation of GPR data typically based on numerical ABA or its variants has been a major issue among transportation authorities as it is not reliable completely. A novel GPR-IBA approach utilizes the expertise of a GPR analyst in visually interpreting GPR data to mark attenuated areas and develop condition maps, and this method overcomes various limitations of amplitude-based analysis. However, the GPR-IBA is prone to human errors, time-consuming, and subjective leading to different interpretations of GPR data. This research aims to automate this GPR-IBA approach to produce consistent and reproducible results by applying scientific analysis with a broader goal of developing a reliable, robust model(s) for assessing GPR data. The following steps provide a concise overview of the research workflow:

1. A literature review of bridge management practices, various types of bridge deck defects, and numerous NDE techniques for detecting subsurface defects in reinforced structural elements, especially bridge decks.
2. The chosen NDE technique has been discussed based on a comprehensive study that ranked GPR as the best among various NDEs for identifying critical subsurface defects effectively.
3. A brief description of GPR principles and a comprehensive list of its data analysis methods that have improved over time has been tabulated.
4. The commonly adopted numerical-ABA method (or its variants) used by transportation agencies for GPR data analysis based on picking amplitude values either at the concrete-

rebar level or relative difference of amplitude from top to bottom of a deck has been discussed.

5. To overcome the limitations of numerical-ABA which majorly neglects profile data of GPR leading to not-always-reliable results, the GPR-IBA methodology of analyzing GPR data based on image-based interpretation by experienced analysts has been briefly reviewed.
6. A *need* for developing an approach to improve the GPR-IBA approach is suggested based on its limitations which include subjectivity, the level of knowledge of an expert, and possible inconsistent results.
7. The *importance of automated hyperbolic detections* is highlighted along with previous efforts in literature which employed numerous algorithms based on image processing for analyzing GPR data and hyperbolic detections.
8. A brief review of various image processing and computer vision tools was conducted along with their application on sample GPR data to investigate potential solutions. A *three-step philosophy* for research methodology was proposed which includes identifying hyperbolic regions, measuring a meaningful property of detected regions, and clustering those regions with better image processing techniques.
9. Three models were developed: X-sim, V-JAM, and RUIM, and their application was demonstrated through case studies. However, it is important to note that only the latter two developed models, V-JAM and RUIM, have been recommended for condition mapping.
10. Finally, laboratory experiments were undertaken to verify the validity of utilizing a measured factor known as entropy.



In achieving the aforesaid objectives, the major contributions of this research along with its benefits are described as follows:

1. **V-JAM:** A comprehensive approach was proposed based on the three-step philosophy which includes the following main steps: a) detect – identifying hyperbolic regions automatically using a trained classifier based on Viola-Jones Algorithm and applying regional comparison and statistical analysis; b) measuring property – evaluating entropy values for detected regions; and c) clustering – K-means clustering of detected regions based on entropy values to develop deterioration scale for each profile and stacking them to generate condition map.
2. A case study to show the application of V-JAM was implemented on a reinforced concrete slab scanned in Côte-des-Neiges, Montréal. The condition maps generated showed extremely good correspondence with the condition maps of both numerical-ABA and GPR-IBA analysis. However, the resulting maps showed a better resemblance with the latter method (GPR-IBA) relatively, and thus, better indicative of the actual condition of the concrete. The results also indicated that having four clusters instead of three didn't show much difference with regard to the percentage of total deteriorated areas (moderate and severe).
3. The advantages of V-JAM include the following: a) results are superior to existing amplitude-based analysis; b) show extremely good correlation with the actual concrete condition; c) rapid method especially in cases of large profiles due to automated detections and consequently, condition mapping; d) extremely useful in cases of structural elements with uniformly spaced rebars as the majority of hyperbolas are clearly defined; d) reduced subjectivity devoid of human errors leading to consistently reliable results.

4. **RUIM:** A user-interactive robust model has been developed which includes the following main steps: a) an optional user-assisted input to determine an optimum number of clusters; b) preprocessing steps which majorly reduce noise in varied GPR profiles; b) a robust model for detecting hyperbolic signatures, especially in cases of ill-defined complex environment based on correlating downward openings with local maximums of the distance transform image; c) regional comparison to detect the required top/bottom layer and eliminating false positives while identifying missing detections based on statistical analysis; d) in case of incorrect detection of the required layer, the model can detect it based on user-input; e) a module which assists the user in detecting anomalies based on a similarity matrix; and f) generate condition map based on detected regions, K-means clustering, and assigning optimal cluster value utilizing user information.
5. Three case studies to show the application of RUIM were implemented on reinforced concrete bridge decks located in Iowa, USA (1) and Quebec, Canada (2). The condition maps generated in all cases showed extremely good correlation with amplitude-based analysis and more importantly, GPR-IBA analysis. Additionally, as part of the validation, the condition maps in all cases corroborated with the results of coring samples (destructive technique).
6. The major advantages of RUIM include the following: a) results are superior to existing amplitude-based analysis; b) shows extremely good correlation with GPR-IBA analysis, coring samples, and thus, the actual concrete condition; c) a robust rapid method especially in cases of large profiles due to automated detections and consequently, condition mapping; d) ability to detect complex hyperbolic signatures and therefore, can be used beyond cases of structural elements with uniformly spaced rebars such as detection of buried objects like

pipelines or unmarked graves; d) reduced subjectivity devoid of human errors leading to consistently reliable and robust results; and e) utilizes user-information to assign optimal clusters and assist in detecting major anomalies, if present.

7. Finally, laboratory tests were conducted in a controlled environment to evaluate the measured factor, entropy, used for detected regions and compare it with the amplitude values for subsurface objects. The results indicated that entropy yielded comparatively better results for all cases (rebars, air gaps, and water gaps).

The V-JAM method is recommended to generate condition maps in case of GPR profiles with majorly well-defined hyperbolas while the RUIM method is recommended, and preferred over V-JAM, for condition mapping of reinforced structural elements and robust detections of hyperbolic signatures in GPR profiles.

## **6.2 Limitations and Future recommendations**

The limitations of developed models along with recommendations for future works are identified as follows:

1. V-JAM requires the hyperbolic signatures in a GPR data set to consist of majorly well-defined hyperbolas whose aspect ratio needs to be stretched/ shortened, if required, to maintain an aspect ratio like that of the trained classifier. Therefore, this model could lead to missing detections in GPR profiles especially in cases of complex signatures.
2. V-JAM does not account for anomalies, nor does it consider any user-assisted information. However, the user-labeled anomalies module and user-assisted input of RUIM can be incorporated into V-JAM to overcome this limitation.

3. While RUIM can detect complex hyperbolic signatures, the anomalies are assigned manually by the user. Advanced ML models can be augmented to reduce this user dependency.
4. While RUIM can be used to obtain complex hyperbolic signatures in any GPR scan such as buried pipelines, some false positives may occur in the absence of layered reinforcement levels. These false positives might need to either be eliminated by enhancing the detection module or removing them manually (time-consuming in the case of large profiles).
5. The RUIM model requires input from the user for optimal clustering and anomaly detection. While this could be a limitation, GPR analysts, typically in practice, are judicious to identify the presence of corrosion (including the distinction of *severe* corrosion) in GPR profiles and/or anomalies, if present.
6. Both models assume that the structural element being inspected has (majorly) uniform rebar spacing with negligible rebar depth variation and that its surface layer has fairly uniform concrete cover thickness. The methods need to be further developed using techniques such as regression analysis to account for such variants.
7. Lastly, the laboratory analysis performed had some limitations, such as the short dimensions of the slab, the absence of embedded rebars, and the fact that actual cracks/gaps of in-situ concrete contain impurities such as salts and corrosion products. As part of ongoing lab work, these drawbacks are being addressed by investigating GPR signals in reinforced (embedded) concrete exposed to varying levels of corrosion & potential in-situ field tests.

Conclusively, two models, V-JAM and RUIM, have been developed for the condition assessment of structural elements, especially bridge decks. These models generate reliable condition maps as they have shown good reliability with existing approaches, especially the GPR-IBA method, and more importantly, validated with destructive cores. Therefore, such maps could be efficiently used

by bridge inspectors in making informed decisions regarding the repair and rehabilitation of reinforced concrete bridges.

## 7 REFERENCES

- Abdel-Qader, I., Krause, V., Abu-Amara, F., & Abudayyeh, O. (2014). Comparative study of deconvolution algorithms for GPR bridge deck imaging. *WSEAS Transactions on Signal Processing*, 10(1).
- Abdul Rahman, M., & Zayed, T. (2016). Developing Corrosion Maps of RC bridge elements based on automated visual image analysis. *Session of the 2016 Conference of the Transportation Association of Canada, Toronto, ON*.
- Abdul Rahman, Mohammed, Donda, D., Latosh, F., Tarussov, A., & Bagchi, A. (2022). Entropy evaluation of subsurface materials and defects in Concrete Slabs using GPR. *11th International Conference on Structural Health Monitoring of Intelligent Infrastructure*.
- Abdul Rahman, Mohammed, Zayed, T., & Abouhamad, M. (2016). Automating Visual Image Analysis of GPR Profiles for Reinforced Concrete Bridges. *Transportation Research Board 95th Annual Meeting*, 16–5898.
- Abdul Rahman, Mohammed, Zayed, T., & Bagchi, A. (2022). Deterioration Mapping of RC Bridge Elements Based on Automated Analysis of GPR Images. In *Remote Sensing* (Vol. 14, Issue 5). <https://doi.org/10.3390/rs14051131>
- Abouhamad, M., Dawood, T., Jabri, A., Alsharqawi, M., & Zayed, T. (2017). Corrosiveness mapping of bridge decks using image-based analysis of GPR data. *Automation in Construction*, 80, 104–117. <https://doi.org/https://doi.org/10.1016/j.autcon.2017.03.004>
- ACI 222R-01. (2001). *Protection of Metals in Concrete Against Corrosion*. ACI Committee 222.
- Adhikari, R. S., Moselhi, O., & Bagchi, A. (2014). Image-based retrieval of concrete crack properties for bridge inspection. *Automation in Construction*, 39, 180–194. <https://doi.org/https://doi.org/10.1016/j.autcon.2013.06.011>
- Adhikari, R. S., Moselhi, O., & Bagchi, A. (2013a). A Study of Image-Based Element Condition Index for Bridge Inspection. In C. Haas (Ed.), *Proceedings of the 30th International Symposium on Automation and Robotics in Construction and Mining (ISARC 2013): Building the Future in Automation and Robotics* (pp. 345–356). International Association for Automation and Robotics in Construction (IAARC). <https://doi.org/10.22260/ISARC2013/0038>
- Adhikari, R. S., Moselhi, O., & Bagchi, A. (2013b). Image-Based Change Detection for Bridge Inspection. In C. Haas (Ed.), *Proceedings of the 30th International Symposium on Automation and Robotics in Construction and Mining (ISARC 2013): Building the Future in Automation and Robotics* (pp. 357–367). International Association for Automation and Robotics in Construction (IAARC). <https://doi.org/10.22260/ISARC2013/0039>

- Adhikari, R. S., Moselhi, O., & Bagchi, A. (2012). Image-Based Retrieval of Concrete Crack Properties. In F. J. M. van Gassel (Ed.), *ISG\*ISARC2012 Full paper proceedings*. International Association for Automation and Robotics in Construction (IAARC). <https://doi.org/10.22260/ISARC2012/0054>
- Adhikari, R. S., Moselhi, O., Bagchi, A., & Rahmatian, A. (2016). Tracking of Defects in Reinforced Concrete Bridges Using Digital Images. *Journal of Computing in Civil Engineering*, 30(5), 4016004. [https://doi.org/10.1061/\(ASCE\)CP.1943-5487.0000566](https://doi.org/10.1061/(ASCE)CP.1943-5487.0000566)
- Ahmed, H., La, H. M., & Tran, K. (2020). Rebar detection and localization for bridge deck inspection and evaluation using deep residual networks. *Automation in Construction*, 120, 103393. <https://doi.org/https://doi.org/10.1016/j.autcon.2020.103393>
- Ahmed, H., Le, C. P., & La, H. M. (2023). Pixel-level classification for bridge deck rebar detection and localization using multi-stage deep encoder-decoder network. *Developments in the Built Environment*, 14, 100132. <https://doi.org/https://doi.org/10.1016/j.dibe.2023.100132>
- Al-Nuaimy, W., Huang, Y., Nakhkash, M., Fang, M. T. ., Nguyen, V. ., & Eriksen, A. (2000). Automatic detection of buried utilities and solid objects with GPR using neural networks and pattern recognition. *Journal of Applied Geophysics*, 43(2–4), 157–165. [https://doi.org/10.1016/S0926-9851\(99\)00055-5](https://doi.org/10.1016/S0926-9851(99)00055-5)
- Ali A., S., & Glenn A., W. (2018). Reliability Analysis of Ground-Penetrating Radar for the Detection of Subsurface Delamination. *Journal of Bridge Engineering*, 23(2), 4017131. [https://doi.org/10.1061/\(ASCE\)BE.1943-5592.0001182](https://doi.org/10.1061/(ASCE)BE.1943-5592.0001182)
- Alsharqawi, M., Zayed, T., & Abu Dabous, S. (2017). Common practices in assessing conditions of concrete bridges. *MATEC Web Conf.*, 120. <https://doi.org/10.1051/mateconf/201712002016>
- Alsharqawi, M., Zayed, T., & Abu Dabous, S. (2018). *A Clustering-Based Model for Rating Concrete Bridges Using k-Means Technique*.
- Alsharqawi, M., Zayed, T., & Shami, A. (2020). Ground penetrating radar-based deterioration assessment of RC bridge decks. *Construction Innovation*, 20(1), 1–17. <https://doi.org/10.1108/CI-08-2019-0076>
- Asadi, P., Gindy, M., Alvarez, M., & Asadi, A. (2020). A computer vision based rebar detection chain for automatic processing of concrete bridge deck GPR data. *Automation in Construction*, 112, 103106. <https://doi.org/https://doi.org/10.1016/j.autcon.2020.103106>
- ASTM D6087. (2015). *Standard test method for evaluating asphalt-covered concrete bridge decks using ground penetrating radar*. American Society for Testing and Materials.
- Barnes, C. L., & Trottier, J.-F. (2004). Effectiveness of Ground Penetrating Radar in Predicting Deck Repair Quantities. *Journal of Infrastructure Systems*, 10(2), 69–76. [https://doi.org/10.1061/\(ASCE\)1076-0342\(2004\)10:2\(69\)](https://doi.org/10.1061/(ASCE)1076-0342(2004)10:2(69))
- Barnes, C. L., Trottier, J. F., & Forgeron, D. (2008). Improved concrete bridge deck evaluation using GPR by accounting for signal depth-amplitude effects. *NDT and E International*, 41(6), 427–433. <https://doi.org/10.1016/j.ndteint.2008.03.005>
- Bay, H., Ess, A., Tuytelaars, T., & Van Gool, L. (2008). Speeded-Up Robust Features (SURF).

- Computer Vision and Image Understanding*, 110(3), 346–359.  
<https://doi.org/https://doi.org/10.1016/j.cviu.2007.09.014>
- Benedetto, A., Manacorda, G., Simi, A., & Tosti, F. (2012). Novel perspectives in bridges inspection using GPR. *Nondestructive Testing and Evaluation*, 27(3), 239–251.  
<https://doi.org/10.1080/10589759.2012.694883>
- Besaw, L. E., & Stimac, P. J. (2015). Deep convolutional neural networks for classifying GPR B-scans. *Proc.SPIE*, 9454, 945413. <https://doi.org/10.1117/12.2176250>
- Bien, J., Elfgrén, L., & Olofsson, J. (2007). *Sustainable bridges : Assessment for future traffic demands and longer lives*. Dolnoslaskie Wydawnictwo Edukacyjne.
- Birkenfeld, S. (2010). Automatic detection of reflexion hyperbolas in gpr data with neural networks. In *World Automation Congress (WAC), 2010* (pp. 1–6).
- Borgefors, G. (1986). Distance transformations in digital images. *Computer Vision, Graphics, and Image Processing*, 34(3), 344–371. [https://doi.org/https://doi.org/10.1016/S0734-189X\(86\)80047-0](https://doi.org/https://doi.org/10.1016/S0734-189X(86)80047-0)
- Bradley, D., & Roth, G. (2007). Adaptive Thresholding using the Integral Image. *Journal of Graphics Tools*, 12(2), 13–21. <https://doi.org/10.1080/2151237X.2007.10129236>
- Canny, J. (1986). A Computational Approach to Edge Detection. *IEEE Transactions on Pattern Analysis and Machine Intelligence*, PAMI-8(6), 679–698.  
<https://doi.org/10.1109/TPAMI.1986.4767851>
- Capineri, L., Grande, P., & Temple, J. A. G. (1998). Advanced image-processing technique for real-time interpretation of ground-penetrating radar images. *International Journal of Imaging Systems and Technology*, 9(1), 51–59.
- Carevic, D. (1999). Wavelet-based method for detection of shallowly buried objects from GPR data. *1999 Information, Decision and Control. Data and Information Fusion Symposium, Signal Processing and Communications Symposium and Decision and Control Symposium. Proceedings (Cat. No.99EX251)*, 201–206. <https://doi.org/10.1109/IDC.1999.754154>
- Carter, C. R., Chung, T., Holt, F. B., & Manning, D. G. (1986). An automated signal processing system for the signature analysis of radar waveforms from bridge decks. *Canadian Electrical Engineering Journal*, 11(3), 128–137.  
<https://doi.org/10.1109/CEEJ.1986.6594049>
- Chaudhari, M., Sondur, S., & Vanjare, G. (2015). A review on Face Detection and study of Viola Jones method. *International Journal of Computer Trends and Technology*, 25(1), 54–61.  
<https://doi.org/10.14445/22312803/IJCTT-V25P110>
- Chenxi, Y., Shuai, L., Hubo, C., & R., K. V. (2018). GPR Signature Detection and Decomposition for Mapping Buried Utilities with Complex Spatial Configuration. *Journal of Computing in Civil Engineering*, 32(4), 4018026.  
[https://doi.org/10.1061/\(ASCE\)CP.1943-5487.0000764](https://doi.org/10.1061/(ASCE)CP.1943-5487.0000764)
- Chung, T., Carter, C. R., Reel, R., Tharmabala, T., & Wood, D. (1993). Impulse radar signatures of selected bridge deck structures. *Proceedings of Canadian Conference on Electrical and Computer Engineering*, 59–62. <https://doi.org/10.1109/CCECE.1993.332236>

- CIRC. (2016). *Canadian Infrastructure Report Card*.  
[http://canadianinfrastructure.ca/downloads/Canadian\\_Infrastructure\\_Report\\_2016.pdf](http://canadianinfrastructure.ca/downloads/Canadian_Infrastructure_Report_2016.pdf)
- CIRC. (2019). *Canadian Infrastructure Report Card*.  
<http://canadianinfrastructure.ca/en/index.html>
- Clemina, G. G. (1983). Nondestructive Inspection of Overlaid Bridge Decks with Ground-Penetrating Radar. *Transportation Research Record*, 899.
- Coleman, Z. W., & Schindler, A. K. (2022). Investigation of ground-penetrating radar defect detection capabilities, influence of moisture content, and optimal data collection orientation in condition assessments of concrete bridge decks. *Journal of Applied Geophysics*, 202, 104655. <https://doi.org/https://doi.org/10.1016/j.jappgeo.2022.104655>
- Conyers, L. B. (2013). *Ground-penetrating radar for archaeology / Lawrence B. Conyers*. (Third edit). Lanham : AltaMira Press, a division of Rowman & Littlefield Publishers, Inc., 2013.
- Dalal, N., & Triggs, B. (2005). Histograms of oriented gradients for human detection. *2005 IEEE Computer Society Conference on Computer Vision and Pattern Recognition (CVPR'05)*, 1, 886–893.
- Dang, K., & Sharma, S. (2017). Review and comparison of face detection algorithms. *Cloud Computing, Data Science & Engineering-Confluence, 2017 7th International Conference On*, 629–633.
- Daniels, D. J. (2005). Ground Penetrating Radar. In *Encyclopedia of RF and Microwave Engineering*. John Wiley & Sons, Inc. <https://doi.org/10.1002/0471654507.eme152>
- Daniels, D.J. (2004). *Ground Penetrating Radar* (David J Daniels (ed.); Second). Institution of Engineering and Technology. <https://digital-library.theiet.org/content/books/ra/pbra015e>
- Dawood, T., Zhu, Z., & Zayed, T. (2020). Deterioration mapping in subway infrastructure using sensory data of GPR. *Tunnelling and Underground Space Technology*, 103, 103487. <https://doi.org/https://doi.org/10.1016/j.tust.2020.103487>
- De Boor, C. (1978). *A practical guide to splines / Carl de Boor*. Springer-Verlag.
- Delbo, S., Gamba, P., & Roccato, D. (2000). A fuzzy shell clustering approach to recognize hyperbolic signatures in subsurface radar images. *IEEE Transactions on Geoscience and Remote Sensing*, 38(3), 1447–1451.
- Dell'Acqua, A., Sarti, A., Tubaro, S., & Zanzi, L. (2004). Detection of linear objects in GPR data. *Signal Processing*, 84(4), 785–799.
- Dinh, K, Zayed, T., Romero, F., & Tarussov, A. (2014). Method for Analyzing Time-Series GPR Data of Concrete Bridge Decks. *Journal of Bridge Engineering*, 20(6), 4014086. [https://doi.org/10.1061/\(ASCE\)BE.1943-5592.0000679](https://doi.org/10.1061/(ASCE)BE.1943-5592.0000679)
- Dinh, Kien, & Gucunski, N. (2021). Factors affecting the detectability of concrete delamination in GPR images. *Construction and Building Materials*, 274, 121837. <https://doi.org/https://doi.org/10.1016/j.conbuildmat.2020.121837>
- Dinh, Kien, Gucunski, N., & Duong, T. H. (2018). An algorithm for automatic localization and detection of rebars from GPR data of concrete bridge decks. *Automation in Construction*, 89, 292–298. <https://doi.org/https://doi.org/10.1016/j.autcon.2018.02.017>



- Dinh, Kien, Gucunski, N., Kim, J., & Duong, T. H. (2016). Understanding depth-amplitude effects in assessment of GPR data from concrete bridge decks. *NDT & E International*, 83, 48–58. <https://doi.org/https://doi.org/10.1016/j.ndteint.2016.06.004>
- Dinh, Kien, Gucunski, N., Kim, J., & Duong, T. H. (2017). Method for attenuation assessment of GPR data from concrete bridge decks. *NDT & E International*, 92, 50–58. <https://doi.org/https://doi.org/10.1016/j.ndteint.2017.07.016>
- Dinh, Kien, Gucunski, N., Tran, K., Novo, A., & Nguyen, T. (2021). Full-resolution 3D imaging for concrete structures with dual-polarization GPR. *Automation in Construction*, 125, 103652. <https://doi.org/https://doi.org/10.1016/j.autcon.2021.103652>
- Dinh, Kien, Gucunski, N., & Zayed, T. (2019). Automated visualization of concrete bridge deck condition from GPR data. *NDT & E International*, 102, 120–128. <https://doi.org/https://doi.org/10.1016/j.ndteint.2018.11.015>
- Dinh, Kien, Zayed, T., Moufti, S., Shami, A., Jabri, A., Abouhamad, M., & Dawood, T. (2015). Clustering-Based Threshold Model for Condition Assessment of Concrete Bridge Decks with Ground-Penetrating Radar. *Transportation Research Record*, 2522(1), 81–89. <https://doi.org/10.3141/2522-08>
- Dojack, L. (2012). *Ground Penetrating Radar Theory, Data Collection, Processing, and Interpretation: A Guide for Archaeologists*. <https://open.library.ubc.ca/collections/42591/items/1.0086065>
- Donda, D., Latosh, F., Abdul Rahman, M., & Bagchi, A. (2021). Detection of subsurface defects in concrete slabs using ground penetrating radar. *Proc.SPIE*, 11592. <https://doi.org/10.1117/12.2582807>
- Dong, X., Wang, G., Pang, Y., Li, W., Wen, J., Meng, W., & Lu, Y. (2011). Fast efficient algorithm for enhancement of low lighting video. *2011 IEEE International Conference on Multimedia and Expo*, 1–6. <https://doi.org/10.1109/ICME.2011.6012107>
- Dou, Q., Wei, L., Magee, D. R., & Cohn, A. G. (2017). Real-Time Hyperbola Recognition and Fitting in GPR Data. *IEEE Transactions on Geoscience and Remote Sensing*, 55(1), 51–62. <https://doi.org/10.1109/TGRS.2016.2592679>
- El-Mahallawy, M. S., & Hashim, M. (2013). Material Classification of Underground Utilities From GPR Images Using DCT-Based SVM Approach. *IEEE Geoscience and Remote Sensing Letters*, 10(6), 1542–1546. <https://doi.org/10.1109/LGRS.2013.2261796>
- Elbhairry, H., Elbeltagi, E., Hegazy, T., & Soudki, K. (2006). Comparison of Two Evolutionary Algorithms for Optimization of Bridge Deck Repairs. *Computer-Aided Civil and Infrastructure Engineering*, 21(8), 561–572.
- Ellis, R. M., Thompson, P. D., Gagnon, R., & Richard, G. (2008). Design and implementation of a new bridge management system for the ministry of transport of Québec. *Proceedings of the 10th International Conference on Bridge and Structure Management*.
- Everitt, B., Landau, S., & Leese, M. (2001). *Cluster Analysis*. A Hodder Arnold Publication. *Wiley, London*.
- Feng, J., Yang, L., Wang, H., Song, Y., & Xiao, J. (2020). GPR-based Subsurface Object Detection and Reconstruction Using Random Motion and DepthNet. *2020 IEEE*

- International Conference on Robotics and Automation (ICRA)*, 7035–7041.
- FHWA. (2005). *Specifications for the National Bridge Inventory, Draft, May 16, 2005, Federal Highway Administration.*
- FHWA. (2021). *Federal Highway Administration (FHWA) National Bridge Inventory (NBI) Bridge Programs Count, Area, Length of Bridges by Highway System.*  
<https://www.fhwa.dot.gov/bridge/fc.cfm>
- Fischler, M. A., & Bolles, R. C. (1981). Random Sample Consensus: A Paradigm for Model Fitting with Applications to Image Analysis and Automated Cartography. *Commun. ACM*, 24(6), 381–395. <https://doi.org/10.1145/358669.358692>
- Fitzgibbon, A. W., Pilu, M., & Fisher, R. B. (1996). Direct least squares fitting of ellipses. *Proceedings of 13th International Conference on Pattern Recognition, 1*, 253–257 vol.1. <https://doi.org/10.1109/ICPR.1996.546029>
- Freund, Y., & Schapire, R. E. (1997). A Decision-Theoretic Generalization of On-Line Learning and an Application to Boosting. *Journal of Computer and System Sciences*, 55(1), 119–139. <https://doi.org/https://doi.org/10.1006/jcss.1997.1504>
- Fritzsche, M. (1998). Classification of GPR data for mine detection based on hidden Markov models. *IET Conference Proceedings*, 96-100(4). [https://digital-library.theiet.org/content/conferences/10.1049/cp\\_19980697](https://digital-library.theiet.org/content/conferences/10.1049/cp_19980697)
- Gader, P. D., Mystkowski, M., & Zhao, Y. (2001). Landmine detection with ground penetrating radar using hidden Markov models. *IEEE Transactions on Geoscience and Remote Sensing*, 39(6), 1231–1244. <https://doi.org/10.1109/36.927446>
- Gamba, P., & Lossani, S. (2000). Neural detection of pipe signatures in ground penetrating radar images. In *IEEE Transactions on Geoscience and Remote Sensing* (Vol. 38, Issue 2, pp. 790–797). <https://doi.org/10.1109/36.842008>
- Gehrig, M. D., Morris, D. V., & Bryant, J. T. (2004). Ground penetrating radar for concrete evaluation studies. *Technical Presentation Paper for Performance Foundation Association*, 197–200.
- Ghodoosi, F., Bagchi, A., & Zayed, T. (2015). System-level deterioration model for reinforced concrete bridge decks. *Journal of Bridge Engineering*, 20(5). [https://doi.org/10.1061/\(ASCE\)BE.1943-5592.0000670](https://doi.org/10.1061/(ASCE)BE.1943-5592.0000670)
- Ghodoosi, F., Bagchi, A., Zayed, T., & Hosseini, M. R. (2018). Method for developing and updating deterioration models for concrete bridge decks using GPR data. *Automation in Construction*, 91, 133–141. <https://doi.org/10.1016/j.autcon.2018.03.014>
- Giachetti, A. (2000). Matching techniques to compute image motion. *Image and Vision Computing*, 18(3), 247–260. [https://doi.org/10.1016/S0262-8856\(99\)00018-9](https://doi.org/10.1016/S0262-8856(99)00018-9)
- Gibb, S., & La, H. M. (2016). *Automated Rebar Detection for Ground-Penetrating Radar BT - Advances in Visual Computing* (G. Bebis, R. Boyle, B. Parvin, D. Koracin, F. Porikli, S. Skaff, A. Entezari, J. Min, D. Iwai, A. Sadagic, C. Scheidegger, & T. Isenberg (eds.); pp. 815–824). Springer International Publishing.
- Gonzalez, R., Woods, R., & Eddins., S. (2010). *Digital Image Processing Using MATLAB®*.

Tata McGraw Hill Education.

- Goulias, D. G., Cafiso, S., Di Graziano, A., Saremi, S. G., & Currao, V. (2020). Condition Assessment of Bridge Decks through Ground-Penetrating Radar in Bridge Management Systems. *Journal of Performance of Constructed Facilities*, 34(5), 4020100. [https://doi.org/10.1061/\(ASCE\)CF.1943-5509.0001507](https://doi.org/10.1061/(ASCE)CF.1943-5509.0001507)
- GSSI. (2017). *BridgeScan Handbook - GPR Inspection of Bridge Decks* (MN72-618 R ed.). Geophysical Survey Systems, Inc.
- GSSI. (2022). *What is GPR?* <https://www.geophysical.com/whatisgpr>
- Gucunski, N., & National Research Council. (2013). *Nondestructive Testing to Identify Concrete Bridge Deck Deterioration*.
- Gucunski, N., Romero, F., Kruschwitz, S., Feldmann, R., & Parvardeh, H. (2011). *Comprehensive bridge deck deterioration mapping of nine bridges by nondestructive evaluation technologies*. Iowa. Dept. of Transportation.
- Gupta, M. V., & Sharma, D. (2014). A study of various face detection methods. *International Journal of Advanced Research in Computer and Communication Engineering*, 3(5), 6694–6697.
- Harkat, H., Elfakir, Y., Bennani, S. D., Khaissidi, G., & Mrabti, M. (2016). Ground penetrating radar hyperbola detection using Scale-Invariant Feature Transform. *2016 International Conference on Electrical and Information Technologies (ICEIT)*, 392–397. <https://doi.org/10.1109/EITech.2016.7519626>
- Harkat, H., Ruano, A., Ruano, M. G., & Bennani, S. D. (2018). Classifier design by a multi-objective genetic algorithm approach for GPR automatic target detection. *IFAC-PapersOnLine*, 51(10), 187–192.
- Harris, C. G., & Stephens, M. J. (1988). A Combined Corner and Edge Detector. *Alvey Vision Conference*.
- Heymfield, E., & Kuss, M. L. (2015). Supplementing Current Visual Highway Bridge Inspections with Gigapixel Technology. *Journal of Performance of Constructed Facilities*, 04015015. [https://doi.org/10.1061/\(ASCE\)CF.1943-5509.0000757](https://doi.org/10.1061/(ASCE)CF.1943-5509.0000757)
- Hou, F, Lei, W., Li, S., & Xi, J. (2021). Deep Learning-Based Subsurface Target Detection From GPR Scans. *IEEE Sensors Journal*, 21(6), 8161–8171. <https://doi.org/10.1109/JSEN.2021.3050262>
- Hou, Feifei, Lei, W., Li, S., Xi, J., Xu, M., & Luo, J. (2021). Improved Mask R-CNN with distance guided intersection over union for GPR signature detection and segmentation. *Automation in Construction*, 121, 103414. <https://doi.org/https://doi.org/10.1016/j.autcon.2020.103414>
- Hugenschmidt, J., & Mastrangelo, R. (2006). GPR inspection of concrete bridges. *Cement and Concrete Composites*, 28(4), 384–392. <https://doi.org/10.1016/j.cemconcomp.2006.02.016>
- Hui-lin, Z., Mao, T., & Xiao-li, C. (2005). Feature extraction and classification of echo signal of ground penetrating radar. *Wuhan University Journal of Natural Sciences*, 10(6), 1009–1012.
- Ishitsuka, K., Iso, S., Onishi, K., & Matsuoka, T. (2018). Object Detection in Ground-

- Penetrating Radar Images Using a Deep Convolutional Neural Network and Image Set Preparation by Migration. *International Journal of Geophysics*, 2018, 9365184. <https://doi.org/10.1155/2018/9365184>
- Jain, A. K. (2010). Data clustering: 50 years beyond K-means. *Pattern Recognition Letters*, 31(8), 651–666. <https://doi.org/https://doi.org/10.1016/j.patrec.2009.09.011>
- Jaufer, R., Ihamouten, A., Guilbert, D., Todkar, S., Yaram, T., & Derobert, X. (2021). Deep learning based automatic hyperbola detection on GPR data for buried utility pipes mapping. *2021 11th International Workshop on Advanced Ground Penetrating Radar (IWAGPR)*, 1–6. <https://doi.org/10.1109/IWAGPR50767.2021.9843151>
- Jiao, L., Ye, Q., Cao, X., Huston, D., & Xia, T. (2020). Identifying concrete structure defects in GPR image. *Measurement*, 160, 107839. <https://doi.org/https://doi.org/10.1016/j.measurement.2020.107839>
- Kaneko, T. (1991). Radar image processing for locating underground linear objects. *IEICE TRANSACTIONS on Information and Systems*, 74(10), 3451–3458.
- Kapur, J. N., Sahoo, P. K., & Wong, A. K. C. (1985). A new method for gray-level picture thresholding using the entropy of the histogram. *Computer Vision, Graphics, and Image Processing*, 29(3), 273–285. [https://doi.org/https://doi.org/10.1016/0734-189X\(85\)90125-2](https://doi.org/https://doi.org/10.1016/0734-189X(85)90125-2)
- Kashif Ur Rehman, S., Ibrahim, Z., Memon, S. A., & Jameel, M. (2016). Nondestructive test methods for concrete bridges: A review. *Construction and Building Materials*, 107, 58–86. <https://doi.org/10.1016/j.conbuildmat.2015.12.011>
- Kaur, P., Dana, K. J., Romero, F. A., & Gucunski, N. (2015). Automated GPR Rebar Analysis for Robotic Bridge Deck Evaluation. In *IEEE Transactions on Cybernetics: Vol. PP* (Issue 99, p. 1). <https://doi.org/10.1109/TCYB.2015.2474747>
- Kim, N., Kim, S., An, Y.-K., & Lee, J.-J. (2019). Triplanar Imaging of 3-D GPR Data for Deep-Learning-Based Underground Object Detection. *IEEE Journal of Selected Topics in Applied Earth Observations and Remote Sensing*, 12(11), 4446–4456. <https://doi.org/10.1109/JSTARS.2019.2953505>
- Kim, Namgyu, Kim, K., An, Y.-K., Lee, H.-J., & Lee, J.-J. (2020). Deep learning-based underground object detection for urban road pavement. *International Journal of Pavement Engineering*, 21(13), 1638–1650. <https://doi.org/10.1080/10298436.2018.1559317>
- Kleinmann, L., Laugks, J., & Nick, K.-P. (1993). Image processing and pattern recognition in ground penetrating radar data. *Proceedings of IGARSS '93 - IEEE International Geoscience and Remote Sensing Symposium*, 1903–1906 vol.4. <https://doi.org/10.1109/IGARSS.1993.322384>
- Krause, V., Abdel-Qader, I., Abudayyeh, O., & Yehia, S. (2007). An image segmentation algorithm for the detection of rebar in bridge decks from GPR scans. *2007 IEEE International Conference on Electro/Information Technology, EIT 2007*, 114–119. <https://doi.org/10.1109/EIT.2007.4374476>
- Kumlu, D. (2022). GPR Image Recovery Effect on Faster R-CNN-Based Buried Target Detection. *J. Electromagn. Eng. Sci*, 22(5), 591–598. <https://doi.org/10.26866/jees.2022.5.r.127>

- Lameri, S., Lombardi, F., Bestagini, P., Lualdi, M., & Tubaro, S. (2017). Landmine detection from GPR data using convolutional neural networks. *2017 25th European Signal Processing Conference (EUSIPCO)*, 508–512.
- Leach, P. (2019). *RADAN 7 for Archaeology, Forensics, and Cemeteries*.
- Lee, K. L., & Mokji, M. M. (2014). Automatic target detection in GPR images using Histogram of Oriented Gradients (HOG). *2014 2nd International Conference on Electronic Design (ICED)*, 181–186. <https://doi.org/10.1109/ICED.2014.7015795>
- Lei, W., Hou, F., Xi, J., Tan, Q., Xu, M., Jiang, X., Liu, G., & Gu, Q. (2019). Automatic hyperbola detection and fitting in GPR B-scan image. *Automation in Construction*, *106*, 102839. <https://doi.org/10.1016/j.autcon.2019.102839>
- Lei, W., Luo, J., Hou, F., Xu, L., Wang, R., & Jiang, X. (2020). Underground Cylindrical Objects Detection and Diameter Identification in GPR B-Scans via the CNN-LSTM Framework. In *Electronics* (Vol. 9, Issue 11). <https://doi.org/10.3390/electronics9111804>
- Leutenegger, S., Chli, M., & Siegwart, R. Y. (2011). BRISK: Binary Robust invariant scalable keypoints. *2011 International Conference on Computer Vision*, 2548–2555. <https://doi.org/10.1109/ICCV.2011.6126542>
- Li, W., Cui, X., Guo, L., Chen, J., Chen, X., & Cao, X. (2016). Tree Root Automatic Recognition in Ground Penetrating Radar Profiles Based on Randomized Hough Transform. In *Remote Sensing* (Vol. 8, Issue 5). <https://doi.org/10.3390/rs8050430>
- Liu, H., Lin, C., Cui, J., Fan, L., Xie, X., & Spencer, B. F. (2020). Detection and localization of rebar in concrete by deep learning using ground penetrating radar. *Automation in Construction*, *118*, 103279.
- Liu, Y., & Dong, X. (2010). Constrained Least Squares Fitting of Ellipse. *2010 International Conference on Computational Intelligence and Software Engineering*, 1–3. <https://doi.org/10.1109/CISE.2010.5676736>
- Liu, Y., Wang, M., & Cai, Q. (2010). The target detection for GPR images based on curve fitting. *Image and Signal Processing (CISP), 2010 3rd International Congress On*, *6*, 2876–2879.
- Luo, T. X. H., & Lai, W. W. L. (2020). GPR pattern recognition of shallow subsurface air voids. *Tunnelling and Underground Space Technology*, *99*, 103355. <https://doi.org/10.1016/j.tust.2020.103355>
- Maas, C., & Schmalzl, J. (2013). Using pattern recognition to automatically localize reflection hyperbolas in data from ground penetrating radar. *Computers & Geosciences*, *58*, 116–125. <https://doi.org/10.1016/j.cageo.2013.04.012>
- Mallat, S. G. (1989). A theory for multiresolution signal decomposition: the wavelet representation. *IEEE Transactions on Pattern Analysis and Machine Intelligence*, *11*(7), 674–693. <https://doi.org/10.1109/34.192463>
- Malof, J. M., III, J. B., Reichman, D., & Collins, L. M. (2018). Improving the histogram of oriented gradient feature for threat detection in ground penetrating radar by implementing it as a trainable convolutional neural network. *Proc.SPIE*, *10628*, 106280D. <https://doi.org/10.1117/12.2305797>

- Manandhar, A., Torrione, P. A., Collins, L. M., & Morton, K. D. (2015). Multiple-Instance Hidden Markov Model for GPR-Based Landmine Detection. *IEEE Transactions on Geoscience and Remote Sensing*, 53(4), 1737–1745. <https://doi.org/10.1109/TGRS.2014.2346954>
- Manjunath, B. S., & Ma, W. Y. (1996). Texture features for browsing and retrieval of image data. *IEEE Transactions on Pattern Analysis and Machine Intelligence*, 18(8), 837–842. <https://doi.org/10.1109/34.531803>
- Marques, O. (2011). *Practical image and video processing using MATLAB*. John Wiley & Sons.
- Martoni, A. L. C., Aditya, R., & Alireza, B. (2022). Review of Machine Learning Algorithms for Automatic Detection of Underground Objects in GPR Images. *Journal of Pipeline Systems Engineering and Practice*, 13(2), 4021082. [https://doi.org/10.1061/\(ASCE\)PS.1949-1204.0000632](https://doi.org/10.1061/(ASCE)PS.1949-1204.0000632)
- Maser, K., & Bernhardt, M. (2000). Statewide Bridge Deck Survey using Ground Penetrating Radar. *Structural Materials Technology IV - An NDT Conference*.
- Maser KR. (1990). *New technology for bridge deck assessment, phase II report*.
- Matas, J., Chum, O., Urban, M., & Pajdla, T. (2002). Robust Wide Baseline Stereo from Maximally Stable Extremal Regions. *BMVC*.
- MathWorks, I. (2016). *Train a Cascade Object Detector*. The MathWorks, Inc.
- MathWorks, I. (2017). *Global image threshold using Otsu's method*. The MathWorks, Inc.
- Mertens, L., Persico, R., Matera, L., & Lambot, S. (2016). Automated detection of reflection hyperbolas in complex GPR images with no a priori knowledge on the medium. *IEEE Transactions on Geoscience and Remote Sensing*, 54(1), 580–596.
- Mitra, S. S. (1988). *Structured techniques of system analysis, design, and implementation*. Wiley.
- Mohamed, A., Mona, A., Mohammed, H. S., & Mohamed, M. (2021). Data Acquisition and Structural Analysis for Bridge Deck Condition Assessment Using Ground Penetration Radar. *Journal of Performance of Constructed Facilities*, 35(5), 4021064. [https://doi.org/10.1061/\(ASCE\)CF.1943-5509.0001645](https://doi.org/10.1061/(ASCE)CF.1943-5509.0001645)
- Montiel-Zafra, V., Canadas-Quesada, F. J., Vera-Candeas, P., Ruiz-Reyes, N., Rey, J., & Martinez, J. (2017). A novel method to remove GPR background noise based on the similarity of non-neighboring regions. *Journal of Applied Geophysics*, 144, 188–203. <https://doi.org/https://doi.org/10.1016/j.jappgeo.2017.07.010>
- Moore, M., Phares, B., Graybeal, B., & Rolander, D. (2001). *Reliability of visual inspection for highway bridges, volume I: Final report*.
- NCHRP Report 300. (1987). *Bridge Management Systems, National Research Council*.
- Negri, L. H., & Vestri, C. (2017). lucashn/peakutils: v1. 1.0. *Zenodo*. *Doi*, 10.
- Ni, S.-H., Huang, Y.-H., Lo, K.-F., & Lin, D.-C. (2010). Buried pipe detection by ground penetrating radar using the discrete wavelet transform. *Computers and Geotechnics*, 37(4), 440–448. <https://doi.org/https://doi.org/10.1016/j.compgeo.2010.01.003>

- Nicolas, G., Dimitrios, G., James, M., Ross, C., & John, A. (2020). Development of Novel Methodology for Assessing Bridge Deck Conditions Using Step Frequency Antenna Array Ground Penetrating Radar. *Journal of Performance of Constructed Facilities*, 34(1), 4019113. [https://doi.org/10.1061/\(ASCE\)CF.1943-5509.0001365](https://doi.org/10.1061/(ASCE)CF.1943-5509.0001365)
- Noman Ahmed, S., Farah, D., & Ashutosh, B. (2013). Health Monitoring of Structures Using Statistical Pattern Recognition Techniques. *Journal of Performance of Constructed Facilities*, 27(5), 575–584. [https://doi.org/10.1061/\(ASCE\)CF.1943-5509.0000346](https://doi.org/10.1061/(ASCE)CF.1943-5509.0000346)
- Noreen, T., & Khan, U. S. (2017). Using pattern recognition with HOG to automatically detect reflection hyperbolas in ground penetrating radar data. *2017 International Conference on Electrical and Computing Technologies and Applications (ICECTA)*, 1–6. <https://doi.org/10.1109/ICECTA.2017.8252064>
- O’Leary, P. L., & Zsombor-Murray, P. (2004). Direct and specific least-square fitting of hyperbolæ and ellipses. *Journal of Electronic Imaging*, 13(3), 492–503. <https://doi.org/10.1117/1.1758951>
- OECD. (1992). *Bridge management / report prepared by an OECD Scientific Expert Group*. (R. T. R. Programme (ed.)).
- Oh, T., Kee, S.-H., Arndt, R. W., Popovics, J. S., & Zhu, J. (2013). Comparison of NDT Methods for Assessment of a Concrete Bridge Deck. *Journal of Engineering Mechanics*, 139(3), 305–314. [https://doi.org/10.1061/\(ASCE\)EM.1943-7889.0000441](https://doi.org/10.1061/(ASCE)EM.1943-7889.0000441)
- Ojala, T., Pietikainen, M., & Maenpaa, T. (2002). Multiresolution gray-scale and rotation invariant texture classification with local binary patterns. *IEEE Transactions on Pattern Analysis and Machine Intelligence*, 24(7), 971–987.
- Olhoeft, G. R. (1984). Applications and limitations of ground penetrating radar. In *SEG Technical Program Expanded Abstracts 1984* (pp. 147–148). Society of Exploration Geophysicists.
- Olhoeft, G. R. (2000). Maximizing the information return from ground penetrating radar. *Journal of Applied Geophysics*, 43(2), 175–187. [https://doi.org/https://doi.org/10.1016/S0926-9851\(99\)00057-9](https://doi.org/https://doi.org/10.1016/S0926-9851(99)00057-9)
- Otsu, N. (1979). A Threshold Selection Method from Gray-Level Histograms. *IEEE Transactions on Systems, Man, and Cybernetics*, 9(1), 62–66. <https://doi.org/10.1109/TSMC.1979.4310076>
- Ozkaya, U., Melgani, F., Belete Bejiga, M., Seyfi, L., & Donelli, M. (2020). GPR B scan image analysis with deep learning methods. *Measurement*, 165, 107770. <https://doi.org/https://doi.org/10.1016/j.measurement.2020.107770>
- Paglieroni, D. W. (1992). Distance transforms: Properties and machine vision applications. *CVGIP: Graphical Models and Image Processing*, 54(1), 56–74. [https://doi.org/https://doi.org/10.1016/1049-9652\(92\)90034-U](https://doi.org/https://doi.org/10.1016/1049-9652(92)90034-U)
- Park, D., Park, H., Han, D. K., & Ko, H. (2014). Single image dehazing with image entropy and information fidelity. *2014 IEEE International Conference on Image Processing (ICIP)*, 4037–4041. <https://doi.org/10.1109/ICIP.2014.7025820>
- Parrillo, R., Roberts, R., & Haggan, A. (2006). Bridge deck condition assessment using ground

- penetrating radar. *Proceedings of the ECNDT, Berlin*.
- Pashoutani, S., & Zhu, J. (2023). Real Depth-Correction in Ground Penetrating RADAR Data Analysis for Bridge Deck Evaluation. In *Sensors* (Vol. 23, Issue 2). <https://doi.org/10.3390/s23021027>
- Pasolli, E., Melgani, F., & Donelli, M. (2009). Automatic Analysis of GPR Images: A Pattern-Recognition Approach. In *Geoscience and Remote Sensing, IEEE Transactions on* (Vol. 47, Issue 7, pp. 2206–2217). <https://doi.org/10.1109/TGRS.2009.2012701>
- PCA. (2016). *Corrosion of Embedded Materials*. Portland Cement Association.
- Pham, M.-T., & Lefèvre, S. (2018). Buried object detection from B-scan ground penetrating radar data using Faster-RCNN. *IGARSS 2018-2018 IEEE International Geoscience and Remote Sensing Symposium*, 6804–6807.
- Qiao, L., Qin, Y., Ren, X., & Wang, Q. (2015). Identification of Buried Objects in GPR Using Amplitude Modulated Signals Extracted from Multiresolution Monogenic Signal Analysis. In *Sensors* (Vol. 15, Issue 12, pp. 30340–30350). <https://doi.org/10.3390/s151229801>
- Qin, Y., & Huang, C. (2016). Identifying underground voids using a GPR circular-end bow-tie antenna system based on a support vector machine. *International Journal of Remote Sensing*, 37, 876–888.
- Rahman, M. A., & Zayed, T. (2018). Viola-Jones Algorithm for Automatic Detection of Hyperbolic Regions in GPR Profiles of Bridge Decks. *2018 IEEE Southwest Symposium on Image Analysis and Interpretation (SSIAI)*, 1–4. <https://doi.org/10.1109/SSIAI.2018.8470374>
- Reichman, D., Collins, L. M., & Malof, J. M. (2017). Some good practices for applying convolutional neural networks to buried threat detection in Ground Penetrating Radar. *2017 9th International Workshop on Advanced Ground Penetrating Radar (IWAGPR)*, 1–5. <https://doi.org/10.1109/IWAGPR.2017.7996100>
- Rhee, J.-Y., Park, K.-E., Lee, K.-H., & Kee, S.-H. (2020). A Practical Approach to Condition Assessment of Asphalt-Covered Concrete Bridge Decks on Korean Expressways by Dielectric Constant Measurements Using Air-Coupled GPR. In *Sensors* (Vol. 20, Issue 9). <https://doi.org/10.3390/s20092497>
- Romero, F. A., Roberts, G. E., & Roberts, R. L. (2000). Evaluation of GPR Bridge Deck Survey Results used for Delineation Of Removal/Maintenance Quantity Boundaries on Asphalt-Overlaid, Reinforced Concrete Deck. *Structural Materials Technology IV - An NDT Conference*.
- Rosin, P. L. (2001). Unimodal thresholding. *Pattern Recognition*, 34(11), 2083–2096. [https://doi.org/https://doi.org/10.1016/S0031-3203\(00\)00136-9](https://doi.org/https://doi.org/10.1016/S0031-3203(00)00136-9)
- Rosten, E., & Drummond, T. (2006). *Machine Learning for High-Speed Corner Detection BT - Computer Vision – ECCV 2006* (A. Leonardis, H. Bischof, & A. Pinz (eds.); pp. 430–443). Springer Berlin Heidelberg.
- Ryall, M. (2009). *Bridge management* (Second). Butterworth-Heinemann.
- Sabamehr, A., Lim, C., & Bagchi, A. (2018). System identification and model updating of



- highway bridges using ambient vibration tests. *Journal of Civil Structural Health Monitoring*, 8(5), 755–771. <https://doi.org/10.1007/s13349-018-0304-5>
- Sagnard, F., & Tarel, J.-P. (2016). Template-matching based detection of hyperbolas in ground-penetrating radargrams for buried utilities. *Journal of Geophysics and Engineering*, 13(4), 491–504. <https://doi.org/10.1088/1742-2132/13/4/491>
- Sakaguchi, R. T., Jr., K. D. M., Collins, L. M., & Torrione, P. A. (2015). Recognizing subsurface target responses in ground penetrating radar data using convolutional neural networks. *Proc.SPIE*, 9454, 94541A. <https://doi.org/10.1117/12.2177747>
- Sepehr, P., & Jinying, Z. (2020). Ground Penetrating Radar Data Processing for Concrete Bridge Deck Evaluation. *Journal of Bridge Engineering*, 25(7), 4020030. [https://doi.org/10.1061/\(ASCE\)BE.1943-5592.0001566](https://doi.org/10.1061/(ASCE)BE.1943-5592.0001566)
- Shan, D., & Li, Q. (2009). Development of a Smart, Client-Based Bridge Management and Maintenance System for Existing Highway Bridges. *International Conference on Transportation Engineering (ICTE)*, 345(41039), 609. [https://doi.org/10.1061/41039\(345\)609](https://doi.org/10.1061/41039(345)609)
- Shapiro, L. G., & Stockman, G. C. (2001). *Computer Vision*. Prentice Hall. <https://books.google.ca/books?id=FftDAQAAIAAJ>
- Sharp, S., & Moruza, A. (2009). *Field Comparison of the Installation and Cost of Placement of Epoxy-Coated and MFMX 2 Steel Deck Reinforcement: Establishing a Baseline for Future Deck*.
- Shaw, M. R., Millard, S. G., Molyneaux, T. C. K., Taylor, M. J., & Bungey, J. H. (2005). Location of steel reinforcement in concrete using ground penetrating radar and neural networks. *NDT & E International*, 38(3), 203–212. <https://doi.org/10.1016/j.ndteint.2004.06.011>
- Shi, J., & Tomasi. (1994). Good features to track. *1994 Proceedings of IEEE Conference on Computer Vision and Pattern Recognition*, 593–600. <https://doi.org/10.1109/CVPR.1994.323794>
- Shihab, S. (2005). *Radius Estimation for Cylindrical Objects Detected by Ground Penetrating Radar*. 6(2). <https://doi.org/10.1007/s11220-005-0004-1>
- Silano, L. G., & Parsons Brinckerhoff. (1993). *Bridge inspection and rehabilitation : A practical guide*. Wiley.
- Simi, A., Bracciali, S., & Manacorda, G. (2008). Hough transform based automatic pipe detection for array GPR: Algorithm development and on-site tests. *2008 IEEE Radar Conference*, 1–6. <https://doi.org/10.1109/RADAR.2008.4720763>
- Singh, N. P., & Nene, M. J. (2013). Buried object detection and analysis of GPR images: Using neural network and curve fitting. In *Emerging Research Areas and 2013 International Conference on Microelectronics, Communications and Renewable Energy (AICERA/ICMiCR), 2013 Annual International Conference on* (pp. 1–6). <https://doi.org/10.1109/AICERA-ICMiCR.2013.6576024>
- Strange, A., Chandran, V., & Ralston, J. (2002). *Signal Processing to Improve Target Detection Using Ground Penetrating Radar*.

- Szeliski, R. (2010). *Computer vision: algorithms and applications*.
- Tamura, H., Mori, S., & Yamawaki, T. (1978). Textural Features Corresponding to Visual Perception. *IEEE Transactions on Systems, Man, and Cybernetics*, 8(6), 460–473. <https://doi.org/10.1109/TSMC.1978.4309999>
- Tarussov, A., Vandry, M., & Blais, J. (2010). Cartographie de la corrosion d'armatures par géoradar. *17e Colloque Sur La Progression de La Recherche Québécoise Sur Les Ouvrages d'art*, Les 10 et 11 mai.
- Tarussov, A., Vandry, M., & De La Haza, A. (2013). Condition assessment of concrete structures using a new analysis method: Ground-penetrating radar computer-assisted visual interpretation. *Construction and Building Materials*, 38, 1246–1254. <https://doi.org/10.1016/j.conbuildmat.2012.05.026>
- Tatu, A., & Bansal, S. (2015). *A Novel Active Contour Model for Texture Segmentation BT - Energy Minimization Methods in Computer Vision and Pattern Recognition* (X.-C. Tai, E. Bae, T. F. Chan, & M. Lysaker (eds.); pp. 223–236). Springer International Publishing.
- Terrasse, G., Nicolas, J.-M., Trouvé, E., & Drouet, É. (2016). Automatic localization of gas pipes from GPR imagery. *2016 24th European Signal Processing Conference (EUSIPCO)*, 2395–2399. <https://doi.org/10.1109/EUSIPCO.2016.7760678>
- The MathWorks, I. (2014). *Image processing toolbox: User's guide*.
- Torrione, P. A., Morton, K. D., Sakaguchi, R., & Collins, L. M. (2014). Histograms of Oriented Gradients for Landmine Detection in Ground-Penetrating Radar Data. *IEEE Transactions on Geoscience and Remote Sensing*, 52(3), 1539–1550. <https://doi.org/10.1109/TGRS.2013.2252016>
- Travassos, X. L., Ávila, S. L., & Ida, N. (2020). Artificial Neural Networks and Machine Learning techniques applied to Ground Penetrating Radar: A review. *Applied Computing and Informatics*.
- Ulriksen, C. P. F. (1982). *Application of impulse radar to civil engineering*. PhD Lund University of Technology.
- Utsi, E. C. (2017). *Ground penetrating radar: theory and practice*. Butterworth-Heinemann.
- Varnavina, A. V., Khamzin, A. K., Torgashov, E. V., Sneed, L. H., Goodwin, B. T., & Anderson, N. L. (2015). Data acquisition and processing parameters for concrete bridge deck condition assessment using ground-coupled ground penetrating radar: Some considerations. *Journal of Applied Geophysics*, 114, 123–133. <https://doi.org/10.1016/j.jappgeo.2015.01.011>
- Viola, P., & Jones, M. J. (2004). Robust Real-Time Face Detection. *International Journal of Computer Vision*, 57(2), 137–154. <https://doi.org/10.1023/B:VISI.0000013087.49260.fb>
- Wang, J., & Su, Y. (2013). Fast detection of GPR objects with cross correlation and hough transform. *Progress In Electromagnetics Research C*, 38, 229–239. <https://doi.org/10.2528/PIERC13022510>
- Wang, Yanhui, Cui, G., & Xu, J. (2020). Semi-automatic detection of buried rebar in GPR data using a genetic algorithm. *Automation in Construction*, 114, 103186.

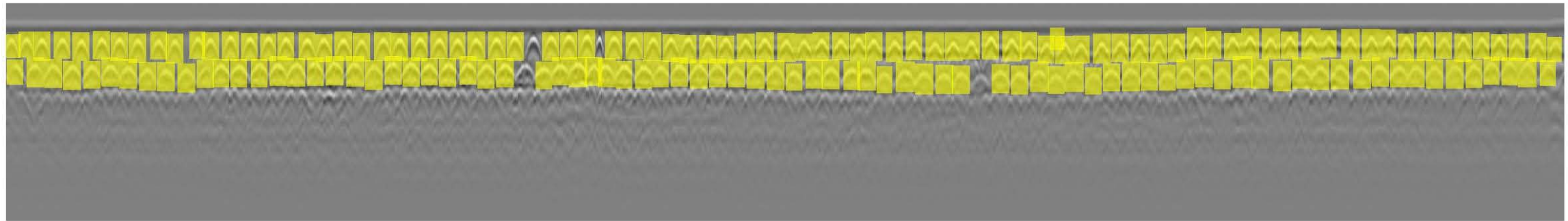
<https://doi.org/https://doi.org/10.1016/j.autcon.2020.103186>

- Wang, YQ. (2014). An analysis of the Viola-Jones face detection algorithm. *Image Processing On Line*.
- Wang, Z. W., Zhou, M., Slabaugh, G. G., Zhai, J., & Fang, T. (2011). Automatic detection of bridge deck condition from ground penetrating radar images. *IEEE Transactions on Automation Science and Engineering*, 8(3), 633–640.
- Windsor, C. G., Capineri, L., & Falorni, P. (2014). A Data Pair-Labeled Generalized Hough Transform for Radar Location of Buried Objects. *IEEE Geoscience and Remote Sensing Letters*, 11(1), 124–127. <https://doi.org/10.1109/LGRS.2013.2248119>
- Wunderlich, T., Wilken, D., Majchczack, B. S., Segschneider, M., & Rabbel, W. (2022). Hyperbola Detection with RetinaNet and Comparison of Hyperbola Fitting Methods in GPR Data from an Archaeological Site. In *Remote Sensing* (Vol. 14, Issue 15). <https://doi.org/10.3390/rs14153665>
- Xu, R., & Wunsch, D. (2005). Survey of clustering algorithms. *IEEE Transactions on Neural Networks*, 16(3), 645–678. <https://doi.org/10.1109/TNN.2005.845141>
- Yan, B., Wang, B., & Li, Y. (2008). Optimal ellipse fitting method based on least-square principle. *Beijing Hangkong Hangtian Daxue Xuebao/Journal of Beijing University of Aeronautics and Astronautics*, 34, 295–298.
- Yanev, B. (2007). *Bridge management*. Wiley.
- Yehia, S., Abudayyeh, O., Nabulsi, S., & Abdelqader, I. (2007). Detection of Common Defects in Concrete Bridge Decks Using Nondestructive Evaluation Techniques. *Journal of Bridge Engineering*, 12(2), 215–225. [https://doi.org/10.1061/\(ASCE\)1084-0702\(2007\)12:2\(215\)](https://doi.org/10.1061/(ASCE)1084-0702(2007)12:2(215))
- Yilmaz, O. (1987). Seismic data processing. *Investigation in Geophysics*, 2, 526.
- Yu-Chen, Z., Ting-Hua, Y., Shibin, L., Hong-Nan, L., & Songtao, L. (2022). Automatic Corrosive Environment Detection of RC Bridge Decks from Ground-Penetrating Radar Data Based on Deep Learning. *Journal of Performance of Constructed Facilities*, 36(2), 4022011. [https://doi.org/10.1061/\(ASCE\)CF.1943-5509.0001712](https://doi.org/10.1061/(ASCE)CF.1943-5509.0001712)
- Zaki, A., Jusman, Y., Johari, M. A. M., & Hussin, W. (2020). Image Processing for Corrosion Quantification in Concrete Slabs using GPR data. *Journal of Physics: Conference Series*, 1471(1), 12049.
- Zhang, X., Bolton, J., & Gader, P. (2014). A New Learning Method for Continuous Hidden Markov Models for Subsurface Landmine Detection in Ground Penetrating Radar. *IEEE Journal of Selected Topics in Applied Earth Observations and Remote Sensing*, 7(3), 813–819. <https://doi.org/10.1109/JSTARS.2014.2305981>
- Zhang, X., Han, L., Robinson, M., & Gallagher, A. (2021). A Gans-Based Deep Learning Framework for Automatic Subsurface Object Recognition From Ground Penetrating Radar Data. *IEEE Access*, 9, 39009–39018. <https://doi.org/10.1109/ACCESS.2021.3064205>
- Zhou, X., Chen, H., & Li, J. (2018). An Automatic GPR B-Scan Image Interpreting Model. *IEEE Transactions on Geoscience and Remote Sensing*, 56(6), 3398–3412. <https://doi.org/10.1109/TGRS.2018.2799586>

Zong, Z., Chen, C., Mi, X., Sun, W., Song, Y., Li, J., Dong, Z., Huang, R., & Yang, B. (2019). A DEEP LEARNING APPROACH FOR URBAN UNDERGROUND OBJECTS DETECTION FROM VEHICLE-BORNE GROUND PENETRATING RADAR DATA IN REAL-TIME. *Int. Arch. Photogramm. Remote Sens. Spatial Inf. Sci.*, XLII-2/W16, 293–299. <https://doi.org/10.5194/isprs-archives-XLII-2-W16-293-2019>

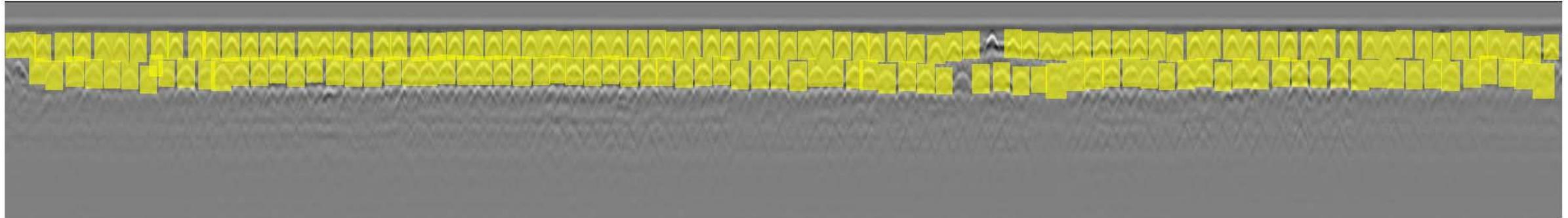
## 8 APPENDIX

This chapter showcases the hyperbolic detections obtained for each profile during the training phase of the V-JAM model. There are twenty-four profiles in the bridge deck, O2, and hyperbolic detections are shown in each profile during the training stage of the custom classifier based on the Viola-Jones Algorithm along with possible missing detections (false negatives) and false detections (false positives) in both layers.



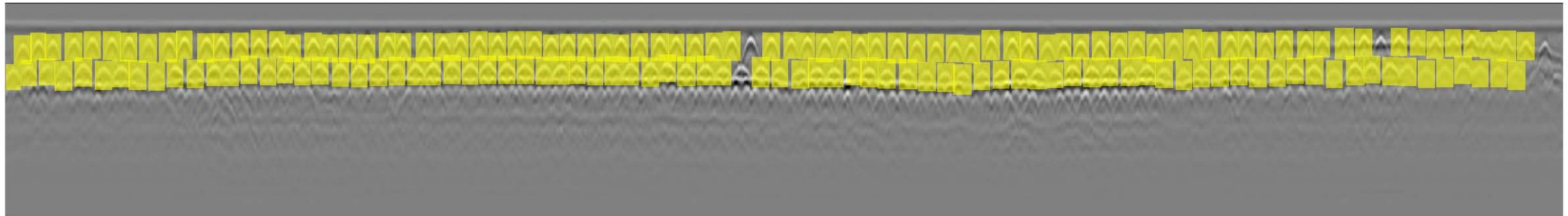
**Profile 1 Total Detections: 164/222**

Possible Missing Detections	False Detections
3	1 (Hyperbola Present but insignificant)



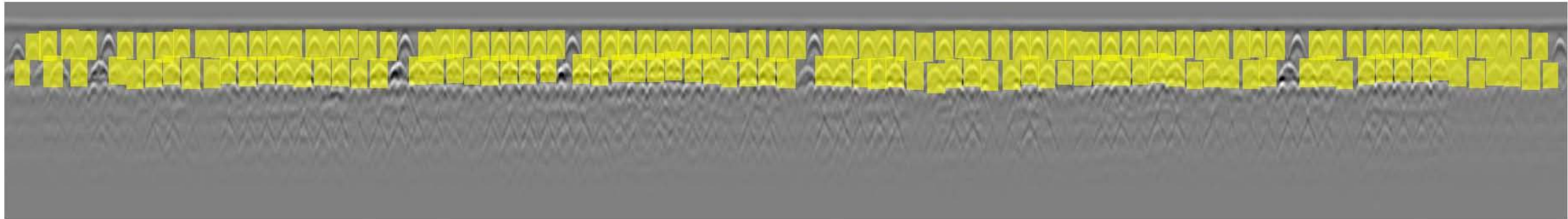
**Profile 2 Total Detections: 165/203**

Possible Missing Detections	False Detections
3	1



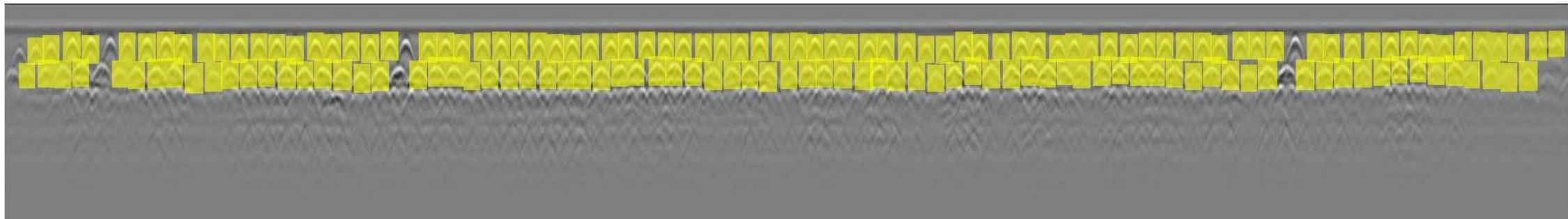
**Profile 3 Total Detections: 163/215**

Possible Missing Detections	False Detections
5	0



**Profile 4 Total Detections: 154/192**

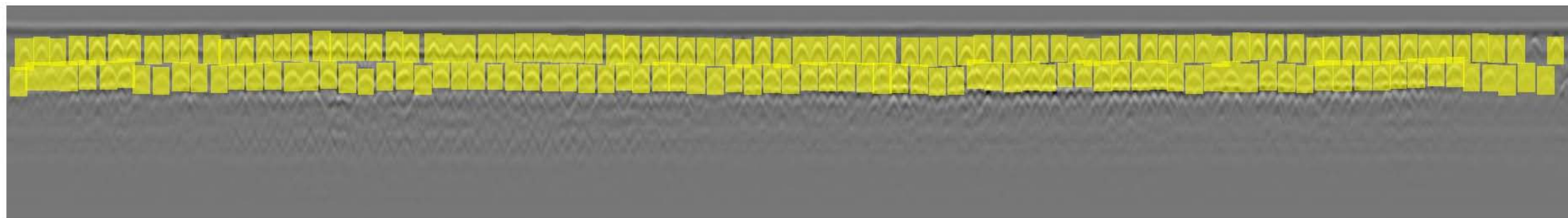
Possible Missing Detections	False Detections
13	0



**Profile 5 Total Detections: 159/220**

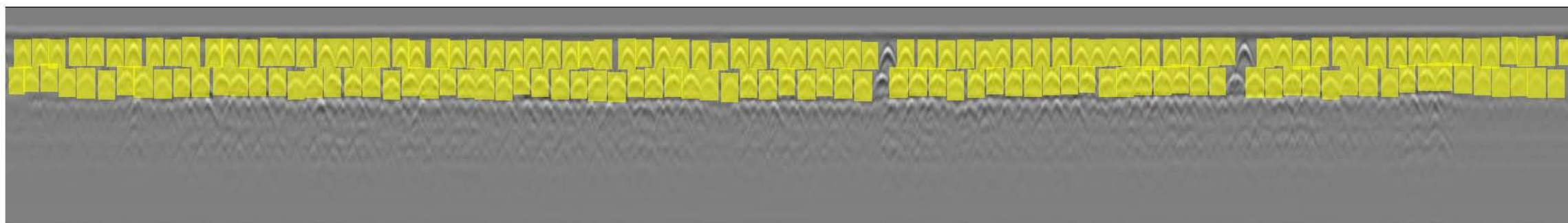
Possible Missing Detections	False Detections
7	0





**Profile 6 Total Detections: 167/200**

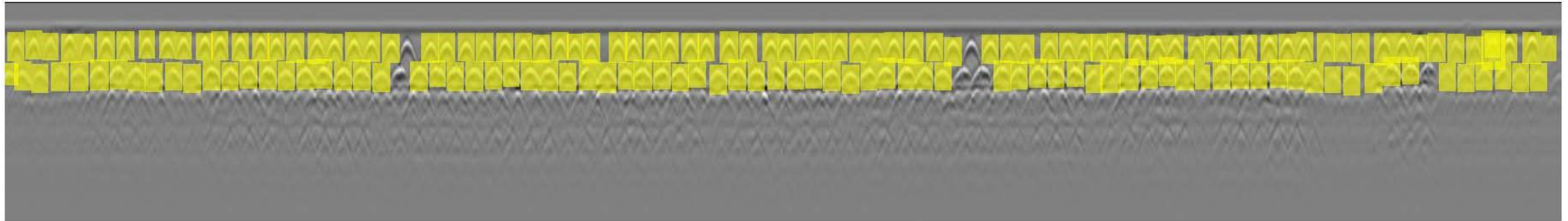
Possible Missing Detections	False Detections
2	0



**Profile 7 Total Detections: 162/219**

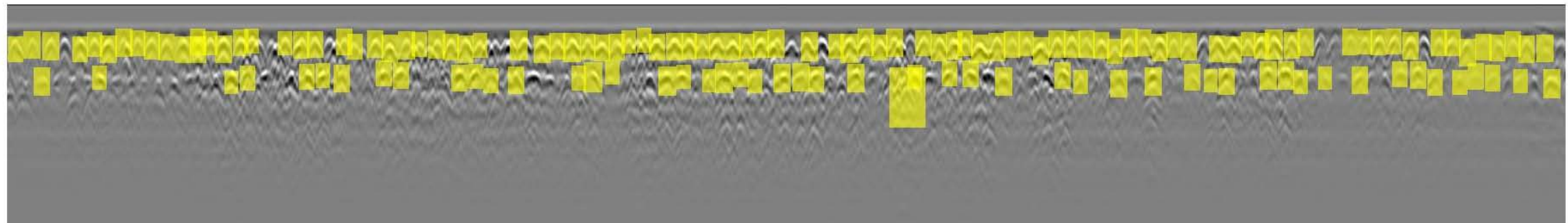
Possible Missing Detections	False Detections
4	0





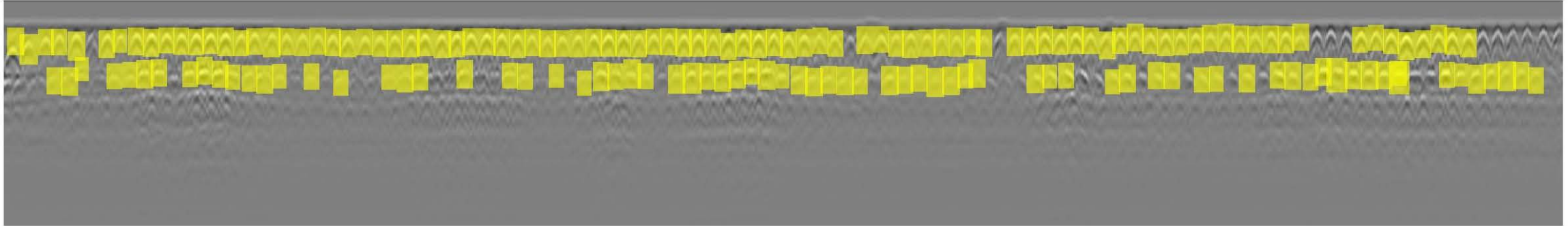
**Profile 8 Total Detections: 161/236**

Possible Missing Detections	False Detections
6	1



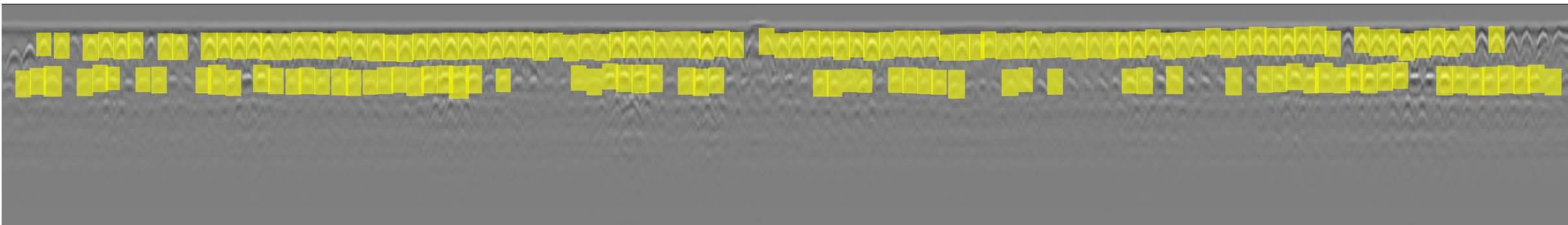
**Profile 9 Total Detections: 144/201**

Possible Missing Detections	False Detections
44	1



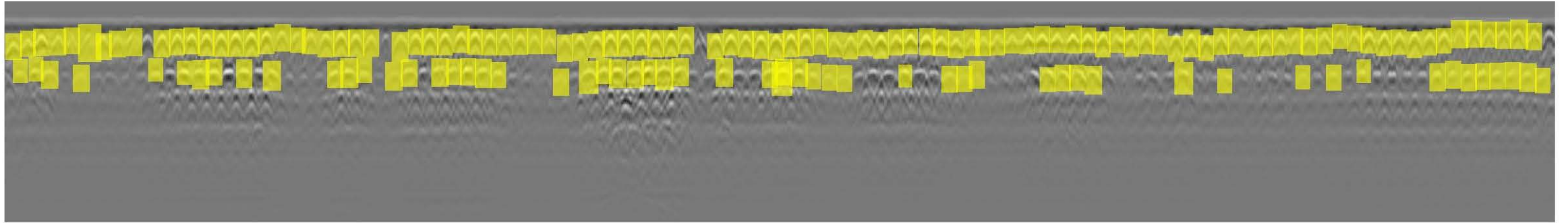
**Profile 10 Total Detections: 166/205**

Possible Missing Detections	False Detections
38	0



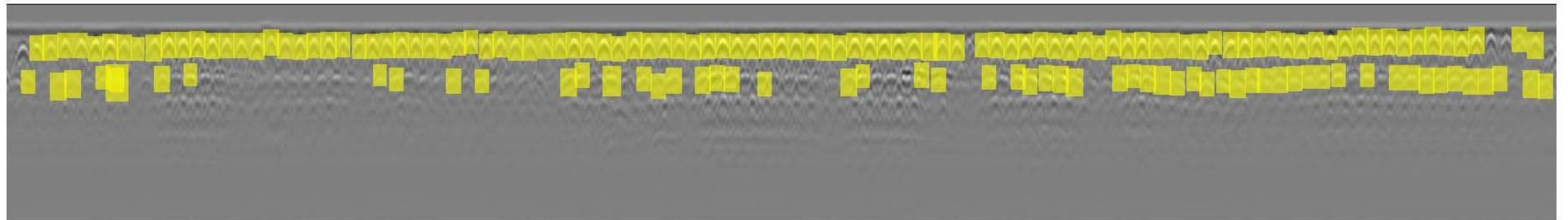
**Profile 11 Total Detections: 162/191**

Possible Missing Detections	False Detections
41	0



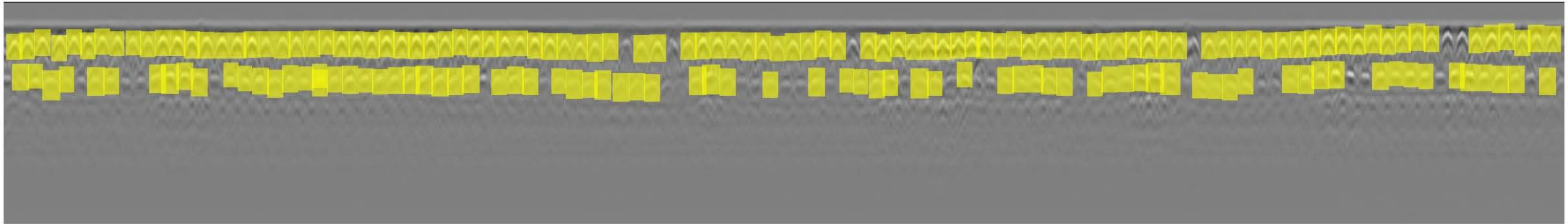
**Profile 12 Total Detections: 157/187**

Possible Missing Detections	False Detections
47	1



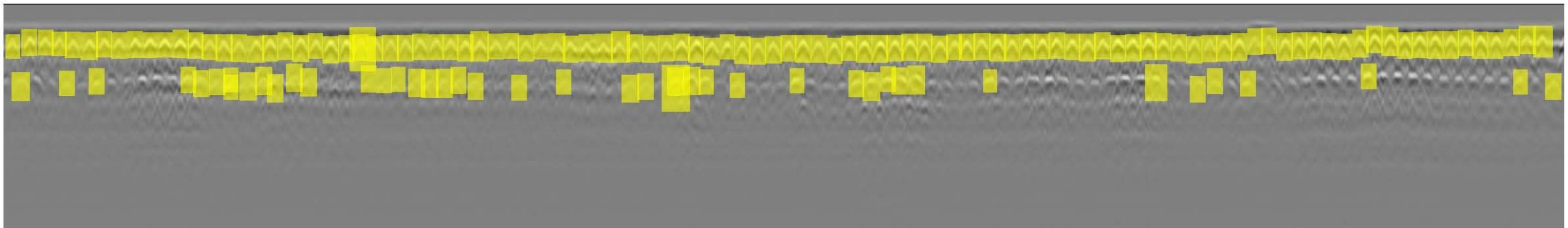
**Profile 13 Total Detections: 160/187**

Possible Missing Detections	False Detections
48	1



**Profile 14 Total Detections: 177/196**

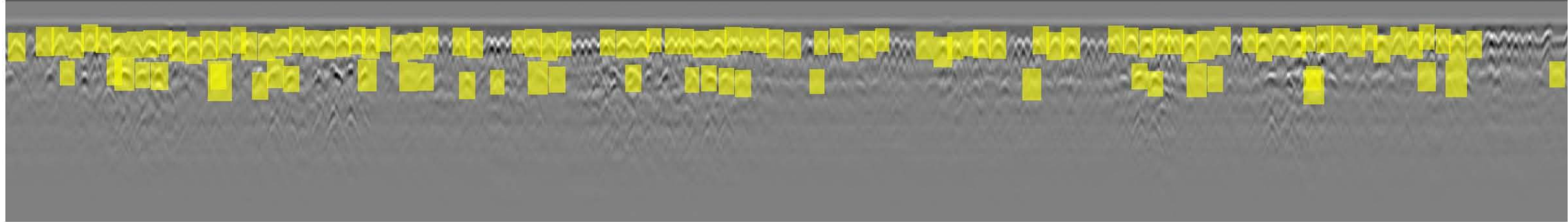
Possible Missing Detections	False Detections
31	1



**Profile 15 Total Detections: 147/156**

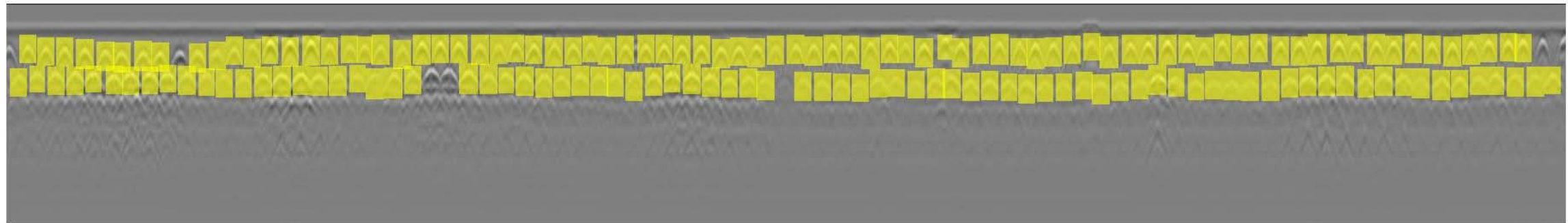
Possible Missing Detections	False Detections
48	2





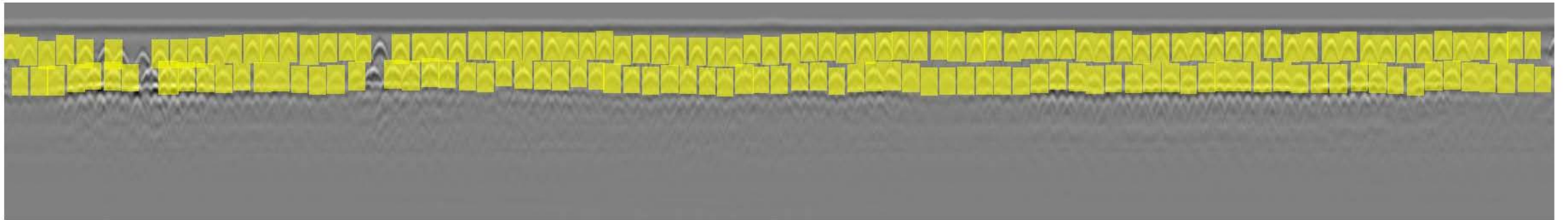
**Profile 16 Total Detections: 153/118**

Possible Missing Detections	False Detections
46	3



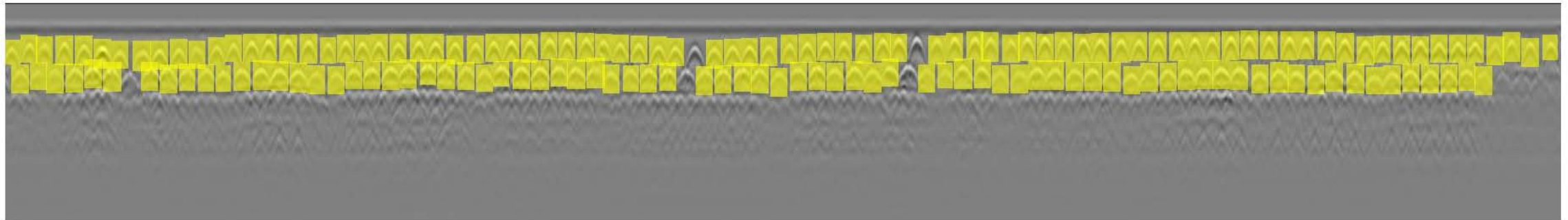
**Profile 17 Total Detections: 160/191**

Possible Missing Detections	False Detections
5	0



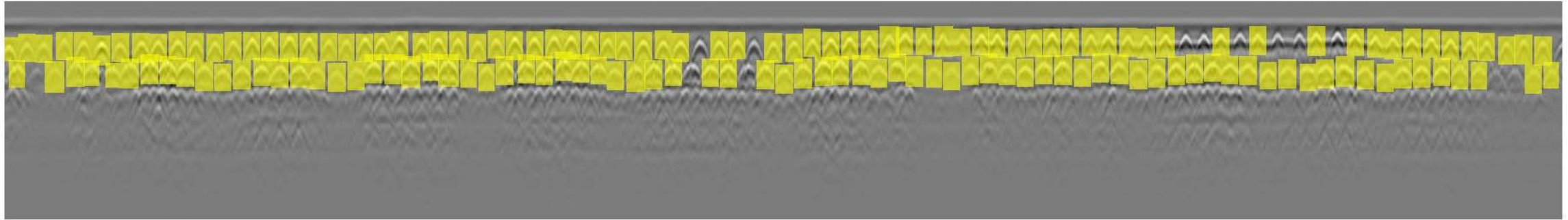
**Profile 18 Total Detections: 161/204**

Possible Missing Detections	False Detections
6	0



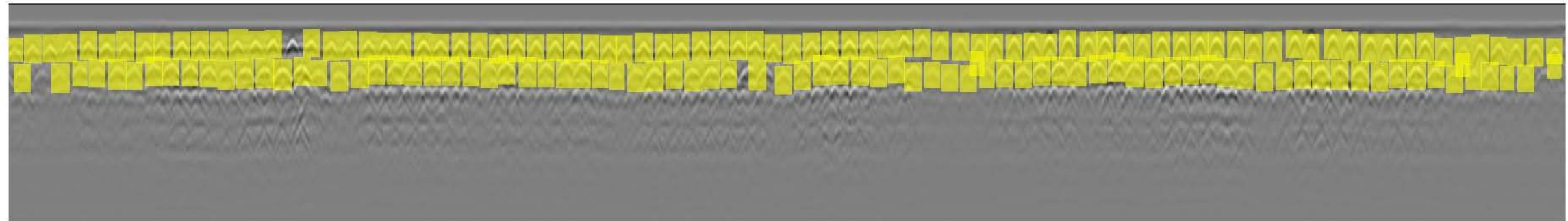
**Profile 19 Total Detections: 159/209**

Possible Missing Detections	False Detections
8	0



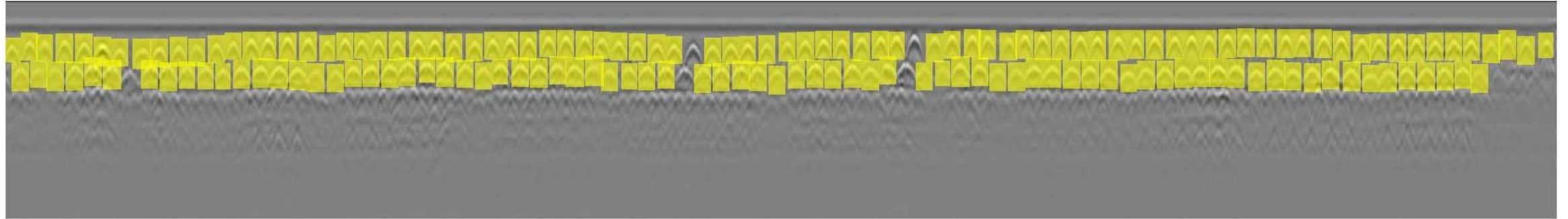
**Profile 20 Total Detections: 153/213**

Possible Missing Detections	False Detections
14	0



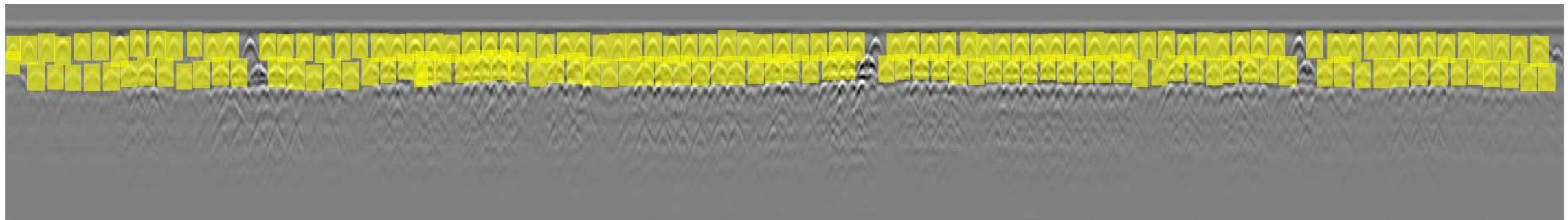
**Profile 21 Total Detections: 166/215**

Possible Missing Detections	False Detections
3	2



**Profile 22 Total Detections: 161/218**

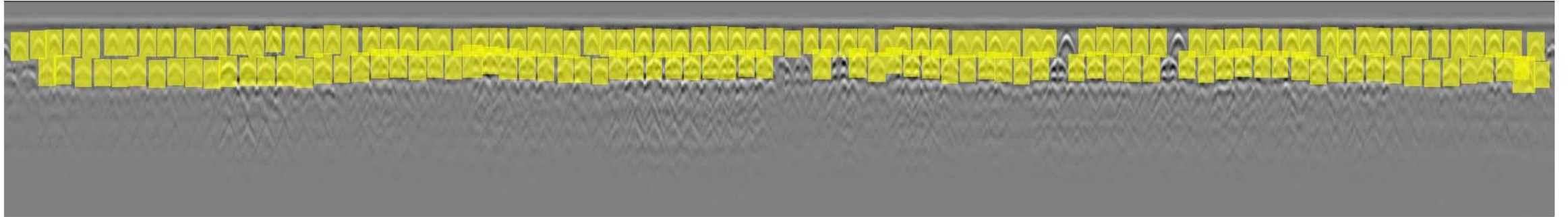
Possible Missing Detections	False Detections
7	0



**Profile 23 Total Detections: 163/207**

Possible Missing Detections	False Detections
6	0





**Profile 24 Total Detections: 159/197**

<b>Possible Missing Detections</b>	<b>False Detections</b>
8	1